



## **Comparative corrosion studies of additive manufactured and conventional Fe-Alloys in physiological electrolytes**

### **Dissertation**

in fulfilment of requirements for the degree of  
Doctor of Science (Dr. rer. nat.)  
at the University Paderborn  
Faculty of Science  
Department of Chemistry

submitted by  
**Jingyuan Huang, M. Sc.**  
born on 01.01.1993 in Shandong, China

at the chair of Prof. Dr.-Ing. Guido Grundmeier  
Technical and Macromolecular Chemistry



**Examination board:**

Chair	Prof. Dr. Martin Brehm
First examiner and the first referee	Prof. Dr.-Ing. Guido Grundmeier
Second examiner and the second referee	Prof. Dr.-Ing. Thomas Niendorf
Third examiner	Dr. Jürgen Schmidtke
Submission of the thesis:	18.09.2023



## **Statutory Declaration**

I hereby declare that I have authored this thesis independently, that I have not used other than the declared sources/resources, and that I have explicitly marked all material which has been quoted either literally or by content from the used sources. I am aware that the respective work can be considered as a "fail" in the event of a false declaration.

Jingyuan Huang  
Paderborn, den 18.09.2023



## Abstract

Iron-based alloys possess excellent mechanical properties and great biocompatibility, rendering them highly promising for use as biodegradable metal implants in orthopedics and cardiovascular medicine applications. The main challenge in the development of Fe-based alloys is their slow degradation. Improving the corrosion rate of Fe must consider its own properties as well as the influence of the target environment.

The primary objective of the thesis is to investigate the corrosion behavior of iron-based biodegradable materials under physiological conditions, with the goal of developing new biodegradable metallic implants for medical applications. The implant material is ultimately faced with the human environment, adsorption of proteins is the first step that happens after the implant is implanted in the body, and it further affects the corrosion properties of metal materials. Therefore, the multiprotein adsorption in diluted human serum on gold and oxidized iron surfaces was first investigated in relation to serum concentration and pH value. The adsorption of serum proteins on the surface shows pH-dependent effects. In order to investigate the performance of Fe-based alloys in the presence of protein, the effect of bovine serum albumin (BSA) and lysozyme (LYZ) on the corrosion of selective laser beam melted and a conventional processed cold-rolled FeMn alloy as well as hot-rolled pure iron was investigated in modified simulated body fluid (m-SBF). FeMn alloys show higher corrosion rates than pure iron, and moreover, additive manufactured FeMn alloys outperform hot-rolled FeMn, which can be explained by differences in microstructure and chemical composition resulting from the manufacturing method. Related corrosion kinetics could be clearly correlated with film formation in m-SBF electrolytes in the presence and absence of proteins. To gain deeper insights into this potential correlation, agar hydrogel film was applied between the pure Fe and m-SBF to investigate surface corrosion. This study shows that the application of hydrogel film on alloy surfaces may affect the interfacial reaction and the formation of interfacial corrosion products. Subsequently, in order to simulate the real in vivo environment more closely and consider the rich variety of proteins present in body fluids along with their possible competing interactions with surfaces, pure Fe was exposed to media containing human serum, which was used to assess the corrosion of Fe in the presence of multi-component proteins.

The possible corrosion mechanisms of iron-based alloys in physiological electrolytes were examined through the application of electrochemical methods (OCP, EIS). Additionally, changes in substrate topography before and after corrosion were assessed using microscopic techniques (AFM, SEM). Spectroscopic methods (PM-IRRAS, FT-IRRAS, ATR-IR, Raman, XPS) were employed to determine the composition of the corrosion product layer and to provide evidence of protein adsorption on the surface.

In summary, this thesis explores the corrosion of promising iron-based alloys in physiological electrolytes from multiple perspectives, including manufacturing methods, alloying, and the influence of proteins. This research contributes to the development of biodegradable medical devices by exploring potential corrosion mechanisms and degradation behavior, facilitating the selection of appropriate materials.

## Table of Contents

<b>Abstract .....</b>	<b>I</b>
<b>1 Introduction .....</b>	<b>1</b>
<b>1.1 Motivation .....</b>	<b>1</b>
<b>1.2 Research objectives and scientific approach.....</b>	<b>2</b>
<b>1.3 Thesis layout.....</b>	<b>5</b>
<b>2 Materials and applications of biodegradable alloys.....</b>	<b>7</b>
<b>2.1 Biodegradable metals alloys .....</b>	<b>7</b>
<b>2.1.1. Biodegradable Mg and Mg alloys.....</b>	<b>8</b>
<b>2.1.2. Biodegradable Zn and Zn alloys .....</b>	<b>9</b>
<b>2.1.3. Biodegradable Fe and Fe alloys .....</b>	<b>10</b>
<b>2.1.3.1 Pure Iron .....</b>	<b>11</b>
<b>2.1.3.2 FeMn Alloy .....</b>	<b>13</b>
<b>2.1.3.3 Other Fe-based materials.....</b>	<b>15</b>
<b>2.2 Manufacturing methods of alloys.....</b>	<b>17</b>
<b>2.2.1. Conventional manufacture techniques .....</b>	<b>19</b>
<b>2.2.2. Additive manufacturing .....</b>	<b>19</b>
<b>3 Corrosion mechanisms in physiological environments.....</b>	<b>22</b>
<b>3.1 Corrosion of metallic implants .....</b>	<b>22</b>
<b>3.1.1. The biological environment .....</b>	<b>23</b>
<b>3.1.2. Commonly used media for in vitro corrosion test .....</b>	<b>23</b>
<b>3.1.3. Corrosion of Fe-based materials in the physiological environment .....</b>	<b>25</b>
<b>3.1.4. The proposed corrosion mechanism of Fe .....</b>	<b>27</b>
<b>3.1.5. The proposed corrosion mechanism of FeMn .....</b>	<b>31</b>
<b>3.2 Protein Adsorption on solid surfaces .....</b>	<b>32</b>
<b>3.2.1. Protein structure .....</b>	<b>32</b>
<b>3.2.2. Surface adsorption of protein on material surfaces.....</b>	<b>32</b>
<b>3.2.3. Effect of protein adsorption on corrosion .....</b>	<b>37</b>
<b>3.2.4. Influence of proteins on corrosion of metallic implants .....</b>	<b>38</b>
<b>4 Fundamentals of applied experimental methods .....</b>	<b>40</b>
<b>4.1 Electrochemical techniques .....</b>	<b>40</b>
<b>4.1.1. Electrochemical impedance spectroscopy .....</b>	<b>40</b>

4.1.2. Application of electrochemical impedance spectroscopy in corrosion .....	43
4.1.3. Cyclic voltammetry .....	45
<b>4.2 Spectroscopic techniques.....</b>	<b>46</b>
4.2.1. Fourier-transformed infrared spectroscopy .....	47
4.2.2. Fourier-transformed infrared reflection absorption spectroscopy.....	48
4.2.3. Polarization modulation infrared reflection-adsorption spectroscopy .....	50
4.2.4. Diffuse reflectance infrared Fourier transform spectroscopy .....	51
4.2.5. Attenuated total reflection FTIR spectroscopy .....	52
4.2.6. Raman spectroscopy.....	54
4.2.7. X-ray photoelectron spectroscopy.....	55
<b>4.3 Ellipsometry .....</b>	<b>57</b>
<b>4.4 Atomic force microscope .....</b>	<b>58</b>
<b>4.5 Scanning electron microscope.....</b>	<b>60</b>
<b>5 Experimental.....</b>	<b>63</b>
<b>5.1 Materials and chemicals .....</b>	<b>63</b>
5.1.1. Chemicals and electrolyte .....	63
5.1.2. Protein .....	64
5.1.3. Metals and preparation of alloys .....	64
<b>5.2 Preparation of additive manufactured Fe alloys .....</b>	<b>64</b>
<b>5.3 Preparation of thin metal oxidized surfaces.....</b>	<b>65</b>
<b>5.4 Surface preparation of metal alloys .....</b>	<b>65</b>
5.4.1. Mechanical polishing .....	65
5.4.2. Electropolishing .....	66
5.4.3. Chemical etching.....	66
<b>5.5 Electrochemical measurements .....</b>	<b>66</b>
5.5.1. EIS measurements .....	66
5.5.2. Cyclic voltammetry measurements .....	66
<b>5.6 Surface analysis.....</b>	<b>67</b>
5.6.1. Ellipsometry .....	67
5.6.2. AFM characterization.....	67
5.6.3. SEM, EDX and FIB characterization.....	67
5.6.4. Infrared spectroscopy .....	68
5.6.4.1 PM-IRRAS .....	68

5.6.4.2 FT-IRRAS .....	68
5.6.4.3 ATR-FTIR .....	68
5.6.4.4 <i>In situ</i> ATR-FTIR.....	68
5.6.5. Raman spectroscopy .....	68
5.6.6. XPS characterization.....	69
<b>6 Results and discussion.....</b>	<b>70</b>
<b>6.1 Multiprotein adsorption on oxidized metal surfaces.....</b>	<b>70</b>
6.1.1. Materials and chemicals.....	71
6.1.2. Experimental approach .....	71
6.1.2.1 Serum exposure .....	71
6.1.2.2 Cyclic voltammetry .....	71
6.1.2.3 Surface analysis .....	72
6.1.3. XPS characterization of deposited Fe films.....	72
6.1.4. AFM characterization .....	73
6.1.5. Cyclic voltammograms .....	77
6.1.6. Analysis of protein adsorption film thickness .....	77
6.1.7. PM-IRRAS results .....	78
6.1.8. Conclusions.....	84
<b>6.2 Influence of proteins on the corrosion of a conventional and selective laser beam melted FeMn alloy .....</b>	<b>85</b>
6.2.1. Materials and chemicals.....	86
6.2.2. Experimental approach .....	87
6.2.2.1 Corrosion testing .....	87
6.2.2.2 Surface analysis .....	87
6.2.3. Microstructural characterization of FeMn-LBM .....	88
6.2.4. Electrochemical analysis.....	89
6.2.5. Microscopic studies of surface layer formation.....	98
6.2.5.1 Optical microscope characterization .....	98
6.2.5.2 AFM characterization.....	99
6.2.5.3 FE-SEM and EDX characterization .....	102
6.2.6. Vibrational spectroscopy of the surface layers .....	105
6.2.6.1 ATR-FTIR and FT-IRRA spectroscopy .....	105
6.2.6.2 Raman spectroscopy.....	109

6.2.7. Conclusions .....	111
<b>6.3 Influence of hydrogel coatings on corrosion of iron in m-SBF .....</b>	<b>112</b>
6.3.1. Materials and chemicals .....	113
6.3.2. Experimental approach.....	113
6.3.2.1 Preparation of hydrogel films .....	113
6.3.2.2 Electrochemical impedance analysis .....	114
6.3.2.3 Attenuated total reflection FTIR spectroscopy .....	114
6.3.2.4 Surface analysis .....	114
6.3.3. Results and discussion.....	114
6.3.3.1 Electrochemical corrosion analysis .....	114
6.3.3.2 ATR-FTIR spectroscopy of electrolyte uptake in hydrogel films .....	118
6.3.3.3 FE-SEM characterization of interface after exposure to m-SBF.....	119
6.3.3.4 Raman spectroscopy and microscopic characterization .....	121
6.3.3.5 DRIFT-FTIR spectroscopy .....	123
6.3.3.6 XPS characterization .....	123
6.3.4. Conclusions .....	125
<b>6.4 Corrosion of pure iron in human serum.....</b>	<b>126</b>
6.4.1. Materials and chemicals .....	127
6.4.2. Experimental approach.....	127
6.4.2.1 Sample preparation .....	127
6.4.2.2 Electrochemical measurements .....	127
6.4.2.3 Surface characterization .....	128
6.4.3. Results and discussion.....	128
6.4.3.1 Electrochemical measurment results .....	128
6.4.3.2 Surface Characterization by SEM .....	132
6.4.3.3 Raman spectroscopy and FT-IRRAS .....	135
6.4.3.4 XPS analysis of iron surfaces after corrosion.....	138
6.4.3.5 Discussion of the influence of HS on iron corrosion in PBS .....	140
6.4.4. Conclusions .....	143
<b>7 Overall conclusions and outlook.....</b>	<b>144</b>
<b>7.1 Overall conclusions .....</b>	<b>144</b>
<b>7.2 Outlook .....</b>	<b>146</b>

<b>References .....</b>	<b>148</b>
<b>List of abbreviations and symbols .....</b>	<b>164</b>
<b>List of publications and conferences .....</b>	<b>170</b>
<b>Funding and Contributions .....</b>	<b>172</b>
<b>Permissions.....</b>	<b>173</b>
<b>Acknowledgement .....</b>	<b>174</b>



## 1 Introduction

### 1.1 Motivation

The concept of biodegradable materials aims at overcoming the disadvantages of conventional permanent implant materials [1]. For example, the function of cardiovascular stents is only to provide effective physical support to the wall of the blood vessel for 6 to 12 months, after which the vessel is functionally stable, and the stent has no further purpose. However, if the stent remains in the body for a long time, the patient will face the risk of developing chronic inflammation, restenosis or late-stage thrombosis [2,3]. In contrast, the ideal biodegradable material would provide only temporary support, subsequently degrade and be safely absorbed by the body [4]. Therefore, the design and development of suitable biodegradable materials is a central goal in the biomedical field [5–7].

In the past decades, extensive research on biodegradable metals has been done. Thereby magnesium (Mg), zinc (Zn), and iron (Fe) alloys are the most studied materials due to their inherent biocompatibility and potential for degradation in the body [8,9]. Among them, focused research has been carried out on Mg-based alloys, which are now in the clinical stage [10–13]. Mg-based alloys have the highest dissolution rates [14], which also means it loses integrity when it is still needed. Zinc alloys have also been considered potential biodegradable materials, but their low tensile strength limits their application [15,16]. More recently, there is a growing interest in the development of Fe-based alloys as biodegradable materials, which are the most promising alternative to magnesium alloys, especially for orthopedic and cardiovascular applications [17], as they have comparable mechanical properties to permanent implant materials such as stainless steel [18–21].

Fe is an essential element involved in many iron-containing enzymes and proteins. The potential biomedical applications of pure iron have been investigated, and *in vivo* animal studies have confirmed the biocompatibility of iron [22]. However, *in vivo* degradation rate is comparable to that of permanently implanted devices [23]. Additionally, its ferromagnetic properties limit its use as an implantable device in modern clinical medicine. The Iron–manganese (FeMn) system has been developed to increase the corrosion rate through galvanic corrosion resulting from the difference in electrochemical properties [24,25]. Additionally, alloying has been shown to solve compatibility issues for magnetic resonance imaging (MRI) devices. FeMn alloys have demonstrated good mechanical properties and biocompatibility, making them promising candidates for use as biodegradable materials [26].

Another focus in the development of Fe-based biomaterials is the processing, which affects the microstructure of the metal material and thus has a significant impact on the mechanical and corrosion properties of the implant. Methods for manufacturing biodegradable implantable devices should have the ability to allow the production of specific shapes and formats, customizing the device to the patient's needs. As a result, additive manufacturing such as selective laser melting, is gaining widespread interest in the medical industry. It has been demonstrated that FeMn scaffolds produced by additive manufacturing processes show promising degradation rates [27–29]. By considering the research findings reported so far, it can be concluded that the development of Fe-based biodegradable materials is highly promising.

To develop suitable medical materials, the influence of physiological environments on material performance must be considered. Currently, the *in vitro* and *in vivo* studies of iron-based alloys have not reached a consensus. For example, iron alloys with differences in corrosion rates in *in vitro* corrosion experiments have shown very similar behavior in animal experiments. This may be due to the complex physiological environment of the human body. In addition to cells and tissues, the human body contains a large number of inorganic components such as phosphates, organic molecules such as sugars, and biological polymers such as proteins, which are dissolved in various body fluids. Implants in contact with such a complex physiological environment are subject to corrosion, protein adsorption, and cell adhesion [30]. As the research on iron-based biodegradable materials is still in the early stages, there is a lack of systematic study on their corrosion behavior in physiological environments. Therefore, it is necessary to evaluate the effects that these different components possibly exert on the implant *in vitro* before the implant can be tested *in vivo*.

## 1.2 Research objectives and scientific approach

The objective of this work is to evaluate the corrosion behavior of iron-based alloys under physiological conditions. With a focus on the potential biomedical applications of the alloys, the corrosion performance of promising iron-based materials was explored by considering various factors, including manufacturing methods, alloying, electrolytes, and protein species. By investigating these factors, the aim is to understand and predict the possible corrosion mechanisms and degradation behavior of iron-based materials under complex physiological conditions, which will help to select suitable materials for the development of degradable implantable medical devices. The approaches are described in detail as follows and schematically shown in Figure 1.1.

- Protein adsorption on surface

Protein adsorption on implantable biomaterial surfaces is a crucial phenomenon influencing material properties. In this context, the present study first explores the key factors influencing protein adsorption, with a particular focus on investigating the effects of pH value, protein concentration, protein types, and metal interface properties. As shown in Figure 1.1, in section 6.1, the adsorption of proteins on the thin metal film surface is studied. Gold is selected as a chemically inert model surface, whereas iron is chemically reactive and prone to corrosion and dissolution in physiological electrolytes; this is related to the subsequent discussion on the corrosion of iron-based alloys in the following sections. The effects of serum concentration and pH value are considered. Atomic force microscopy (AFM) is used to obtain information about changes in surface topography due to the adsorbed protein film. Polarization-modulation infrared reflection absorption spectroscopy (PM-IRRAS) is used to assess the total amount of adsorbed protein and additionally allows qualitative detection of changes in film composition.

- Corrosion studies in physiological electrolytes

The forthcoming sections center on exploration on the corrosion behavior exhibited by iron-based alloys. Specifically, section 6.2 aims to comprehend the impact of manufacturing processes on corrosion performance by comparing FeMn alloys produced through both traditional methods and additive manufacturing, with the focus on selective laser melting (SLM) technology, which is a promising technique for crafting biodegradable implants. Assessing the performance and suitability of materials generated via SLM is of paramount importance, as it holds the potential to advance the field of bioresorbable materials in medical applications. Consequently, this study selects FeMn alloys fabricated using SLM technology as the focal point of investigation. To investigate the influence of proteins on the corrosion behavior of promising iron-based materials, two distinct protein species are selected for examination. The primary objective is to gain a comprehensive understanding of the underlying mechanisms by which proteins impact the corrosion process (see section 6.2). The corrosion properties are investigated by electrochemical impedance spectroscopy (EIS), which provides valuable information about corrosion kinetics and possible corrosion mechanisms through the analysis of spectra and fitting of impedance data. Surface characterization is carried out by AFM, field emission scanning electron microscopy (FE-SEM), Raman spectroscopy, and Fourier-Transform Infrared Spectroscopy (FTIR) to

correlate the surface material and the adsorbate layer composition with the corrosion behavior.

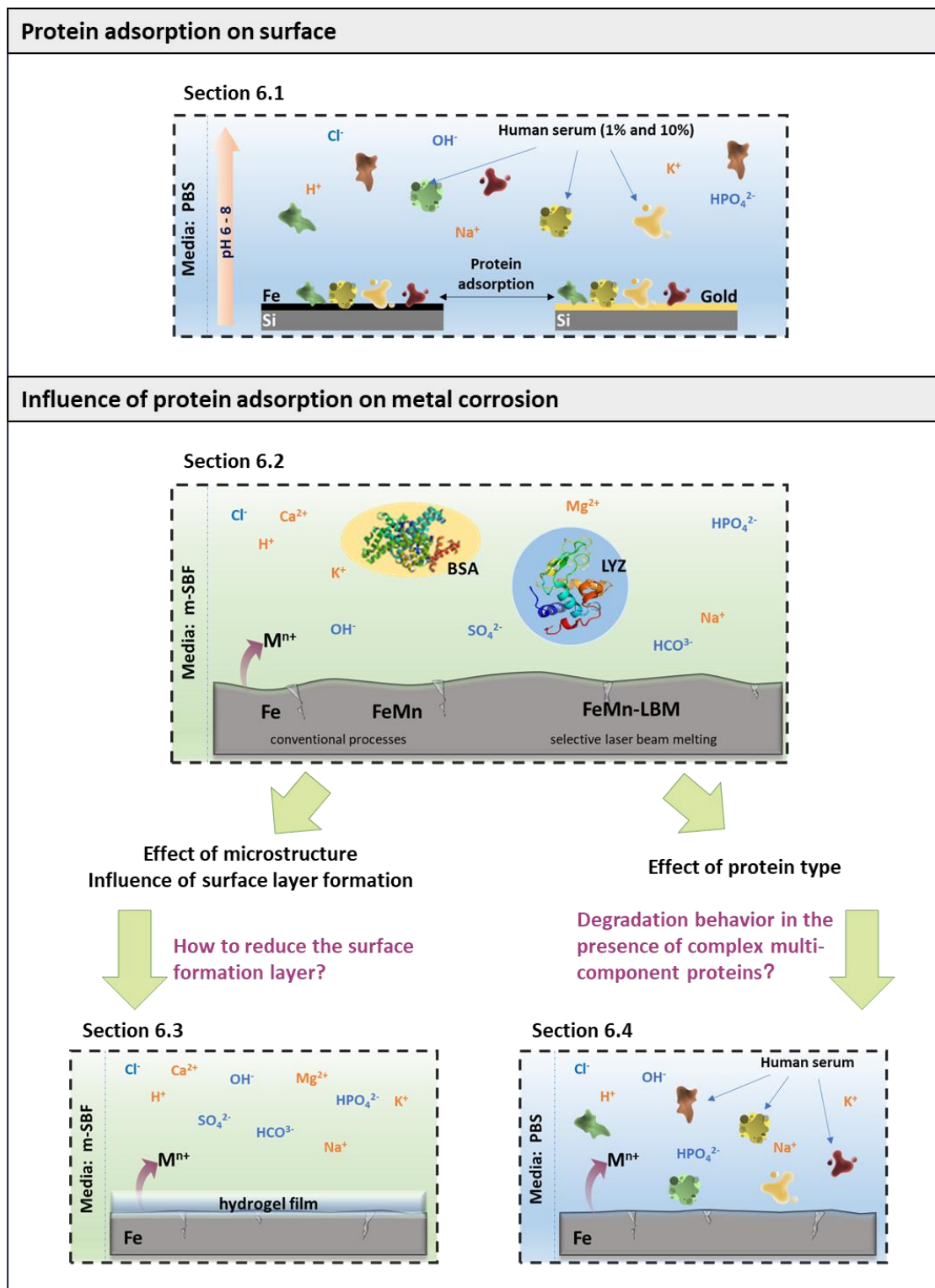


**Figure 1.1** Schematic diagram of the main research content of the thesis.

As is widely recognized, the inadequate corrosion rate represents a critical challenge in the development of iron-based bioresorbable materials. The formation of corrosion product layers may play a significant role in regulating the corrosion stability and rate of these materials. Consequently, a hydrogel film is devised and applied to the surface of pure iron with the purpose of elucidating the potential corrosion behavior and the mechanisms governing the formation of corrosion product layers at the interface (see section 6.3). This endeavor aims to provide valuable insights for the subsequent development process, specifically in devising strategies to mitigate the formation of corrosion inhibition layers. The corrosion properties of Fe alloys are studied using EIS with and without an applied agar hydrogel film. The swelling process of the hydrogel film is effectively analyzed with the use of *in situ* FTIR in attenuated total reflection (ATR). FE-SEM, Raman spectroscopy and X-ray photoelectron spectroscopy (XPS) are employed with the aim of correlating the surface composition and morphology after the corrosive attack of the corrosive environment."

In order to further assess the suitability of iron-based materials as resorbable implants, it is essential to consider the complexity of real physiological environments in more detail. Among the influencing factors that cannot be ignored is the high abundance of serum proteins. As such, the corrosion behavior of pure iron in serum with varying concentrations is meticulously investigated (see section 6.4). The aim is to simulate the intricate conditions of *in vivo* environments by applying human serum as a relevant experimental medium. The evaluation results contribute to better predicting the performance of the material and biocompatibility when implanted in the actual body, thereby providing stronger support for its clinical application.

### 1.3 Thesis layout

This thesis consists of **7 chapters**, and part of the presented results has been published by the author of this thesis [31–33].

**Chapter 1** introduces the relevant background information and outlines the objectives of the study. It also provides an overview of the entire thesis.

**Chapter 2** presents the current status of research and offers an extensive literature review on the development of biodegradable metal biomaterials, with a particular emphasis on iron-based biomaterials. This chapter also includes an overview of the manufacturing process of biodegradable metallic materials.

**Chapter 3** focuses on the corrosion process of iron-based alloys and their influencing factors in physiological environments. The basic concepts are introduced, including electrolytes, corrosion mechanisms, protein adsorption on solid surfaces, and the factors that influence them.

The basic principles of the experimental methods used are described in **Chapter 4** describes.

**Chapter 5** described in detail the experimental setup and specifications of the samples, chemicals, and methods used in the study.

**Chapter 6** discusses the experimental results and evaluates the corrosion behavior of iron-based alloys under different physiological conditions.

Finally, **Chapter 7** summarizes this dissertation of this study and provides an outlook for future developments.

## 2 Materials and applications of biodegradable alloys

### 2.1 Biodegradable metals alloys

Bioresorbable and biodegradable are two terms commonly used in the field of biomaterials, particularly in relation to temporary biomedical implants. While the terms are often used interchangeably, they actually have distinct meanings [34]. Biodegradable refers to materials that are able to break down or degrade through natural processes when partially or fully exposed to the physiological environment over time. This process may involve the complete breakdown of the material or its remodeling in the human body. Bioresorbable refers to materials where the implant or its degradation products are removed through cellular activity in a biological environment. This process is different from biodegradation in that it involves the breakdown of the material by cells in the body itself. Not all degradable materials are absorbable, as some degradation processes may not render the material soluble and therefore will not permit its elimination from the body. Ultimately, these terms describe different aspects of the transformation and/or disappearance of a material or implant after introduction into the body. In the development of temporary biomedical implants, biodegradable materials are considered desirable for applications in orthopedic and vascular devices, where most medical researchers reserve the term degradation for the transformative step that changes the material physicochemical properties [35]. In this thesis, the primary emphasis is placed on metallic materials that exhibit significant potential as biodegradable materials.

Biodegradable metals can consist of pure metals, alloys, or metal matrix composites, and they can be used in medical applications to design biodegradable implants [9]. The selection of the appropriate metal and alloying elements is a crucial step in the design and development of biodegradable implants, as the alloying elements and material microstructure play a significant role in determining the mechanical properties, corrosion behaviors, and biocompatibility of implants. The purpose of biodegradable implants is to provide temporary support to the tissue. After implantation, they are exposed to the physiological environment and gradually begin to corrode, producing corrosion products and causing a host reaction. During the entire degradation process, it is required to maintain biocompatibility, not induce inflammatory reactions or toxicity, and ensure that the degradation products can be safely absorbed. In consideration of the design intent of absorbable metal materials, metals selected for development need to be non-toxic and metabolizable by the human body. Table 2.1 provides a summary of the essential and potentially essential nutrients, metals, and common alloying elements present in the human body, along with their concentrations and

thresholds [1]. It is important to note that imbalances in these concentrations, whether too high or too low, can have negative impacts on human health. Therefore, the selection and use of alloying elements must be carefully adjusted to meet the mechanical requirements of the implant while maintaining biocompatibility. The three most promising biodegradable metals in clinical use are Fe, Mg, and Zn. Other trace elements in the human body, such as manganese (Mn) or calcium (Ca), can be considered suitable candidates for alloying elements.

**Table 2.1** The summary of the pathophysiology and toxicology of Mg, Fe, Zn, and the commonly used alloying elements [1].

Element	Human amount	Blood serum level	Daily allowance	Bone cell <sup>d</sup>	Vascular cell <sup>d</sup>
Essential nutrients					
Mg	25 g	0.73 – 1.06 mM	0.7 g	+	+
Fe	4-5 g	5.0 – 17.6 g/l	10 – 20 mg	+-	+-
Ca	1100 g	0.919 – 0.993 mM	0.8 g	+	+
Zn	2 g	12.4 – 17.4 $\mu$ M	15 mg	-	-
Mn	12 mg	< 0.8 $\mu$ g/l	4 mg	-	-
Potential essential metal					
Sr	0.3 g	0.17 mg <sup>a</sup>	2 mg	+	+
Si	-	-	-		
Sn	30 mg	-	-	+-	+-
Other elements					
Li		-	0.1 g <sup>b</sup>	+	+
Al	< 300mg	2.1 – 4.8 $\mu$ g/l	-	+	+
Zr	< 250 mg		3.5 g	+	+
Y and lanthanides	-	< 47 $\mu$ g <sup>c</sup>	-	+-	+-

<sup>a</sup> Sr concentration in total blood [36].

<sup>b</sup> The therapeutic dose for lithium carbonate is up to about 0.1 g/d in divided doses [36].

<sup>c</sup> The concentrations for Y and lanthanides (La, Ce, Nd, Sm, Eu, Gd, Tb, Dy, Ho, Er, Tm and Yb) are below 0.1, 0.44, 0.03, 0.07, 0.2, 0.1, 0.09, 0.1, 0.2, 0.03, 0.1 and 0.1 mg/l, respectively [36].

<sup>d</sup> The toxicity levels for bone- and vascular-related cells are according to the cytotoxicity test of the metal salts [37–39]; (+-) stands for the mild toxicity, (+) stands for the moderate toxicity, and (-) stands for the severe toxicity.

### 2.1.1. Biodegradable Mg and Mg alloys

Mg was first developed as a resorbable implant material. Mg is the fourth most common cation in our body, is non-toxic and easily tolerated, and its deficiency can lead to cardiovascular disease. Magnesium is the closest biomechanical material to natural bone

among all biodegradable metallic materials. Due to the poor mechanical properties of pure magnesium, early clinical applications were limited. In 1878, physician Edward C. Huse [40] first used the biodegradable properties of Mg for clinical applications when he used magnesium wires as ligatures to stop vascular bleeding in a radial artery and varicocele surgery in human patients. This led to a large number of scientific studies about the medical applications of Mg. Soon some study scholars pointed out the limitations of the application, the insufficient mechanical properties of pure magnesium, and the release of hydrogen gas during corrosion [41,42]. However, the lack of mature metallurgical technology to control the rapid degradability of Mg at that time limited the development of Mg materials. The addition of appropriate alloying elements can effectively improve the mechanical properties of Mg. Therefore, with the improvement of metal purification technology and various alloying techniques, Mg and Mg alloys have attracted the attention of researchers again. Over the past two decades, Mg-based materials have been recognized as having potential for development in various medical fields such as orthopedic implants, cardiovascular stents, sutures, surgical clips, and staples, and have made leaps from in vitro testing to successful implantation. In 2013, a biodegradable magnesium alloy coronary stent from Biotronic, Germany, and a biodegradable magnesium alloy screw used in clinical trials for the treatment of bunion surgery from Syntellix Co., Germany, received the CE mark. Mg-based screws MAGNEZIX® (Syntellix, Hannover, Germany) are now commercially available and used in clinical trials to heal/repair bone defects in children, young people, and adults. Currently, Mg-based biodegradable substrates can be divided into four major groups: pure Mg, aluminum-containing alloys (AZ91, AZ31, LAE422, AM60, etc.), rare-earth elements containing alloys (AE21, WE43, etc.), and aluminum-free alloys (WE43, MgCa, MgZn).

Nevertheless, Mg-based degradable alloys still face a number of fundamental challenges for medical applications, mainly focusing on improving mechanical properties, slowing down the degradation rate, and the generation of hydrogen gas, which accompanies the process of rapid biodegradation.

### 2.1.2. Biodegradable Zn and Zn alloys

Zinc is one of the essential nutrients, along with Mg, present mainly in skeletal muscles and bones (86%) [43]. Zinc plays a role in the structure, catalysis and regulation of more than 300 enzymes and is a component of many proteins, making it a vital factor in human health [44]. Therefore, the zinc ions released by degradation can be well metabolized and absorbed without systemic toxicities [45]. Because the chemical potential of Zn is between Mg and

Fe, they exhibit more suitable biodegradation rates. The biodegradation process of Zn does not produce hydrogen gas, which is an advantage over Mg-based alloys in this respect. In addition to this, the biodegradation products of Zn are biocompatible, while those of Fe-based alloys have been reported to aggregate in organs [16,46]. Zn-based biodegradable materials have been gaining interest in recent years and are considered to be a new class of biodegradable materials. The starting application of Zn in biodegradable materials was used as an alloying element. In 2007, Wang et al. [47] designed Zn-Mg alloys with Mg content ranging from 35 to 45 wt% and evaluated the mechanical properties and corrosion behavior in simulated body fluid (SBF). The limitation of pure Zn as an implant material is based on its low strength (UTS 30 MPa) and plasticity ( $\epsilon < 0.25\%$ ) [9], which does not satisfy clinical needs. Hence improving the mechanical properties is the focus of developing Zn-based materials. For pure Zn, the mechanical properties can be improved by the thermomechanical refinement of grain size, extrusion, rolling, etc [48]. To achieve higher strength and hardness, alloying is one of the most powerful tools. Currently, binary Zn alloy systems with Mg, Ca, Sr, Li, Mn, Fe, Cu, and Ag and ternary alloy systems such as Zn-Al-Mg, Zn-Ag-Zr, Zn-Ca-Sr, etc, have been constructed [43].

There is no denying the potential of Zn-based alloys as possibilities for biodegradable materials. However, research on biomedical Zn-based materials is still in its early stages and confronts several challenges.

### 2.1.3. Biodegradable Fe and Fe alloys

Iron is a metal element that is abundant and essential in the body. As shown in Table 2.1, for adults, the recommended daily intake of iron is approximately 10-20 mg, with a maximum allowable intake of 45 mg/day. The total body weight of a normal adult person contains 3-5 g of Fe. [49] Up to 70% of Fe in the human body is stored in hepatocytes and reticuloendothelial macrophages, about 30% is held in hemoglobin in circulating erythrocytes, and the remaining amounts are found in cytochromes, iron-containing enzymes, and myoglobin. [50] Depending on the chemical properties of iron, it can exhibit a variety of oxidation states (-2 to +6), of which Fe(II) and Fe(III) are two common valence states, and the redox processes that occur between the different valence states provide the driving force for a variety of biological functions, including but not limited to the oxygen sensing, transport, short-term oxygen storage, catalysis, electron transfer and energy generation [49].

In 2001 the first iron biodegradable stent was implanted in New Zealand white rabbits aorta, the stent was made of pure iron by laser cut [22]. During the follow up of 6-18 months, there were no pronounced inflammatory responses, systemic toxicity and other harmful effects. Since then, iron has been widely investigated by researchers as a developable biodegradable material. The significant advantage of iron as a biodegradable material is its mechanical properties, especially in cardiovascular stent applications. Iron has high strength, ductility, and formability in comparison with Mg and Zn (Table 2.2), which means that thinner structures and struts or the manufacture of specially shaped stands are available.

**Table 2.2** *The mechanical properties of biodegradable metals [19].*

	<b>Yield Strength (MPa)</b>	<b>Young's Modulus (GPa)</b>	<b>Tensile Strength (MPa)</b>	<b>Shear Modulus (GPa)</b>	<b>Elastic Modulus (GPa)</b>	<b>Hardness (HV)</b>	<b>Ref.</b>
Mg	51	44 – 45.5	175 – 235	16 – 18	44 – 48	38	[51,52]
Zn	285 – 325	90 – 110	90 – 200	35 – 45	14 – 32	42	[53]
Fe	108 – 122	204 – 212	230 – 345	78 – 84	195 – 235	157	[54,55]
316SS	190	193 – 200	515 – 860	80 – 83	193	150	[1]

However, iron and iron-based alloys show too low biodegradation rates to complete degradation in the desired time period. Nevertheless, due to their great biocompatibility and excellent mechanical properties, there are still high expectations for Fe-based alloys and continuing development of feasible methods to accelerate corrosion.

#### 2.1.3.1 Pure Iron

Pure iron has mechanical properties close to SS316L and has the most advantages as a cardiovascular stent material in competition with Zn and Mg, thanks to its tensile strength and ductility. Iron stents can theoretically be manufactured thinner, and the great ductility of the Fe stents permits good plastic deformation during vascular deployment [56]. The corrosion of metals *in vivo* generally initiates with anodic dissolution, and Fe(II) is released from the iron metal surface, where they could either be oxidized to Fe(III) or interact with nearby cells. Restenosis in stents caused by excessive neointimal smooth muscle cell (SMC) growth is a common issue in implantation, and studies have shown that Fe(II) could reduce the vascular SMC proliferation rate and inhibit excessive neointimal growth [57]. Iron and its alloys are promising to be an alternative to permanent stents, especially in cardiovascular and orthopedic applications.

Biomedical materials require extensive in vitro and in vivo testing in order to evaluate their structure and function, toxicology, biocompatibility, and many other properties before they are introduced into the clinic.

So far, an in vivo evaluation of pure iron implants has been carried out in rabbit, minipig, rat and mouse animal models. In 2001, the first pure iron stent implanted in rabbits had no signs of inflammation, neointima proliferation, or systemic toxicity during the 18-month follow-up period [22]. Subsequently, in 2006, Pausel et al. [23] implanted stents made of pure iron (>99.5 mass%) into the aorta of piglets and followed for 12 months, which showed no signs of iron overload or iron-related organ toxicity. In 2007 Waksman et al. [58] compared the performance of iron stents with conventional cobalt chromium stents in the coronary arteries of juvenile domestic pigs, and the safety and efficacy of iron stents were reconfirmed. In 2013 Wu et al. [59] evaluated the degradation of iron stents and the safety of the degradation products using a mini-swine model, where corrosion of the iron stents was observed after four weeks, and the iron staining in the tissue surrounding the iron stents at 28 days was positive, and no abnormal histopathological changes were detected in coronary arteries or major organs. In 2017, Liu et al. [60] conducted a long-term observational trial using porcine and rabbit models in which nitride iron scaffolds were implanted in rabbit aorta for 36 months and porcine aorta for 53 months, respectively, and both showed good long-term biocompatibility. Recently, a novel nitride iron scaffold has been investigated in vivo. Feng et al. [61] reported histopathological evaluations of a scaffold in coronary arteries of mini-swine after 4, 12, 26, 52 weeks and even seven years of implantation, with results showing long-term biocompatibility. In addition, for orthopedic applications, bioabsorbable iron-Based porous interference Screws (ISs) developed through additive manufacturing were implanted in rabbits for short- and long-term observation and Fe-based ISs provided mechanical superiority and high absorptivity [46,62].

In vitro testing of biomaterials is typically performed in a physiological environment according to ISO 10993-5:2009 guidelines for immersion testing and electrochemical testing to assess their biocompatibility and corrosion properties. Among them, immersion experiments can be further divided into static and dynamic types. By designing the experiments properly, the effects of various environmental factors such as temperature, pH, flow rate, ionic composition, and protein on the materials can be investigated separately. By assessing cytotoxicity, hemocompatibility, mutagenesis/carcinogenesis, and cell bio function, biocompatibility is evaluated [63]. For example, Zhu et al. [64] investigated the in

vitro degradation kinetics of iron by immersing pure iron in SBF. They adjusted the flow rate of SBF to simulate the same shear stress as the in vivo environment and, by measuring the mass loss, estimated the mean degradable rate of pure iron as  $20.4 \text{ } \mu\text{g}/(\text{cm}^2 \cdot \text{h})$ . Biocompatibility was assessed by observing the metabolic activity of endothelial cells in different Fe (III) concentrations, and the results showed that higher iron ion concentrations decreased metabolic activity. The degradation rates reported in in vitro tests are usually very different from those in vivo. This is due to the complex environment in the human body, where multiple factors, such as inorganic, organic, cellular, osmotic pressure, blood flow rate, etc., act together on the implanted material. It is difficult for in vitro testing to fully simulate the complex physiological environment in vivo. Therefore, the biocompatibility of medical devices needs to be assessed jointly through in vitro and in vivo tests that carefully examine local and systemic effects on cells, tissues, or the entire body.

Even though pure iron is considered biocompatible, the in vivo corrosion rate of pure iron as an implant material is poor. Pure iron stent still exists after 18 months of implantation in white rabbits [22,23]. Moreover, pure iron implants are not compatible with MRI devices due to their ferromagnetic nature.

### 2.1.3.2 FeMn Alloy

Alloying is a process that accelerates the corrosion of pure iron and ensures its mechanical properties. The corrosion rate of Fe can be increased by alloying with different elements to create micro galvanic corrosion processes in two main ways [65]:

- i. The reduction in corrosion resistance of the substrate is achieved by adding elements with a lower electrochemical potential than iron and which are soluble in iron.
- ii. The addition of metals more noble than iron creates a second phase with a greater electrochemical potential, resulting in electrochemical corrosion where iron acts as the anode and the nobler metal acts as the cathode.

Mn, as an essential element in the human body, has a lower chemical potential ( $-1.18 \text{ V vs. SHE}$ ) than Fe and can be soluble in each other, thus making it a suitable alloying element. In addition, alloying with Mn promotes antiferromagnetic behavior and solves the MRI incompatibility of pure iron. Considerable results have been achieved with FeMn alloys. In 2007, Hermawan and his team first approached the feasibility of FeMn alloys as promising biodegradable materials [24]. They fabricated an iron-35 wt% manganese (Fe-35Mn) alloy

by a powder metallurgy (PM) process and investigated their degradation properties in circulating modified Hank's solution. Fe-35Mn is an austenitic alloy with a low magnetic susceptibility of  $148 \text{ nm}^3/\text{kg}$ , and its behavior is not significantly changed by successive cold rolling and sintering cycles. Its mechanical properties are similar to those of 316L stainless steel. Preliminary degradation tests also showed suitable degradation behavior with a uniform corrosion mechanism as well as ion release within physiological levels. Since then, Hermawan and Mantovani et al. [66] have continued to work on the effects of fabrication, alloying elements, and weight percentage on the properties of FeMn alloys. They developed a series of FeMn alloys with Mn contents between 20 and 35 wt% with the aim of obtaining mechanical properties similar to 316L stainless steel and a more suitable degradation behavior than pure iron [66]. The mechanical properties of a series of FeMn alloys and the degradation properties in modified Hank's solution at  $37 \pm 1 \text{ }^\circ\text{C}$  are shown in Table 2.3 and Table 2.4, respectively. Upon evaluation of the various indicators, Fe-30%Mn and Fe-35%Mn stood out as candidate alloys worthy of further development.

**Table 2.3** Mechanical properties of FeMn alloys [66].

Material	Ultimate Strength (MPa)	Yield Strength (MPa)	Elongation at Break (%)	Hardness (Rockwell A)
Fe20Mn	$702 \pm 11$	$421 \pm 27$	$7.5 \pm 1.5$	$59 \pm 1$
Fe25Mn	$723 \pm 19$	$361 \pm 33$	$4.8 \pm 0.4$	$56 \pm 1$
Fe30Mn	$518 \pm 14$	$239 \pm 13$	$19.0 \pm 1.4$	$40 \pm 1$
Fe35Mn	$428 \pm 7$	$234 \pm 7$	$32.0 \pm 0.8$	$38 \pm 2$

**Table 2.4** Corrosion rate of FeMn alloys in Comparison to pure iron [66].

Material	$I_{corr}$ ( $\mu\text{A}/\text{cm}^2$ )		CR (mm/year)	
	Quenched	Cold Rolled	Quenched	Cold Rolled
Fe20Mn	$113 \pm 4$	$39 \pm 2$	$1.3 \pm 0.1$	$0.5 \pm 0.1$
Fe25Mn	$91 \pm 4$	$40 \pm 1$	$1.1 \pm 0.1$	$0.5 \pm 0.1$
Fe30Mn	$56 \pm 5$	$57 \pm 2$	$0.7 \pm 0.1$	$0.7 \pm 0.1$
Fe35Mn	$37 \pm 3$	$55 \pm 3$	$0.4 \pm 0.1$	$0.7 \pm 0.1$
Iron <sup>a</sup>	$16 \pm 2$		$0.2 \pm 0.1$	

$I_{corr}$ , corrosion current density; CR, corrosion rate.

<sup>a</sup>Iron (99.8% purity), annealed plate, Goodfellow Corporation, Oakdale, PA, USA.

Further, Hermawan and Mantovani et al. [26] went on to study the biocompatibility of FeMn alloys, which is a necessary step for the development of degradable biomaterials. Degradation tests, as well as cell viability tests, were performed on FeMn alloys with Mn content between 20 and 35 produced by the PM process. The degradation medium was modified Hank's solution at 37°C and was observed in a test bench designed to mimic blood flow conditions in the human coronary artery for three months. A water-soluble tetrazolium test method was used to study the effect of the degradation product of FeMn alloys on the viability of fibroblast cells. The results show that the average corrosion rate of FeMn alloy is about twice as fast as that of pure iron and has a lower inhibition effect on the metabolic activities of 3T3 mouse fibroblast cells. This study further confirms the development potential of FeMn alloys as a biocompatible degradable biomaterial [26].

Based on this favorable evidence, FeMn alloys have received increasing attention in the last decade, and multiple alloys have been developed based on them. For example, Hong et al. [67] designed FeMn-Ca and FeMn-Mg alloys and reported that the 3D printed FeMn-Ca exhibited high corrosion rates than FeMn. Theoretically, the degradation rate can be increased by adding noble metals such as Cu, Ag, and Pb as alloying elements, which can induce micro galvanic corrosion [68–70]. The addition of carbon to Fe-Mn can produce a compositionally consistent alloy of twinning-induced plasticity (TWIP) steels.

### 2.1.3.3 Other Fe-based materials

Liu et al. [71] developed a series of Fe-3 at.%X (X =Mn, Co, Al, W), Sn, C, B and S binary alloys to investigate the effect of common alloying elements on the corrosion rate and biocompatibility of pure iron. They prepared six binary alloys in a vacuum induction furnace under an argon atmosphere and evaluated their microstructure, mechanical properties, corrosion rate, cytotoxicity, and hemocompatibility. The corrosion rates obtained by static and dynamic immersion tests in Hank's solution and by the electrochemical approach are summarized in Table 2.5. Both pure iron and Fe-X binary alloys showed localized corrosion in Hank's solution and exhibited similar corrosion rates. Mechanical test results showed that the addition of alloying elements, except for Sn, which reduced the yield strength of the alloy, improved the mechanical properties of pure iron after rolling. However, it should be noted that ferromagnetism is still present in the case of low content of alloying elements, which has a negative impact on clinical MRI examination. Overall, the results of all experiments recommended the development of Co, W, C and S as suitable alloy elements and suggested to try high content alloy additions and multi-component iron alloys.

**Table 2.5** *Electrochemical data and corrosion rates calculated from different measurements of Fe-X binary alloys with pure iron as a control in Hank's solution [71].*

	$V_{corr}$ (V)	$I_{corr}$ ( $\mu\text{A cm}^{-2}$ )	$v_{corr}$ ( $\text{mm year}^{-1}$ )	Corrosion rate ( $\text{g m}^{-2} \text{d}$ )		
				Electrochemical	static	Dynamic
Pure iron						
As-cast	-0.748	8.961	0.105	2.240	0.256	4.033
As-rolled	-0.702	8.768	0.103	2.192	0.166	3.133
Fe-Mn						
As-cast	-0.711	9.004	0.105	2.251	0.038	0.956
As-rolled	-0.68	7.454	0.087	1.863	0.028	0.678
Fe-Co						
As-cast	-0.713	10.966	0.128	2.741	0.250	1.367
As-rolled	-0.693	12.099	0.142	3.025	0.220	1.956
Fe-Al						
As-cast	-0.704	9.538	0.112	2.385	0.140	1.544
As-rolled	-0.721	9.485	0.111	2.372	0.116	1.056
Fe-W						
As-cast	-0.717	12.89	0.151	3.223	0.350	1.122
As-rolled	-0.709	12.663	0.148	3.166	0.361	0.822
Fe-B						
As-cast	-0.698	14.962	0.175	3.741	0.142	1.033
As-rolled	-0.728	10.309	0.121	2.577	0.070	1.111
Fe-C						
As-rolled	-0.68	15.964	0.187	3.991	0.231	3.456
Fe-S						
As-rolled	-0.703	12.351	0.145	3.088	0.230	2.58

$V_{corr}$ , corrosion potential;  $I_{corr}$  corrosion current density; and  $v_{corr}$ , corrosion rate in terms of penetration rate.

The addition of highly noble metals has also been used to improve the biodegradability of pure iron. Huang et al. [72] fabricated Fe-Ag and Fe-Au composites by powder metallurgy using spark plasma sintering, and the results showed that the addition of Ag and Au could improve the corrosion rate of the iron matrix in Hank's solution, especially Ag. Jaroslav Čapek et al. [73] compared the microstructure, mechanical and corrosion properties, and cytotoxicity of FePd2 (wt%) alloys prepared by three different routes: casting, mechanical alloying, and spark plasma sintering (SPS). The results show that the addition of Pd enhanced both mechanical properties and corrosion rates and did not decrease the

cytocompatibility. Cheng et al. [74] prepared Fe-Fe<sub>2</sub>O<sub>3</sub> composites with Fe<sub>2</sub>O<sub>3</sub> contents of 2, 5, 10, and 50 wt % by spark plasma sintering. The addition of Fe<sub>2</sub>O<sub>3</sub> in small amounts improved the corrosion rate. And the prepared materials showed good hemocompatibility.

### 2.2 Manufacturing methods of alloys

Manufacturing methods are pivotal in the development of biodegradable metal materials. This is because the production process allows not only different shapes and formats but can also significantly affect the mechanical properties and corrosion rate of the implants [19]. Only a few of the main methods available for the design and production of biodegradable metals are briefly described here. The technical details, process parameters and procedures are not in the scope of this thesis.

The main manufacturing methods that can be used for the development of iron-based biodegradable metal materials are powder metallurgy (PM), casting, electroforming, and additive manufacturing (AM). Among them, AM is relatively considered as an advanced process, while the other methods are tentatively classified as conventional metallurgical techniques in the following description. Their respective advantages and disadvantages are summarized in Table 2.6.

**Table 2.6** Advantages and disadvantages of various methods for manufacturing Fe-based biodegradable devices [75].

Method	Advantages	Disadvantages
Powder metallurgy	Allows the direct production of relatively complex shapes; Materials with tuned properties can be obtained; The degradation rate and mechanical characteristics can be varied across a large range by making minor modifications to production parameters; A suitable method for developing alloys, composites, and porous materials; Ease of tailoring biodegradability by optimising porosity.	Difficulties in powder preparation; Chances of inhomogeneity during the mixing/milling process leads to poor mechanical properties.
Casting	Affordability of alloy component customization; Easy to make complicated geometry.	High probability of casting defects (segregation, blowholes, and shrinkage); Post-processing is required after casting; Cannot produce Fe-bioceramic composite; High-stress shielding.
Additive manufacturing	The best method to produce porous scaffolds; Ease of tailoring biodegradability by optimising porosity; The shape and geometry of pores can be controlled (these decide the osteoconduction and osseointegration); Allows implant materials to have mechanical characteristics similar to human bone. (Reduce stress shielding); Accuracy and adaptability.	Difficulties in powder preparations.
Electroforming	Simple method; Does not require complex equipment; Less amount of energy consumption.	Only thin sections/sheets can be made.

### 2.2.1. Conventional manufacture techniques

Casting is one of the oldest metalworking techniques, with a history of nearly 7000 years. It was initially used to develop Fe-based biodegradable materials. For example, Liu et al. prepared Fe-3%X (X= Mn, Co, Al, W, Sn, B, C, S) binary alloys by casting when testing available alloying elements. Microstructure and corrosion properties of FeMnPd alloys forged by Schinhammer et al. [76–78] can be improved by heat-treatment processes such as recrystallisation and precipitation. Powder Metallurgy is one of the methods widely used to produce metallic materials that can produce high purity products and allow the mixing of metals and non-metals to create composite materials. PM generally consists of four basic steps, namely (i) Powder production and preparation, (ii) mixing and blending, (iii) shaping and (iv) sintering. As previously described, the Fe-Mn alloy for biomedical applications proposed by Harmawan et al. was fabricated by the PM process [24,25,66]. Otherwise, the degradation rate and mechanical properties of electroformed iron (E-Fe) are reported to be better than those of iron fabricated by casting and thermomechanical treatment (CTT-Fe) and present a fine microstructure [79–81].

The traditional casting process offers lower construction costs and relatively mature processing technology. However, it may not meet the complex geometry required for clinical implant materials. To address the limitations of conventional machining processes, such as casting composition segregation and inhomogeneous grain structure leading to poorer mechanical properties and degradation behavior, unconventional fabrication techniques should be considered, depending on the specific application of the metal implant material.

### 2.2.2. Additive manufacturing

Additive manufacturing, also known as additive fabrication, 3D printing, or rapid manufacturing, is an advanced manufacturing process where solid parts are built by depositing materials layer by layer. The advancements in additive manufacturing technologies have brought revolutionary changes in the development of biodegradable implants. 3D printing of metals enables the use of existing biomaterials to provide patients with customized devices that can be designed and manufactured with matching geometries according to the required properties of different implant locations. The design can also be engineered to specifically load any drugs or biologically active substances. Currently, AM has been applied in the medical field, especially in orthopedics [82–87]. The bone structure that matches the patient is designed by a computer-aided design (CAD) model. Then, a custom bone implant is printed by a printer, and finally, an implantation procedure is

performed to attach the custom plate to the affected site. In addition, parts produced by AM are also widely applied in the aerospace industry, structure fabrication, dentistry, automobile industry and other fields [88].

Powder bed fusion (PBF), selective laser melting (SLM) and electron beam melting (EBM) are three major existing AM technologies. Among them, SLM occupies a special place because it is able to mix different materials with functional gradients and can be used to produce not only metals but also ceramics and polymers [89]. SLM was developed by Dr. M. Fockele and Dr. D. Schwarze of F & S Stereolithographietechnik GmbH, with Dr. W. Meiners, Dr. K. Wissenbach, and Dr. G. Andres of Fraunhofer ILT, and this technology patented in Germany in 1997 [90]. Figure 2.1 shows a schematic of the SLM process setup [91]. A thin layer of metal powder is evenly spread over a build platform, and the laser selectively melts the powder particles based on a digital 3D model. After each layer is melted, the build platform is lowered, and a new layer of powder is applied, repeating the process until the entire object is formed. Due to the intricate nature of SLM systems and the underlying mechanisms involved, process parameters play a crucial role in determining the final quality of parts produced through this technology.

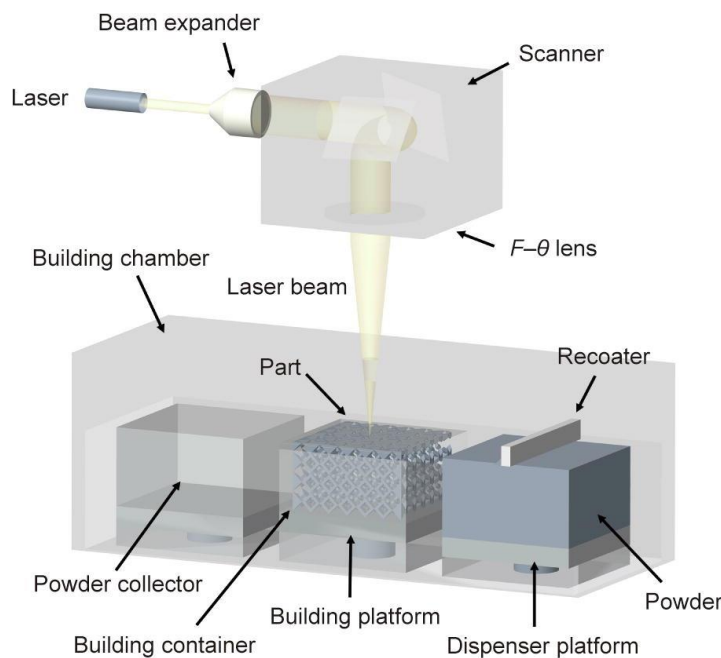


**Figure 2.1** Schematic illustration of the principle of operation of SLM process (Reprinted with permission from Ref. [91]. Copyright @ 2019, Elsevier)

Compared to Mg and Zn, Fe and Fe-based materials are relatively easier to process using SLM. Carluccio et al. [92] fabricated pure iron for biodegradable metal applications using selective laser melting, laser metal deposition, and conventional casting techniques. They

then compared the microstructural, mechanical, and corrosion properties of samples produced by the three different processes. The results showed that the manufacturing method significantly affects the microstructure. As shown in Figure 2.2, the cast pure Fe had an average grain size of over 30 times larger than that of SLM and double that of LMD. The grain size is dependent on the cooling rate, the cooling rate of the laser-based AM process is significantly higher due to the small melt pool, which results in higher mechanical properties of the pure iron processed by SLM. The corrosion rate is further increased due to the finer grain size. Furthermore, they fabricated and evaluated the feasibility of SLM processed Fe-35Mn scaffolds as bone scaffolds [28]. The microstructure of the scaffold consisted primarily of  $\gamma$ -austenite, leading to high ductility of the scaffold. The Fe-35Mn scaffold maintained adequate mechanical properties after 28 days of immersion in Hank's solution, and the cell viability test results also showed good biocompatibility. In addition, they performed in vivo tests where the scaffold was implanted in the defective calvarium of rats, and the implant successfully bonded to the original bone and stimulated bone formation only four weeks after implantation.

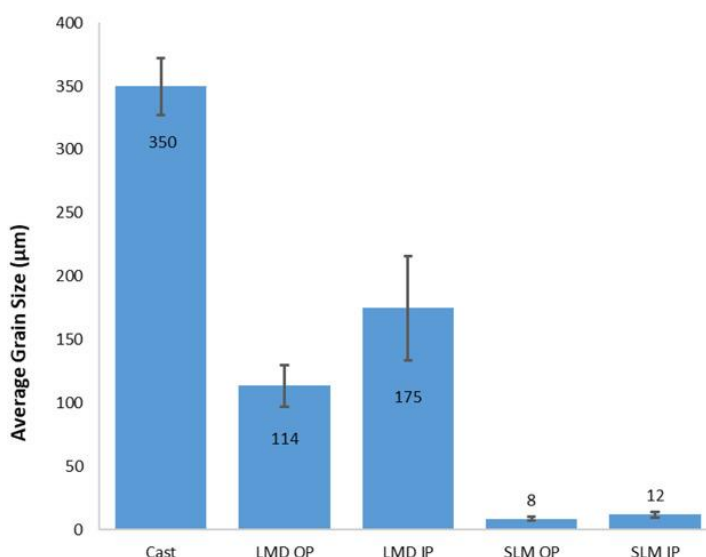


**Figure 2.2** Average grain size of each manufacturing method. Error bars represent SD. IP denotes build direction in the plane, OP denotes build direction out of the plane (Reprinted with permission from Ref. [92]. Copyright @ 2019, Wiley Online Library).

A remarkable advantage of SLM is the ability to achieve the processing of immiscible materials. Krüger et al. [93,94] developed the FeMnAg alloy by dispersing the Ag phase in the FeMn substrate, with the strategy of inducing galvanic corrosion through the high potential of Ag and thus increasing the corrosion rate. In addition, Ag has good biocompatibility and antibacterial properties.

### 3 Corrosion mechanisms in physiological environments

#### 3.1 Corrosion of metallic implants

Corrosion is an important factor in the design and selection of metals and alloys for use in implants. During corrosion, allergenic, toxic/cytotoxic or carcinogenic substances may be released into the body [95]. In addition, corrosion can lead to loosening and failure of implants [96,97]. The corrosion behavior of metal implants is influenced by many factors of their own properties as well as the environment, as shown in Figure 3.1.

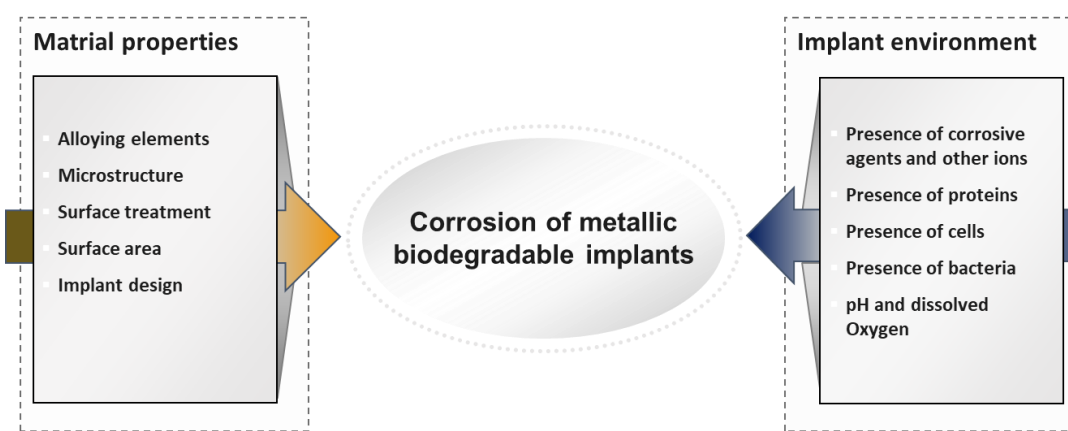


**Figure 3.1** Factors affecting the corrosion of metallic implants (based on [98]).

Corrosion testing is an effective means of material selection and understanding degradation mechanisms. Thus, extensive corrosion testing is necessary to evaluate the corrosion properties of implants before they are applied in the clinical trial. Due to constraints of ethics, cost considerations, and the need for additional equipment, space, and skills, there are currently more in vitro studies of iron-based materials than in vivo [19]. Furthermore, the results of in vivo experiments have indicated that corrosion rates based on in vitro tests often show inconsistencies with the results of in vivo tests [63]. Corrosion rates from in vivo tests tend to be low. This is due to the fact that not all factors (e.g. blood flow rate, pH, reactive oxygen species, ion concentration, proteins, cells, etc.) affecting the corrosion process can be fully taken into account under the pseudo-physiological conditions.

In the literature, only approximative values of the degradation rate of different iron-based materials can be found, depending on the different testing methods, applied test environments, time periods of observation (e.g. initial corrosion vs. corrosion after a longer time) and material combinations, as well as fabrication and preparation of samples [99].

### 3.1.1. The biological environment

The fluids in the human body are composed of water and inorganic salts, and organic compounds dissolved in water together, collectively known as body fluids. Water is the main component of body fluid, constituting 55% to 65% of body weight [100]. Body fluids that exist outside the cells are defined as extracellular fluids (ECF). They mainly include tissue fluid, plasma, lymph and cerebrospinal fluid. The fluid inside the cell is named the intracellular fluid (ICF). Biodegradable metallic materials are mainly considered for orthopedic and cardiovascular applications [34,65,101], where implants are faced with a physiological environment that is typically ECF. The main components of the extracellular and intracellular fluids are listed in Table 3.1. Body fluids are buffer solutions whose pH is usually maintained between 7.0 and 7.35 [100].

**Table 3.1** Electrolyte concentrations per 1 L water (mEq) [102].

Species	Extracellular fluid		Intracellular fluid
	Serum	Interstitial	
Na <sup>+</sup>	152	143	14
K <sup>+</sup>	5	4	157
Ca <sup>2+</sup>	5	5	-
Mg <sup>2+</sup>	3	3	26
Cl <sup>-</sup>	133	117	-
HPO <sub>4</sub> <sup>2-</sup>	2	2	113(PO <sub>4</sub> <sup>3-</sup> )
SO <sub>4</sub> <sup>2-</sup>	1	1	-
HCO <sub>3</sub> <sup>-</sup>	27	27	10
Organic acid	6	6	-
Protein	16	2	74

### 3.1.2. Commonly used media for in vitro corrosion test

Biomaterials have to face the complex human environment, so when developing biomaterials, it is necessary to make the used test media as close as possible to the real human physiological environment. Differences in the composition of the corrosion test medium have a significant impact on corrosion behavior. Mai et al. [103] have reviewed a variety of different corrosive media used to evaluate the degradation properties of biomedical implants, ranging from simple inorganic electrolytes to complex corrosive media containing organic biomacromolecules, as illustrated in Figure 3.2.

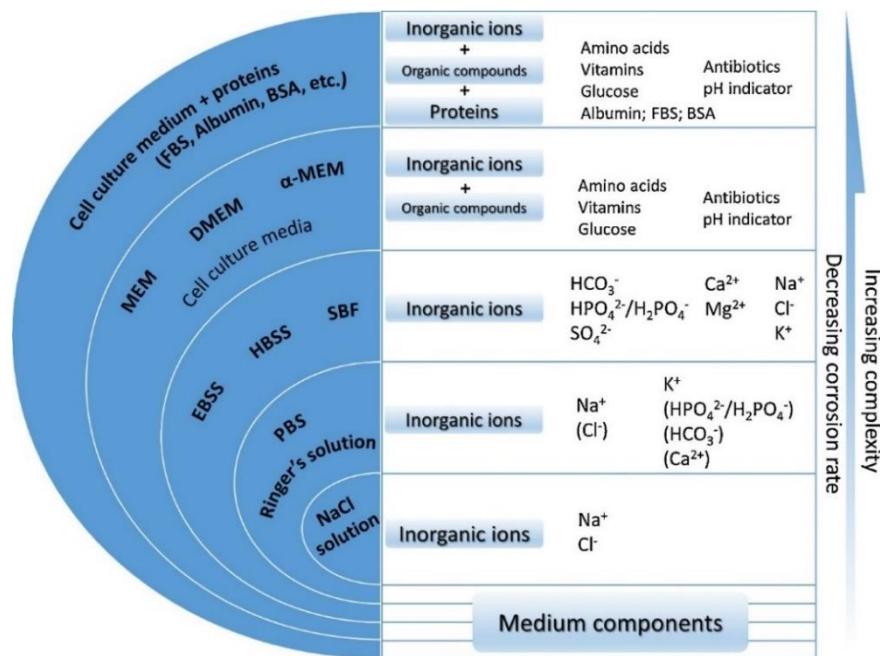


**Figure 3.2** Commonly used corrosive media for testing bio-absorbable metals. Typically, the corrosion rate of magnesium is decreased as a function of the increasing complexity of the media. Ions in the brackets occasionally added to corresponding medium (Reprinted with permission from Ref. [103]. Copyright @ 2020, Elsevier).

As shown in Table 3.1, the most important electrolytes in the ECF environment to which the implanted material is exposed are Na, K, Cl, Ca, HCO<sub>3</sub><sup>-</sup>, and phosphate. Among them, Na<sup>+</sup> and Cl<sup>-</sup> are the main ions, and NaCl solutions were rightly chosen as the initial corrosion medium. The commonly used NaCl solution with a concentration of 0.9%, also known as saline, has the same osmotic pressure as human plasma. Saline is not only the simplest corrosive medium but also the most aggressive. In addition, it does not have buffering capacity, which may lead to local pH changes. Phosphate buffered saline (PBS) contains NaCl, KCl, KH<sub>2</sub>PO<sub>4</sub> and Na<sub>2</sub>HPO<sub>4</sub> salts, and it was designed for biological studies. It is also often used as a corrosive medium to test the suitability of biological materials. H<sub>2</sub>PO<sub>4</sub><sup>-</sup>/HPO<sub>4</sub><sup>2-</sup> buffers the pH of the solution in the range of 5.8-8.0. Although PBS has a pH buffering capacity compared to NaCl, it still lacks several important inorganic salt ions that have a significant impact on corrosion behavior, such as Ca<sup>2+</sup> and carbonate. SBF refer to media containing all major inorganic ions present in human serum and interstitial fluid, which further improves the deficiencies of NaCl and PBS. SBF was proposed by Kokubo et al. in the 1990s, and its ion concentrations are approximately equal to those of human blood plasma [104,105]. The material forms a calcium phosphate surface phase in SBF similar to that found in natural bone, which has led to the widespread use of SBF for bone tissue engineering. Oyane et al. [106] modified the conventional SBF and recommended m-SBF (modified simulated body fluid) for in vitro evaluation of biomaterials. The composition of

NaCl, PBS and SBF in comparison to human plasma is shown in Table 3.2. Then, to better fit the real body environment, the researchers continued to add proteins, amino acids, vitamins, sugars and other biomolecules to the electrolyte solution, creating more complex corrosion media, such as Dulbecco's Modified Eagle's Medium (DMEM).

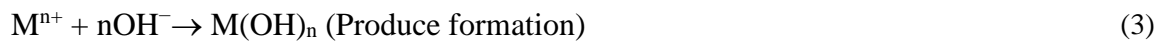
**Table 3.2** Components of simulated body fluid in comparison to those of blood plasma [103,107].

	Concentration (mM)			
	NaCl	PBS	SBF	Plasma
<b>Na<sup>+</sup></b>	145.3-153.8	146-157	142.0	135-147
<b>K<sup>+</sup></b>	-	4.1	5.0	3.5-5.0
<b>Mg<sup>+</sup></b>	-	-	1.0-1.5	1.5-2.5
<b>Ca<sup>2+</sup></b>	-	-	2.5	8-11
<b>Cl<sup>-</sup></b>	145.3-153.8	140.6	103-148.8	22-28
<b>HCO<sub>3</sub><sup>-</sup></b>	-	-	4.2-27	27.0
<b>HPO<sub>4</sub><sup>2-</sup></b>	-	9.5-11.5	1.0	1.0
<b>SO<sub>4</sub><sup>2-</sup></b>	-	-	0-0.5	0.5
<b>pH buffer</b>	-	-	50.5 (Tris) 25.0-50.0 (HEPES)	-
<b>Protein</b>	-	-	-	6-8 g dl <sup>-1</sup>
<b>Glucose</b>	-	-	-	70-110
<b>Uric acid</b>	-	-	-	2-8

HEPES: 2-(4-(2-hydroxyethyl)-1-piperazinyl)ethanesulfonic acid; TRIS: tris(hydroxymethyl)aminomethane.

### 3.1.3. Corrosion of Fe-based materials in the physiological environment

Metal implant materials begin to corrode after implantation, and the metal (M) oxidizes to metal cations ( $M^{n+}$ ), which react with  $OH^-$  produced by the cathode to form corrosion products:



The corrosion behavior of Fe-based materials in various physiological solutions such as SBF, PBS, and DMEM has been reported. Schinhammer et al. [78] investigated the degradation behavior of Fe, FeMnC, and FeMnC-Pd in aerated ( $O_2$ -containing) SBF and established the degradation mechanism in oxygenated physiological solutions of iron-based alloys. The degradation products consist mainly of oxides of Fe and Mn and a mixture of Ca and P. The

protective oxide layer formed acts as a degradation barrier affecting the degradation rate. Hermawan et al. [108] studied the degradation behavior of FeMn alloy in modified Hank's solution, and the results indicated that the degradation products consisted of metal hydroxides and calcium/phosphorus layers, as shown in Figure 3.3. In addition to this, due to the presence of defects in the hydroxide layer and chloride ions from electrolyte concentrates in preferential sites (Figure 3.3b). The formed metal chloride was then hydrolysed by water to the hydroxide and free acid, lowering the pH value in the pits while the bulk solution remained neutral. Corrosion pits grow wider and deeper over time, and  $\text{Fe(OH)}_2$  is converted to magnetite ( $\text{Fe}_2\text{O}_3$ ) and lepidocrocite ( $\gamma\text{-FeOOH}$ ) as the final corrosion product.

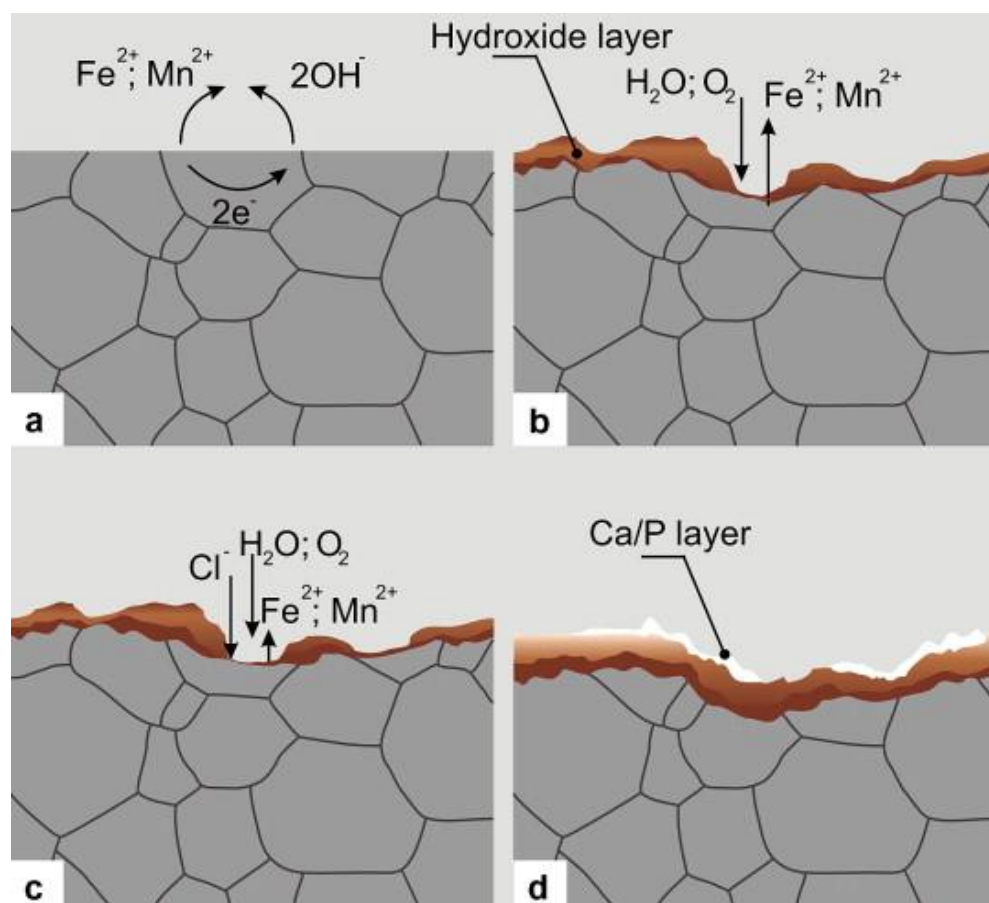


**Figure 3.3** Illustration of the corrosion mechanisms for Fe–Mn alloys: **a**) initial corrosion reaction, **b**) formation of hydroxide layer, **c**) formation of pits, and **d**) formation of calcium/phosphorus layer (Reprinted with permission from Ref. [108]). Copyright @ 2010, Elsevier).

Chen et al. [109] compared the long-term corrosion behavior of Fe, Mg and Zn in PBS. The pH change in the case of Fe during the degradation by continuous immersion was minimal, and there was no hydrogen precipitation. The surface layer of Fe thickened with increasing immersion time, and in addition to this, pitting was observed, and some of it had developed into deep holes. As mentioned before, this is elicited by the confined self-promoting

hydrolysis of the  $\text{Cl}^-$  ions. Dong et al. [110] compared the degradation behavior of Fe, Mg, and Zn in SBF and DMEM under the same experimental conditions. In SBF, Fe shows the lowest corrosion rate compared to Mg and Zn, which is consistent with its thermodynamic activity. And the difference is reduced in DMEM. Fe forms a porous corrosion layer in SBF, while it is more dense in DMEM. Chemical elemental analysis results show that the corrosion product layer of Fe consists of  $\text{Fe}_3\text{O}_4$ ,  $\text{FeOOH}$ ,  $\text{Fe}_2\text{O}_3$ ,  $\text{FePO}_4$ ,  $\text{Ca}_{10}(\text{PO}_4)_6(\text{OH})_2$ ,  $\text{Ca}_3(\text{PO}_4)_2$ , and  $\text{CaCO}_3$ .

Implants and byproducts often cause inflammation, and macrophages in the immune system release reactive oxygen species (ROS) such as hydrogen peroxide ( $\text{H}_2\text{O}_2$ ) and superoxide ( $\text{O}_2^-$ ) when dealing with inflammation, thus changing the local corrosive environment [111]. In order to simulate the degradation of Mg and Fe under inflammatory conditions, Liu et al. [111] added different concentrations of  $\text{H}_2\text{O}_2$  to PBS. The degradation of iron was accelerated with increasing  $\text{H}_2\text{O}_2$  concentration, and the formation of corrosion products was inhibited.

The corrosion performance of Fe-based implants has been studied so far in a variety of physiological solutions, and protective corrosion products are considered to be one of the causes of low degradation rates under physiological conditions. The results of several reported in vitro corrosion experiments have shown that the most common types of corrosion products resulting from the corrosion of Fe-based alloys are  $\text{FeOOH}$ ,  $\text{Fe}_2\text{O}_3$ ,  $\text{Fe}_3\text{O}_4$ ,  $\text{Fe}(\text{OH})_3$ , and Ca/P-based precipitates [110,112,113]. However, no studies have been conducted to specifically identify the type of corrosion products after in vivo implantation [114]. In fact, the corrosion rates of in vivo tests are generally lower than those of in vitro tests due to the complex physiological conditions in the body [63].

#### 3.1.4. The proposed corrosion mechanism of Fe

Generally, the mechanism of iron corrosion under physiological conditions is considered to begin with the oxidation of iron as an anodic reaction and the reduction of oxygen as a cathodic reaction, as shown in the following equation:

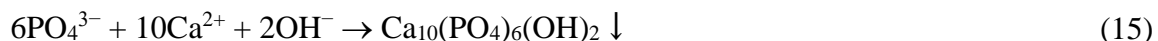


$\text{Fe}^{2+}$  can continue to be reduced to  $\text{Fe}^{3+}$  in the presence of oxygen. The iron ions react further with the OH produced by the cathode to form insoluble substances. In the presence of oxygen

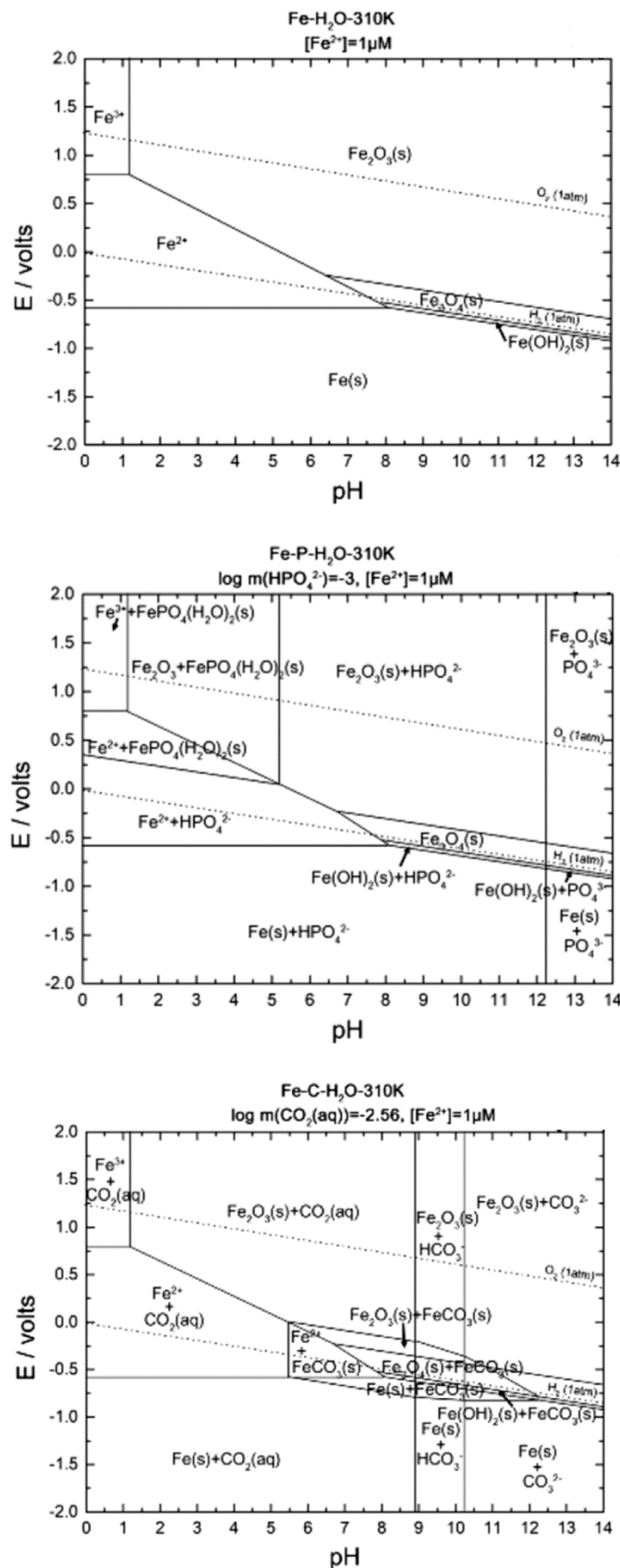
and chloride ions,  $\text{Fe(OH)}_3$  is hydrolysed and goethite ( $\alpha\text{-FeOOH}$ ) precipitates.  $\text{Fe(OH)}_2$  will then react with a part of  $\text{FeO(OH)}$ , and the formation of  $\text{Fe}_3\text{O}_4$  occurs [115,116]. The related reactions are shown below.



The  $\text{Fe}^{2+}$  released from the anode during corrosion can also interact with other anions present in the physiological environment. The alkalinization of the interface due to corrosion and the increase in pH can indeed favor the precipitation and deposition of phosphates. As a result, the following reactions occur in solutions containing phosphate [116].

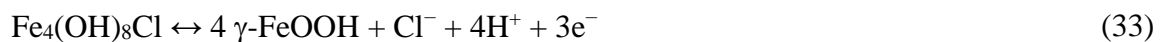
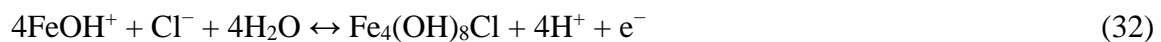
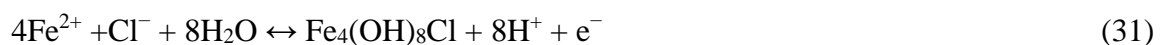
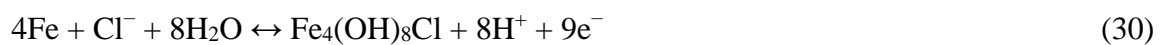
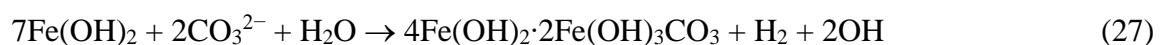
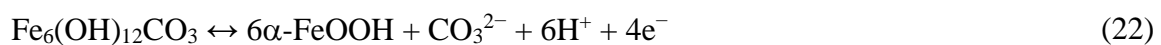
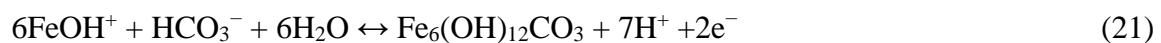
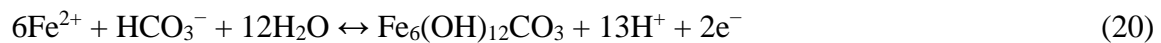
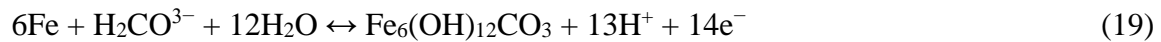
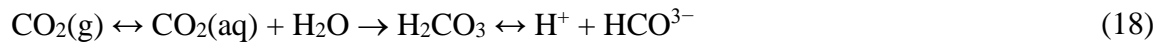


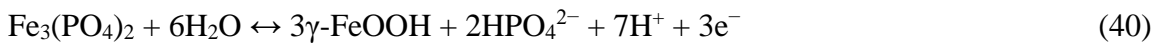
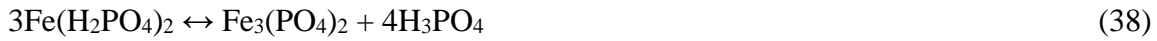
Pourbaix diagrams depict graphical representations of the stability of different substances in aqueous solutions as a function of their oxidation state and the pH of the solution, which are widely used in the field of electrochemistry and corrosion science to predict the stability of different species and to understand the behavior of electrochemical systems, including corrosion reactions and the formation of protective oxide layers on metal surfaces. Figure 3.4 displays the Pourbaix diagram demonstrating the interaction of pure iron with various ions present in bodily fluids, based on physiological conditions ( $T = 37^\circ\text{C}$ ,  $\text{pH} = 7.4$ ) that are in line with the service site of the iron-based implant material.



**Figure 3.4** Pourbaix diagrams for Fe in physiological concentration and body temperature: Fe-H<sub>2</sub>O diagram, Fe-P-H<sub>2</sub>O diagram and Fe-C-H<sub>2</sub>O diagram, respectively (Reprinted with permission from Ref. [117]. Copyright @ 2019, Wiley Online Library).

Under physiological conditions,  $\text{Fe}^{2+}$ ,  $\text{OH}^-$ ,  $\text{Cl}^-$ ,  $\text{H}_2\text{PO}_4^{4-}/\text{HPO}_4^{2-}$  and  $\text{HCO}_3^{2-}$  ions are present (see Figure 3.4). However, no species of carbonate ions are anticipated to exist. The equilibrium equations for the iron ions with other present ions and chemical species are listed below [95,118,119].

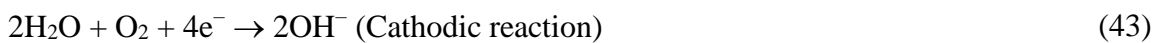




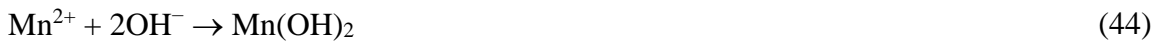
The phases formed in the intermediate steps are unstable and tend to be rapidly oxidized, tending to convert to more stable compounds, such as FeOOH or  $\text{Fe}_3\text{O}_4$ . During in vitro corrosion testing, exposing the degradation surface to the atmosphere can alter the degradation pattern and the degradation products formed. This could result in the production of chemicals that are distinct from those observed in vivo studies [118].

### 3.1.5. The proposed corrosion mechanism of FeMn

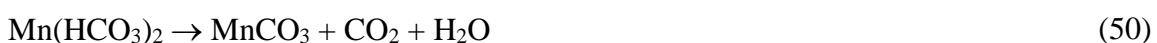
The main degradation processes for Mn are similar to those described previously for Fe:



Then the metal ions released from the anodic reaction react with the hydroxide ions released from the cathodic reaction to form insoluble hydroxides:



In  $\text{CO}_2$ -rich environments, there may be additional reaction processes that affect the nature, chemical composition and morphology of the degradation layer. The main reason is that the dissolution of  $\text{CO}_2$  changes the concentration of  $\text{HCO}_3^-$  and  $\text{CO}_3^{2-}$ . The formation of possible insoluble products is described as [120]:



### 3.2 Protein Adsorption on solid surfaces

#### 3.2.1. Protein structure

Protein is a macromolecule with certain biological functions and is also the most abundant macromolecule in living organisms. Each protein has its own specific structure, which can be generally described at four distinct levels (Figure 3.5).

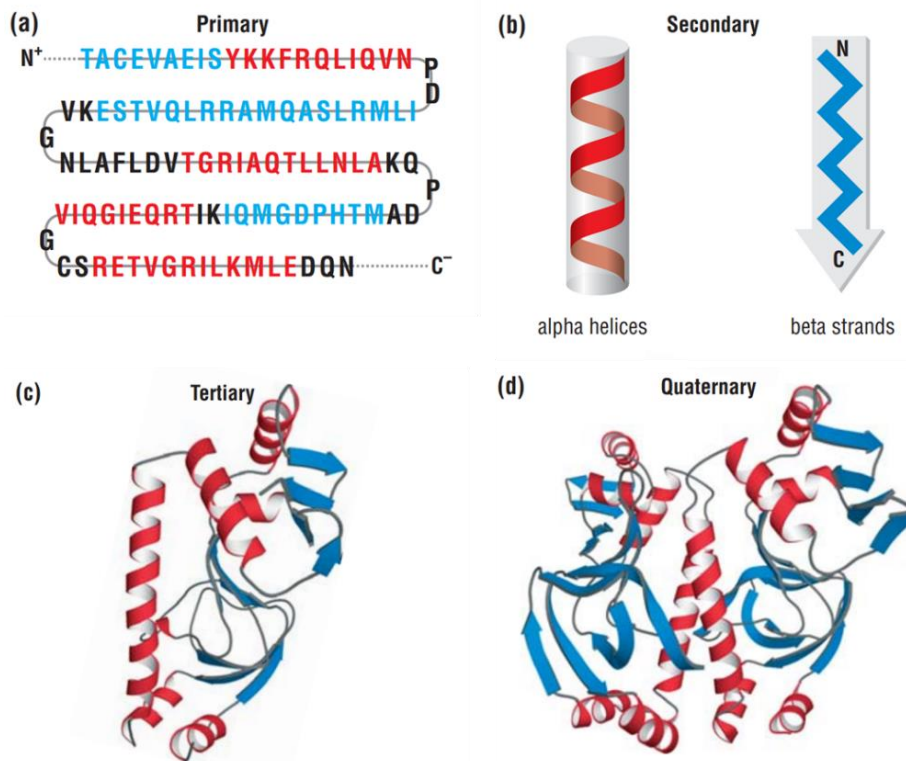


**Figure 3.5** Representation of the four levels of the protein structure (Re-drawn from Ref. [121]).

The primary structure describes the linear structure of the protein, i.e. the sequence of covalently linked amino acid residues. The secondary structure of a protein refers to the local spatial arrangement of the main chain atoms in its molecule, of which there are two main conformations, i.e.  $\alpha$ -helix and the  $\beta$ -strand or  $\beta$ -sheets. Tertiary structure refers to the overall arrangement of a peptide chain, where the main chain and side chains form a spatial structure through hydrophobic interactions, electrostatic forces, hydrogen bonds etc. A quaternary structure is a multimer formed by two or more polypeptide chains with independent tertiary structures bound to each other by non-covalent bonds. [121–124]

#### 3.2.2. Surface adsorption of protein on material surfaces

The structure of proteins indicates that they are large complex amphipathic molecules composed of amino acids. The specific three-dimensional structure built by amino acid side

chain groups and multiple forces allows the protein to expose a combination of hydrophobic, hydrophilic, polar and non-polar regions in the medium (Figure 3.6). This allows them to interact with material surfaces, for example, hydrophobic effects, formation of ionic bonds, electron transfer, etc.

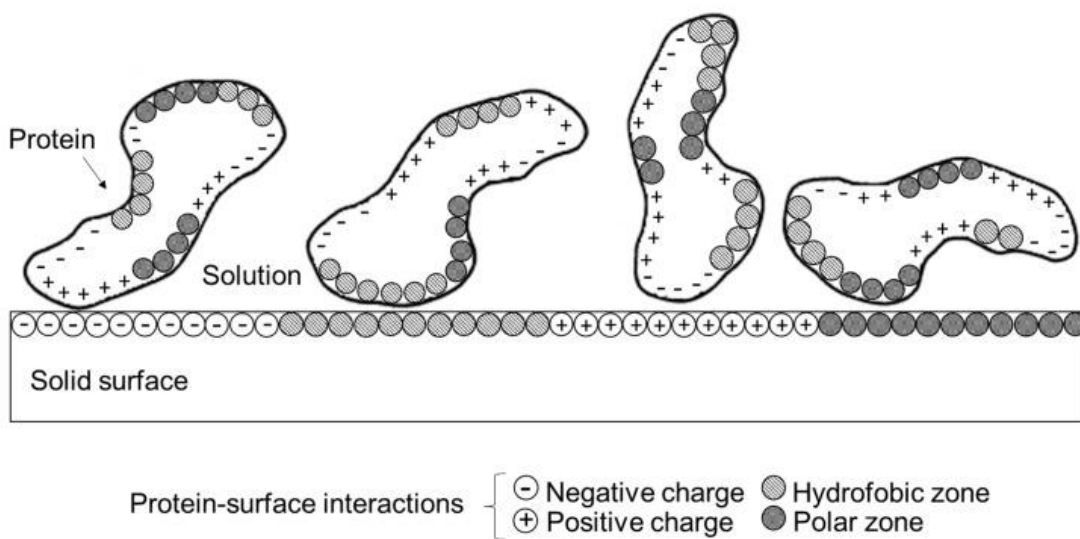


**Figure 3.6** Schematic illustration of proteins domains and respective interactions with surfaces of different nature: polar zone, hydrophobic zone, positively charged and negatively charged [122].

The adsorption of proteins on material surfaces involves a large number of processes. Over the past decades, researchers have observed the adsorption behavior of different proteins on the surface of various biomaterials, and the experimental results indicate that properties of proteins such as their size, shape and structure, and isoelectric point influence their interaction with the surface of biomaterials. Meanwhile, surface properties such as surface chemistry, charge, morphology, hydrophobicity and mechanical properties, as well as temperature, ion concentration, pH value and other environmental factors, also affect protein adsorption. The main factors affecting protein adsorption are summarized in Figure 3.7. [125]

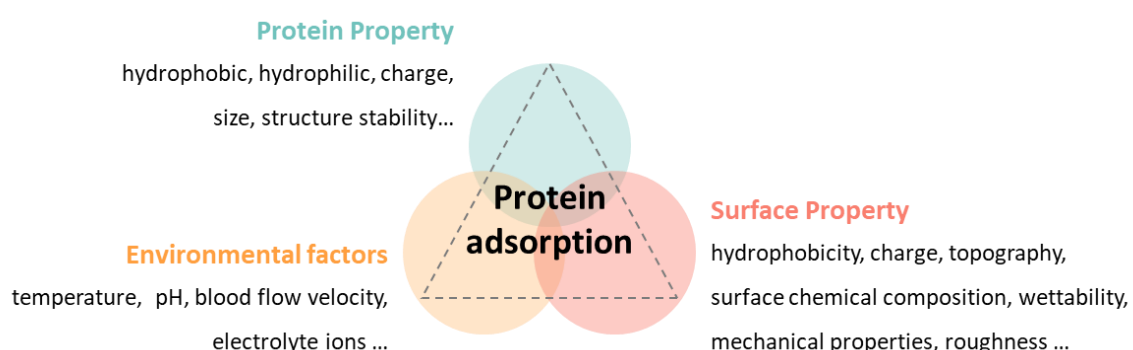


**Figure 3.7** Main factors affecting protein adsorption.

#### Protein property

- i. Amphipathic nature: The amphipathic nature of proteins is reflected in their different structural domains, i.e. hydrophobic, hydrophilic, positive and negative charges. This is determined by the local amino acid composition and environmental factors. In aqueous media, the hydrophilic amino acid side chains are more often located outside the protein molecule and tend to adsorb on polar material surfaces. The isoelectric point of proteins depends on the amino acids and conformations that make up the protein, can carry different charges depending on the pH of the environment, and readily adsorbs to regions of the material surface that carry the opposite charge. In general, proteins tend to adsorb more readily near the isoelectric point.
- ii. Structural stability: Proteins undergo different degrees of conformational changes upon adsorption. Compared to proteins with high conformational stability (hard proteins), protein molecules with lower thermodynamic stability (soft proteins) tend to undergo conformational changes upon adsorption, unfolding to a greater extent on the surface to optimize interfacial energy.
- iii. Size: Smaller proteins have faster diffusion rates and reach the surface of the substrate more quickly. Larger proteins have more binding sites to interact with areas of the material surface.

#### Surface property

- i. Surface chemical composition: The chemical composition of the material surface can strongly influence protein adsorption. Surface functional groups such as  $-\text{CH}_3$ ,  $-\text{OH}$ ,  $-\text{COOH}$ , etc., can influence surface polarity, hydrophobicity, hydrophilicity, and the specific adsorption of proteins. The chemical composition determines the type of intermolecular forces and also the surface charge at environmental pH.
- ii. Charge: The surface potential affects the distribution of ions in the solvent and the interaction with proteins. Negatively charged surfaces are more likely to attract positively charged proteins.
- iii. Topography: Differences in surface topography may affect the conformation and amount of proteins adsorbed on the material surface. Compared to smooth surfaces, topographic features have a greater specific surface area and surface energy, thus increasing the adsorption sites for proteins.

- iv. Heterogeneity: Biomaterials present heterogeneity at the microscopic scale, such as some metallic materials exhibiting different phases and the presence of grain boundaries. Non-homogeneity creates different regions of interaction with the protein.

#### **Environmental factors**

Numerous environmental factors can also affect the interaction of proteins with surfaces.

- i. Temperature: Temperature has a strong influence on protein behavior, and high temperatures can accelerate the diffusion rate of proteins, thereby increasing the amount of adsorbed proteins. However, too high temperatures can lead to protein denaturation and inactivation.
- ii. Environmental pH affects the charge of proteins and material surfaces.

As mentioned above, protein adsorption on a surface is a very complex process, and the overall adsorption behavior is influenced by numerous factors. The exact mechanism of protein adsorption is not fully understood, so it cannot be assumed that the adsorption behavior of proteins on the material and the structure of the adsorbed proteins are deterministic. Nevertheless, by studying the adsorption of different types of proteins at the solid-liquid interface under a variety of experimental conditions, it is possible to predict the possible adsorption behavior of proteins and to develop models to explain the adsorption kinetics. Generally accepted that proteins can unfold with a distribution of charges in the interface after arriving at the surface and followed by a structural rearrangement. Eventually, they can adsorb on the surface reversibly or irreversibly through electrostatic interactions, hydrogen bonding, hydrophobic interactions and van der Waals forces. Overall, protein adsorption is an entropically driven process and tends toward monolayer and near-monolayer adsorption.

#### **Competitive adsorption behavior**

In complex biological mediums such as blood, plasma, tears, saliva or other body fluids, there exist multiple different proteins. For example, plasma contains about 7% of proteins and more than 150 species. Among them, Albumin is the most abundant protein in plasma, accounting for about 60% of total plasma protein, followed by Globulins (35%) and Fibrinogen (4%). The major component proteins in plasma are listed in Table 3.3.

**Table 3.3** Plasma Proteins with the Highest Concentration [126].

Plasma Protein	Concentration (mg/ml)	Molecular Weight(KDa)	Diffusion Coefficient ( $10^{-7}$ cm $^2$ /s)
Albumin	40	66	6.1
IgG*	15	150	4.0
$\alpha_1$ -Antitrypsin	3	54	5.2
Fibrinogen	3	340	2.0
Low-density lipoprotein (LDL)	3	5000	5.4
$\alpha_2$ -Macroglobulin	3	725	2.4
Transferrin	2.6	77	5.0
IgA*	2.3	162	3.4
$\alpha_2$ -Haptoglobins	2	1000	4.7
High-density lipoprotein (HDL)	2	195	4.6
Complement 3	1.6	180	4.5

\*IgG, Immunoglobulin G; IgA, Immunoglobulin A.

In multicomponent solutions, in addition to considering protein-surface interactions, there is also protein-protein competition on the surface, as shown in Figure 3.8.

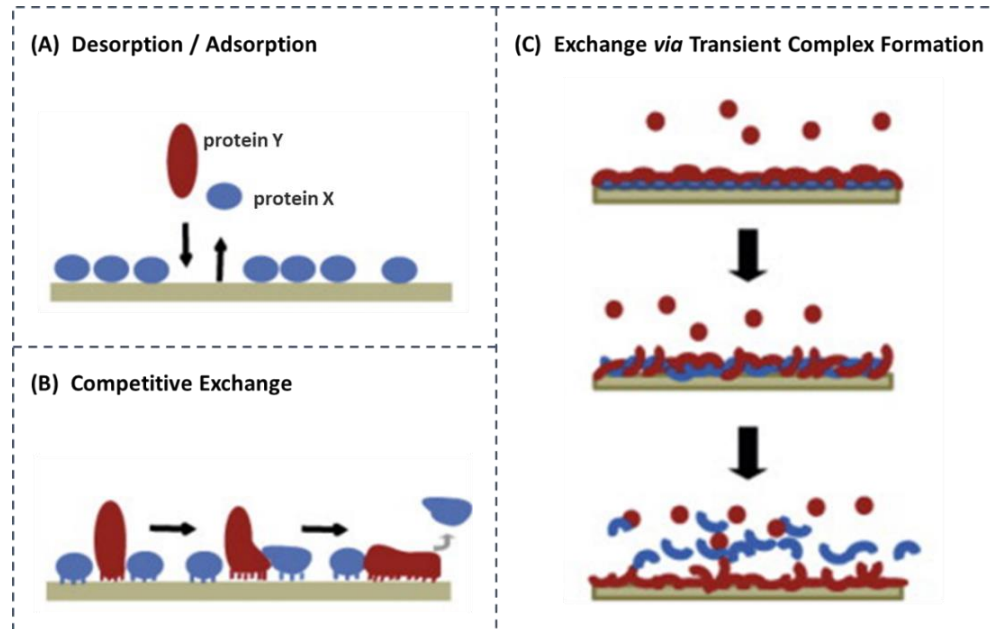


**Figure 3.8** A schematic illustrating three different processes proposed for the change in composition of a layer adsorbed from a mixture solution by exchange of earlier adsorbed proteins with other proteins. **A)** Initially adsorbed protein X (blue) desorbs, leaving a vacancy for protein Y (red) to adsorb. **B)** Initially adsorbed protein X is displaced by protein Y which has a stronger binding affinity to the surface. **C)** Protein Y embeds itself in previously adsorbed protein X to form a transient complex (top); the complex then turns, exposing protein X to solution (middle); protein 1 desorbs into the solution; and protein Y remains on the surface (bottom)(Re-drawn and Reprinted with permission from Ref. [127]. Copyright @ 2013, Elsevier).

The adsorption area and the adsorption sites of the material are finite. As previously described factors, protein in higher concentration has more opportunities to reach surfaces (e.g., Albumin) and proteins with smaller sizes have faster diffusion rates, so they can preferentially occupy the surface. Those proteins with greater affinity for the surface (e.g., Fibrinogen) may reach the surface later due to their concentration and size, but they can compete with previously adsorbed proteins for binding sites through conformational transitions leading to their desorption from the surface. At the same time, due to their more flexible conformation, they are able to adsorb more strongly to the surface. Thus, the composition of the adsorbed layer is time-dependent, and this dynamic competitive adsorption following the diffusion principle was first mentioned in the 1960s by Vroman and Adams and was afterwards widely known as the “Vroman effect” [128], whereby the initially adsorbed protein in a multicomponent solution can be replaced from the surface over time by a subsequent arriving protein.

#### 3.2.3. Effect of protein adsorption on corrosion

The process of protein adsorption is multifaceted and influenced by several factors, including the characteristics of the protein, material, and solution, as discussed in section 3.2.2. Due to the complexity of this process, there is so far no definitive evidence on how proteins affect the corrosion of implants. The currently accepted possible mechanisms by which proteins affect the corrosion behavior of metals are [95]:

- i. Proteins can bind with metal ions and remove them from the surface of the implant, disrupting the balance of the electrical double layer and inducing further metal dissolution.
- ii. Proteins can alter the electrode potential through their electron-carrying ability, while bacteria can alter the local pH by producing acidic metabolic products.
- iii. The adsorption of proteins onto biomaterial surfaces can restrict the diffusion of oxygen to certain areas, leading to preferential corrosion of oxygen-deficient regions and passive layer breakdown.
- iv. A protein layer adsorbed on the surface can act as a barrier, inhibiting corrosion.
- v. In cases of wear or wear-assisted corrosion reactions, proteins can serve as lubricants on the surface.

The corrosion rate is influenced by kinetic factors, such as the rate of the corrosion reaction, the availability of corrosion agents, and the mass transport of reactants and products [119,129]. Thermodynamic factors, such as the electrode potential, pH, and stability of corrosion products, can provide information about the driving force for corrosion, but they do not determine the rate at which the corrosion occurs [119,129]. Thus, proteins can increase or decrease the corrosion rate by interfering with anodic or cathodic reactions in different ways [98,130,131]. Protein adsorption can act as a corrosion inhibitor mechanism, as the adsorbed proteins create a protective layer on the metal surface that reduces metal release. This protective layer forms a barrier that blocks corrosive agents from entering the surface and inhibits the process of electrochemical dissolution. On the other hand, the interaction between metal ions and proteins can lead to the formation of metal-protein complexes at the surface. The transport of the complex compounds away from the interface increases the corrosion rates.

Despite a significant amount of research on the influence of proteins on metal corrosion in metal implants, no single study has definitively demonstrated the effect. The relationship between proteins and metal corrosion is multifaceted and can be influenced by several factors. Overall, the effects of proteins on metal corrosion is a dynamic and evolving field of research, with new discoveries frequently arising. Therefore, to gain a comprehensive understanding of the topic, it would be essential to review the pertinent literature and account for the specific conditions and methodologies employed in each study.

#### 3.2.4. Influence of proteins on corrosion of metallic implants

In the body, fluid contains a variety of biomolecules, especially proteins. Adsorption of proteins is considered to be the first step that happens after the implant is implanted in the body, and it further affects the corrosion properties of metal materials [132]. The research has shown that the impact of the degradation of Mg-based alloys can be either accelerating or inhibiting, depending on the specific proteins involved and their interaction with both the surface of the implant and the medium [133]. In comparison, the effect of protein adsorption on Fe-based alloys has received less attention, and there is a need for further experimental work to understand the possible mechanism.

In the in-vitro testing of metallic implant materials, proteins are incorporated into the testing media. The most widely used model protein is serum albumin, as it is the most abundant protein class found in plasma [134]. Bovine serum albumin (BSA) is commonly used as an

alternative to human serum albumin (HSA) in various in vitro studies because of its structural similarity [134]. Studies related to protein adsorption on iron-based alloys under physiological conditions showed a system-dependent behavior. Hedberg et al. [135,136] reported that BSA induced an increased release of iron ions from stainless steel (AISI 304, 310, 316L, 430, and 2205) in PBS but slightly reduced the corrosion rate of pure iron. Other studies on 316L indicated that protein adsorption in physiological saline containing reactive oxygen species (e.g.  $H_2O_2$ ) could reduce the cathodic reaction rate while accelerating anodic dissolution [137]. Additionally, the presence of BSA in PBS was reported by Karimi et al. [138] to enhance the stability of the passivated film of 316L steel. Wagener et al. [139] showed that the adsorption of BSA slightly increased the corrosion rate of pure iron in SBF. In a study on hot rolled Fe20Mn–1.2C austenitic alloy, it was found that the degradation behavior is medium-dependent, with different kinds of corrosion products and degradation layers formed in physiological solutions with and without proteins [140].

However, using only serum albumin to assess the corrosion behavior of metals in the physiological environment is usually not sufficient, and several studies have reported differences in the influence of different protein species on the corrosion properties of metallic materials. Kocjan et al. [141] reported the corrosion behavior of pure iron in Hank's solution containing either albumin,  $\gamma$ -globulin, fibrinogen or transferrin and observed different effects of particular proteins on iron dissolution. Hedberg et al. [142] investigated the effect of different proteins and protein mixtures on metal release from stainless steel and found that the total amount of released metal is greater in protein mixtures than in the presence of a single protein species. Wagener et al. [139] compared the interaction of BSA and lysozyme (LYZ) with Mg and Fe surfaces. These two proteins are different in size, charge and physiological concentration, and the results demonstrate that the protein-surface interactions depend on the type of protein.

Based on those research works, proteins can have different effects on metallic implants, depending on the type of metal, the type of protein, and the environment [143,144]. Proteins can corrode or stabilize metals, promoting or inhibiting degradation. Proteins can also interact with metals to form a complex, which can modify the metal's physical and chemical properties and impact its biocompatibility and biodegradability. Overall, the effect of proteins on biodegradable metals is complex and multi-faceted, and further research is needed to fully understand the underlying mechanisms.

## 4 Fundamentals of applied experimental methods

### 4.1 Electrochemical techniques

#### 4.1.1. Electrochemical impedance spectroscopy

Electrochemical impedance spectroscopy (EIS) is an electrochemical measurement method that uses a small amplitude sinusoidal potential (or current) as a perturbation signal. It has been widely used in many scientific fields, such as materials science, physical science, biology, and medicine. EIS is a frequency domain measurement method where impedance measurements are obtained as a function of frequency to study the electrode system, thus providing more kinetic information and information about the electrode interface structure than other conventional electrochemical methods. By analyzing the impedance data across a range of frequencies, researchers can gain insights into the charge transfer processes, adsorption phenomena, and interfacial properties, enabling a comprehensive understanding of the electrochemical behavior of the system.

In direct current (DC) techniques, resistance is defined by Ohm's law as the ratio of the voltage  $V$  across a conductor to the current  $I$  through the conductor, as shown in Figure 4.1a. When dealing with alternating current (AC) systems, the impedance  $Z$  represents the overall impeding effect of resistance, inductance, and capacitance on the AC current in the circuit. Impedance  $Z$  can be expressed as  $\frac{E_t}{I_t}$ , following the equation of Ohm's law for AC circuits, as shown in Figure 4.1. [145]

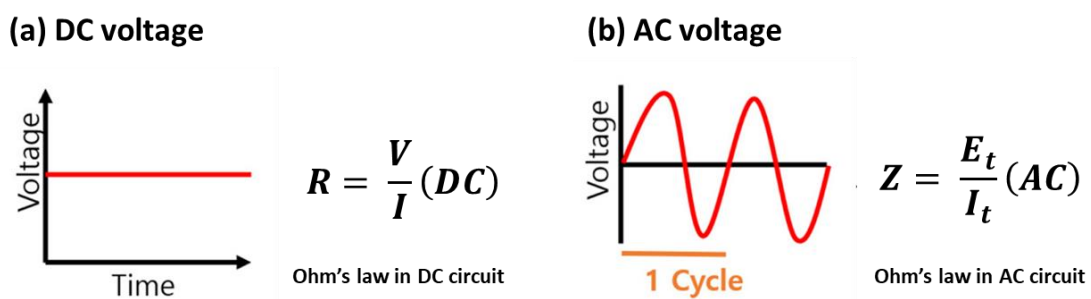


Figure 4.1 Ohm's law in a) DC circuits and b) AC circuits (Based on Ref. [145]).

Where  $R$  is the resistor ( $\Omega$ ),  $V$  is the voltage (volts), and  $I$  is the current (amps) for direct current, and  $E$  is the potential (volts), and  $Z$  is the impedance ( $\Omega$ ) for alternating current.

When a sinusoidal excitation signal is applied to the electrochemical system, it acts as a function of time as follows:

$$E_t = E_0 \sin(\omega t) \quad (51)$$

where  $E_t$  is the potential at time  $t$ ,  $E_0$  is the amplitude of the signal. The  $\omega$  in Equation 51 is the angular frequency, and its relationship with frequency ( $f$  in hertz units) is expressed as:

$$\omega = 2\pi f \quad (52)$$

In a linear system, the response current resulting from the applied sinusoidal perturbation excitation signal passing through the circuit has an offset in time ranging from 0 to 90 degrees (see Figure 4.2), which is called the phase angle shift ( $\varphi$ ), as shown below:

$$I_t = I_0 \sin(\omega t + \varphi) \quad (53)$$

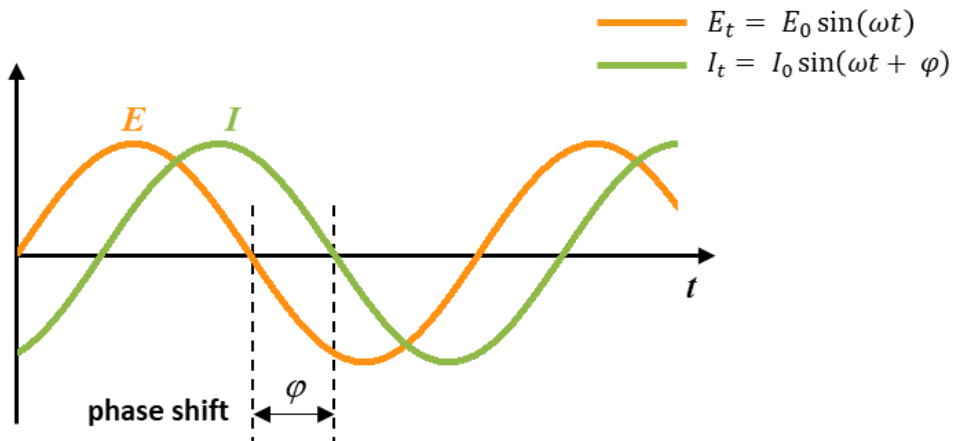


**Figure 4.2** The illustration and equation about the relationship between the voltage and current when applying an AC voltage with the angular frequency  $\omega$ .

Applying Equations (51) and (53) to Ohm's Law in AC, the impedance of the applied AC potential can be expressed as

$$Z = \frac{E(t)}{I(t)} = \frac{E_0 \sin(\omega t)}{I_0 \sin(\omega t + \varphi)} = Z_0 \frac{\sin(\omega t)}{\sin(\omega t + \varphi)} \quad (54)$$

Further introducing the concept of complex numbers  $j = \sqrt{-1}$ , according to Euler's formula:

$$e^{jx} = \cos x + j \sin x \quad (55)$$

The sinusoidal voltage and response current can be modified as follows:

$$E_t = E_0 e^{j\omega t} \quad (56)$$

$$I_t = I_0 e^{(j\omega t - \varphi)} \quad (57)$$

The complex form of impedance is expressed as:

$$Z(\omega) = \frac{E_t}{I_t} = Z_0 e^{j\varphi} = Z_0 (\cos \varphi + j \sin \varphi) = Z_{Re} + j Z_{Im} \quad (58)$$

where  $Z_{Re}$  is related to the real component and  $Z_{Im}$  is the imaginary component.

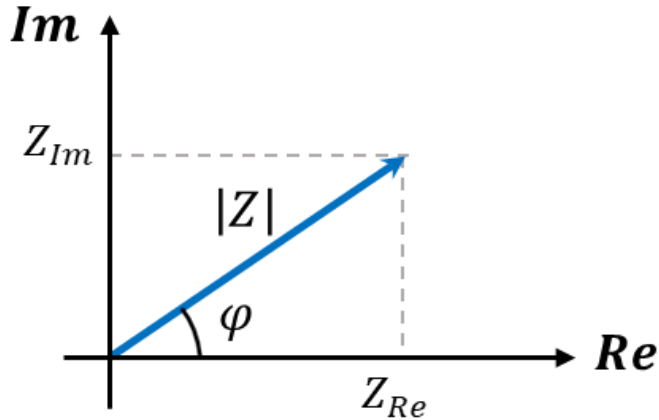


**Figure 4.3** Vector representation of impedance as complex number  $|Z|$ ;  $Z_{Re}$  real component and  $Z_{Im}$  imaginary part of the impedance.

As shown in Figure 4.3, the real and imaginary parts of the impedance in Equation (59) are expressed in cartesian coordinates to obtain a vector (blue arrow) of length  $|Z|$ . The vector  $|Z|$  represents the magnitude of the impedance, and the angle  $\varphi$  between the vector and the X-axis is called the phase angle, represented as follows:

$$|Z| = \sqrt{Z_{Re}^2 + Z_{Im}^2} \quad (59)$$

$$\tan(\varphi) = \frac{Z_{Im}}{Z_{Re}} \quad (60)$$

Based on the form of expression of impedance values, there are two ways to visualize electrochemical impedance spectra: the Nyquist plot and the Bode plot. The Nyquist plot, shown in Figure 4.4a, consists of the real and imaginary parts of the impedance, with each point representing the impedance at a specific frequency. On the other hand, the Bode plot (Figure 4.4b) displays  $|Z|$  (magnitude of impedance) and the phase angle as functions of frequency. The advantage of the Bode plot is that it provides frequency information along with impedance characteristics.

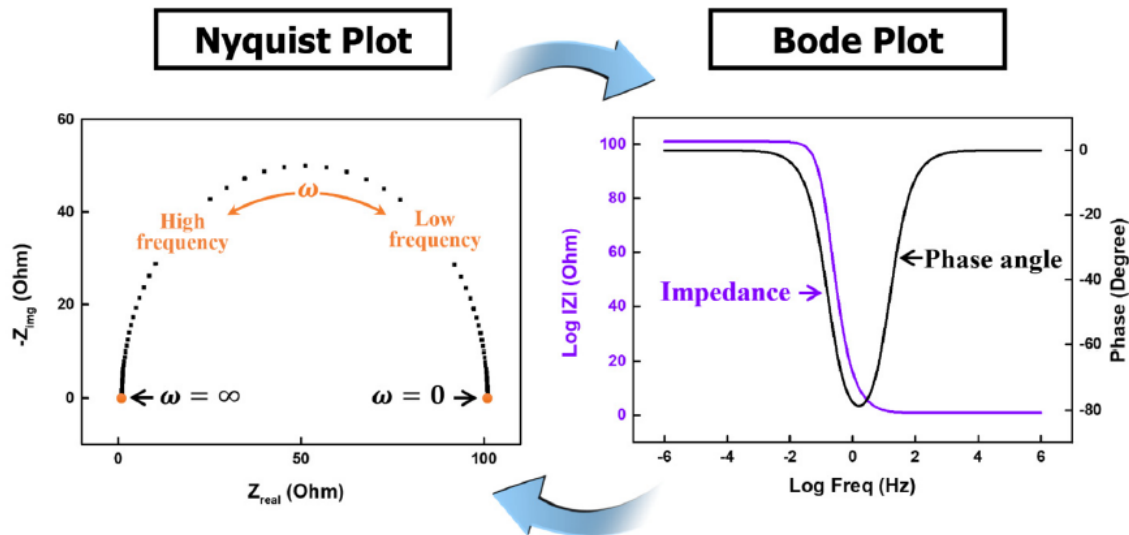


**Figure 4.4** Graphical representation of Impedance using Nyquist and Bode plot (Based on Ref. [145]).

Resistor ( $R$ ), capacitor ( $C$ ) and inductor ( $L$ ) are common circuit elements that are composed of circuits. Additional constant phase elements (CPE) are often used to describe the non-ideal behavior of electrodes. The corresponding impedance equations for the various circuit elements are shown in Table 4.1 [145].

**Table 4.1** Commonly used circuit elements in EIS modeling (Based on Ref. [145]).

Circuit Element	Symbol Used	Impedance
Resistor( $R$ )		$Z_R = R$
Capacitor( $C$ )		$Z_C = \frac{1}{j\omega C}$
Inductor( $L$ )		$Z_L = j\omega L$
Constant phase element ( $Q_{CPE}$ )		$Z_{CPE} = \frac{1}{Q(j\omega)^\alpha}$

#### 4.1.2. Application of electrochemical impedance spectroscopy in corrosion

Electrochemical impedance spectroscopy is one of the most important methods for studying metal corrosion processes because the vast majority of corrosion processes in metals are electrochemical in nature.

When a metal electrode is immersed in an electrolyte, metal ions dissolve, and charge transfer occurs. The charge builds up on the surface of the metal electrode and attracts ions from the solution, which leads to the formation of a double-layer structure with two parallel layers of charge at the interface between the metal electrode and the electrolyte, as shown in Figure 4.5. The dense layer close to the metal electrode contains solvent molecules as well as specifically adsorbed ions, and this layer is called the Inner Helmholtz Plane (IHP). The plane through the charge center of the ions is called the Outer Helmholtz Plane (OHP). In addition, the non-specifically adsorbed ions are distributed in the diffusion layer. The structure of the double layer at the interface is similar to the behavior of a parallel-plate capacitor. Thus, the metal/electrolyte interface allows the construction of equivalent circuits to study the corrosion behavior. At the interface, there is resistance to the charge transfer process ( $R_{ct}$ ) with the capacitance of the double layer ( $C_{dl}$ ) and the electrolyte generates the solution resistance ( $R_s$ ). By analyzing the electrochemical impedance spectrum, the contribution of each element to the impedance and its relationship with the electrochemical process can be derived.

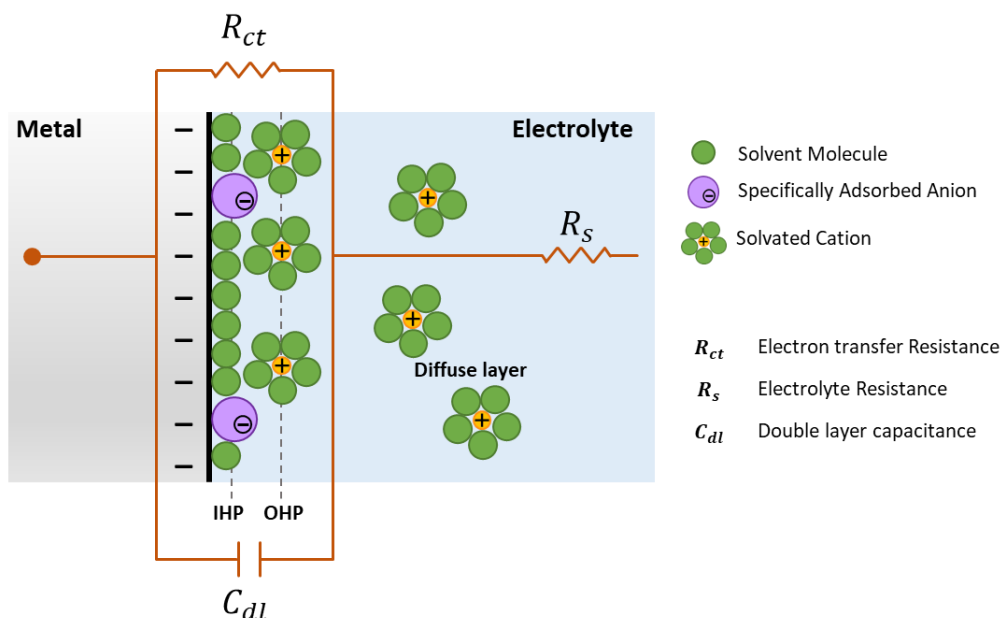


**Figure 4.5** Schematic simulation of the electrochemical interface metal/electrolyte, also known as the electrical double layer. IHP is Inner Helmholtz Plane and OHP is outer Helmholtz Plane. This interface is represented by an equivalent electrical circuit (EEC) model. In the model,  $R_{ct}$  is the electron transfer resistance,  $R_s$  is the electrolyte resistance,  $C_{dl}$  is the capacity of the double layer.

In an EIS experiment, the total resistance of the investigated system can be measured and evaluated in the frequency range of MHz to mHz. Electrochemical impedance spectroscopy can distinguish different electrochemical processes in a system by scanning in the frequency domain, enabling the detection of electrochemical processes on different time scales. By

measuring impedance values and resolving impedance spectra, it is possible to study the possible behavior and mechanisms in electrochemical systems such as corrosion systems.

#### 4.1.3. Cyclic voltammetry

Cyclic voltammetry (CV) is an electrochemical technique commonly used to study the redox behavior of electroactive species in a solution. It provides information about the oxidation and reduction processes occurring at an electrode surface and allows for the determination of electrochemical parameters such as redox potentials, electron transfer kinetics, and diffusion coefficients.

CV, also known as triangle wave linear potential scanning, involves applying a pulsed voltage of triangular waveform to the closed circuit formed by the working electrode and the counter electrode. This waveform rapidly changes the potential at the working electrode/electrolyte interface at a specified rate (Figure 4.6a). As a result, it induces the oxidation/reduction reaction of the active material on the working electrode, allowing us to measure the magnitude of the response current during the electrochemical process. The electrode potential and the response current magnitude are recorded throughout the process, resulting in the corresponding current-potential curve, which is called a cyclic voltammogram (Figure 4.6b). [146]

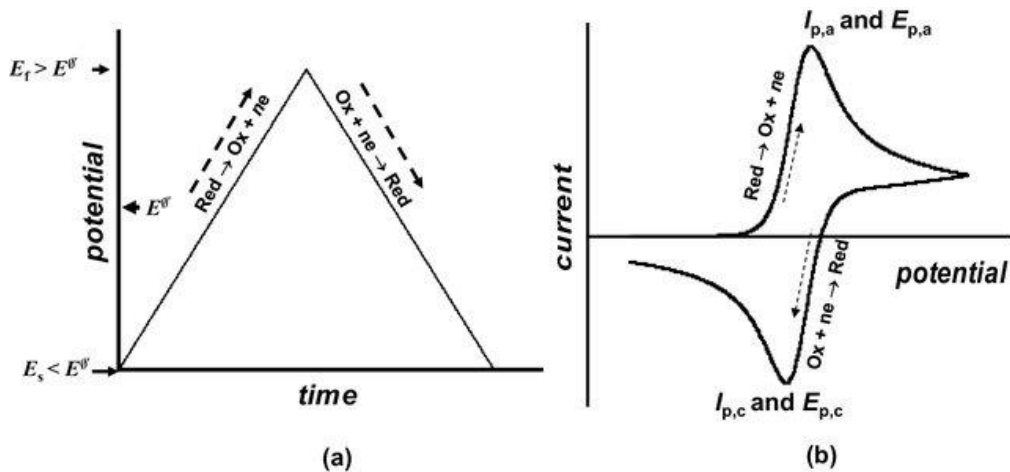


**Figure 4.6 a)** Typical potential variation and **b)** A typical cyclic voltammogram. The top curve represents increasing voltage, and the bottom curve represents decreasing voltage (Reprinted with permission from Ref. [146]. Copyright @ 2018, Springer Link)

In performing a CV measurement, the potential range is scanned in one direction starting from the initial potential. In general, the potential is scanned along the forward direction to the potential limit, and as the potential increases, the electroactive species on the electrode surface is oxidized, increasing current. At a specific potential, known as the oxidation

potential, the species loses electrons and is oxidized. After reaching the potential limit, the potential is then swept in the reverse direction (negative potential) back to the starting potential. This reverse potential scan allows the reduced form of the electroactive species to be regenerated, causing a reduction in current. At a specific potential, known as the reduction potential, the species gains electrons and is reduced. By analyzing the shape, magnitude, and position of the current peaks in the cyclic voltammogram, various parameters, such as peak current, peak potential, etc., can be determined, thus providing information about the electrode reaction, electrode reaction rate, and electrode surface properties, etc.

## 4.2 Spectroscopic techniques

Spectroscopy is a science that deals with the interaction of matter with light or electromagnetic radiation. It involves analyzing the spectrum of matter to identify substances and determine their chemical composition, structure, or relative content. Spectroscopic techniques are categorized into absorption, emission, and scattering spectra based on the principle of analysis.

According to classical physics, electromagnetic waves consist of alternating electric and magnetic fields propagating through space with specific frequency, intensity, and speed. Different electromagnetic waves have different wavelength  $\lambda$  or frequency  $f$ , and their relationship is given as follows:

$$f = \frac{v}{\lambda} \quad (61)$$

Where  $f$  is frequency in hertz (Hz),  $\lambda$  is wavelength in meter (m),  $v$  is wave speed in meter per second (m/s).

Electromagnetic waves can interact with charged particles, leading to an exchange of energy between the waves and matter. Spectral analysis is based on this energy exchange phenomenon. Matter is composed of atoms, and when an atom in its ground state absorbs external energy, its electrons transition to higher energy levels known as the excited state. However, the excited state is unstable, and the electrons will eventually return to the ground state or other lower energy levels, releasing the excess energy in the form of electromagnetic waves. The energy of the radiation can be expressed as follows:

$$\Delta E = E_2 - E_1 = h\nu = \frac{hc}{\lambda} \quad (62)$$

Where  $\Delta E$  is energy differences,  $E_2$  and  $E_1$  are the energy of high and low energy levels, respectively,  $c$  is the speed of light ( $c = 2.9 \times 10^{10} \text{ cm}\cdot\text{s}^{-1}$ ), and  $h$  is Planck's constant ( $h = 6.626 \times 10^{-34} \text{ J}\cdot\text{s}$ ).

As shown by Equation (62), the wavelength of each emitted spectral line depends on the energy differences. A series of characteristic spectral lines at different wavelengths can be created for the atoms of a particular element and recording them in wavelength order presents the spectrum.

Infrared spectroscopy, Raman spectroscopy, and X-ray spectroscopy are all branches of spectroscopy. They use different wavelengths or frequency ranges of electromagnetic radiation for their studies

### 4.2.1. Fourier-transformed infrared spectroscopy

Infrared spectroscopy (IR) is a branch of spectroscopy that deals with the infrared region of the electromagnetic spectrum, covering wavelengths between 0.7 and 1000  $\mu\text{m}$ . IR is primarily based on absorption spectroscopy, which takes advantage of the fact that molecules can absorb specific frequencies unique to their structure. Molecules can undergo vibrational motions, either in the form of stretching or bending. When a continuous wavelength infrared radiation passes through a substance, and its vibration or rotation frequency matches that of a group within the molecule, the molecule absorbs the infrared radiation, transitioning from the ground state energy level to a higher energy vibrational state. Selection rules for infrared spectroscopy indicate that a change in the molecule's dipole moment during vibration is necessary for infrared absorption, making the molecule "infrared active."

As most organic compounds possess infrared activity, infrared spectroscopy finds widespread use in the qualitative and quantitative analysis of organic molecules. Its ability to identify characteristic absorption bands associated with specific functional groups makes it an invaluable tool in various fields, including chemistry, biochemistry, and materials science, among others. With the advancement of infrared spectroscopy technology, various infrared techniques have been developed to cater to different sample types and analytical needs. Among these, Fourier-transformed infrared spectroscopy (FTIR) is particularly widespread and forms the core of many infrared applications. A typical setup of the FTIR is illustrated in Figure 4.7.

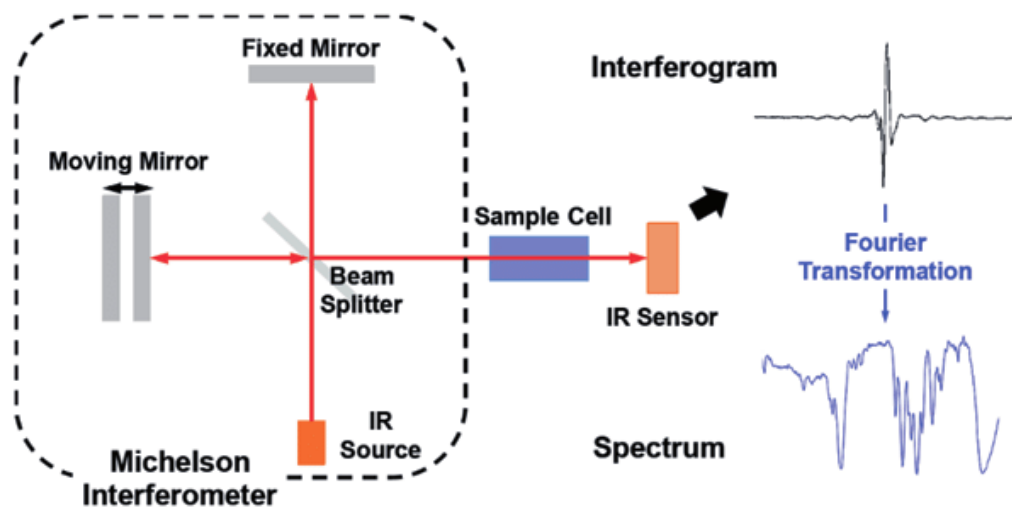


**Figure 4.7** A representative setup for FTIR microscopy (Reprinted with permission from Ref. [147]. Copyright @ 2014, Springer Link).

The IR radiation from the source is directed to the interferometer as a collimated beam. The interferometer consists of two perpendicular mirrors and a beamsplitter. The beam obliquely incidents on the semitransparent mirror and splits into transmitted and reflected beams (see Figure 4.7). The two beams are brought together again in the semi-transparent mirror after being reflected by the fixed mirror and the moving mirror, resulting in interference patterns. When a sample is placed in the beam path, the interferogram changes depending on the optical properties of the sample. The interferogram is a function of time and gives information about the relative intensity of the optical path difference. The spectrum is then obtained by performing the Fourier transform on the detector.

#### 4.2.2. Fourier-transformed infrared reflection absorption spectroscopy

Incident waves can be reflected, absorbed, transmitted or scattered at the material surface (see Figure 4.8a). Based on the different interaction modes, a variety of infrared spectra have been developed.

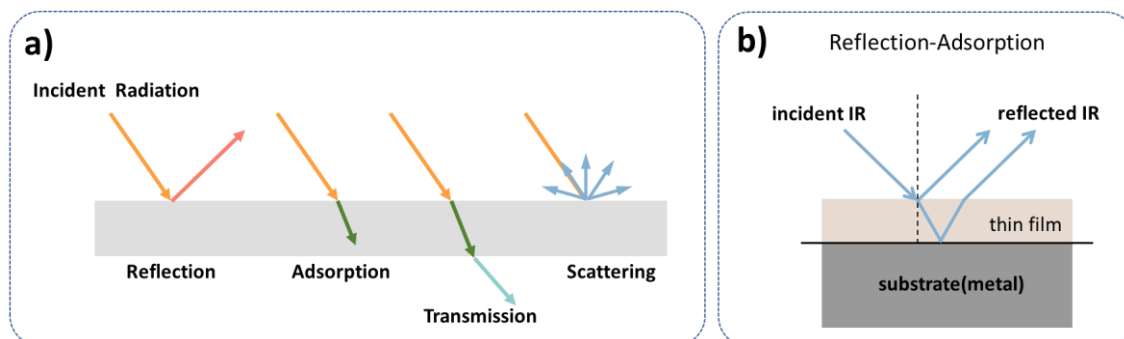


**Figure 4.8** a) Reflection, adsorption, transmission, and scattering at the surface; b) Schematic illustration of infrared reflection-absorption on a metallic sample with a thin film (Re-drawn from Ref. [148] and Ref. [149]).

Fourier-transformed infrared reflection absorption spectroscopy (FT-IRRAS) is one of the FTIR techniques based on reflection-absorption for the characterization of adsorbed substances and thin films on metal surfaces. The IR beam penetrates the sample, is reflected by the substrate, and passes the sample a second time. A reflective substrate (e.g., metals) is a prerequisite for IRRAS (see Figure 4.8b).

Due to the dielectric behavior of metals, when a molecule is adsorbed on a metal substrate, the molecule induces a mirror image dipole on the substrate. The dipole moment of the molecule can be oriented parallel or perpendicular to the surface. The electrical component of the incident IR light interacts with charges present on the surface, leading to polarization of the metal at the surface (Figure 4.9a).

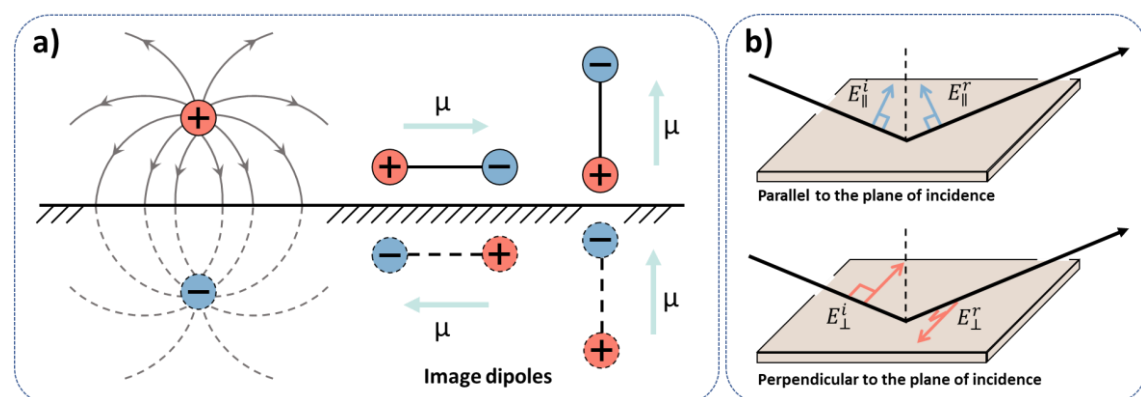


**Figure 4.9** a) Real and image dipoles at a metal surface; b) Electric vectors of the incident and reflected (Re-drawn from Ref. [150] and Ref. [151]).

As shown in Figure 4.9b, the E-field of the incident wave is split at the surface into components perpendicular ( $E_{\perp}$ ) and parallel ( $E_{\parallel}$ ) to the plane of incidence. The incident and reflected waves are shifted in phase by about 180° at the position of a reflection. For the direction perpendicular to the plane of incidence, the external electric field and the field resulting from polarization cancel each other out. This eliminates the causal electrical force, and no further polarization charges are built up. In contrast, the field component directed parallel to the plane of incidence generates a polarization field that aligns with the external field and adds to it. This enhances the component of the incident field. Hence, only those adsorbed species with a dipole moment perpendicular to the metal surface are IR active. The amplitude of the electric field oscillating normal to the metal surface is strongly dependent on the angle of incidence. For layers 0.5-20  $\mu\text{m}$  thick, the angle of incidence is usually between 10° and 60°, and thin layers in the range of a few nanometers show a maximum at grazing incidence. [152]

#### 4.2.3. Polarization modulation infrared reflection-adsorption spectroscopy

Polarization modulation infrared reflection-absorption spectroscopy (PM-IRRAS) is a highly sensitive technique usually used to detect thin films adsorbed on smooth metal surfaces [153]. In PM-IRRAS, the incident light is modulated with two polarizations, referred to as p- and s-polarizations. The p-polarized light oscillates parallel to the plane of incidence, while the s-polarized light oscillates perpendicular to the plane of incidence. When a smooth metal surface, e.g., gold, is illuminated with p-polarized light at a grazing angle, the electric field component perpendicular to the substrate is enhanced, while s-polarized light nearly eliminates the electric field component parallel to the substrate, which is known as the *metal surface selection rule*. PM-IRRAS makes use of this principle, where the phase change upon reflection for perpendicular polarization is constant, while for parallel light, it varies with the angle of incidence. As shown in Figure 4.10, the intensity of the electric field for parallel-polarized light increases with the angle of incidence, peaking near grazing incidence, while the intensity of the electric field for perpendicular-polarized light remains negligible [154]. As a result, only the parallel-polarized light provides information about the adsorbed species on the surface. The absorption of gas phase molecules is independent of the orientation of the electric field vector due to their random orientation. Consequently, phase-modulated spectroscopy effectively eliminates the sample environment's absorption interference. [149,153]

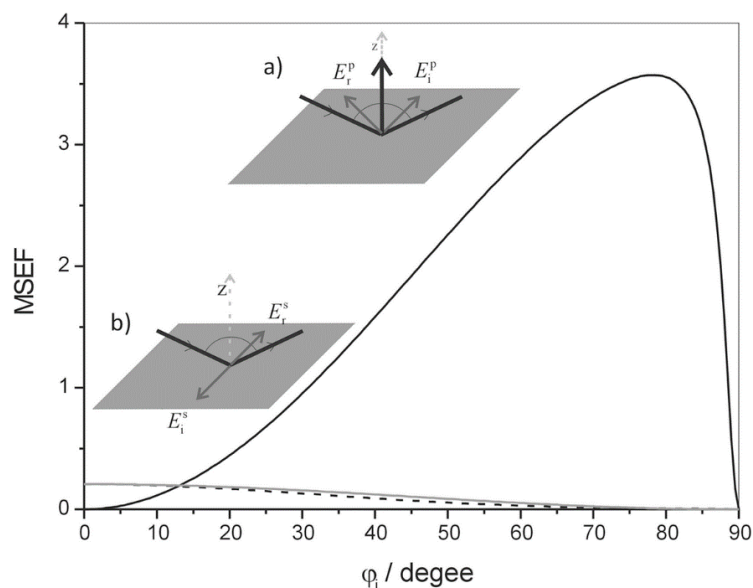


**Figure 4.10** Mean square electric field vector strength vs angle of incidence of the incoming IR radiation at  $\lambda = 3000 \text{ cm}^{-1}$  at the air/gold interface: normal component of the p-polarized (black solid line), in-plane component of the p-polarized (black dashed line) and s-polarized (grey solid line) IR light. Schematic representation of the direction of the  $E$  of the p-polarized **a**) and s-polarized **b**) before and after reflection from the gold surface at  $\varphi_i^{\text{Air}} = 88.5^\circ$  (Reprinted with permission from Ref. [154]. Copyright @ 2020, Springer Link).

In PMIRRAS measurements, polarized modulated infrared radiation is directed onto the sample surface. By recording the reflected intensity under different polarization states, two absorption spectra are obtained. The species adsorbed on the reflecting surface do not interact with the s-polarized light, providing the reference spectrum. On the other hand, the molecules adsorbed on the metal surface interact with p-polarized infrared radiation, providing the sample spectrum. [149,155] The intensities of the  $I_s$  and  $I_p$  are correlated with the intensity of the incoming IR radiation by the Beer law:

$$A_s = -\log\left(\frac{I_s}{I_{0s}}\right) \quad (63)$$

$$A_p = -\log\left(\frac{I_p}{I_{0p}}\right) \quad (64)$$

where  $A_s$  is the absorption for perpendicular-polarized light ( $I_{0s}$ ),  $A_p$  is the absorption for parallel-polarized light ( $I_{0p}$ ).

The absorbance spectrum ( $\Delta A$ ) of the surface layer is then obtained through the difference between the absorption under parallel-polarized and perpendicular-polarized light. [149] The  $\Delta A$  is equal to:

$$\Delta A = A_p - A_s \quad (65)$$

#### 4.2.4. Diffuse reflectance infrared Fourier transform spectroscopy

Diffuse Reflectance Infrared Fourier Transform Spectroscopy (DRIFT) is an IR technique based on the scattering of radiation within the sample, usually applied to the analysis of powders or rough surfaces.

The incident radiation has different interactions between the surface and the particles. Firstly, specular and diffuse reflected radiation can occur at the sample grain interface. Specular reflectance occurs at any interface between two materials with different refractive indices, where the angle of reflection is equal to the angle of incidence, which is also called Fresnel reflectance. [156] Diffuse reflected radiation occurs at surface grain interfaces that are not parallel to the surface of the macroscopic sample, and the angle of reflection is not equal to the angle of incidence. However, this diffusely reflected radiation will not carry information about the sample because it is isotropically scattered and is called diffuse Fresnel reflection. Different from the first two types of reflected radiation, which occur at the outer surface only,

the other type of radiation is transmitted through the sample grain and is called diffuse Kubelka-Munk reflectance. This radiation has been transmitted through one or more sample grains and carries information about the analyzed sample, and is isotropically scattered. [156] In DRIFT, the diffuse reflectance spectra obtained from the sample are typically expressed as a ratio of the diffuse reflectance to the reflectance of a reference material. The Kubelka-Munk function allows for the transformation of the diffuse reflectance spectra into a more straightforward representation and allows for the quantification of the sample's absorption and scattering contributions, enabling a more accurate analysis of the sample's molecular composition and surface properties. [157]

#### 4.2.5. Attenuated total reflection FTIR spectroscopy

Attenuated total reflection FTIR spectroscopy (ATR - FTIR) is equipped with an ATR attachment which is designed based on the phenomenon of total internal reflection and is able to realize the in-situ characterization of solid-liquid interfaces (see Figure 4.11). Internal reflection elements (IRE), also called ATR crystals, Ge, Si, Diamond, and Thallium bromide/iodide (KRS-5), are the commonly utilized materials which have a known and comparatively higher refractive index. [158,159]

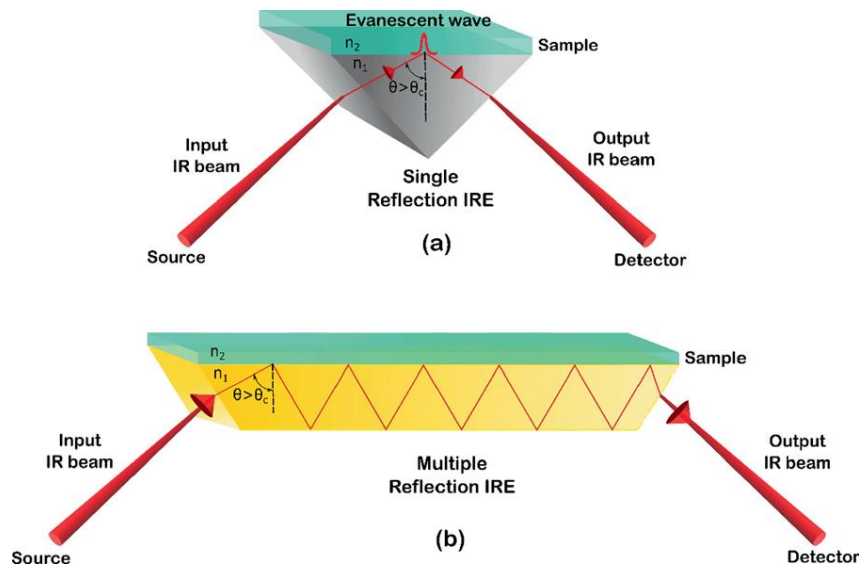


**Figure 4.11** Optical ray diagram of a single reflection and b multiple reflection internal reflection (IRE) geometries of ATR-FTIR spectrometer (Reprinted with permission from Ref. [160]. Copyright @ 2021, Springer Link).

At the boundary between two media, when the condition is met: the refractive index  $n$  of medium 1 ( $n_1$ ) is greater than the refractive index  $m$  of medium 2 ( $n_2$ ), i.e., light enters the optically rare medium from the optically dense medium, and the angle of incidence  $\theta$  is greater than the critical angle  $\theta_c$ , total reflection of the incident light beam will occur. In fact,

when infrared radiation is reflected from the surface, it penetrates the sample surface to a certain depth before it is reflected. In this process, the IR-active species at the interface have selective absorption in the frequency region of the incident light, and the intensity of the reflection is reduced and producing a spectrum, thus obtaining structural information on the chemical composition of the surface layer.

The internal reflection causes evanescent waves, which decay exponentially in the optically rare medium according to the relation:

$$E = E_0 \cdot e^{-z/d_p} \quad (66)$$

where  $E$  is the amplitude of the evanescent wave that decays exponentially with the distance from the interface ( $z$ ),  $E_0$  represents the amplitude of the electric field of IR radiation at the interface. The penetration depth  $d_p$  is defined as the penetration distance when the electric field intensity of the radiated wave decays to  $1/e$  of its value at the surface, i.e.:

$$d_p = \frac{\lambda}{2\pi n_1 \sqrt{\left[\sin^2 \theta - \left(\frac{n_2}{n_1}\right)^2\right]}} \quad (67)$$

From Equation (67), the penetration depth  $d_p$  depends on the wavelength of the radiation beam, the refractive index of the reflecting material and sample, and the angle of incidence. The commonly used infrared radiation wavelengths range from 4000 to 400  $\text{cm}^{-1}$  (2.5 - 25  $\mu\text{m}$ ). Thus ATR spectra give spectral information only at the micron level or thinner layers from the interface. After an attenuated total reflection, the depth of light penetration into the surface is limited, and the sample absorbs less light, so the energy change of the beam is less. The absorption band is weak, and the signal-noise ratio (S/N) is poor. In order to enhance the intensity of the absorption peaks and improve the S/N, most IRE enhance the absorption spectrum by increasing the number of total reflections. This is called multiple attenuation total reflection (see Figure 4.11). When multiple reflections occur, the summation of discrete reflections is obtained. The total effective depth is expressed as follows:

$$d_{eff} = \sum_i N_i \cdot d_i \quad (68)$$

where  $N_i$  is the number of total internal reflections, each with penetration depth  $d_i$ .

The total number of internal reflections  $N$  is related to the length  $l_{IRE}$  and the thickness of the crystal  $d_{IRE}$  of the ATR crystal. In general,  $l_{IRE}$  and  $d_{IRE}$  of are determined, and the

angle of incidence  $\theta$  can be varying within a certain range. The total number of internal reflections  $N$  can be calculated as follows:

$$N = \frac{l_{IRE}}{2 \times d_{IRE} \times \tan\theta} \quad (69)$$

#### 4.2.6. Raman spectroscopy

Raman spectroscopy, similar to IR spectroscopy, provides information about the vibrational and rotational states of molecules. Raman spectroscopy is based on the Raman scattering effect discovered by Indian physicist C.V. Raman [161], which analysis the scattered light with different frequencies than the incident light to obtain information about the vibrational energy modes of a sample.

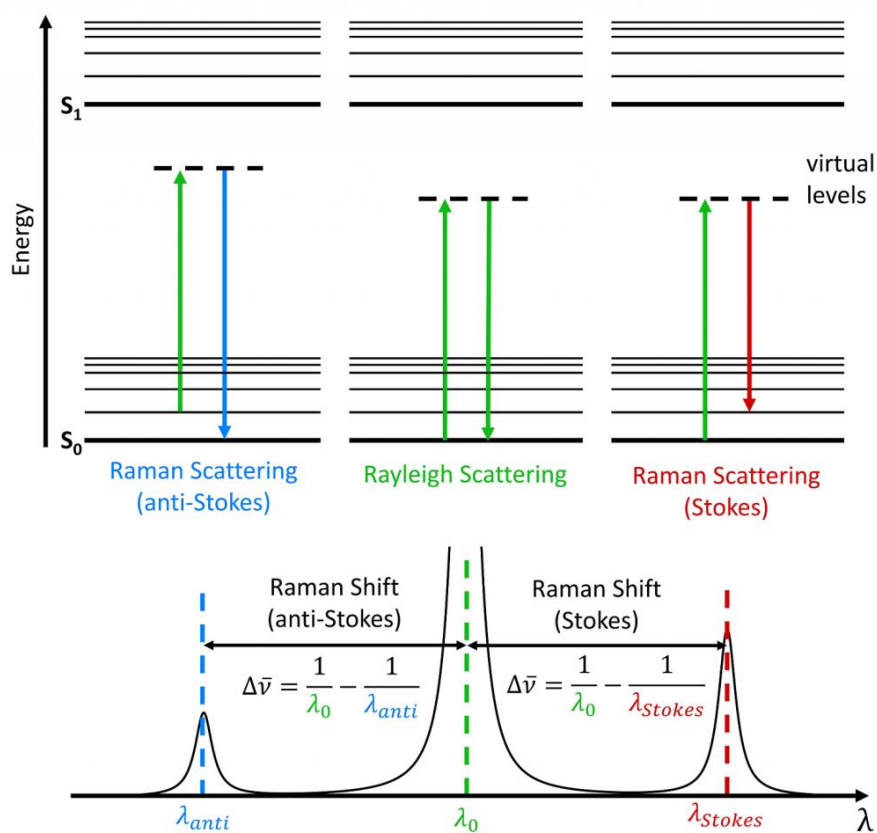


**Figure 4.12** Schematic representation of the energetic states of a molecule with regard to Rayleigh scattering and the two possible Raman scatterings (Reprinted with permission from Ref. [162]. Copyright @ 2023, Springer Link).

Unlike IR spectroscopy, the Raman effect is practically independent of the wavelength of the excitation radiation and is brought about by the interaction of electromagnetic radiation with the electron shell of the molecule. The incident radiation's photons interact with the electron cloud of the molecule, acting as the scattering center, resulting in molecular deformation and excitation from a ground state to a virtual state. Most of the photons change

direction and are scattered, while the frequency of the light remains the same as the excitation source. This scattering is called Rayleigh scattering and is the dominant process. On the other hand, a minor part of the photons (approximately  $10^{-6} \% \sim 10^{-10} \%$ ) undergoes inelastic scattering, known as Raman scattering. This is due to the transfer of energy between the molecule and scattered photons. As shown in Figure 4.12, molecules can gain or lose energy from photons during the scattering process. When a molecule in the ground state absorbs the energy of photons and is excited to the virtual state, and then returns to the vibrationally excited state, the energy of the scattered photons is lower than that of the incident radiation, this process is called Stokes scattering. In contrast, anti-Stokes scattering is when a molecule in a vibrationally excited state is excited to a virtual state and then releases photons to jump back to the lower energy state, i.e., the energy released is greater than the energy absorbed. In fact, according to Boltzmann's law, there are more molecules in the ground state than in the excited state, so the intensities of the Stokes-shifted Raman bands are more intense.

#### 4.2.7. X-ray photoelectron spectroscopy

X-ray Photoelectron Spectroscopy (XPS) is a widely used analytical technique in the fields of materials science, chemistry, and physics. It provides information about the chemical composition, electronic structure, and oxidation state of a sample by analyzing the X-rays emitted when the sample is subjected to a high-energy photon source [163].

In XPS, a sample is placed in a vacuum chamber with a pressure typically below  $10^{-3}$  Pa and exposed to a beam of high-energy X-rays, typically with an energy range of 1200-1500 eV, which causes the emission of photoelectrons from the sample's surface. The intensity and the relatively low kinetic energy ( $E_{kin}$ ) distribution of the photoelectrons is recorded by an electron spectrometer. The energy of the emitted photoelectrons is dependent on the binding energy ( $E_b$ ) of the electrons in the sample [164]. The binding energy of an electron located at the Fermi level can be defined as:

$$E_b = h\nu - \Phi - E_{kin} \quad (70)$$

where  $\Phi$  is the work function of the spectrometer,  $h\nu$  is energy of X-ray.

By analyzing the binding energies of electrons, which are affected by their chemical environment, it is possible to determine the orbital from which a measured electron originates. Figure 4.13 illustrates the photoemission process, whereby an electron from the 1s orbital is escaped.

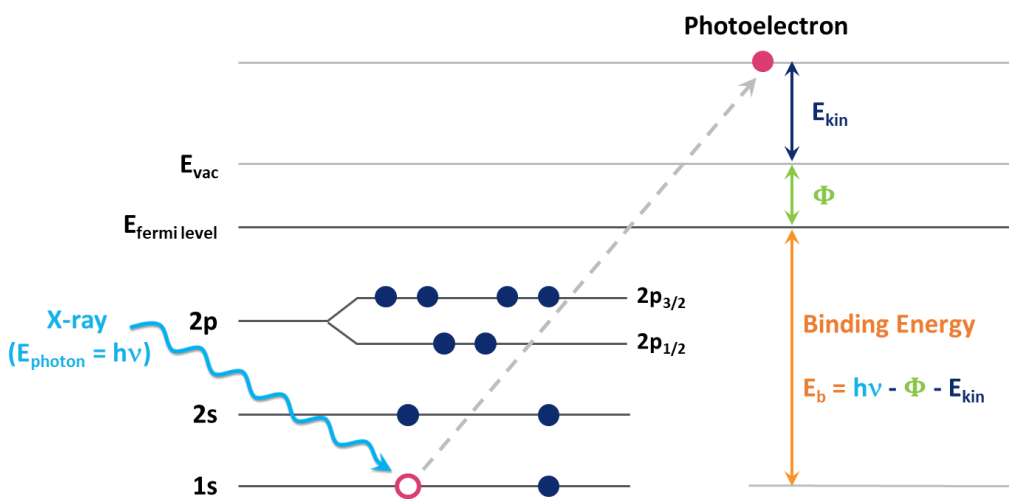


**Figure 4.13** Schematic illustration of the photoelectron emission process (Re-drawn from Ref. [163]).

The kinetic energy of the photoelectrons emitted during the XPS process is indicative of the element from which they originated. Information about the chemical state and quantity of each element can then be obtained by analyzing the position and intensity of the peaks in the energy spectrum. The surface sensitivity of XPS is determined by the distance that the photoelectron can travel through the material without losing any kinetic energy. During the process of photoemission, a photoelectron can interact with other electrons within the surface, thereby losing a fraction of its kinetic energy to them before leaving the material. Inelastic scattering events that cause the photoelectrons to lose some kinetic energy before they leave the sample contribute to the background signal in the energy spectrum, while elastically scattered photoelectrons contribute to the photoelectron peaks. Prior to performing data analysis, appropriate techniques must be employed to account for the background signal in the energy spectrum. One common approach involves subtracting a linear background from the spectrum before evaluating the peak areas. The spectra are dependent on the core electrons of the investigated system, which are influenced by its chemical environment. Spectra of the same element exhibit differences in core electron binding energy of up to a few electronvolts (eV), depending on its chemical form. This is referred to as a chemical shift. By determining the charge distribution within a chemical compound, the oxidation state of an atom or group of atoms can also be inferred. Thus, the shape of the spectra can provide information about the valence state of an element. In addition, photoemission is accompanied by various physical processes, such as photoluminescence or the generation of Auger electrons, which have been used as separate measurement techniques in their own right.

### 4.3 Ellipsometry

Ellipsometry is a non-destructive and non-invasive optical technique used for characterizing thin films and surfaces [165]. It is based on the principle of measuring changes in the polarization state of light reflected or transmitted from a sample. The polarized light is usually elliptically polarized after reflection of the sample, therefore, the technique is well known as ellipsometry [166].

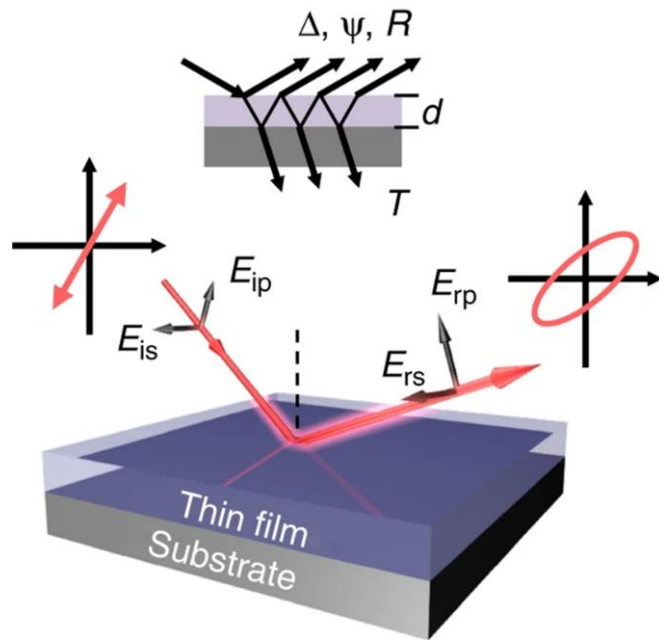


**Figure 4.14** Schematic illustration of ellipsometry (Based on Ref. [167]).

As shown in Figure 4.14, a thin film of unknown optical constants (refractive index  $n$ , extinction coefficient  $k$  and thickness  $d$ ) is positioned on a substrate with known optical properties. Incident light ( $E_i$ ) is directed at an oblique angle onto the film, as illustrated in the inset. Within the film, multiple beam interference occurs, leading to different reflection coefficients ( $rp$  and  $rs$ ) for the orthogonal polarization components ( $E_p$  and  $E_s$ ). Consequently, the reflected light ( $E_r$ ) becomes elliptically polarized. The designations "p" and "s" correspond to polarizations with electric fields parallel and perpendicular to the plane of incidence, respectively [167]. The ellipsometer measures the amplitude ratio ( $\Psi$ ) and the phase difference ( $\Delta$ ) between the p-polarized and s-polarized components of the reflected or transmitted light. These parameters are sensitive to the optical properties and thickness of the sample layer. By comparing the measured values with a mathematical model, the optical constants ( $n, k, d$ ) of the thin film can be determined.

#### 4.4 Atomic force microscope

Atomic force microscopy (AFM) is a technique for characterizing the three-dimensional structure of a sample at the nanoscale, introduced in 1986 by Binnig, Quate, and Gerber [168]. The main principle involves using a microcantilever with a thin probe to sense and amplify forces between the cantilever and the atoms on the target sample's surface, enabling the study of material surface structure and properties. AFM allows the analysis of various materials and samples in both atmospheric and liquid environments with atomic-level resolution.

The schematic setup of an AFM is shown in Figure 4.15. The AFM consists of a microscopic and force-sensitive cantilever with a sharp tip on the head, which is used to raster-scan over the sample surface using a feedback loop. As the fine tip approaches a solid surface, there is an attractive force between the tip's foremost atoms and the surface atoms, followed by a repulsive force. The force acting on the tip causes the cantilever arm to bend. A laser beam is reflected from a point on the cantilever onto a quartered photodiode, which detects the tip's movement. The optical signals of the beam deflection are directly measured and further processed at the signal processor.

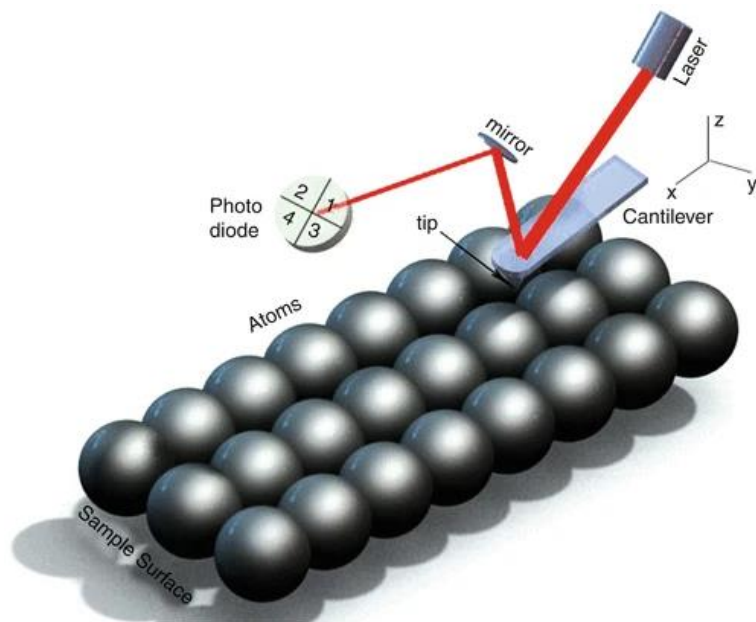


**Figure 4.15** Illustration depicting the operation principle of the AFM (Reprinted with permission from Ref. [169]. Copyright @ 2023, Springer Link).

The effective force with distance dependence corresponds to the LENNARD-JONES-POTENTIAL, and different force regions correspond to the three typical modes of AFM, which is shown in Figure 4.16.

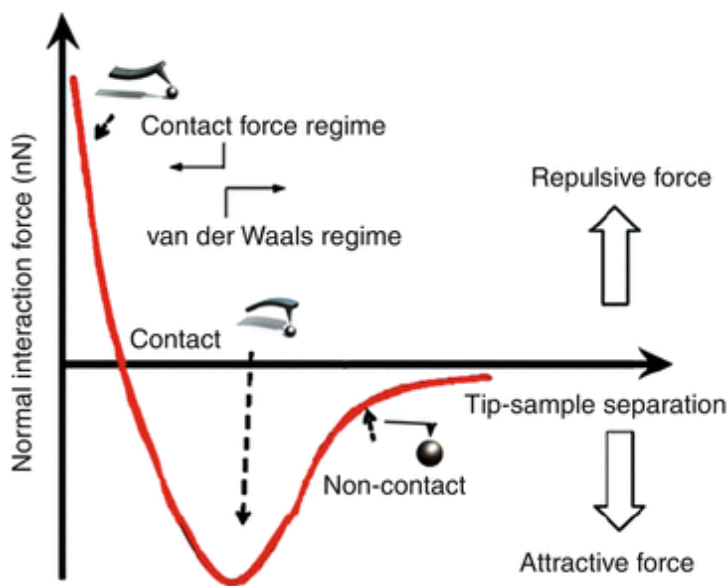


**Figure 4.16** Distance dependence of the acting force between the tip and the surface (Reprinted with permission from Ref. [169]. Copyright @ 2023, Springer Link).

For the contact mode, the tip is in soft physical contact with the sample surface during the entire measuring time, and there is a strong repulsive force between the tip and the sample surface. The tip moves above the surface at a specific height or under a constant force. This movement is strongly influenced by friction and adhesion forces. When measuring under ambient pressure or in a liquid film, the surface tension forces may attract the tip. If these forces are sufficient, the sample's surface can be damaged. The use of the Contact mode is suitable for hard sample surfaces. However, for softer materials, such as biological specimens, this mode is disruptive [170].

Compared to the statically operated contact mode, there are two dynamically operated modes: the tapping mode and the non-contact mode. In the non-contact mode, the tip is several nanometers distant from the sample surface, and the cantilever is excited to oscillate close to its resonant frequency. In this mode, attractive forces dominate. A further dynamic mode of operation is the tapping mode, which is used more frequently than the non-contact mode. When operating in tapping mode, the cantilever is moved to oscillate up and down at or near its resonant frequency. In this mode, the cantilever oscillates with a higher amplitude than in the non-contact mode. As the tip approaches the sample surface, the forces between the tip and the sample cause the amplitude to dampen. Intermittently approaching the surface can effectively eliminate friction and reduce the trouble caused by adhesion. Tapping mode is less destructive than the contact mode and is a suitable choice for testing soft samples.

[168]

## 4.5 Scanning electron microscope

Scanning Electron Microscopy (SEM) is a powerful imaging technique that uses an electron beam to create high-resolution images of samples and can also produce detailed 3D images of a sample's surface using stereoscopic imaging. The basic principle of SEM involves the use of a focused electron beam that is scanned across the surface of the sample in a raster pattern [171].

The main components of the SEM are electron sources, electron lenses, a sample stage, detectors, and an image display system (Figure 4.17). The electron source is a critical component of SEM, responsible for continuous and uniform electron emission. Tungsten (W) and lanthanum hexaboride ( $\text{LaB}_6$ ) are widely used electron sources in conventional SEM, which maintain stable electron emission through the application of the necessary filament heating current. Field Emission Scanning Electron Microscopy (FE-SEM) represents another type of SEM, utilizing a field emission gun (FEG) as the electron source. FEG operates by exciting electrons through the potential difference between the cathode and anode. FE-SEM can provide higher resolution and greater surface sensitivity compared to conventional SEM.

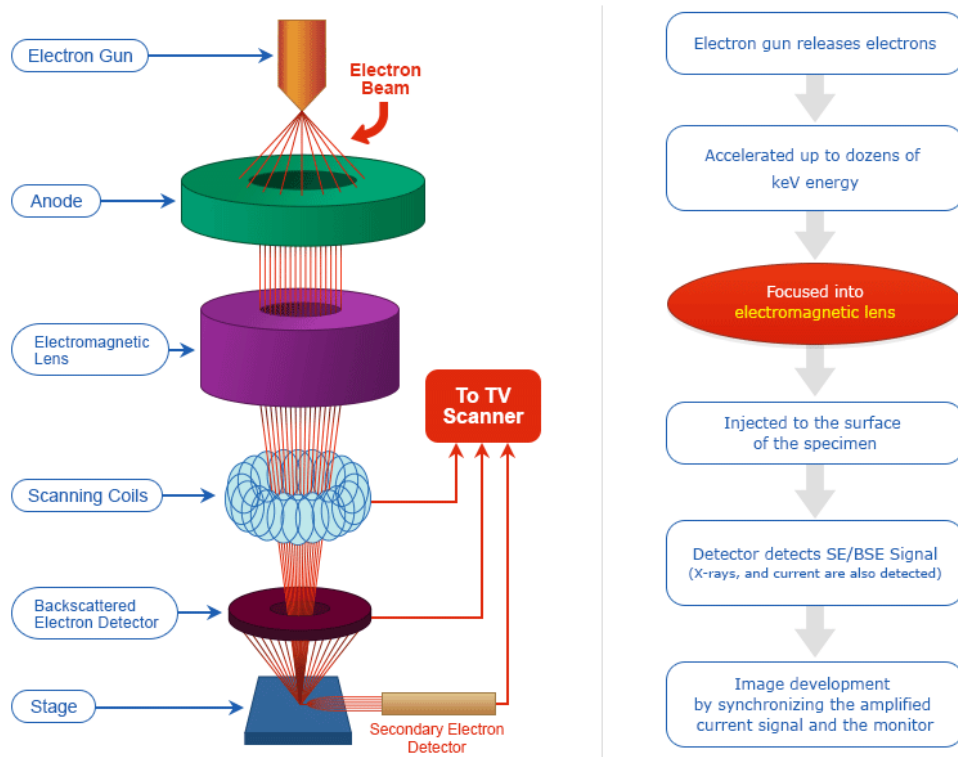


**Figure 4.17** Schematic representation of a scanning electron microscope (Based on Ref. [172]).

As shown in Figure 4.17, the electron beam emitted by the electron sources is focused and accelerated by magnetic lenses and electric fields in the SEM and is then directed onto the sample. The beam electrons interact with the nuclei or outer-shell electrons of the atoms in the sample, causing scattering that alters the direction or energy of the beam electrons, thereby producing various signals that reflect the characteristics of the sample. The scattering process is divided into elastic and inelastic scattering and occurs simultaneously. The former causes the incident electrons to deviate from their original direction of motion and to diffuse inside the sample, while the latter causes the electrons' energy to decrease gradually until they are completely absorbed by the sample, limiting the diffusion range of the electron beam. The energy of the electron beam is fully deposited in the interaction region, and a large amount of detectable secondary radiation is generated. This region is called the interaction volume. Elastic scattering results in backscattered electrons, whereas inelastic scattering produces secondary electrons, Auger electrons, and X-rays [171]. The interaction volume and the type of signal generated are illustrated in Figure 4.18. Generally, the higher the energy of the electron beam, the deeper the electron penetration depth, and the larger the interaction region. The larger the atomic number of the sample, the more elastic scattering events the beam electrons experience per unit distance traveled, resulting in a larger average scattering angle and shallower penetration depth in the sample.

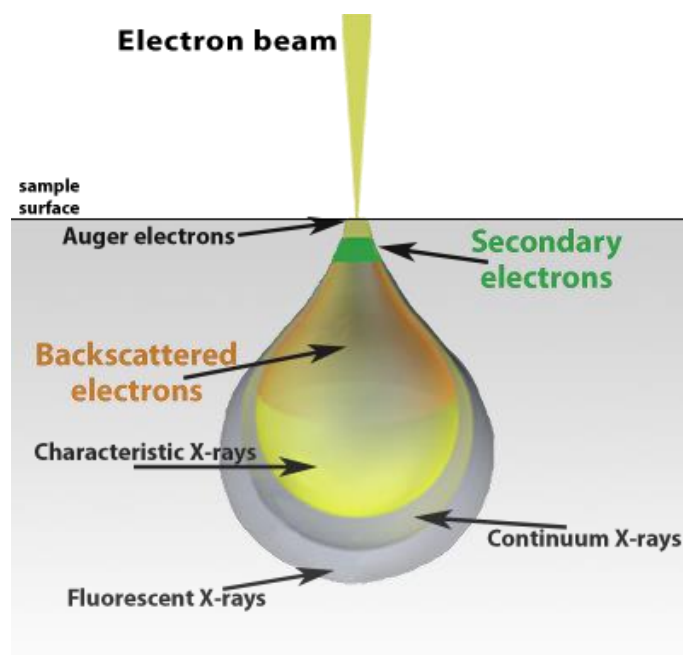


**Figure 4.18** Interaction volume and signal emission (Based on Ref. [173]).

The emitted signals are then detected by specialized detectors and used to generate images of the sample. Secondary electrons are low-energy electrons that are generated by the sample through inelastic scattering with incident high-energy electrons. These electrons typically originate from the first few nanometers of the sample surface. The detection of these secondary electrons is accomplished using an Everhart-Thornley detector (ETD), also referred to as an InLens detector, which is primarily used to produce images of the surface morphology of the sample [174]. Backscattered electrons are high-energy electrons that are backscattered from the atoms in the sample because of elastic collisions between the incident electrons and the atomic nuclei. The energy of the backscattered electrons is proportional to the atomic number of the element being struck, so it is useful for characterizing the composition of the sample. Backscattered electrons are collected by an SE2 detector, which is located on the side of the primary beam. Simultaneously, the detector also detects secondary electrons that are emitted from the sample surface due to the inelastic scattering of the primary electron beam [174]. The SE2 detector is suitable for characterizing the spatial morphology of the sample and can be used in conjunction with the InLens detector to obtain images with complementary information during detection. Furthermore, the inelastic interaction between the sample atoms and the electron beam leads to the appearance of characteristic X-rays and continuous radiation. The produced characteristic radiation is measured as wavelength or energy-dispersive radiation, which provides valuable information regarding the chemical composition of the sample. This analytical technique is referred to as energy-dispersive X-ray spectroscopy (EDX) [175].

## 5 Experimental

### 5.1 Materials and chemicals

#### 5.1.1. Chemicals and electrolyte

In the experiments of this work, ultrapure in HPLC quality water purchased from Carl Roth was utilized for all electrolyte configurations. The ethanol (EtOH) was an analytical grade reagent from Merck KGaA, Darmstadt, Germany, and was used without further purification.

Phosphate buffered saline (PBS, powder form, PPB006) was purchased from Sigma-Aldrich, Steinheim, Germany. One pouch was dissolved in 500 mL of deionized water to obtain a PBS solution containing 10 mM Na<sub>2</sub>HPO<sub>4</sub>, 1.8 mM KH<sub>2</sub>PO<sub>4</sub>, 138 mM NaCl and 2.7 mM KCl with a pH of 7.4. PBS was used as a model electrolyte in sections 6.1 and 6.4 of this thesis.

Modified simulated body fluid (m-SBF) used in sections 6.2 and 6.3 was prepared according to the recipe of Oyane et al. [106]. The final solution contained 142 mM Na<sup>+</sup>, 5 mM K<sup>+</sup>, 1.5 mM Mg<sup>2+</sup>, 2.5 mM Ca<sup>2+</sup>, 103 mM Cl<sup>-</sup>, 10 mM HCO<sub>3</sub><sup>-</sup>, 1 mM HPO<sub>4</sub><sup>2-</sup> and 0.5 mM SO<sub>4</sub><sup>2-</sup>. 2-[4-(2-hydroxyethyl)-1-piperazinyl]ethanesulfonic acid (HEPES) and 1.0 M NaOH aqueous solution were used to adjust pH to 7.4. The chemicals used are listed in Table 5.1.

**Table 5.1** Overview of chemicals used in the preparation of m-SBF solution.

Reagents	Purity	Provider
NaCl	>99.5%	VWR
NaHCO <sub>3</sub>	>99.5%	VWR
Na <sub>2</sub> CO <sub>3</sub>	>99.5%	VWR
KCl	>99.5%	Merck
K <sub>2</sub> HPO <sub>4</sub> · 3H <sub>2</sub> O	>99.0%	Merck
MgCl <sub>2</sub> · 6H <sub>2</sub> O	>98.0%	Merck
NaOH	—	Merck
HEPES	>99.9%	Roth
CaCl <sub>2</sub>	>95.0%	Merck
Na <sub>2</sub> SO <sub>4</sub>	>99.0%	Merck

HEPES, (4-(2-hydroxyethyl)-1-piperazineethanesulfonic acid)

### 5.1.2. Protein

Table 5.2 provides detailed information about the used proteins. All protein-containing solutions were freshly prepared prior to each use. Human serum (HS) was added into the test medium in section 6.1 and 6.4. In section 6.2, BSA and LYZ were used as model proteins.

**Table 5.2** Overview of protein reagents used.

Protein	Product Nr.	Biologische quelle	Assay	Provider	Section
Human serum	H5667	Human male AB plasma		Sigma-Aldrich	6.1, 6.4
BSA	A3294,	Heat shock fraction	≥98%	Sigma-Aldrich	6.2
LYZ	L6876	Lyophilized powder, hen egg white	≥90 %	Sigma-Aldrich	6.2

### 5.1.3. Metals and preparation of alloys

Conventional FeMn steel X-IP<sup>TM</sup> 1000 (FeMn), FeMn alloy fabricated by selective laser beam melting (FeMn-LBM), and pure Fe were used in this thesis. Table 5.3 lists the metallic materials used in this thesis.

**Table 5.3** Overview of metallic substrates.

Substrate	Manufacturing	Dimension/mm	Provider	Section
<b>FeMn-LBM</b>	LBM	20 × 20 × 2	-	6.2
<b>FeMn</b>	cold rolling	20 × 20 × 2	ArcelorMittal Germany Holding GmbH	6.2
<b>Fe</b>	hot rolling	20 × 20 × 2	ALLIEDPUREIRON®, Allied Metals Corporation	6.2
<b>Fe</b>	hot rolling	15 × 15 × 3	ARMCO®	6.3
<b>Fe</b>	hot rolling	20 × 20 × 5	ARMCO®	6.4

## 5.2 Preparation of additive manufactured Fe alloys

The FeMn-LBM samples were produced and provided by Jan Tobias Krüger, University of Paderborn, Direct Manufacturing Research Center, and the production was performed following Niendorf et al. [176] with an SLM 250HL (SLM Solutions Group AG, Lübeck,

Germany) using gas-atomized FeMn-powder (Nanoval GmbH & Co. KG, Berlin, Germany) with a nominal particle size of 20  $\mu\text{m}$  – 63  $\mu\text{m}$ . As a feedstock for the powder, pure elements have been used and were processed under an argon gas atmosphere. Processing parameters followed by Reference by Niendorf [177], samples were built up in 30  $\mu\text{m}$  layers based on the same set of processing parameters, applying 175 W laser power at a scan velocity of 750  $\text{mm s}^{-1}$  and a hatch distance of 0.12 mm.

The chemical compositions of FeMn-LBM measured by optical emission spectroscopy (OES) are presented in Table 5.4.

**Table 5.4** Chemical composition (wt-%) of FeMn-LBM measured via OES.

	Mn	C	V	Si	Cr	Fe
<b>FeMn-LBM</b>	20.31	0.58	0.03	0.02	0.06	bal.

### 5.3 Preparation of thin metal oxidized surfaces

The thin metal films were deposited on commercial Si(100) wafers (p-doped, Siegert Wafer GmbH, Germany) with native surface oxide. After RCA1 cleaning and subsequent rinsing in water and ethanol, a 10 nm Cr (99.95%, Umicore AG & Co. KG, Germany) buffer layer followed by 150 nm Au (99.999%, Goodfellow GmbH, Germany) were deposited by thermal evaporation (tectra GmbH, Germany). The Fe (99.95%, Angstrom Engineering Inc, Canada) films (30 nm) were deposited on top of the Au films with an intermediate 3 nm Cr (99.95%, EVOCHEM Advanced Materials GmbH, Germany) buffer layer by magnetron sputter deposition (Angstrom Engineering Inc, Canada). Right before each adsorption experiment, the sample surfaces were rinsed with ethanol and dried in a stream of nitrogen.

### 5.4 Surface preparation of metal alloys

#### 5.4.1. Mechanical polishing

All samples performing mechanical polishing were ground iteratively using silicon carbide (SiC) papers of P600, P1000, P2500, and P4000 grit to achieve a mirror-like finish and subsequently polished with 1  $\mu\text{m}$  diamond paste (Schmitz). The mechanically pretreated samples were ultrasonically cleaned (Ultrasonic Cleaner, 45 kHz, 120 W, VWR International GmbH, Darmstadt, Germany) for 10 min in ethanol abs. (p.a., Merck KGaA, Darmstadt, Germany). After cleaning, the samples were rinsed with ethanol abs. and dried with a stream of nitrogen.

#### 5.4.2. Electropolishing

In section 6.3, Fe samples that were performed electropolished were done and provided by Steffen Wahrkenrohe, Leibniz University Hannover, Materials Science. The specimens were electropolished with a lectro pol 5© system. The removal height was 150  $\mu\text{m}$ , so that further surface defects due to the cutting process could be excluded.

#### 5.4.3. Chemical etching

In this work, the etching solution was a mixture of nitric acid and ethanol, with a nitric acid volume concentration of 5% (5% Nital). The specimens underwent a mechanical polishing and cleaning process before being etched. The cleaned samples were immersed in the 5% Nital solution for 5 seconds, followed by an immediate rinse with ethanol, and finally dried using nitrogen.

### 5.5 Electrochemical measurements

All electrochemical experiments were performed using a Gamry Ref. 600 galvanostat/potentiostat (Gamry Instruments, Philadelphia, PA, USA).

#### 5.5.1. EIS measurements

EIS experiments are used to understand the possible corrosion mechanisms at the metal/electrolyte interface. EIS experiments were carried out in an electrochemical cell provided with a thermostatic jacket and a three-electrode set-up. A graphite rod or platinum sheet were used as a counter electrode and Ag/AgCl (sat. KCl) as the reference electrode. The open-circuit potential (OCP) and the EIS measurements of a working electrode with a sample area of 0.5  $\text{cm}^2$  were performed in the electrolyte at 37 °C for 24 hours. For the EIS measurements at OCP, the frequency was varied between 100,000 Hz and 0.1 Hz with 10 points/decade and a perturbation amplitude of  $\pm 20$  mV. All electrochemical measurements were done at least three times to ensure reproducible behavior trends. The EIS spectra were analysed using the Echem Analyst™ software.

#### 5.5.2. Cyclic voltammetry measurements

In order to investigate the effect of protein adsorption on the electrochemical activity of surfaces CV experiments were performed. In section 6.1, CV experiments were done on the gold and iron films after protein adsorption in a three-electrode cell. The working electrode was the sample, the counter electrode was a gold wire, and the reference electrode was a standard Ag/AgCl electrode (sat. 3 M KCl). The cyclic voltammograms were recorded in

electrolyte between 0.25 and -0.8 V (relative to Ag/AgCl) with a scan rate of 50 mV s<sup>-1</sup>. Three cycles were recorded each time, using the first cycle for comparison.

## 5.6 Surface analysis

### 5.6.1. Ellipsometry

Ellipsometry is an optical technique that can be used to obtain the dielectric properties of thin films. The thickness of the adsorbed protein layers at the gold surfaces was determined by ellipsometry (auto nulling ellipsometer, Ep3, Accurion GmbH, Göttingen, Germany). Two-zone measurements were performed in the wavelength range from 363.7 nm to 550.1 nm at an incidence angle of 70°, and three points were measured for each sample. A blank gold substrate without adsorbed proteins was also measured. A model of the blank substrate and the adsorbed protein layer was constructed, and the data were fitted in the EP4 software using a Cauchy dispersion function:

$$n(\lambda) = A + \frac{B}{\lambda^2} \quad (71)$$

with the refractive index  $n$ , the Cauchy parameters  $A$  and  $B$ , and the wavelength  $\lambda$ .

### 5.6.2. AFM characterization

AFM is used to characterize the surface topography. In section 6.1, the surface topography of the dry samples was analyzed by AFM using an Agilent 5500 operated in intermittent contact mode in air with MikroMasch NSC18/AIBS cantilevers (NanoAndMore GmbH, Germany). Images were recorded at a scan size and resolution of 3 x 3 μm<sup>2</sup> and 512 x 512 px, respectively. The images were analyzed using Gwyddion 2.60 open source software [178]. In section 6.2, AFM imaging was performed in air using a MFP-3D-AFM setup (Asylum Research, Santa Barbara, CA, USA) in intermittent contact mode (AC mode) with NSC15/AIBS cantilevers (325 kHz, 40 N/m, MikroMasch, Wetzlar, Germany). Images were collected with scan sizes of 5 x 5 μm<sup>2</sup> and a resolution of 512 x 512 px<sup>2</sup>. At least three different regions were scanned for each sample.

### 5.6.3. SEM, EDX and FIB characterization

FE-SEM and focused ion beam (FIB) milling were performed using a NEON®40 electron microscope (Carl Zeiss SMT AG, Oberkochen, Germany) with a SE2 and an InLens detector at Paderborn University, CMP (Coatings, Materials & Polymers). FIB cuts were milled using a Ga beam from a liquid metal ion source (LMIS) at an energy of 30 keV. Elemental distributions were recorded using the additional built-in EDX (energy-dispersive X-ray)

device (Thermo Fisher Scientific Ultra Dry, Waltham, MA, USA) at a probe voltage of 10 kV.

#### 5.6.4. Infrared spectroscopy

##### 5.6.4.1 PM-IRRAS

PM-IRRAS was performed using a Bruker Vertex 70 spectrometer with a photoelastic ZnSe modulator (PMA50, Bruker Corporation, USA). The angle of incidence was 80° with respect to the surface normal. The reflected light was detected using a liquid nitrogen-cooled mercury cadmium telluride (MCT) detector (Bruker Corporation, USA). The recorded spectra were processed and analyzed using OPUS 5.5 (Bruker Corporation, USA).

##### 5.6.4.2 FT-IRRAS

FT-IRRAS was done with a Bruker Vertex 70 FTIR spectrometer with a deuterated triglycine sulfate (DTGS) detector. The incidence angle was 45°. Each spectrum was recorded with 256 scans and a resolution of 4  $\text{cm}^{-1}$  at room temperature. The respective polished alloy served as a reference.

##### 5.6.4.3 ATR-FTIR

ATR-FTIR was performed using a “Spectrum Two” spectrometer (PerkinElmer, Beaconsfield, UK) equipped with a LiTaO<sub>3</sub> detector, and a diamond ATR crystal. As a reference, the spectra of pure electrolyte were collected. All the spectra were collected at a resolution of 4  $\text{cm}^{-1}$  and 128 scans.

##### 5.6.4.4 *In situ* ATR-FTIR

In This thesis, the in-situ FTIR-cell for attenuated total reflection studies was mounted on an attachment for ATR measurements (IRUBIS, Germany) within the sample compartment of a Bruker Vertex 70v FTIR spectrometer, equipped with a narrow-band MCT detector. Spectra were recorded at room temperature at a resolution of 4  $\text{cm}^{-1}$  by co-adding 128 scans. The Si-crystal served as reference. The agar film was applied to the Si-ATR crystal in the same way as for the iron samples. Spectra of the Agar film were recorded before and after exposure to m-SBF.

#### 5.6.5. Raman spectroscopy

Raman spectra were recorded using an InVia Renishaw Raman microscope (Renishaw, Gloucesterhire, UK) with a CCD detector. A 50X objective was used for all measurements. A YAG-Laser (532 nm), an 1800 l/mm grating were used for all metal samples. A NIR-

Laser (785 nm), an 1200 l/mm grating was used to measure agar film. The Raman spectrometer was calibrated using the peak position of  $520.0\text{ cm}^{-1}$  ( $\pm 0.5\text{ cm}^{-1}$ ) of a reference silicon wafer. The recording time was set to 10 s with 10 accumulations. Each sample was measured three different points. The program "Wire 5.0" (Renishaw, Gloucestershire, UK) was used for data recording and processing.

#### 5.6.6. XPS characterization

The surface chemical composition of samples was analyzed by XPS using an ESCA+ ultra-high vacuum system (Scienta Omicron, Germany) with monochromatic Al K $\alpha$  radiation (1486.7 eV) at a working pressure of below  $5 \times 10^{-10}$  mbar. A take-off angle of  $30^\circ$  was used for XPS characterization of thin iron film in section 6.1, and the experiments were performed by Jiangling Su, Paderborn University, Technical and Macromolecular Chemistry (TMC). Spectra of metal samples as well as the agar hydrogel film in section 6.3 and 6.4 were obtained by Markus Voigt, Paderborn University TMC, at a take-off angle of  $60^\circ$  with respect to the surface. Survey spectra with a spectral resolution of 0.5 eV and high-resolution spectra with a spectral resolution of 0.1 eV were recorded using a pass energy of 100 eV and 20 eV, respectively. The electron binding energies were referenced to the C 1s peak at 285.0 eV. The peaks were fitted using a peak shape consisting of a convolution of a Gaussian (30%) and Lorentzian (70%) shape. Peak fitting and data analysis of the spectra were carried out by CasaXPS (Casa Software Ltd., Wilmslow, UK).

## 6 Results and discussion

### 6.1 Multiprotein adsorption on oxidized metal surfaces

Protein adsorption occurs on the surfaces of most materials, and it is a crucial consideration for biomedical materials, such as implantable devices. Therefore, before evaluating the corrosion performance of candidate iron-based biomaterials, the focus was first on exploring protein adsorption on the material surfaces. This work involved evaluating the influence of factors such as pH value, types, and concentrations of proteins, as well as the impact of material surface properties on protein adsorption (see Figure 6.1). The following section has been published in reference [33] by the author of this thesis.

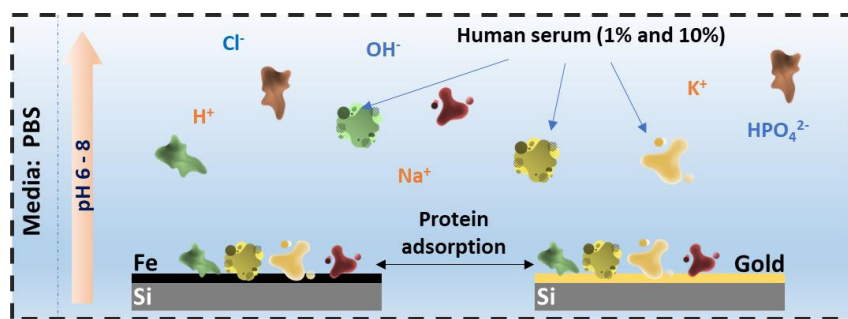


**Figure 6.1** The sketch overviews the main content of section 6.1, adsorption of serum proteins on gold and oxidized iron surfaces under different conditions.

Multiprotein adsorption from complex body fluids represents a highly important and complicated phenomenon in medicine. Numerous studies have investigated protein adsorption at the surfaces of relevant materials *in vitro* with the aim of understanding and ultimately controlling the involved mechanisms and interactions [179–189]. The vast majority of such *in-vitro* studies focused on the adsorption of one or few selected proteins from single-component solutions. Body fluids, however, are composed of a multitude of protein species, with the total body-fluid proteome comprising more than 15,000 different proteins [190]. Among the different body fluids, blood plasma is not only the most relevant with regard to implants but also the most complex. Therefore, in this study, human serum was chosen as a suitable example of body fluid containing multiple protein components. Protein adsorption from such complex multi-component solutions is highly competitive and leads to the formation of a dynamic adsorbate film with changing composition that is determined by the individual concentrations and surface affinities of all the proteins in the solution [191]. Investigating multiprotein adsorption under such conditions is experimentally challenging. In the work studied in this section, the potential of AFM and

PM-IRRAS was evaluated to provide insights into multiprotein adsorption from diluted human serum. AFM is used to obtain information about changes in surface topography due to the adsorbed protein film, while PM-IRRAS enables the assessment of the total adsorbed protein amount and additionally allows to qualitatively detect changes in film composition. In this way, multiprotein adsorption at the surfaces of gold and iron thin films is studied *ex-situ* at different serum concentrations (1% and 10%) and pH values ranging from pH 6 to pH 8. This rather modest variation around neutral pH was chosen in order to minimize the contribution of protein denaturation in bulk solution. Gold was selected as a chemically inert model surface, whereas iron is chemically reactive and prone to corrosion and dissolution in physiological electrolytes; a phenomenon strongly influenced by the presence of proteins [31]. In addition, evaluating protein adsorption on iron thin films is of guiding significance for the subsequent investigation of the influence of proteins on the corrosion of candidate iron-based metal materials.

### 6.1.1. Materials and chemicals

The thin metal films were deposited on commercial Si(100) wafers with native surface oxide. After RCA1 cleaning and subsequent rinsing in water and ethanol, a 10 nm Cr buffer layer followed by 150 nm Au were deposited by thermal evaporation. The Fe 30 nm films were deposited on top of the Au films with an intermediate 3 nm Cr buffer layer by magnetron sputter deposition.

Heat-inactivated human serum from male AB clotted whole blood was diluted in aerated PBS, to obtain the desired concentration (1% or 10%). The pH of the PBS was adjusted between pH 6 and pH 8 using HCl (35%) and NaOH (>99%).

### 6.1.2. Experimental approach

#### 6.1.2.1 Serum exposure

Serum dilutions of different concentrations for adsorption experiments were prepared fresh each day to ensure comparability of the results. The different serum samples (100  $\mu$ l) were deposited on the different sample surfaces (1 x 1 cm<sup>2</sup>) and incubated for 2 hrs at room temperature. After incubation, the sample surfaces were rinsed with ca. 3 ml HPLC-grade water (Carl Roth, Germany) and dried in a stream of ultra-pure air.

#### 6.1.2.2 Cyclic voltammetry

CV experiments were performed on the gold and iron films after protein adsorption in a three-electrode cell using a Reference 600 potentiostat (Gamry Instruments). The working

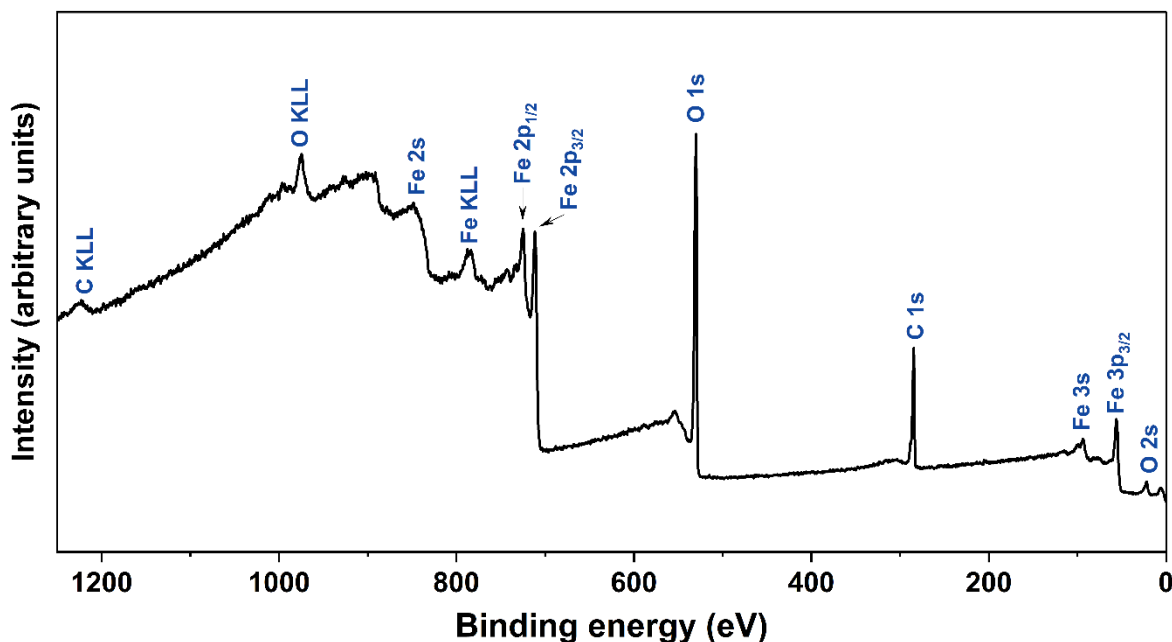
electrode was the sample, the counter electrode was a gold wire, and the reference electrode was a standard Ag/AgCl electrode (sat. 3 M KCl). The cyclic voltammograms were recorded in PBS between 0.25 and -0.8 V (relative to Ag/AgCl) with a scan rate of 50 mV s<sup>-1</sup>. Three cycles were recorded each time, using the first cycle for comparison.

#### 6.1.2.3 Surface analysis

The deposited Fe films were characterized by XPS. The thickness of the adsorbed protein layers at the gold surfaces was determined by ellipsometry. To quantify adsorption-induced changes in surface topography and the total amount of adsorbed proteins, AFM and PM-IRRAS are employed, respectively. The experimental methods are described in detail in Chapter 5. The spectra recorded by PM-IRRAS were analyzed using OPUS 5.5. For determining the amide I and amide II band areas, the integral between the respective bands and a straight line drawn between the intensity values of two specified frequencies (amide I: 1700 – 1600 cm<sup>-1</sup>; amide II: 1600 – 1480 cm<sup>-1</sup>) was calculated. This was done using the original spectra without background correction.

#### 6.1.3. XPS characterization of deposited Fe films

The survey spectrum of the iron film as shown in the Figure 6.2 confirms the presence of C, O, Fe on the surface. The atomic percentage composition of iron film is summarized in the Table 6.1.

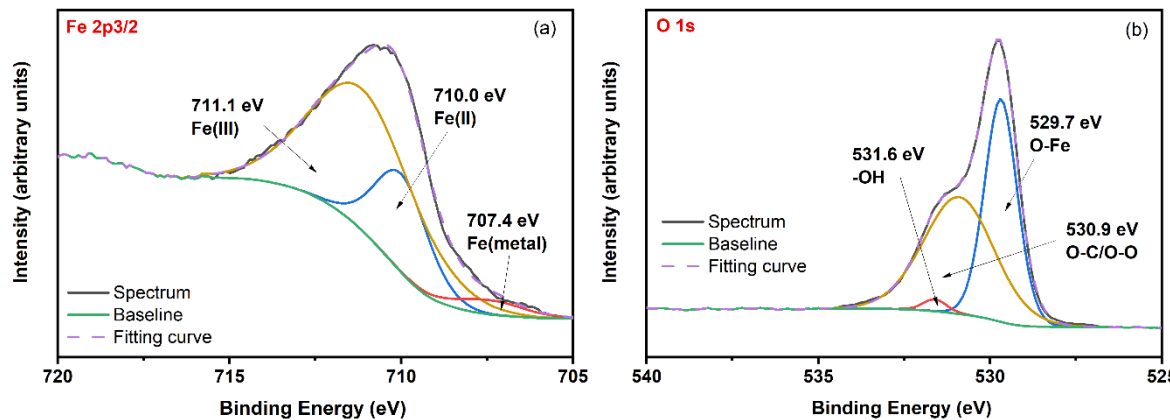


**Figure 6.2** XPS survey spectrum of the deposited iron film.

**Table 6.1** Results of the XPS elemental analysis of the deposited iron film.

Element	C 1s	O 1s	Fe 2p <sub>3/2</sub>
Concentration (at%)	43.5	47.3	9.2

Figure 6.3 shows the high-resolution XPS spectra in the regions of Fe 2p<sub>3/2</sub> (a) and O 1s (b), respectively, used for analyzing the potential compositional components at the surface of the iron thin film.

**Figure 6.3** High-resolution XPS spectra of a) Fe 2p<sub>3/2</sub> and b) O 1s.

The high-resolution Fe 2p<sub>3/2</sub> spectrum shown in Figure 6.3a could be fitted with three components, i.e., the peaks of Fe 2p<sub>3/2</sub> at 710.0 eV, 711.1 eV, and 707.4 eV which are attributed to Fe(II), Fe(III), and Fe(metal), respectively [192,193]. The high-resolution O 1s spectrum in the Figure 6.3b shows two components. The peak at 529.7 eV is attributed to iron oxides [194], the one at 530.9 eV is attributed to the bulk oxygen and surface adsorbed oxygen [195], and the one at 531.6 eV is attributed to the FeOOH [193]. In summary, the XPS characterization suggests the formation of a mixed oxide layer consisting of Fe<sub>2</sub>O<sub>3</sub>, Fe<sub>3</sub>O<sub>4</sub> and FeOOH on the deposited iron films.

#### 6.1.4. AFM characterization

Before serum exposure, the surface topographies of the films were characterized by AFM. As can be seen in Figure 6.4a, the gold surface has a grainy appearance, resulting from the polycrystalline texture of the film. From the AFM images, a root-mean-square (RMS) surface roughness of the gold films of  $S_q = 4.39 \pm 0.20$  nm is obtained. After serum exposure under the different conditions, the topographies of the gold films differ only slightly from the as-prepared sample. As can be seen in the AFM images in Figure 6.4b-g, the overall grainy morphology is largely preserved with no apparent changes. This indicates the

formation of a rather homogeneous protein film at the gold surface. However, for all conditions, the overall height contrast appears to be lower than for the as-prepared substrate in Figure 6.4a. Such a smoothing of the apparent surface topography may occur during the adsorption of relatively small and soft proteins such as serum albumin at comparably rough surfaces as a result of preferential adsorption of the proteins in topographic depressions, which allows them to can maximize their contact area with the surface [179].

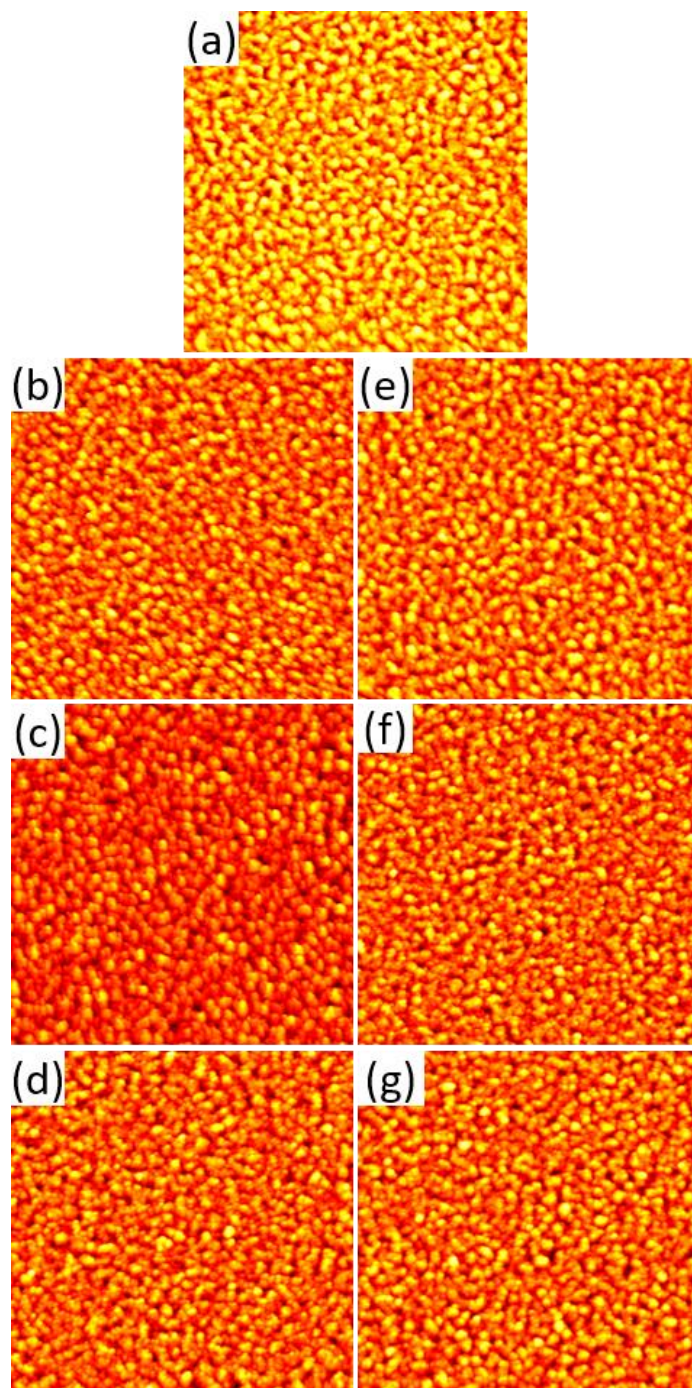


**Figure 6.4.** AFM images of the gold films before (a) and after exposure to 1% (b-d) and 10% (e-g) human serum at pH 6 (b, e), 7 (c, f), and 8 (d, g), respectively. The images have a size and height scale of  $3 \times 3 \mu\text{m}^2$  and 35 nm, respectively.

The adsorption-induced changes in the topography of the gold surfaces are quantified in Figure 6.5a, which shows the surface roughness values after serum exposure. In line with the qualitative observations discussed above, the RMS roughness values of the serum-exposed gold surfaces are significantly lower than that of the as-prepared substrate. The only exceptions are observed for 10% serum at pH 6 and pH 7, which do not yield significant differences. As another interesting observation, the  $S_q$  values obtained under the different exposure conditions are very similar and do not seem to depend on pH or serum concentration.

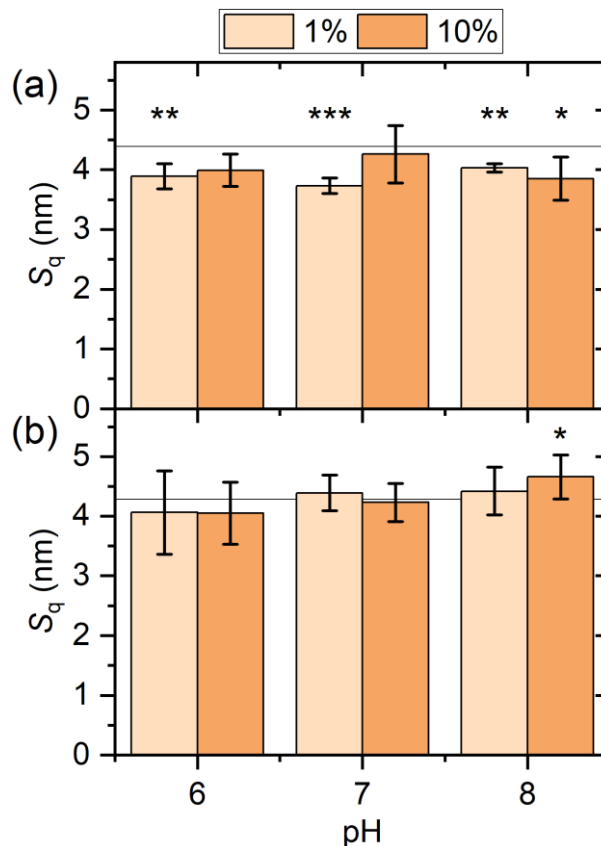


**Figure 6.5** RMS surface roughness values  $S_q$  of the gold (a) and iron (b) films after exposure to human serum at different concentrations and pH values. The horizontal lines indicate the average  $S_q$  values of the as-prepared substrates prior to serum exposure. Values represent averages of four to eight AFM images recorded at different positions on the surfaces of two to four identically treated samples. Error bars indicate standard deviations. Significances (two-tailed distribution, homoscedastic) are given with respect to the as-prepared substrates and indicated as \* ( $p < 0.05$ ), \*\* ( $p < 0.01$ ), and \*\*\* ( $p < 0.001$ ).

For the reactive iron surface, the situation is similar with the overall grainy surface morphology being largely preserved (see Figure 6.6). However, in contrast to the gold films in the RMS surface roughness ( $S_q = 4.28 \pm 0.15$  nm for the as-prepared film) does not change significantly upon serum exposure under most conditions (see Figure 6.6b). As the only exception, a significant increase in RMS surface roughness is observed for 10% serum at

pH 8. This behavior most likely reflects the complex interplay between protein adsorption and surface dissolution. However, it should be noted that serum exposure did not lead to any notable corrosion of the iron films, which maintained their mirror finish during all experiments.

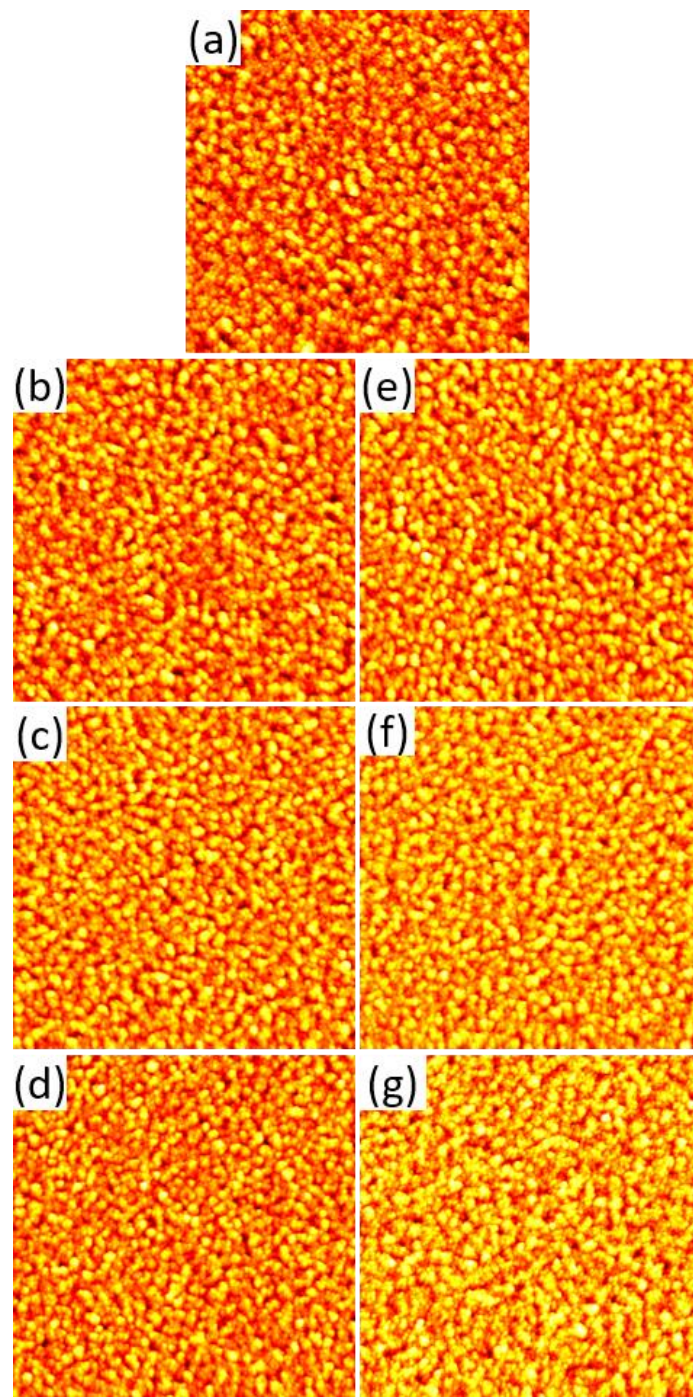


**Figure 6.6** AFM images of the iron films before (a) after exposure to 1% (b-d) and 10% (e-g) human serum at pH 6 (b, e), 7 (c, f), and 8 (d, g), respectively. The images have a size and height scale of  $3 \times 3 \mu\text{m}^2$  and 35 nm, respectively.

### 6.1.5. Cyclic voltammograms

In order to verify whether serum protein adsorption passivates the surface of the metal films, the samples after serum exposure were characterized also by CV. The corresponding cyclic voltammograms are shown in Figure 6.7

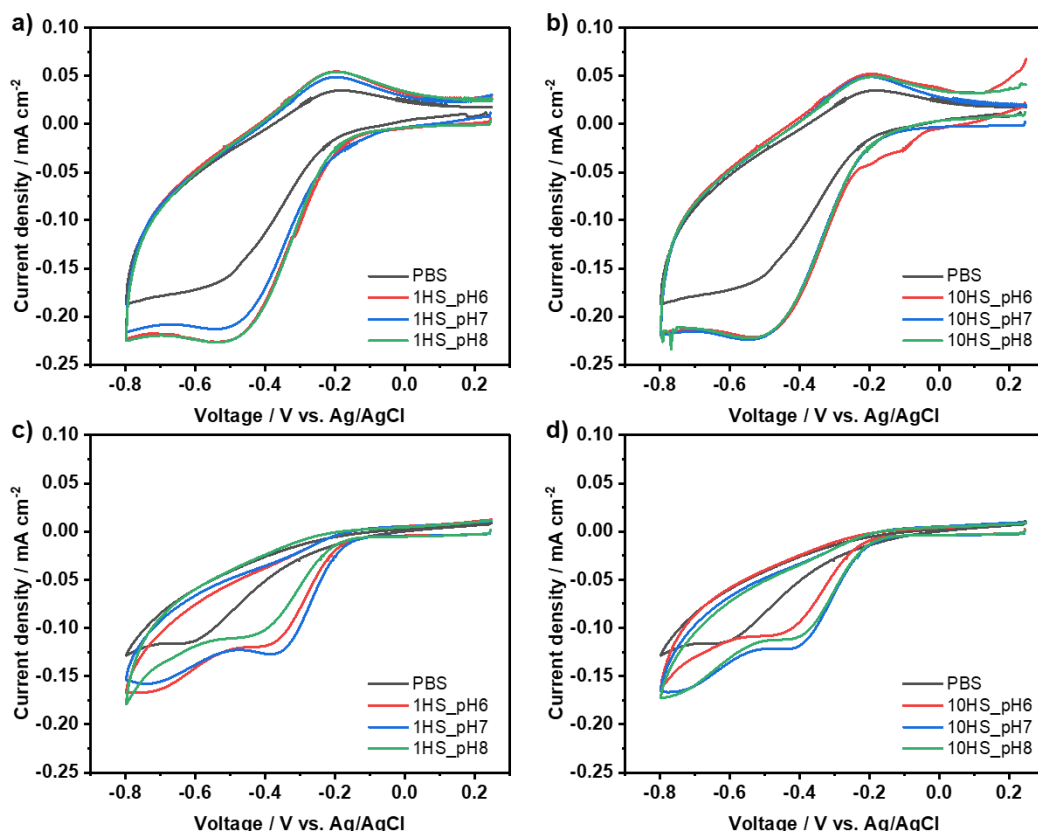


**Figure 6.7** Cyclic voltammograms of the iron (**a, b**) and gold (**c, d**) films in PBS after exposure to 1% (**a, c**) and 10% (**b, d**) human serum. The curves shown in the plots always represent the first cycle.

As can be seen in Figure 6.7, there is rather an increase than a decrease of the peak areas after protein adsorption. Furthermore, while the Fe oxidation/reduction cycle is visible for the Fe substrates, but no superimposition of the reduction peaks is observed on both Au and Fe substrates. Therefore, CV indicates no inhibition of the electrochemical surface activity due to serum protein adsorption.

### 6.1.6. Analysis of protein adsorption film thickness

The thickness of the protein film adsorbed on the gold surface was measured by ellipsometry. A blank gold substrate without adsorbed proteins was measured. A model of the blank substrate and the adsorbed protein layer was constructed, and the data were fitted in the EP4

software using a Cauchy dispersion function. The determined thickness values are shown in Figure 6.8.

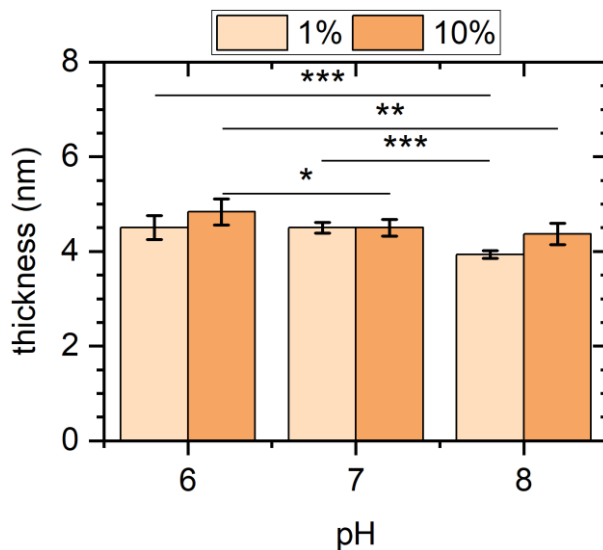


**Figure 6.8** Thickness of the protein films adsorbed at the gold surfaces after exposure to human serum at different concentrations and pH values. Values represent averages of six measurements recorded on the surfaces of two identically treated samples. Error bars indicate standard deviations. Significances (two-tailed distribution, homoscedastic) are indicated as \* ( $p < 0.05$ ), \*\* ( $p < 0.01$ ), and \*\*\* ( $p < 0.001$ ).

It can be seen in Figure 6.8 that the adsorbed layer is slightly thicker at pH 6 than in the case of pH 7 and pH 8 at both concentrations (1% HS and 10% HS). At pH 6 and pH 8, high serum concentration results in a slightly thicker surface layer compared to low concentration, but under neutral conditions, there is almost no difference.

#### 6.1.7. PM-IRRAS results

To obtain more quantitative information regarding the total amount of adsorbed proteins and possibly the composition of the protein films, PM-IRRAS was utilized. In this regard, emphasis was placed on the amide I to amide III region, which encompasses IR absorption bands that are specific to the polypeptide backbone. As can be seen in Figure 6.9, the amide I and amide II bands at about  $1650\text{ cm}^{-1}$  and  $1550\text{ cm}^{-1}$ , respectively, can be clearly identified in all recorded spectra. The amide III bands, however, are rather weak and barely distinguishable from the background noise.

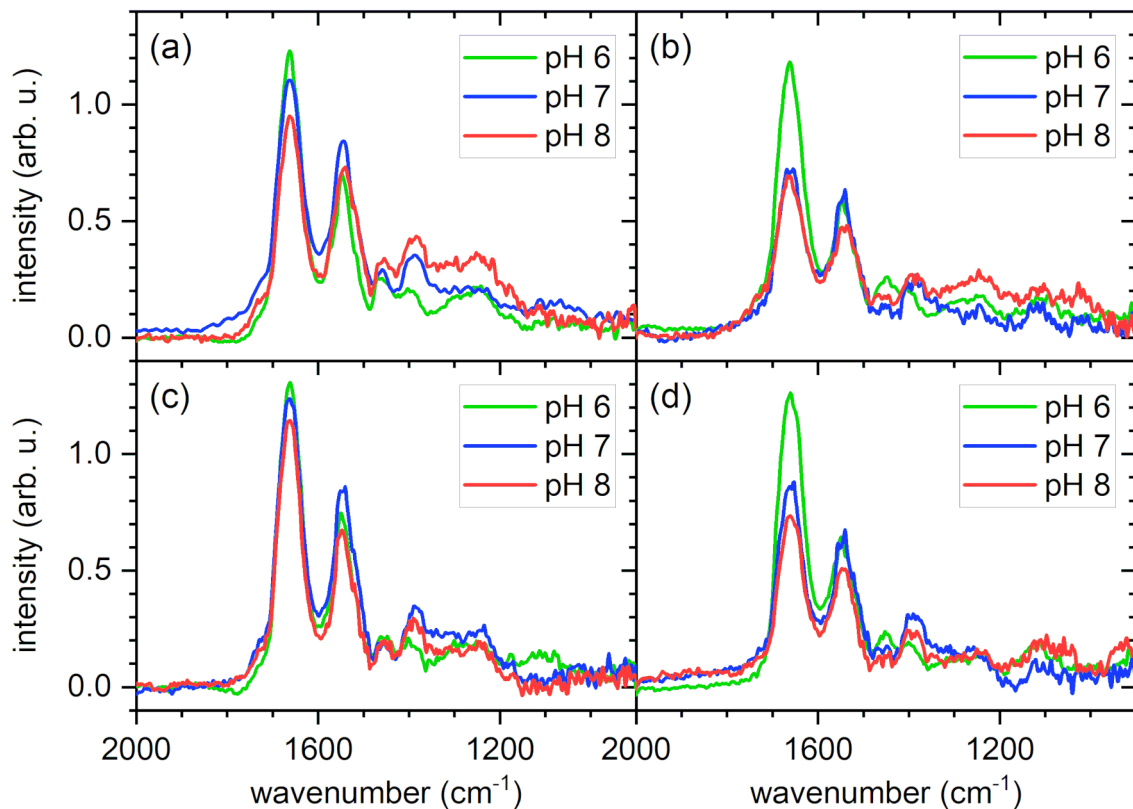


**Figure 6.9** PM-IRRA spectra of the gold (**a, c**) and iron (**b, d**) films after exposure to 1% (**a, b**) and 10% (**c, d**) human serum at different pH values, showing the amide I to amide III region.

The PM-IRRA spectra shown in Figure 6.9 reveal some interesting dependencies. In particular, the intensities of the amide I bands exhibit rather similar pH dependencies for both surfaces and serum concentrations. In general, it seems that the amide I intensity is increasing with decreasing pH. Since the amide I band is composed mostly of C=O stretching vibrations with a smaller contribution from C-N stretching vibrations, both of which originate in the polypeptide backbone, its integrated intensity is a measure of the total amount of adsorbed proteins [185]. The observed increase in amide I intensity with decreasing pH thus indicates enhanced serum protein adsorption at pH 6 compared to pH 7 and pH 8 for both surfaces. To quantify this effect, the amide I band areas have been integrated for all conditions (see Figure 6.10). Indeed, for all investigated conditions, pH 6 shows the largest amide I integral, even though the observed trends are not in all cases statistically significant, such as for the gold surface in contact with 10% serum (Figure 6.10a). Notably, the thickness of the adsorbed protein films on the gold surface has also been quantified through ellipsometry, exhibiting a comparable pH dependence (see Figure 6.8).

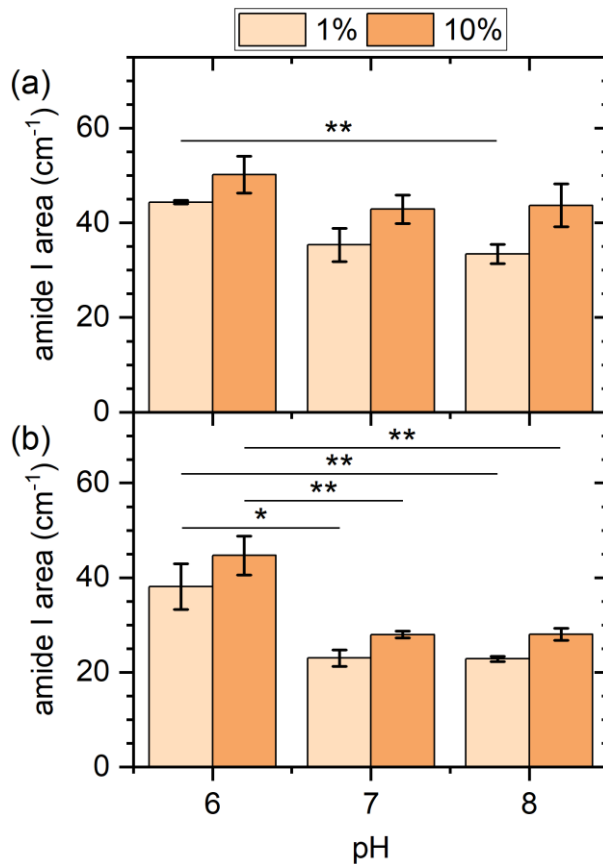


**Figure 6.10** Integrated amide I band area values for the gold (a) and iron (b) films after exposure to human serum at different concentrations and pH values. Values represent averages of two to four spectra recorded on the surfaces of two to four identically treated samples. Error bars indicate standard deviations. Significances (two-tailed distribution, homoscedastic) are indicated as \* ( $p < 0.05$ ), \*\* ( $p < 0.01$ ), and \*\*\* ( $p < 0.001$ ).

The apparent pH dependence of the total amount of adsorbed proteins may be explained by considering that at a serum concentration of about 40 mg/ml [196], HSA is the major protein component in human serum [197]. Since HSA has an isoelectric point around 4.7 [198], shifting the pH closer to that value, albeit rather modestly, results in a lower absolute net charge (see Table 3.3). Considering that protein adsorption in general reaches its maximum when the protein is uncharged [196], it appears reasonable that the adsorption of this already abundant protein is further enhanced at pH 6. For comparison, IgG, which is another abundant plasma protein with a serum concentration around 15 mg/ml [196] has an isoelectric point closer to 7 [199] and should thus show the inverse trend. This interpretation is further supported by the fact that both surfaces show a similar behavior, which suggests that the effect originates in protein properties instead of surface properties. Furthermore, Figure 6.10 also shows a weak to modest concentration dependence of protein adsorption at both surfaces, with exposure to 10% serum resulting in a  $\sim 10$  to  $\sim 30\%$  increases in the amide I area.

Table 6.2 Calculated net charge of HSA at the different pH values used in the present study [200].

pH	net charge
6	-0.6
7	-12.2
8	-24.2

When it comes to surface-specific differences, the data in Figure 6.10 indicate a larger total amount of adsorbed proteins at the gold surface for all conditions. Increased protein adsorption at gold compared to other surfaces is a phenomenon frequently observed for many proteins and peptides [201–203], including serum albumin [204]. Increased protein adsorption at the gold surface would also provide an explanation for the smoothing of the surface topography revealed by AFM in Figure 6.4, which was observed only for the gold but not for the iron film. It should be noted, however, that the enhanced intensities of the amide I bands observed for the gold surface may also be due to a larger IR reflection coefficient compared to the iron film.

As discussed above, the pH dependence of the total amount of adsorbed proteins observed in Figure 6.10 hints at an increased adsorption of HSA at the lower pH value. Since multiprotein adsorption from a complex mixture is considered here, increased adsorption of one or few protein species will most likely result in a different composition of the adsorbed protein films. Therefore, the assessment of such compositional changes was pursued through a closer examination of the amide I bands. The chemical groups in the polypeptide backbone that contribute to the amide I band participate in the H bonds that stabilize the secondary structure elements of the protein, so that different secondary structure elements can be assigned to different wavenumbers within the amide I region [185]. For a large protein with complex secondary structure, this results in a broad amide I band with a complex shape that can be considered the protein's structural fingerprint. In order to assess whether a change in the composition of the adsorbed protein film results in a change in the amide I shape, normalization of the spectra displayed in Figure 6.9 has been performed relative to the peak intensity of the amide I band. As can be seen in Figure 6.11, the normalized spectra unfortunately do not reveal any clearly identifiable differences in the shapes of the amide I bands obtained at different pH values. This is most likely because the recorded amide I bands are superpositions of many differently shaped amide I bands specific for the large number of protein species present in the adsorbed films. Furthermore, many proteins and in particular serum albumin undergo denaturation during adsorption at solid surfaces, which often is

accompanied by drastic changes in the relative occurrence of some secondary structure elements [185].

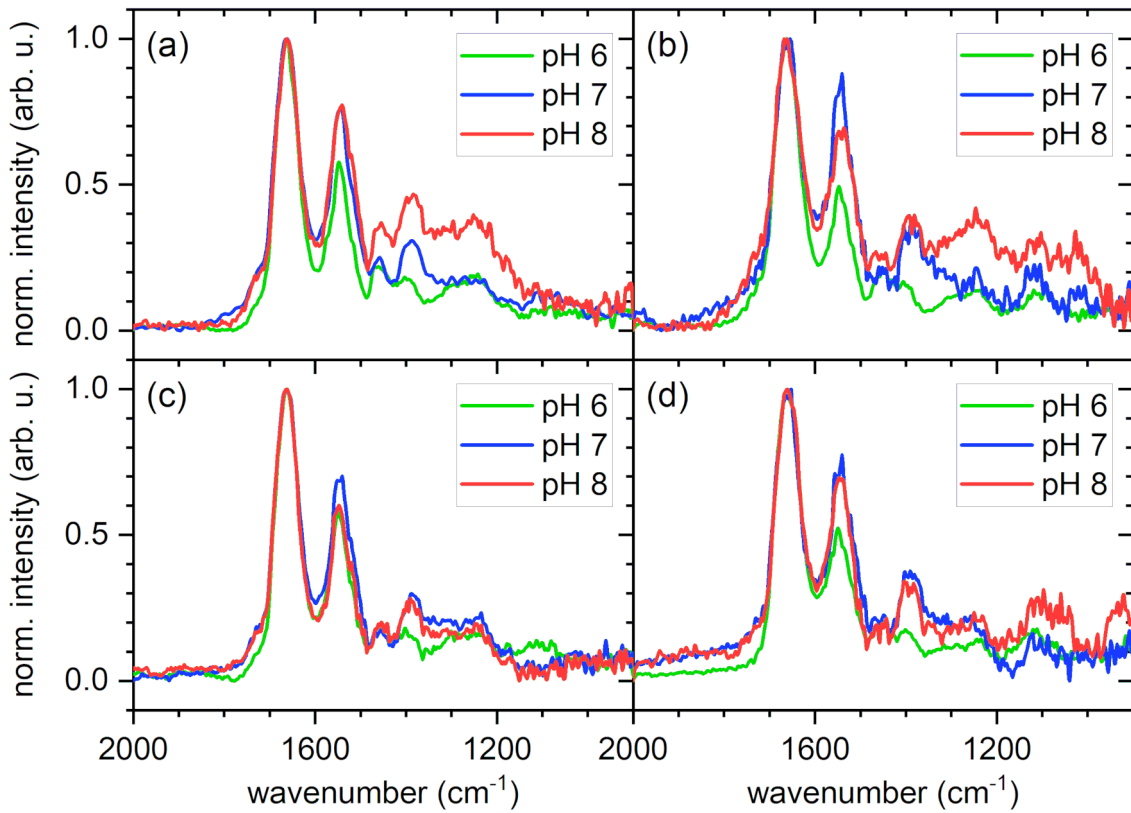


**Figure 6.11** Same spectra of the gold (**a, c**) and iron (**b, d**) films after exposure to 1% (**a, b**) and 10% (**c, d**) human serum at different pH values as shown in Figure 4, but normalized to the maximum intensity of the amide I peak.

Even though no changes in the shapes of the amide I bands can be identified in the normalized spectra shown in Figure 6.11, there are nevertheless some variations in other features that may hint at different film compositions. The first feature is the amide II band. The amide II band is more complex than the amide I band and derives mostly from the in-plane bending vibration of N-H groups with smaller contributions from C-N and C-C stretching vibrations. Therefore, it shows a similar sensitivity to secondary structure as the amide I band. As can be seen in Figure 6.11 for both surfaces and serum concentrations, changes in pH lead to rather drastic changes in the intensity of the normalized amide II bands, while the normalized amide I bands are barely affected. To quantify this effect, the amide II/I area ratio has been calculated for all spectra and is displayed in Figure 6.12. For both surfaces and serum concentrations, we find a minimum amide II/I area ratio at pH 6, even though the large error bars sometimes result in the differences being non-significant. Two effects may contribute to this decrease in the amide II/I area ratio. The most obvious is a change in the protein composition of the adsorbed film, which would be in line with above

interpretation. However, also changes in a protein's secondary structure can account for such a change in the amide II/I area ratio [205], since different secondary structure elements may have different absorption coefficients. Such changes in secondary structure may result from both, different pH values in bulk solution and differences in adsorption-induced protein denaturation. Therefore, it is not clear whether this change in the amide II/I area ratio is indicative of a change in protein film composition, structure, or both.

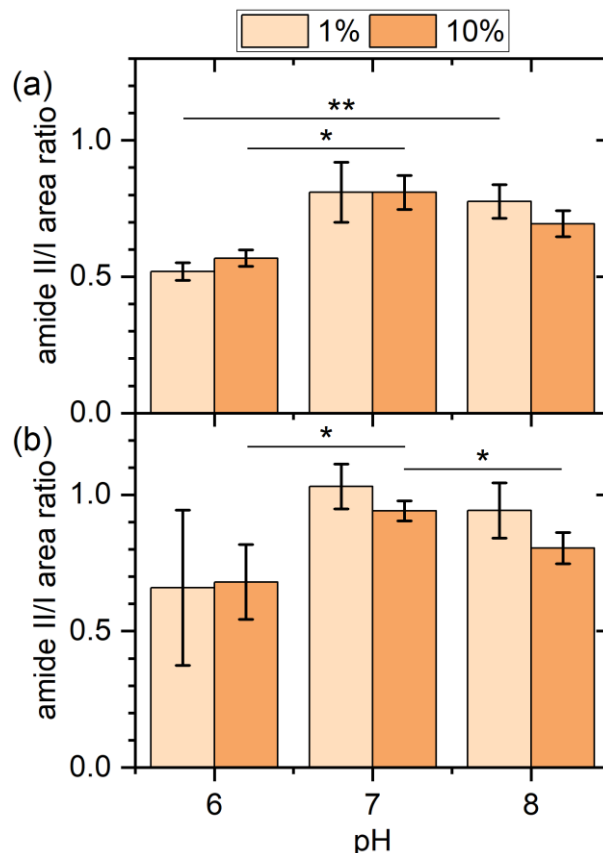


**Figure 6.12** Ratios of the amide II and amide I peak areas for the gold (a) and iron (b) films after exposure to human serum at different concentrations and pH values. Values represent averages of two to four spectra recorded at different positions on the surfaces of two to four identically treated samples. Error bars indicate standard deviations. Significances (two-tailed distribution, homoscedastic) are indicated as \* ( $p < 0.05$ ), \*\* ( $p < 0.01$ ), and \*\*\* ( $p < 0.001$ ).

The second interesting feature is the weak high-wavenumber shoulder of the amide I band between  $1750$  and  $1700\text{ cm}^{-2}$ . IR absorption bands beyond  $1700\text{ cm}^{-2}$  are usually attributed to the protonated carboxyl groups located in the side chains of Asp and Glu [185,206]. In all spectra shown in Figure 6.11, it is observed that the high-wavenumber shoulder of the amide I band is weaker or entirely absent at pH 6 when compared to the higher pH values. This is particularly obvious for the gold surfaces, where the high-pH spectra exhibit a rather well resolved shoulder. For the oxidized iron surface, the effect is less pronounced, which may be attributed to the lower amount of adsorbed proteins that contribute to the overall intensity.

The disappearance of the high-wavenumber shoulder at low pH values is rather surprising, since one would expect a lower pH to result in an increase in the number of protonated carboxyl groups and not in a decrease. Even more surprising is the fact that the same trend can also be observed for the weak absorption band around  $1400\text{ cm}^{-1}$ , which corresponds to the deprotonated carboxylate group [206]. Here, a decrease in intensity is also observed with decreasing pH, suggesting a decrease in the number of deprotonated carboxylate groups. Together, both observations are indicative of a loss of Asp and/or Glu, which can only be the result of a change in the composition of the adsorbed protein films. Since HSA and IgG have a rather similar Asp/Glu content of 10 – 20 w% [207,208], the observed decrease in Asp/Glu absorption at pH 6 furthermore suggests the involvement of other, less abundant protein species, which show stronger adsorption at higher pH values.

### 6.1.8. Conclusions

In summary, the investigation focused on the pH dependence of multiprotein adsorption at gold and oxidized iron surfaces exposed to human serum, using AFM and PM-IRRAS. AFM facilitated the quantification of adsorption-induced changes in surface topography, while PM-IRRAS was employed to quantify the total amount of adsorbed proteins and qualitatively evaluate compositional changes in the adsorbed protein films. AFM revealed that on average, serum protein adsorption at the gold surface resulted in a smoother surface morphology, without any pronounced dependencies on pH or serum concentration. For the iron surface, however, no statistically significant changes in morphology due to protein adsorption were observed. PM-IRRAS showed a pH dependence of the total amount of adsorbed proteins for both surfaces, which was even more pronounced than the dependence on serum concentration. Finally, close inspection of the amide I and amide II region of the PM-IRRAS spectra, in particular with regard to the absorption of the amino acid side chains, revealed clear differences in the composition of the adsorbed multiprotein films at pH 6 compared to pH 7 and pH 8. Since the observed pH-dependent effects are rather similar for both the gold and the oxidized iron surface, it is suggested that they are not primarily governed by surface properties but rather by the pH sensitivity of the adsorbing proteins. Due to its isoelectric point of approximately 4.7 and its high abundance in serum, the assumption is made that protein adsorption at pH 6 is primarily influenced by HSA, which replaces other proteins with lower surface affinities in the multiprotein film. The presented results show the potential of PM-IRRAS in quantifying protein adsorption on metallic surfaces from complex mixtures like serum. It also enables assessing compositional changes in adsorbed multiprotein films, albeit indirectly and qualitatively.

## 6.2 Influence of proteins on the corrosion of a conventional and selective laser beam melted FeMn alloy

This section mainly concerns the effect of different proteins on the corrosion of FeMn alloys produced by conventional and additive manufacturing and compares the results to those of pure Fe (Figure 6.13). The following section has been published in reference [31] by the author of this thesis.

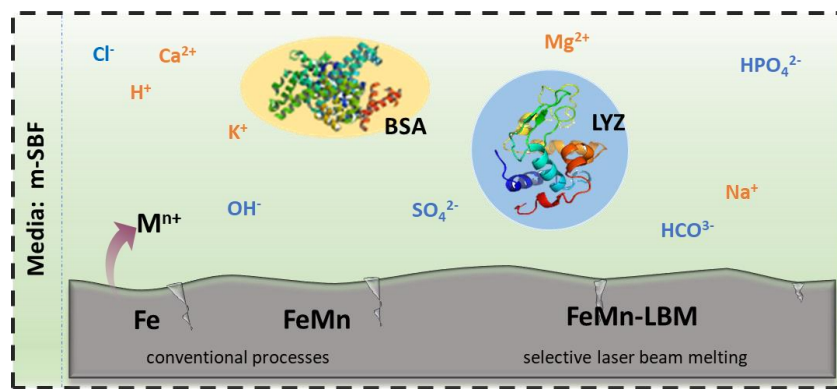


**Figure 6.13** The sketch overviews the main content of section 6.2, the effect of different types of proteins on the corrosion behavior of Fe and of FeMn alloys produced by two different processes in m-SBF.

The process route influences both the microstructure and the resulting corrosion properties of iron alloys. Selective laser beam melting (LBM) has been employed in this work, as the most important additive manufacturing process of iron alloys [176]. As mentioned in section 3, the effect of proteins on the corrosion and degradation behavior of Fe-based alloys is not negligible. Due to their zwitterionic characteristics, different proteins have different charges and may interact in different ways with the surfaces of the materials [135,139]. Therefore, in this study, BSA and LYZ were selected as model proteins. Albumin is the most abundant protein in plasma and thus represents one of the major components of proteinaceous deposits on biomaterial surfaces in contact with blood [126]. BSA is a 69 kDa globular protein with an isoelectric point (IEP) of 4.7-5.2 [209] and is widely used as a model protein for investigating protein adsorption [210–213]. The antimicrobial enzyme LYZ is a small globular protein that is part of the innate immune system and can be found in numerous tissues and bodily fluids [214]. With an IEP of 11 and a molecular weight of 14.1 kDa [215].

The corrosion properties of Fe and FeMn alloys were investigated by electrochemical analysis. Surface characterization was carried out by AFM, FE-SEM, Raman spectroscopy, and FTIR to correlate the surface material and the adsorbate layer composition with the corrosion behavior.

### 6.2.1. Materials and chemicals

In this section, conventional FeMn steel X-IP<sup>TM</sup> 1000 (FeMn), FeMn alloy fabricated by LBM (FeMn-LBM), and pure iron (Fe) were investigated. Both FeMn alloys are austenitic high-manganese steels containing nominally 22 wt.-% Mn and 0.6 wt. The chemical compositions of the pure Fe, FeMn steel and the LBM processed material measured by OES are presented in Table 6.3. The Fe, FeMn, and FeMn-LBM samples were cut in 20 mm (length) × 20 mm (width) × 2 mm (thickness) plates. All samples were performed mechanical polishing prior to the experiment.

**Table 6.3** Chemical composition (wt.-%) of the investigated Fe, FeMn and FeMn-LBM measured via OES. Compositions of the Fe and FeMn materials are taken from Ref. [216] and [217], respectively.

	Mn	C	V	Si	Cr	Fe
<b>Fe</b>	0.03	0.002	-	0.003	0.01	99.9
<b>FeMn</b>	22.36	0.52	0.25	0.25	0.20	bal.
<b>FeMn-LBM</b>	20.31	0.58	0.03	0.02	0.06	bal.

m-SBF was used as a physiological electrolyte in the studies of this section and prepared according to the description in section 5.1.

For protein solution preparation, BSA and LYZ were dissolved in m-SBF with a concentration of 10 g/L BSA and 50 mg/L LYZ, respectively (see Table 6.4).

**Table 6.4** Characteristics of the studied proteins.

Protein	Mw/kDa	IEP[139]	Concentration (in m-SBF)
BSA	69	4.7-5.2	10 g/L
LYZ	14.1	11	50 mg/L

The normal albumin concentration in human plasma is 40 – 60 g/L [126], whereas the concentration of human lysozyme in serum is 7-13 mg/L [218]. Hedberg et al. [135] investigated the effect of BSA concentration (ranging from 0.01 to 100 g/L BSA in PBS) on protein-induced metal release in their study of surface protein interactions. The results showed that the release of metal ions correlates proper with protein concentration. The concentration of 10 g/L was chosen because it is a suitable concentration for BSA monolayer adsorption (> 0.5g/L) [143]. On the other hand, there is already a significant effect on metal release and interactions at this concentration. In addition, there are several previous studies that have used 10 g/L BSA as experimental conditions [139,219,220]. Therefore, similar

concentrations were selected in the work of this section to enable comparison of the results with those of previous studies. LYZ was selected because it has the opposite charged property to BSA, i.e. BSA has a net positive charge at pH 7 while LYZ has a net negative charge. A lower LYZ concentration of only 50 mg/L was chosen to roughly reflect the lower serum concentration. The protein-containing solutions are freshly prepared to ensure their activity.

### 6.2.2. Experimental approach

#### 6.2.2.1 Corrosion testing

The corrosion behavior was studied by electrochemical measurements. EIS and OCP were carried out in an electrochemical cell provided with a thermostatic jacket and a three-electrode set-up. A graphite rod was used as a counter electrode and Ag/AgCl (sat. KCl) as the reference electrode. The OCP and the EIS measurements of a working electrode were performed in m-SBF with and without the respective proteins at 37 °C for 24 hours. The electrical equivalent circuit (EEC) in Figure 6.14 was used to analyze the EIS data [221,222].

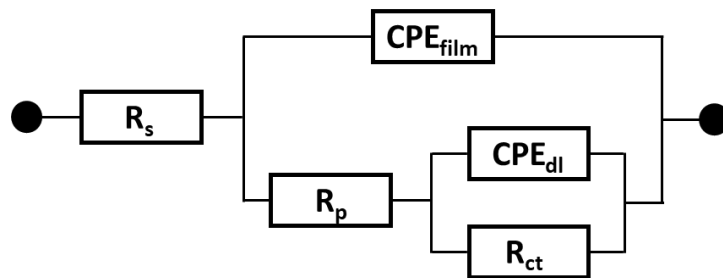


**Figure 6.14** Equivalent circuit used to model the EIS data.

The model EEC contained the electrolyte resistance ( $R_s$ ), charge transfer resistance ( $R_{ct}$ ), and the resistance of the surface film ( $R_p$ ). The non-ideal capacitive behavior is described by the CPE in the model EEC.  $CPE_{dl}$  and  $CPE_{film}$  are the capacitive elements of the electrolyte/metal interface and the formed corrosion product layer on the metal surface, respectively.

#### 6.2.2.2 Surface analysis

The microstructure of FeMn alloys fabricated by LBM was characterized by FE-SEM with electron backscattered diffraction (EBSD) using an EBSD-Detector (DIGIVIEW 5 form AMETEK, Berwyn, Pennsylvania, USA). For data collection, a step size of 0.35 mm was applied. SEM and EBSD characterization of FeMn-LBM before corrosion tests was done by Jan Tobias Krüger, University of Paderborn, Direct Manufacturing Research Center.

Surface characterization after corrosion was carried out by AFM, FE-SEM, EDX, Raman spectroscopy, and FTIR. The experimental methods are described in detail in Chapter 5.

### 6.2.3. Microstructural characterization of FeMn-LBM

The microstructure of cold-rolled conventionally produced FeMn is characterized by nearly equiaxed grains with a mean grain size of approximately  $2\text{ }\mu\text{m}$  [217,223,224]. The texture is weak and consequently, no preference in orientation is observed. To characterize the microstructure of FeMn-LBM, EBSD-analyses have been conducted by Krüger and the results are shown in Figure 6.15 [31].

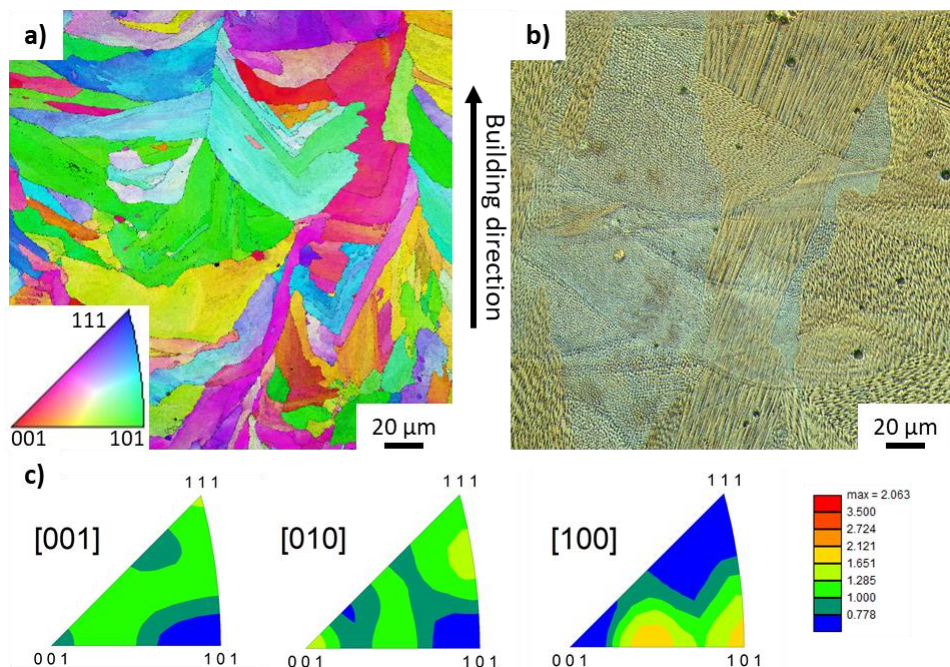


**Figure 6.15** Microstructure of FeMn-LBM samples: a) Inverse pole figure obtained by EBSD-analysis referred to the building direction, b) Light microscopy of an etched sample, c) Microtexture-analysis calculated from the EBSD-data [31].

Figure 6.15 shows the analysis of a section along the building direction. As the scanning direction in the LBM process is rotated by  $67^\circ$  after each layer, the evolving microstructure is representative for all sections along the building direction. A section across the building direction shows different shapes of grains and solidification structures, but the main characteristics are similar. For FeMn-LBM, an average grain size of  $12\text{ }\mu\text{m}$  is calculated according to the EBSD-map with a size of  $550 \times 450\text{ }\mu\text{m}^2$ . As Figure 6.15a) shows, the grain structure of FeMn-LBM is more inhomogeneous than for FeMn. The structure of FeMn-LBM consists of larger, partly elongated grains, as well as some small grains. In a section crosswise the building direction, the grains are less elongated. Hence, the grains are elongated along the building direction, respectively along the solidification direction.

Although the shape of the grains of FeMn-LBM is more inhomogeneous than for FeMn, no strong texture could be observed (Figure 6.15c). For better comparability, the scale for the texture analysis is set similar to Niendorf et al. [39]. The texture analysis in Figure 6.15c is calculated from EBSD-data and thus, the analysis is not in detail but gives a general impression. The results indicate that no distinct texture is present.

The FeMn-LBM specimens were examined in the as-built conditions. Therefore, the solidification structure resulting from the LBM-process differs from the homogenously cold-rolled FeMn. The LBM-typical boundaries of the melt pools and the columnar-dendritic solidification structure can be determined on the etched sample (Figure 6.15b). The etching enhances these structures due to differences in the local chemical composition. The local variation of Mn in the alloy is proven by SEM-EDX mappings as shown in Figure 6.16.

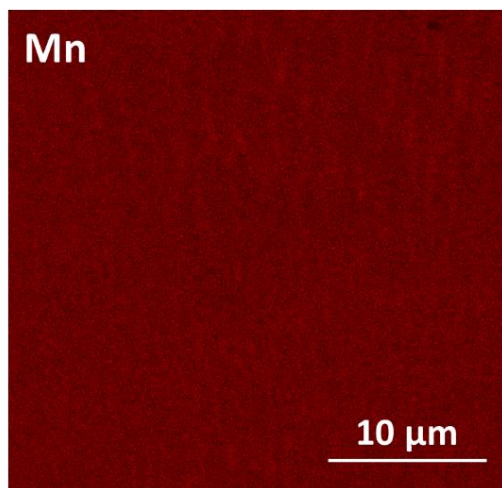


**Figure 6.16** EDX mapping of Mn distribution registered for FeMn-LBM sample. Images was done by Jan Tobias Krüger, University of Paderborn, Direct Manufacturing Research Center [31].

As described by Zhong et.al. [225] the columnar structure is accompanied by segregation of alloying elements and since Mn is the major alloying element of FeMn-LBM the columnar dendritic structure is characterized by segregations of Mn. From the cross-section, it can be seen that manganese segregates during the solidification process along with the columnar dendritic solidification structure and is enriched along the melt pool boundaries. Similar findings were observed for Fe-35Mn scaffolds produced by LBM [226].

### 6.2.4. Electrochemical analysis

Upon immersion in m-SBF, a rather complex surface process occurs comprising metal dissolution and oxygen reduction which is gradually superimposed with hydroxide/oxide formation and precipitation of carbonates, phosphates, sulphates, and other degradation

products. First, the electrochemical behavior of these FeMn-alloys in m-SBF solutions containing BSA or LYZ is characterized. The electrochemical responses registered for pure iron under the same experimental conditions are also shown for comparison.

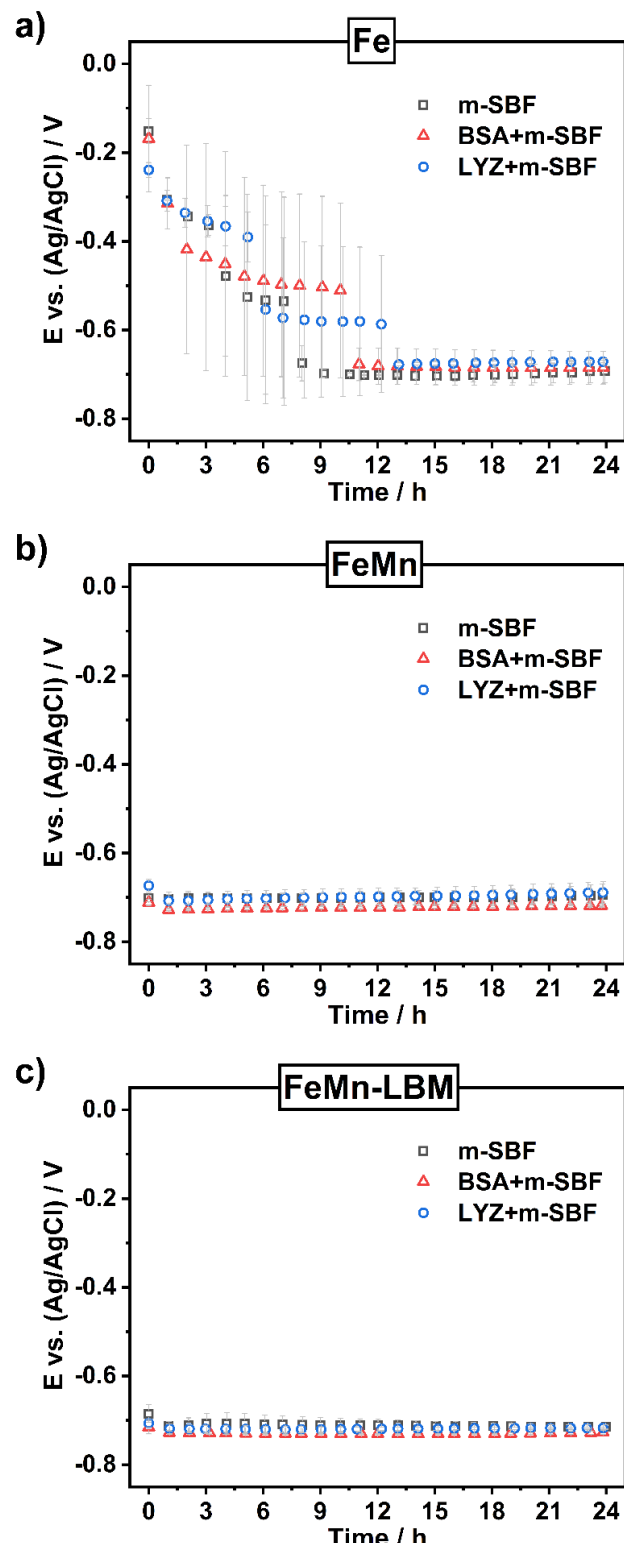


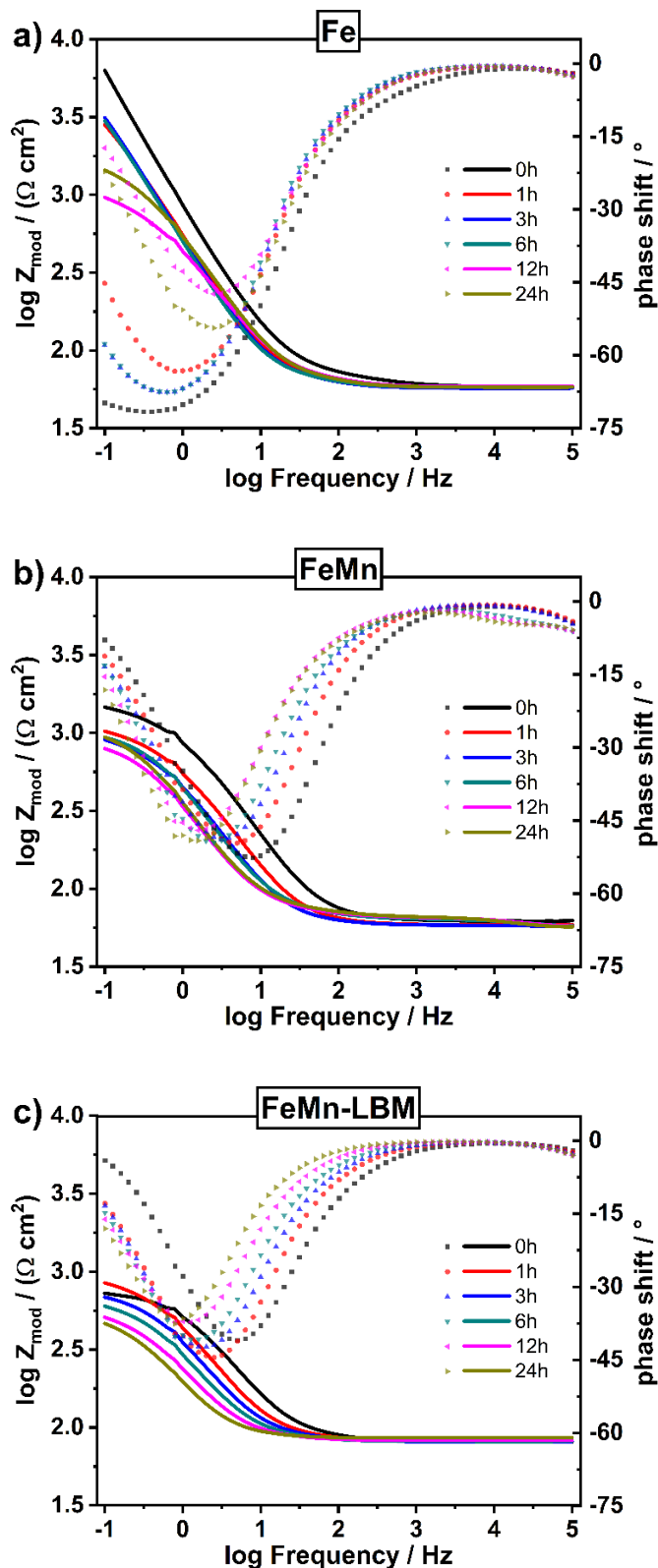
**Figure 6.17** Open circuit potential (OCP) for Fe, FeMn and FeMn-LBM as a function of time for immersion in with and without BSA or LYZ for 24 hours. The error bars were obtained from the standard deviation of three measurements.

The transients of the open circuit potentials of the studied Fe alloy as shown in Figure 6.17 indicate accelerated corrosion of the FeMn-alloys in comparison to the reference pure iron alloy. The shift in the OCP of pure iron to more negative values during the initial stages of immersion, which is typically related to the breakdown of the native iron oxide film, was not observed for FeMn-alloys indicating a very fast corrosive attack. The OCP values of pure iron exhibited instability during the first 12 hours. The addition of the proteins did not lead to a significant change in the OCP transients as expected for samples that actively corrode even after the formation of an adsorbate layer.

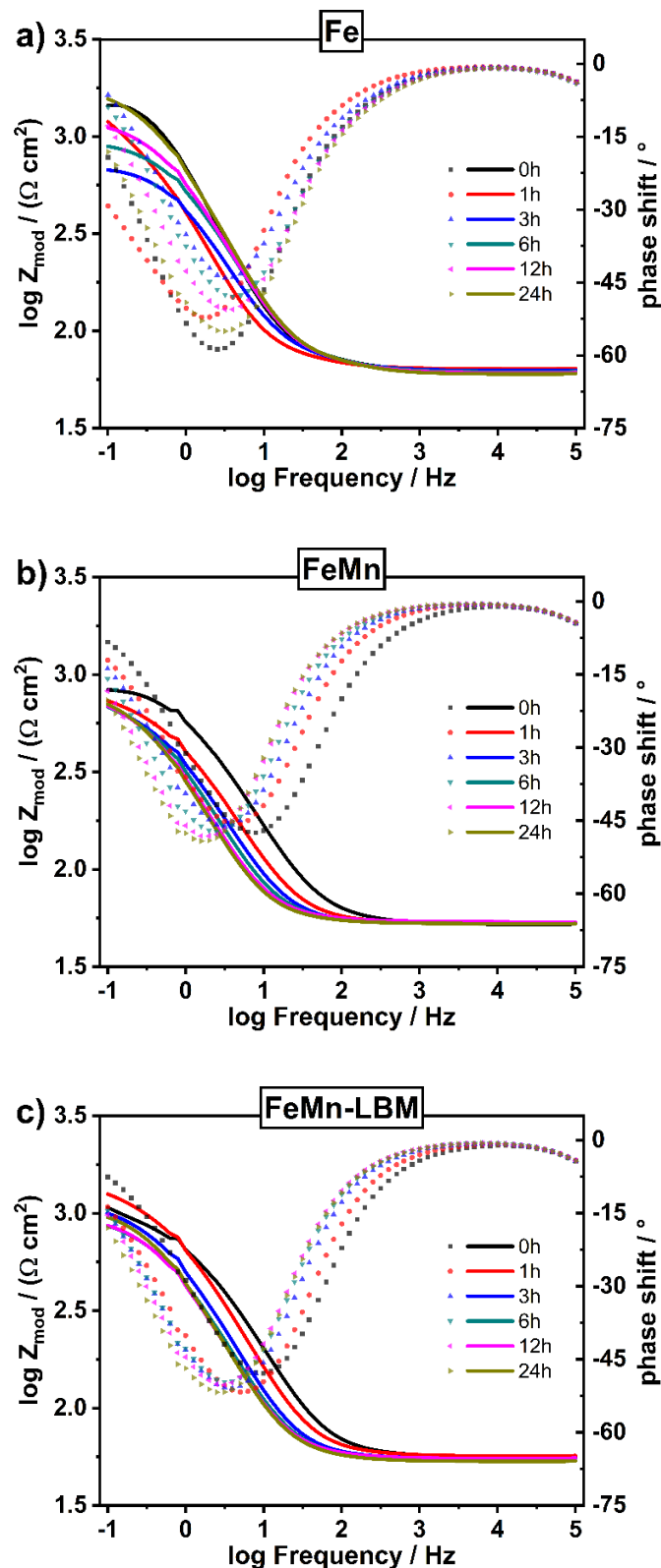
The interfacial corrosion reactions were studied by EIS at the free corrosion potential over 24 hours of immersion in the electrolyte to further characterize the influence of proteins on the corrosion behavior of Fe, FeMn, and FeMn-LBM. Figures 6.18 to 6.20 show the Bode plots recorded for the three different electrodes immersed in m-SBF, BSA + m-SBF, and LYZ + m-SBF solutions.

Initially, Fe immersed in m-SBF shows a relatively high impedance and a related strong phase shift at low frequencies indicating a dominating double-layer capacitance and a low corrosion rate (Figure 6.18a) [227]. On the contrary, the Bode plots of FeMn-alloys in Figures 6.18b and 6.18c show a low polarization resistance and Ohmic behavior at 0.1 Hz already during the initial phases of immersion. In all cases, the polarization resistances decreased with immersion time. Most importantly, the lowest corrosion resistance values were registered for the LBM-FeMn alloy indicating that laser processing promotes increased corrosion in these FeMn alloys.

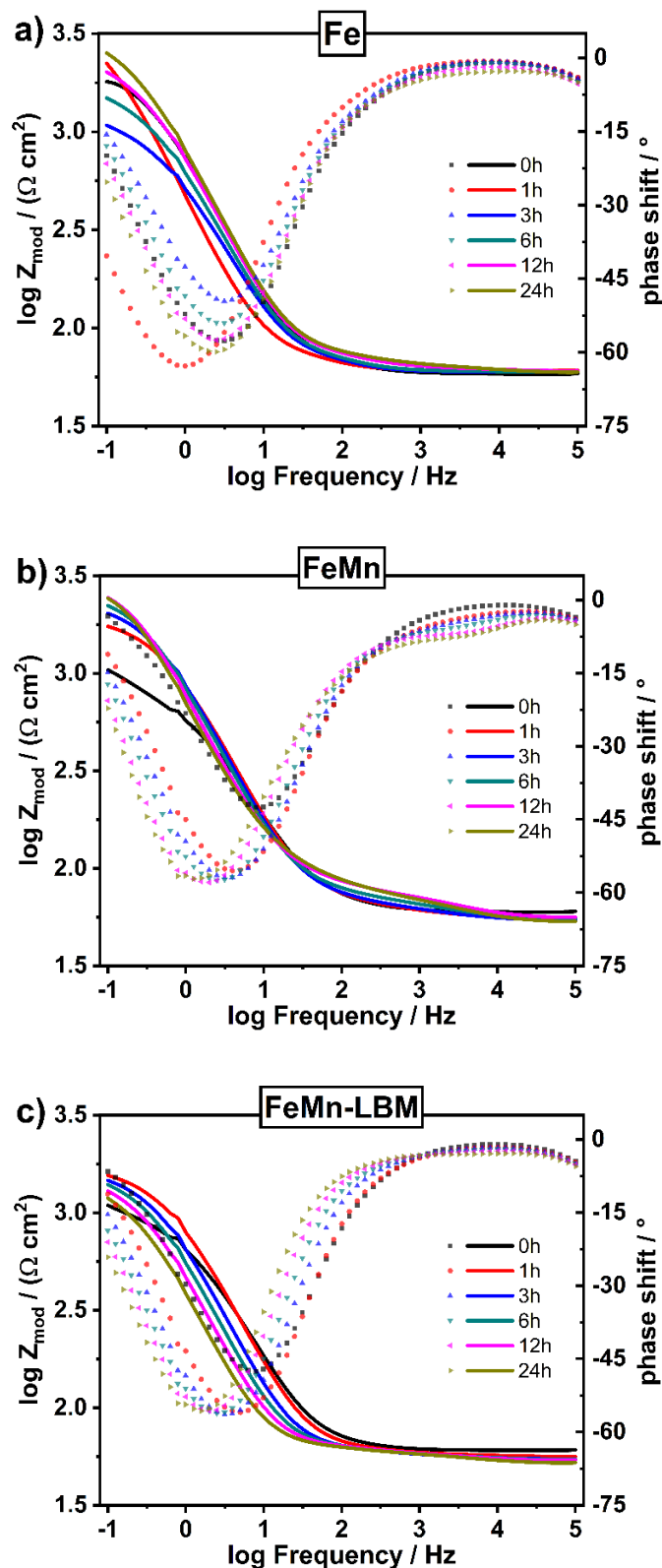
The effect of the presence of BSA in the m-SBF solution on the impedance values of Fe, FeMn, and FeMn-LBM substrates is shown in Figure 6.19. In the presence of BSA, the impedance value of Fe decreases at the initial stage of immersion (roughly three hours), however, tends to increase again slightly with longer immersion time. Although the presence of BSA did not lead to an obvious effect on the EIS data of FeMn and LBM FeMn alloy samples, a different trend to that seen on pure Fe could be inferred. For the cases of FeMn alloys, the impedance values read at low frequencies, i.e., 0.1 Hz, are progressively getting lower as the immersion time increases. Thus, the corrosion rate seems to increase with time indicating that the barrier properties of the formed corrosion layer films in the presence of BSA are progressively reduced.



**Figure 6.18** Bode plots of a) Fe, b) FeMn, c) FeMn-LBM electrodes immersed in *m*-SBF. The different immersion times are displayed in the legend of every plot. The solid lines represent the changes in impedance value and the dotted lines represent the phase shifts.



**Figure 6.19** Bode plots of a) Fe, b) FeMn, c) FeMn-LBM electrodes immersed in BSA + m-SBF. The different immersion times are displayed in the legend of every plot. The solid lines represent the changes in impedance value and the dotted lines represent the phase shifts.



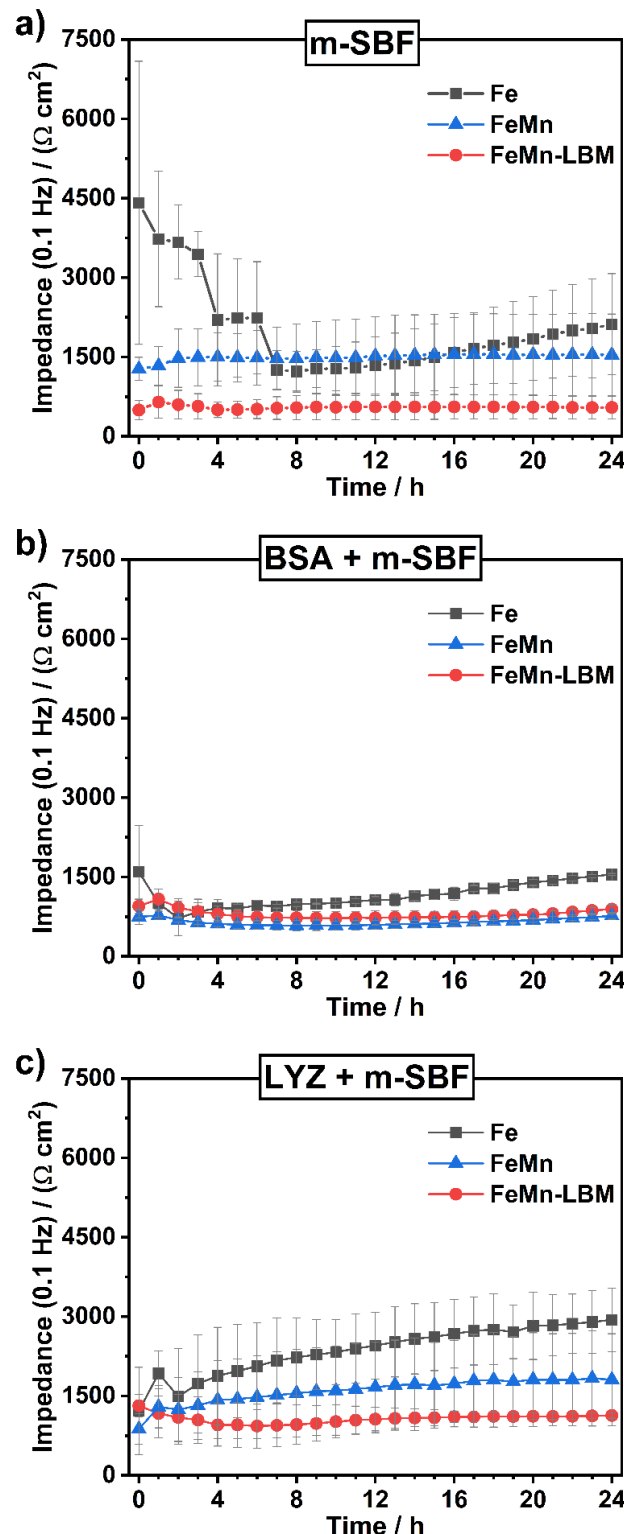
**Figure 6.20** Bode plots of a) Fe, b) FeMn, c) FeMn-LBM electrodes immersed in LYZ + m-SBF. The different immersion times are displayed in the legend of every plot. The solid lines represent the changes in impedance value and the dotted lines represent the phase shifts.

Figure 6.20 shows the EIS spectra recorded for Fe, FeMn, and FeMn-LBM immersed in an LYZ-containing m-SBF electrolyte solution. When compared to FeMn and FeMn-LBM in m-SBF (Figure 6.18) and BSA + m-SBF (Figure 6.19), a higher value of the phase shift and increased impedance values at low frequencies were observed in the presence of LYZ (see Figure 6.20). In this regard, it should be noted that the formation of thicker films on Fe and Fe-based substrates from LYZ-containing (in contrast to BSA) solutions at pH 7.4 have been previously reported [135,136,139]. This can be attributed to the preference of BSA for monolayer adsorption on the surface while LYZ rather forms multilayers [143]. For the neutral or negatively charged iron oxyhydroxide surface [139], the adsorption of positively charged LYZ proteins should be favored. Protein-based films may cover corrosion active sites and reduce the corrosion rate or the metal release at similar experimental conditions [136].

Independent of the addition of proteins, the corrosion of Fe and FeMn samples in m-SBF electrolytes leads to the formation of inorganic surface layers such as hydroxides, carbonates and phosphates of the respective metal [228]. Such layers may contribute to the effective corrosion rate [136]. The addition of proteins to m-SBF solution should lead to the formation of a complex surface layer comprising of both the respective proteins and inorganic compounds [135,139,229]. In this regard, a comparison of the evolution of the low-frequency impedance values with time is provided in Figure 6.21 to illustrate the different behavior of the studied alloys in the complex electrolytes used herein. As shown in Figure 6.21, in m-SBF, the low-frequency impedance values of pure Fe first decrease from 4.4 to 1.2  $\text{k}\Omega \text{ cm}^2$ , however, start to increase again after about 8 hours, while in the presence of BSA the impedance values of pure Fe decrease from 1.6 to 0.7  $\text{k}\Omega \text{ cm}^2$  in the first 3 hours and then increase slightly to 1.5  $\text{k}\Omega \text{ cm}^2$ . In the case of LYZ, the impedance values of pure Fe show a lower impedance from the beginning (1.2  $\text{k}\Omega \text{ cm}^2$ ) and increase reaching about 3.0  $\text{k}\Omega \text{ cm}^2$ . It is assumed that the complexing interactions between proteins and surface metal ions in the oxide layer cause an accelerated metal dissolution at the early stages of immersion. However, when the formed protein-containing surface layer gets thicker, it progressively starts to act as a barrier film on the pure Fe sample.

Compared to Fe, the impedance values at 0.1 Hz of FeMn and FeMn-LBM were significantly lower, and the values remained rather constant over the time of exposure. In this regard, the recent results reported by Tonna et al. [230] also indicate that the corrosion resistance exhibited by pure iron in  $\text{Ca}^{2+}$ -containing Hank's solution is higher than those shown by

FeMn alloy. Hot-rolled FeMn showed a slightly higher corrosion resistance in comparison to FeMn-LBM which might be assigned to the smaller grain size and the more homogeneous element distribution.



**Figure 6.21** Development of the impedance modulus of Fe, FeMn, and FeMn-LBM read at 0.1 Hz with time in a) m-SBF, b) BSA + m-SBF, c) LYZ + m-SBF. The error bars were obtained from the standard deviation of three measurements.

Moreover, it was also noticed that the scattering of low frequency impedance values was very low in the presence of BSA (see Figure 6.21b). Similar observations were reported by Harandi et al. [221] in their study to investigate the effect of BSA on corrosion of Mg-alloys. The EIS results showed that the impedance values of Mg in Hank's solution containing BSA were consistently lower than in the absence of protein. The presence of BSA also appeared to reduce the variation in impedance values. Also with regard to Mg, Mei et al. [231] analyzed the effect of albumin addition on pH buffering. They reported that the presence of albumin effectively buffered the local and overall solution pH at the Mg surface. It can be concluded that albumin, as the main protein in plasma, has a significant effect on the corrosion kinetics of metal surfaces in physiological electrolytes.

The equivalent circuit (EEC) in Figure 6.14 was used to analyze the EIS data of Fe, FeMn, and FeMn-LBM in BSA and LYZ-containing m-SBF after 24 hours of immersion. The corresponding electrochemical parameters are presented in Table 6.5.

**Table 6.5** Equivalent circuit parameters of Fe, FeMn and FeMn-LBM after 24 h immersion in m-SBF, BSA + m-SBF and LYZ + m-SBF, respectively.

Samples	Medium	$R_s$ ( $\Omega \text{ cm}^2$ )	$R_{ct}$ ( $\Omega \text{ cm}^2$ )	$R_p$ ( $\Omega \text{ cm}^2$ )	Goodness
Fe	m-SBF	58	1789	12	$2.5 \times 10^{-4}$
	BSA	63	2164	20	$1.9 \times 10^{-4}$
	LYZ	61	4330	17	$1.8 \times 10^{-4}$
FeMn	m-SBF	57	2470	16	$5.0 \times 10^{-4}$
	BSA	50	941	3	$5.4 \times 10^{-4}$
	LYZ	52	2801	27	$8.5 \times 10^{-4}$
FeMn-LBM	m-SBF	52	856	3	$1.0 \times 10^{-3}$
	BSA	45	1212	8	$5.4 \times 10^{-4}$
	LYZ	49	1501	13	$3.6 \times 10^{-4}$

In agreement with the prior discussion, it is noted that for all alloys the charge transfer resistance  $R_{ct}$  values are higher in LYZ containing electrolytes. This inhibiting effect observed for iron alloys in the presence of LYZ is in agreement with a recent study, which showed that LYZ-based composite films inhibit metal dissolution/release by the inhibition charge-transfer processes on stainless steel substrates [232,233]. Hedberg and Wagener et al. reported about thicker and more compact LYZ-based films formed on iron substrates,

which showed lower metal release ratios in comparison to surface layers formed in the presence of BSA [136,139].

Consistent with previous research, it was observed that, on the contrary, the addition of BSA to m-SBF tended to decrease the  $R_{ct}$  values. In this regard, the inhibiting effect of metal phosphate formation on Fe-based alloys should be taken into account. While proteins appear to act mainly by adsorption, phosphates mostly change the film growth kinetics [229,234]. However, this inhibiting effect of phosphate seems to be reduced when albumin is present in the solution. In addition, the capability of BSA proteins to complex Fe ions released by the oxide layer could contribute to the effect of BSA addition. Finally, the adsorption of negatively charged BSA proteins on Fe-based alloys is known to lower the surface pH, which could account for an increased release rate of Mn [235]. In this regard, BSA has been shown to exhibit stronger metal surface-protein complexation capabilities and higher amounts of released metals than LYZ [135,136,235]. In comparison, the reduced corrosion rates in the case of LYZ could be attributed to the formation of improved barrier LYZ-containing corrosion product layers, the positive charge of LYZ, and the lower metal-complexation capabilities of LYZ [139].

The LBM FeMn-alloy shows both in the case of pure m-SBF and LYZ-containing m-SBF a higher corrosion rate which is assumed to be due to the higher and more inhomogeneous grain size and higher number of defects in the additive manufactured alloy in comparison to the hot-rolled alloy.

#### 6.2.5. Microscopic studies of surface layer formation

##### 6.2.5.1 Optical microscope characterization

After immersion in m-SBF with and without BSA and LYZ, the Fe, FeMn, and FeMn-LBM samples were gently rinsed with pure water, causing some loosely bound corrosion products to detach. Subsequently, the rinsed surfaces were characterized using optical microscopy to visually observe the surface changes after corrosion. The microscopic images of the samples are shown in Figure 6.22. After rinsing with pure water, the corrosion product layer remained adhered to the surface.

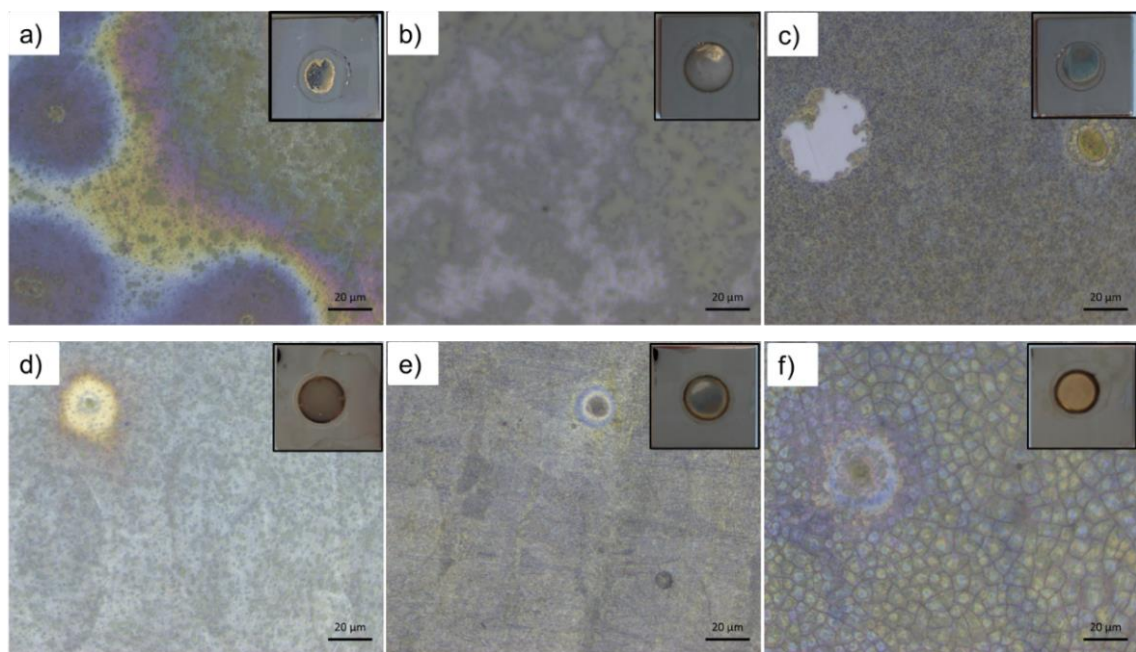


**Figure 6.22** Microscope images of Fe after immersion in **a)** m-SBF, **b)** BSA + m-SBF, **c)** LYZ + m-SBF and FeMn-LBM after immersion in **d)** m-SBF, **e)** BSA + m-SBF, **f)** LYZ + m-SBF.

Photographic images taken after the exposure to the respective electrolytes and subsequent thorough rinsing indicate that the macroscopic adhesion of the corrosion product layer and the homogeneity in its thickness is strongly affected by the presence of proteins. Especially the addition of LYZ leads to quite homogeneous yellow films in comparison to rather inhomogeneous layers formed in pure m-SBF.

#### 6.2.5.2 AFM characterization

AFM images of the Fe, FeMn, and FeMn-LBM surfaces before and after 24 h immersion in the different test solutions are shown in Figure 6.23.

After 24 h immersion in m-SBF, the morphology of all surfaces has visibly changed and the RMS surface roughness (w) increased drastically (see Figure 6.23a-f). Surface roughening was stronger for FeMn and FeMn-LBM than for Fe, which can be attributed to their higher corrosion susceptibilities. Fe developed the largest RMS roughness after immersion in LYZ + m-SBF (Figure 6.23j), whereas the maximum RMS roughness of the FeMn and FeMn-LBM surface was obtained after immersion in BSA + m-SBF (Figure 6.23h, i).

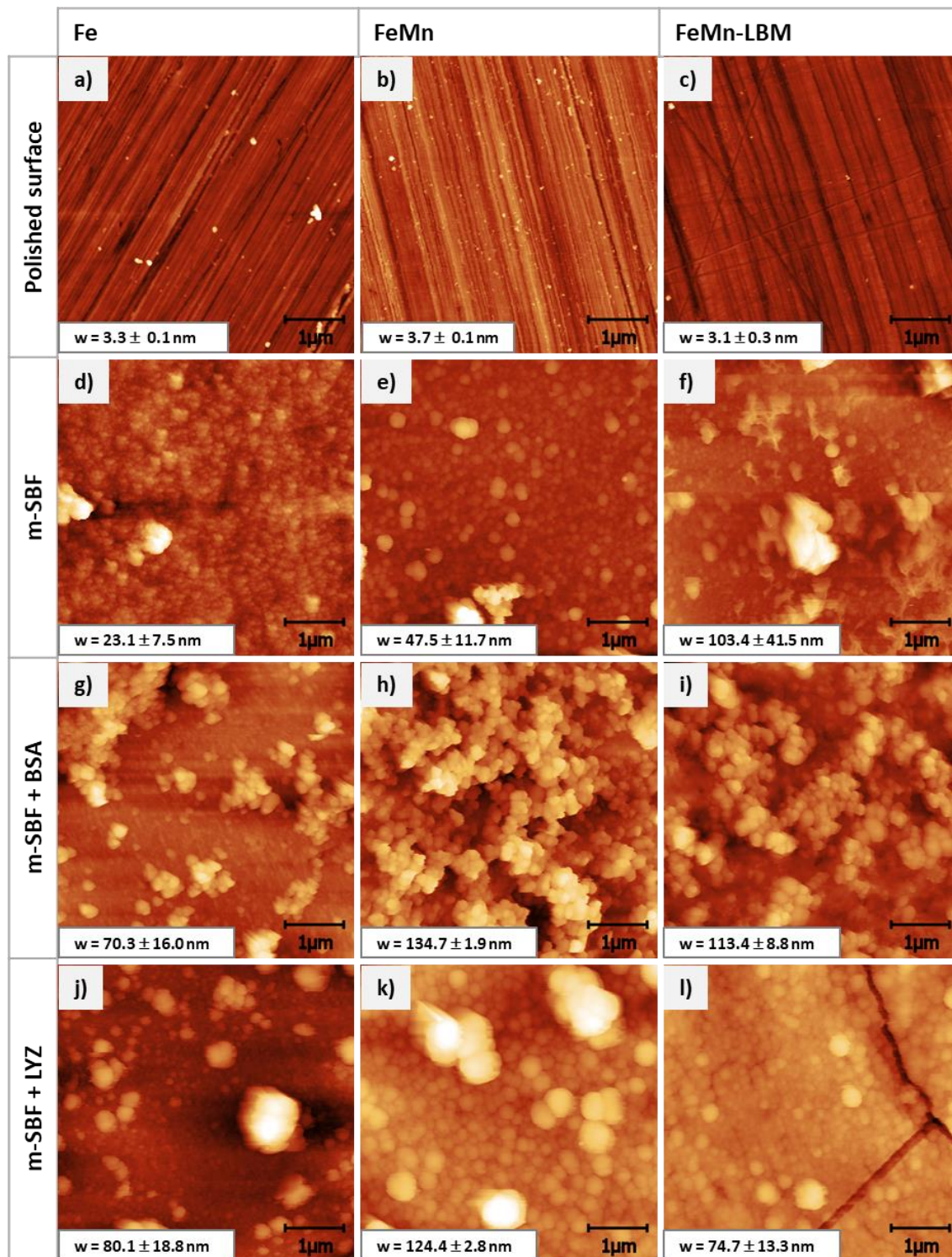


**Figure 6.23** AFM images of a) Fe, b) FeMn, c) FeMn-LBM before immersion; AFM images of d) Fe, e) FeMn, f) FeMn-LBM after 24h immersion in m-SBF; AFM images of g) Fe, h) FeMn, i) FeMn-LBM after 24h immersion in BSA + m-SBF; AFM images of j) Fe, k) FeMn, l) FeMn-LBM after 24h immersion in LYZ + m-SBF. Root-mean-square (RMS) roughness values ( $w$ ) are given in the images. The height scales of the AFM image are 50nm (a, b, c), 200 nm (d), 600 nm (g), 700 nm (e, f, j, l), and 900 nm (h, I, k) respectively.

The AFM data indicate that the addition of BSA led to the formation of cauliflower-like clusters. The cluster structure formed on the pure iron surface is more dispersed compared

to the FeMn alloy, which may be related to the difference in pH due to local corrosion of the pure iron surface during the early immersion. In the case of FeMn alloys, it has been shown that the local pH variation deviates slightly from that of pure iron in physiological solutions, such as Hank's solutions [236]. Studies on protein behavior on passive alloy surfaces have shown that BSA adsorption is related to the microstructure of the substrate surface. Sand et al. [237] investigated the adsorption of BSA on biomedical austenitic stainless steel surfaces with different grain sizes and their results showed that the surface coverage of adsorbed proteins increased with decreasing grain size, which was attributed to the increased number of physical or chemical bonds on the surface of the substrate. Rahimi et al. [238] found that BSA can form a network-like or cluster structure on the Ti6Al4V alloy surface due to the heterogeneity between the different phases ( $\alpha$ - and  $\beta$ -phases) on the substrate surface. In contrast, for CoCrMo alloys with low fraction of grain boundaries, the adsorption of proteins on the surface was more disordered [220]. The studies by Rabe et al. [239,240] combined experiments and simulations to describe possible mechanisms concerning the adsorption behavior of proteins at solid interfaces. The results demonstrate that proteins readily form a heterogeneous distribution on the solid surface under cooperative effects due to the pre-adsorbed proteins on the surface.

In the experimental system discussed in this section, although there are differences in the microstructure between the two FeMn alloys, the adsorption behavior of BSA on the surface does not show significant differences, and it can be seen that both surfaces form porous films consisting not only of adsorbed proteins but also of various corrosion and mineralization products. However, the anodic dissolution of the FeMn alloys leads to a dynamic situation in which the surface topography and surface chemical composition rapidly changes.

In the presence of LYZ more compact films were formed. This tendency was observed independent of the immersed alloy. In the case of m-SBF containing LYZ, for LBM-FeMn even crack formation (occurred due to fast drying-dehydration) in the formed surface film was observed (see Figure 6.23l). This indicates that the formed layer shows an enhanced cohesion in comparison to the films formed in m-SBF and BSA-containing m-SBF.

As m-SBF electrolytes contain bivalent cations as well as anions which promote the formation of metal oxides, phosphates and carbonates [241]. It is difficult to analyze the exact structure of the film under the given conditions, however, it can be assumed that both inorganic precipitation, metal dissolution and protein adsorption occur simultaneously

[242,243]. Therefore, AFM images show the surface morphology of a complex layer and not that of the proteins alone.

#### 6.2.5.3 FE-SEM and EDX characterization

FE-SEM and EDX measurements were performed to further characterize the surface morphology of the samples and to analyze the chemical composition of the sample surface, respectively. FE-SEM images displayed in Figure 6.24 show the Fe, FeMn, and FeMn-LBM surface topographies after 24 h of immersion in the different electrolytes.

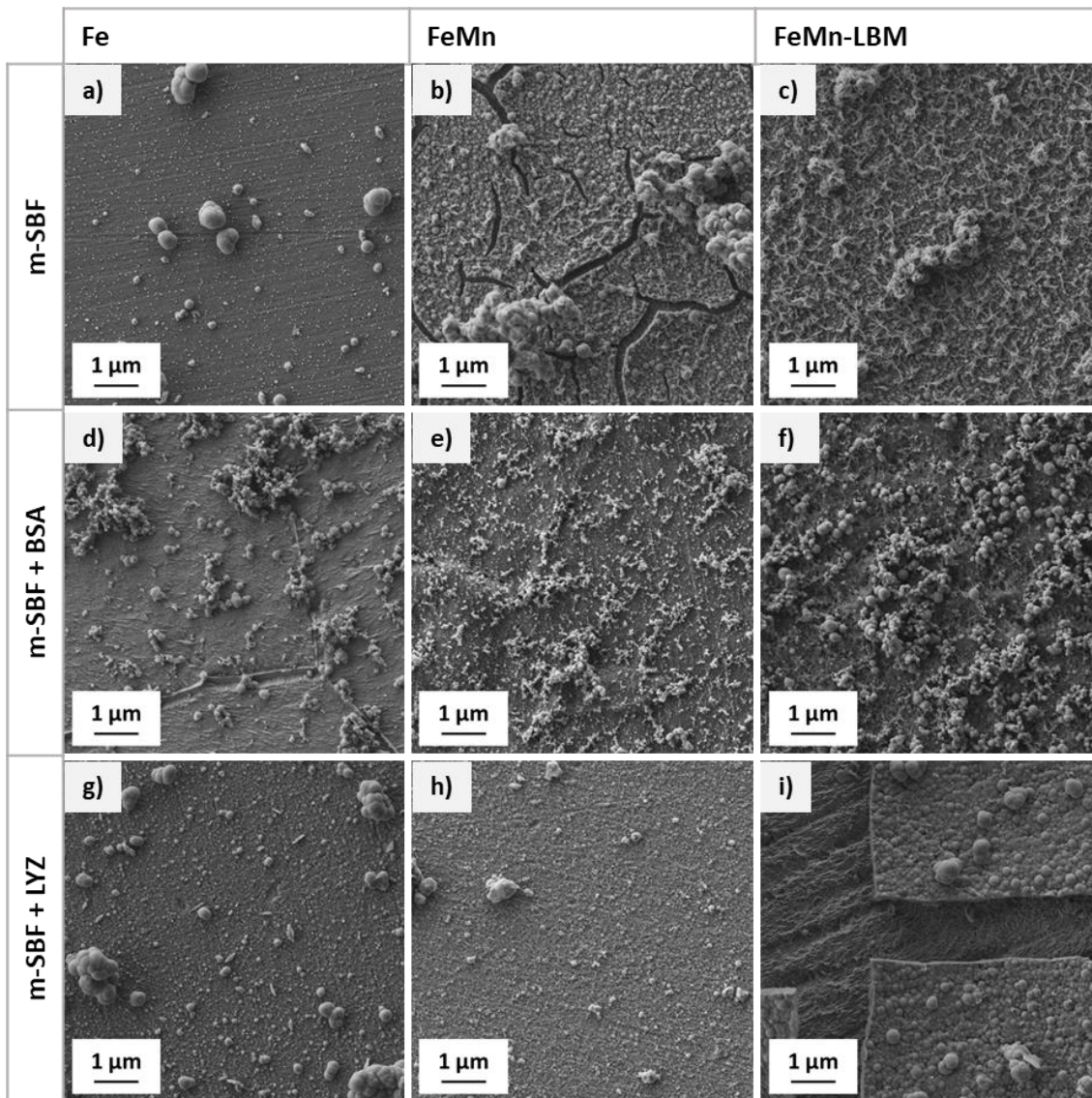


**Figure 6.24** FE-SEM images of sample surfaces after 24h immersion in m-SBF: **a)** Fe, **b)** FeMn, **c)** FeMn-LBM; SEM images of sample surfaces after 24h immersion in BSA + m-SBF: **d)** Fe, **e)** FeMn, **f)** FeMn-LBM; SEM images of sample surfaces after 24h immersion in LYZ + m-SBF: **g)** Fe, **h)** FeMn, **i)** FeMn-LBM.

In Figure 6.24, particulate corrosion products could be observed on the Fe, FeMn, and FeMn-LBM surfaces, and the EDX results (EDX mapping not displayed) show that these clusters

contain mainly phosphate and calcium. The form and composition of this corrosion product are consistent with the reported corrosion of other iron alloys in SBF [78,228,244]. The scale-like morphology exhibited by some of the corrosion product films may be the result of dehydration as previously stated by Schinhammer and co-workers [78]. As can be seen from Figure 6.24a-c, FeMn and FeMn-LBM appear to form a thicker corrosion layer after corrosion in m-SBF in comparison to Fe. In addition, the corrosion of Fe in m-SBF was non-uniform and the occurrence of pitting could be observed on the surface (see Figure 6.25).

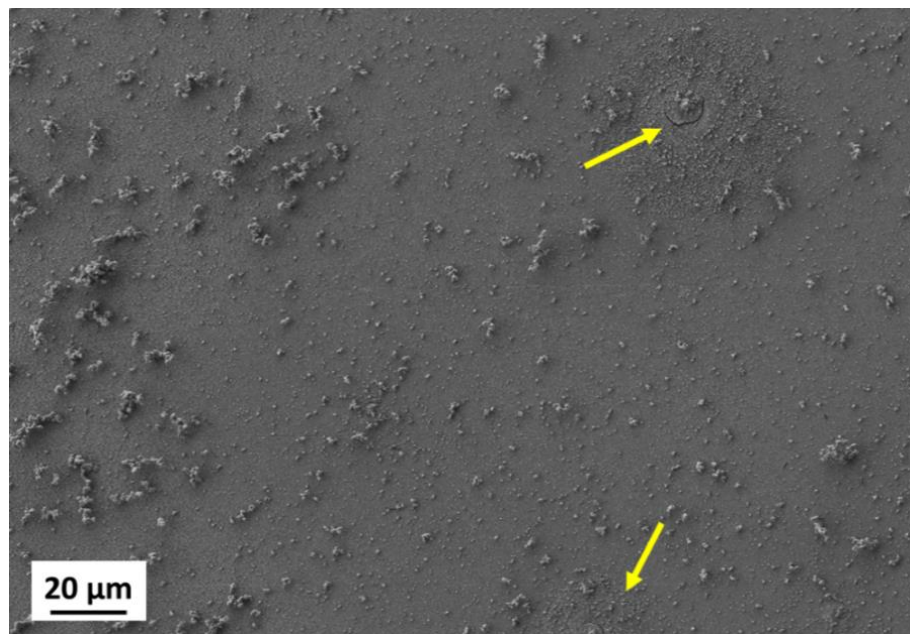


**Figure 6.25** SEM image of Fe surface morphology after 24 hours of immersion in m-SBF. The location of the pitting is indicated by the arrows.

In comparison to pure Fe, the layers formed on FeMn and FeMn-LBM in m-SBF were more uniform in agreement with their higher corrosion activity. No variation in the Fe/Mn ratio was observed for both the FeMn and FeMn-LBM alloys on a 20×20 micrometer image after the immersion in the respective electrolyte. The surface of the investigated metal exposed to m-SBF containing BSA was rougher compared to that in m-SBF only (Figure 6.24 d-f).

As revealed by FE-SEM, the corrosion layer on top of the Fe after exposure to the BSA-containing m-SBF was not homogeneous (see Figure 6.26). The presence of LYZ in m-SBF seems to give rise to the formation of denser and more compact films on the investigated metal surface (Figure 6.24 g-i). The scale formation seems to be slightly more pronounced for FeMn-LBM in comparison to FeMn after corrosion in the test solutions.

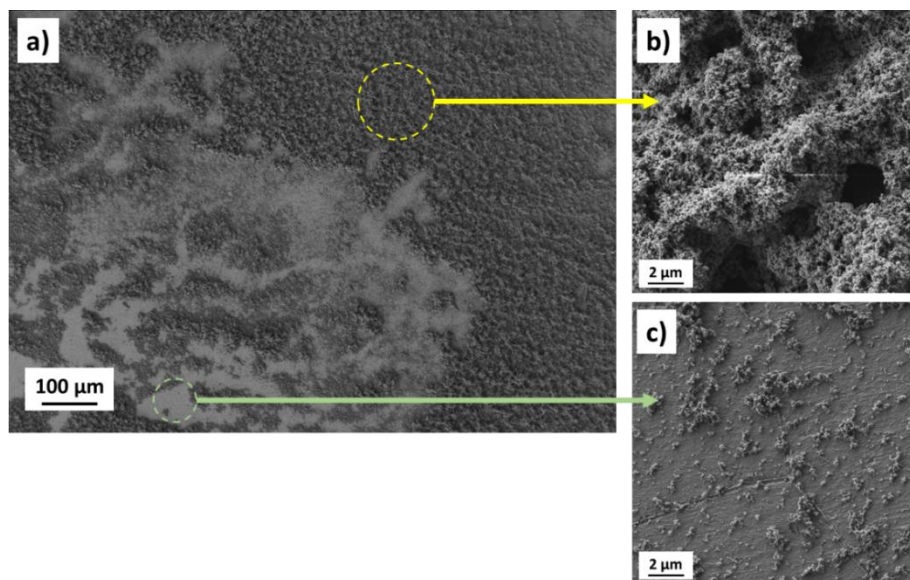


**Figure 6.26** *a)* SEM image of Fe after immersion in BSA + m-SBF for 24 hours. *b)* Detail of the surface morphology in the yellow circle from *a*), *c)* Surface morphology in the green circle from *a*).

The results of the EDX analyses (EDX mapping not displayed) are given in Table 6.6.

**Table 6.6** Surface composition of investigated Fe, FeMn, and FeMn-LBM samples after immersion in m-SBF with and without protein as determined by EDX.

Electrolyte	Samples	Composition (at. %)						
		Fe	Mn	Ca	C	N	O	P
m-SBF	Fe	66.8	-	1.9	4.3	2.3	20.9	3.0
	FeMn	47.3	17.0	1.8	4.2	1.4	22.9	3.7
	FeMn-LBM	51.9	15.9	2.0	3.4	1.1	21.4	3.9
m-SBF + BSA	Fe	87.9	0.2	0.2	5.6	3.0	2.6	0.5
	FeMn	43.3	20.3	0.4	19.0	2.7	10.4	1.5
	FeMn-LBM	57.4	18.8	0.4	11.5	3.3	7.1	0.9
m-SBF + LYZ	Fe	61.7	0.2	1.9	3.5	2.2	26.1	3.8
	FeMn	55.9	20.5	1.1	4.6	1.8	12.3	2.4
	FeMn-LBM	35.9	11.1	2.9	3.9	1.9	37.0	6.0

EDX data show that in the presence of BSA less Ca and P are incorporated in the corrosion product layer in comparison to m-SBF and LYZ containing m-SBF. The observed inhibited formation of calcium and phosphate in the presence of BSA is in agreement with a study of Virtanen et al. [139]. The FeMn-LBM samples showed the highest calcium and phosphate concentrations both for the m-SBF and the m-SBF+LYZ electrolyte.

Overall, it can be concluded that compact composite films are formed in the presence of LYZ. Conversely, the co-deposition of BSA brings about a reduction of the incorporation of phosphates and the resulting barrier properties. The latter is supported by the AFM and FE-SEM images which point out the formation of porous and defective films.

#### 6.2.6. Vibrational spectroscopy of the surface layers

##### 6.2.6.1 ATR-FTIR and FT-IRRA spectroscopy

The FTIR reflection spectra of Fe, FeMn, and FeMn-LBM samples after rinsing and drying treatments are shown in Figure 6.27. It can be observed that after immersion in the different protein-containing solutions for 24 hours, the FTIR spectra of Fe, FeMn, and FeMn-LBM exhibit typical amide bands (as shown in Figure 6.27). These bands serve as clear evidence for the adsorption of proteins on the sample surfaces. Information about the protein secondary structure can be obtained by Gaussian fitting of the amide I band from  $1700\text{ cm}^{-1}$  to  $1600\text{ cm}^{-1}$  [245].

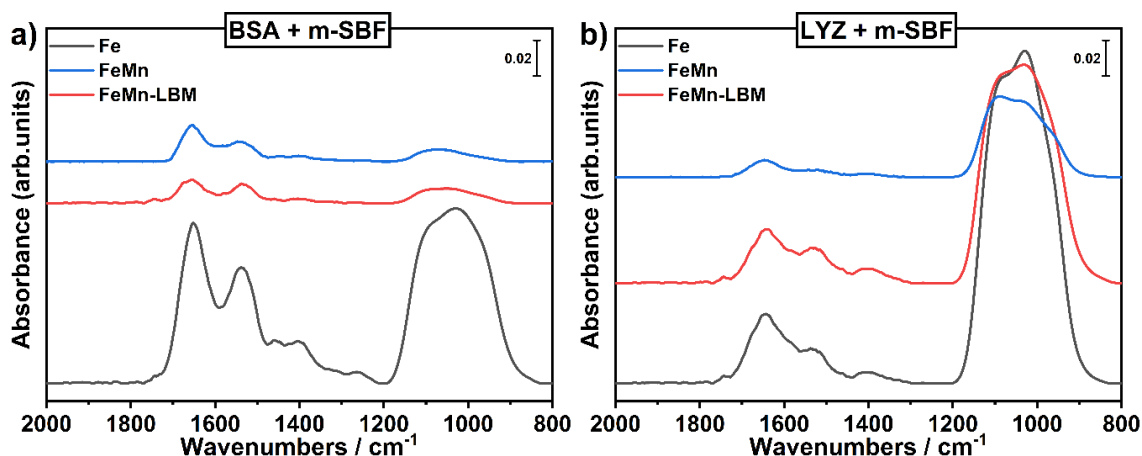


**Figure 6.27.** FTIR reflection spectra collected in the region of  $2000\text{--}800\text{ cm}^{-1}$  for Fe, FeMn and FeMn-LBM substrates after 24 h immersion in a) BSA + m-SBF and b) LYZ + m-SBF.

Information on the secondary structure of the protein was determined by fitting the amide I bands. First, selected the band between  $1710\text{ cm}^{-1}$  and  $1590\text{ cm}^{-1}$  of the original spectra and fitted the baseline, then determine the position and number of peaks to be used for peak fitting by means of the analysis of the second derivatives, and finally fitted the identified peaks by Gaussian curves. The sum of the peak areas of all peaks was used to determine the relative contributions of the different secondary structures. Figures 6.28 and 6.29 shows the spectra of the fitted amide I bands.

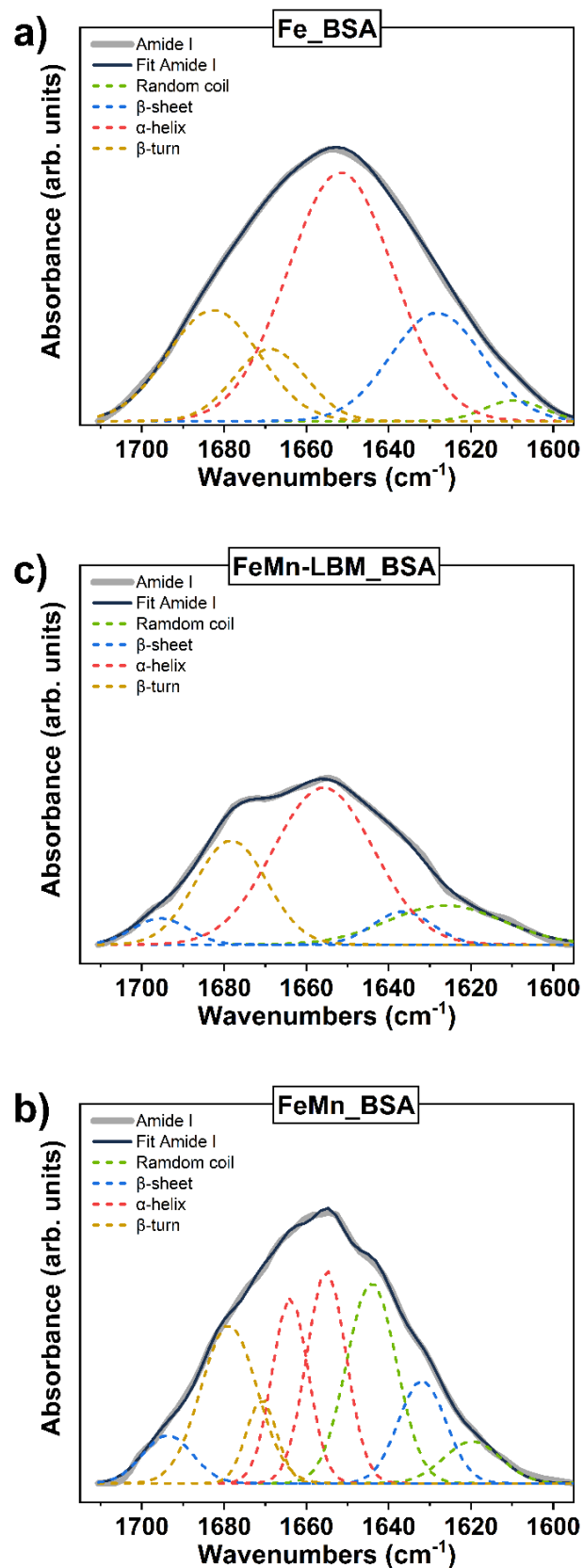


**Figure 6.28.** Fitting of Amide I band collected for adsorbed BSA on a) Fe, b) FeMn, c) FeMn-LBM.

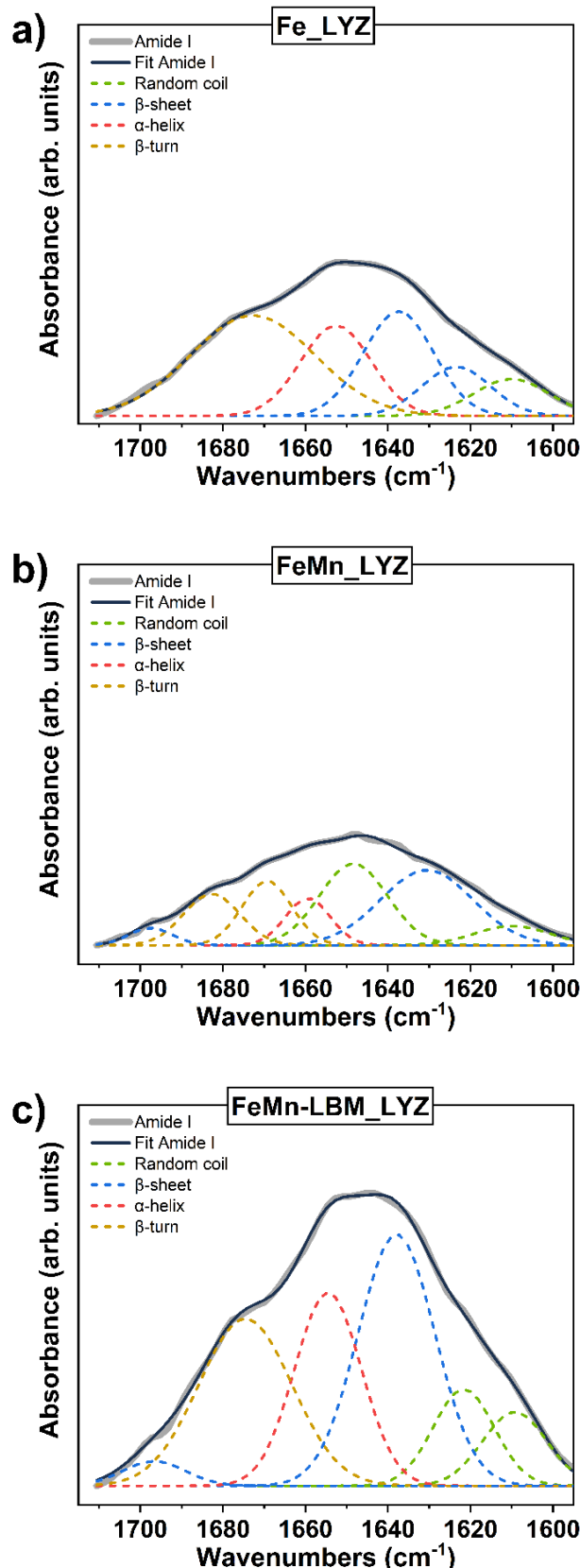


**Figure 6.29.** Fitting of the Amide I band collected for adsorbed LYZ on a) Fe, b) FeMn, c) FeMn-LBM.

The results of the fit of the protein secondary structure are listed in Table 6.7 and Table 6.8. The ratio of the integral of amide I to phosphate bands is presented in Table 6.9.

**Table 6.7** Integral areas of the amide I band and composition of BSA secondary structure determined by FTIR reflection spectroscopy.

Samples	Integral of the amide I	Secondary structure (%)			
		Random coil	$\beta$ -sheet	$\alpha$ -helix	$\beta$ -turn
Fe	4.1	$2.3 \pm 0.1$	$29.0 \pm 18.2$	$46.0 \pm 10.8$	$24.0 \pm 6.0$
FeMn	0.7	$30.0 \pm 2.9$	$14.0 \pm 1.8$	$32.0 \pm 0.5$	$23.8 \pm 1.4$
FeMn-LBM	0.5	-	$24.4 \pm 2.6$	$50.6 \pm 0.5$	$25.0 \pm 2.1$
BSA in aqueous solution [246]	-	16	14	53	4

**Table 6.8** Integral areas of the amide I band and composition of LYZ secondary structure determined by FTIR reflection spectroscopy.

Samples	Integral of the amide I	Secondary structure (%)			
		Random coil	$\beta$ -sheet	$\alpha$ -helix	$\beta$ -turn
Fe	1.1	$9.0 \pm 0.3$	$32.7 \pm 2.2$	$25.8 \pm 5.3$	$32.7 \pm 5.7$
FeMn	0.3	$24.9 \pm 13.7$	$32.3 \pm 4.4$	$13.4 \pm 7.9$	$29.4 \pm 2.6$
FeMn-LBM	0.8	$17.8 \pm 2.2$	$36.3 \pm 4.5$	$27.1 \pm 3.4$	$18.7 \pm 5.4$
LYZ in aqueous solution [245]	-	17	12	52	19

**Table 6.9** Ratio of the integral of amide I to phosphate bands obtained from the FTIR spectra.

Electrolyte	Samples	The ratio of the integral of amide I to phosphate (%)
m-SBF + BSA	Fe	$15.0 \pm 4.5$
	FeMn	$74.2 \pm 1.2$
	FeMn-LBM	$34.5 \pm 0.5$
m-SBF + LYZ	Fe	$3.5 \pm 0.3$
	FeMn	$4.6 \pm 0.1$
	FeMn-LBM	$3.4 \pm 0.1$

Based on the integral of the amide I band in Figure 6.27a, which is proportional to the total amount of adsorbed protein, more BSA was adsorbed on the Fe surface than on FeMn and

FeMn-LBM (see Table 6.7). As revealed by FE-SEM, the corrosion layer on top of the Fe surface after exposure to the BSA-containing m-SBF was not homogeneous (see Figure 6.26), and the thickened BSA layer led to a significant increase in the amide I band. In the case of LYZ, the adsorption of LYZ on the Fe surface is slightly stronger than for the FeMn alloys. Both Fe and FeMn showed lower amounts of adsorbed protein for LYZ than for BSA, which can be attributed to the widely different solution concentrations. In contrast, FeMn-LBM shows a LYZ adsorption that is about 50% higher than the corresponding BSA adsorption, despite LYZ having a 200 times lower concentration.

The information from the fitted amide I band indicates that the secondary structure of the two proteins is differentially affected by the incorporation in the growing surface layers. For example, Table 6.7 shows that the  $\alpha$ -helix content of BSA decreased from 53 % in solution to 46.0 %, 32.0 %, and 50.6 % after adsorption on Fe, FeMn, and FeMn-LBM, respectively. The loss of the helical structure of BSA was lowest on FeMn-LBM. For LYZ, the  $\alpha$ -helix content decreased even more drastically from 52 % in solution to 25.8 %, 13.4 %, and 27.1 % after adsorption on Fe, FeMn, and FeMn-LBM, respectively.

In addition to the amide bands, the spectra in Figure 6.27 show obvious metal phosphate and metal hydroxide absorption bands in the wavenumber range 900-1200  $\text{cm}^{-1}$  for all alloys [140]. After immersion in LYZ-containing m-SBF, the resulting phosphate peaks are more dominant than in the case of BSA containing m-SBF, as can be deduced from Table 6.9. This is in accordance with the FE-SEM and EDX results, which showed higher phosphate concentrations for the sample immersed in LYZ containing m-SBF in comparison to the BSA-containing electrolyte.

#### 6.2.6.2 Raman spectroscopy

Raman spectra in Figure 6.30 reveal the formation of metal oxides and phosphates on all samples. In Figure 6.30a, the peaks at 230  $\text{cm}^{-1}$ , 258  $\text{cm}^{-1}$ , 485  $\text{cm}^{-1}$ , and 630  $\text{cm}^{-1}$  were observed. It can be assumed that the scale formed on Fe, FeMn, and FeMn-LBM contains iron oxides and oxyhydroxides for m-SBF [247]. After immersion in BSA + m-SBF, peaks at 281  $\text{cm}^{-1}$ , 330  $\text{cm}^{-1}$ , 490  $\text{cm}^{-1}$  and 670  $\text{cm}^{-1}$  were found (see Figure 6.30b), which are characteristic of  $\text{Fe}_2\text{O}_3$  and  $\text{Fe}_3\text{O}_4$  [247]. In the presence of LYZ (Figure 6.30c), the characteristic peaks of  $\text{Fe}_2\text{O}_3$  at 285  $\text{cm}^{-1}$  and 485  $\text{cm}^{-1}$ , and the peak of  $\text{Fe}_3\text{O}_4$  at 663  $\text{cm}^{-1}$  were observed. Unlike the case of BSA, Figure 6.30b shows that  $\text{Fe}_2\text{O}_3$  appears to be the predominant oxide form. With  $\text{MnO}_x$  typically containing manganese in  $\text{Mn}^{4+}/\text{Mn}^{3+}$  mixed

oxidation states, some vibration bands arising at 360-370  $\text{cm}^{-1}$  and 630-670  $\text{cm}^{-1}$ , with the latter mostly overlapping with magnetite contributions, can be attributed to Mn(III)-O and Mn(IV)-O bond vibrations, respectively [248–250]. The Raman shift spectra showed the characteristic contributions due to phosphate ions at 980-1100  $\text{cm}^{-1}$  [251], which is also visible in the corresponding FTIR spectra in Figure 6.27.

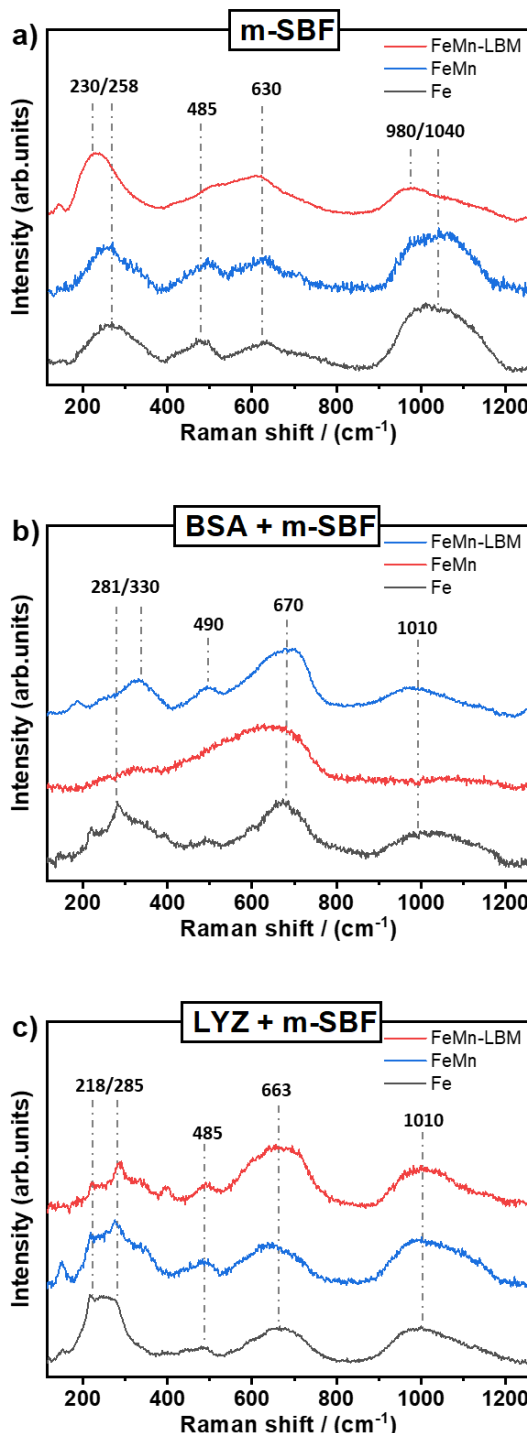


**Figure 6.30** Raman spectra of Fe, FeMn and FeMn-LBM after immersion in **a)** m-SBF, **b)** BSA + m-SBF and **c)** LYZ + m-SBF.

The results of FTIR and Raman spectroscopy showed that Fe, FeMn, and FeMn-LBM after immersion in protein-containing m-SBF, formed a corrosion layer that incorporated protein, metal oxides, carbonate and phosphate. LYZ containing m-SBF led to a stronger metal phosphate formation than BSA containing m-SBF which explains the formation of the more compact and barrier-like layer.

### 6.2.7. Conclusions

The influence of different types of proteins (BSA and LYZ) in simulated body fluid on the corrosive properties of selective laser beam melted FeMn in comparison to hot-rolled FeMn and pure iron could be revealed by complementary analytical approaches. The electrochemical impedance data clearly demonstrate that both FeMn alloys show higher corrosion rates in comparison to pure iron with and without the additional proteins.

The FeMn-LBM alloy showed an increase in corrosion in comparison to hot-rolled FeMn, especially in pure and LYZ containing m-SBF. This finding could be explained by the increased grain size of the additive manufactured FeMn alloy and the dendritic columnar structure with local enrichments of manganese. The addition of BSA seems to attenuate the differences between the different alloys concerning their corrosion rates. LYZ shows on average an inhibitive effect, which could be correlated with the structure and morphology of the formed surface corrosion layer. On the contrary, BSA rather slightly promotes the corrosion process, which could be again justified by the defective structure of the film and the ability to complex iron ions. The structure and morphology of the different surface films could be revealed by FTIR spectroscopy in reflection, Raman spectroscopy, AFM topographic images, and EDX studies. Both FTIR and Raman spectroscopy, in agreement with EDX data, showed higher concentrations of phosphates in the formed surface layers in the presence of LYZ compared to surface layers formed in the presence of BSA. This formation of inorganic protective compounds is likely to contribute to the corrosion inhibiting effect of LYZ in m-SBF electrolyte.

In summary, the studies in this section illustrate that the resulting corrosion rate of FeMn alloys in m-SBF strongly depends on the specific microstructure and the presence of proteins. However, both FeMn alloys show distinctly higher corrosion rate than pure iron both in the presence and absence of the studied proteins. Additive manufacturing thereby allows the variation of the corrosion kinetics of FeMn-based alloys as a bioresorbable alloy based on the variation of their composition and microstructure.

### 6.3 Influence of hydrogel coatings on corrosion of iron in m-SBF

The influence of an applied agar film on the surface corrosion of pure iron in m-SBF was investigated. The following section has been published in reference [32] by the author of this thesis.

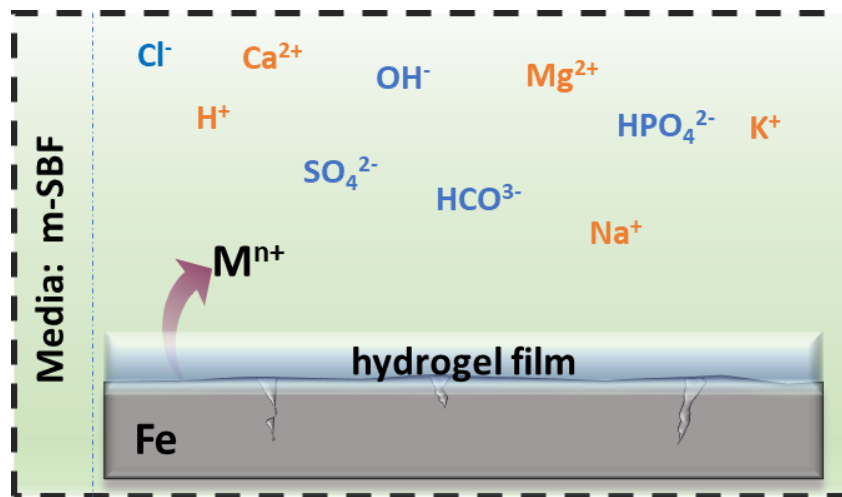


**Figure 6.31** The sketch overviews the main content of section 6.3. In this section, the effect of applied Agar films on the corrosion behavior of pure iron in m-SBF was investigated.

Metal implants in SBF tend to form a CaP layer on their surface [252,253]. For Mg alloys, the formation of this layer can effectively decelerate their corrosion rate and enhance their biocompatibility [254–256]. However, for Fe-based alloys which already suffer from a comparatively low corrosion rate, the accumulation of corrosion products and the formation of a calcium-containing degradation layer on their surface is detrimental [70,257]. Gebert et al. [228] studied the corrosion behaviour of Fe-30Mn-1C in NaCl, Tris-buffered saline, and SBF and noticed the precipitation of phosphate compounds already at an early stage of immersion. The degradation mechanism of austenitic Fe-Mn-C-Pd alloys in SBF was studied by Schinhammer et al. [78]. They reported that the surface product layer consisting of hydroxides and carbonates reduced the degradation rate by limiting the diffusion of oxygen and ions to the metal surface. As discussed in section 6.2 the presence of surface layers may weaken the effect of microstructure.

Concerning the corrosive medium, hydrogel films have been discussed as an alternative to liquid electrolytes [258–261]. However, so far the influence of a hydrogel on the corrosion behaviour of iron alloys in contact with a physiological electrolyte was not studied in detail.

So in this section, surface corrosion of pure iron were performed in m-SBF electrolyte with and without applied agar films as a typical hydrogel film. The corrosion properties of Fe

alloys were studied by means of EIS in m-SBF with and without an applied agar hydrogel film. The swelling process of the agar film was measured by in-situ FTIR spectroscopy in attenuated total reflection. Surface characterization was carried out by FE-SEM, Raman spectroscopy, and XPS with the aim to correlate the surface composition and morphology after the corrosive attack with the corrosive environment.

### 6.3.1. Materials and chemicals

In this section present work, ARMCO® Fe with dimensions of 15 mm x 15 mm x 3 mm was cut from the rolled stick. The specimens were electropolished [32]. m-SBF was prepared according to the preparation by Oyane et al. [106].

### 6.3.2. Experimental approach

#### 6.3.2.1 Preparation of hydrogel films

Figure 6.32 illustrates a Schematic of preparing the agar film. Agar films were prepared using agar powder from AppliChem GmbH. 0.25 L of distilled water was heated to boiling in an oil bath, after which 5 g of agar powder was added. After stirring until the agar powder was fully dissolved, 5 ml of the hot agar solution was spread on a Teflon plate and left to stand at room temperature for 3 days. The thoroughly dried films were recovered from the Teflon plates and re-immersed in water for few seconds in order to form transparent and malleable hydrogel films. Finally, the produced hydrogel films were applied to the iron sample. They exhibited a film thickness of 300  $\mu\text{m}$ .

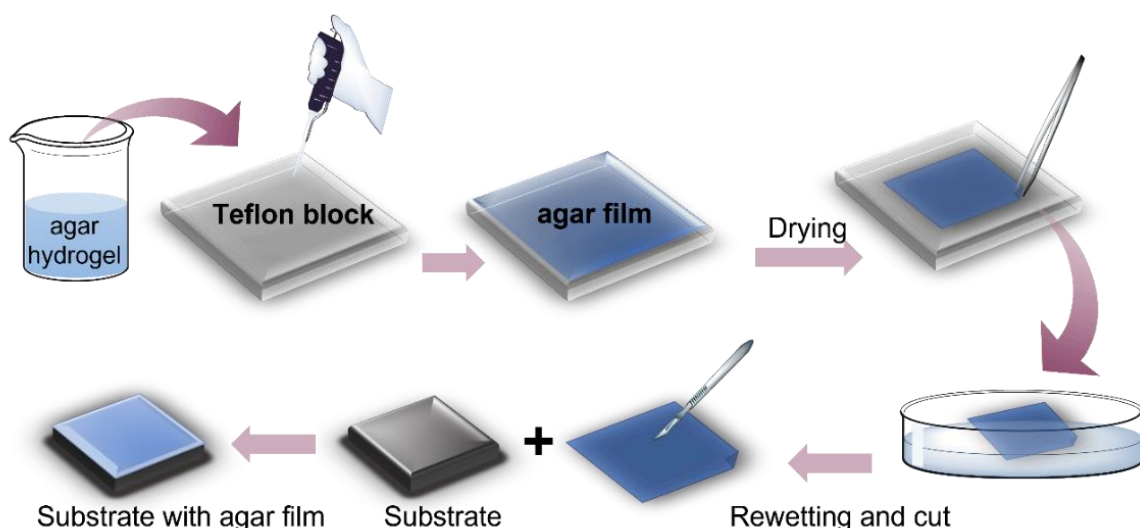


**Figure 6.32.** Schematic illustration of the hydrogel film preparation.

### 6.3.2.2 Electrochemical impedance analysis

EIS measurements were performed in a three electrode configuration using a Gamry Ref. 600 galvanostat/potentiostat. The electropolished substrates with and without applied agar film were used as working electrode. A Ag/AgCl (sat. KCl) electrode was used as the reference electrode and a Pt platinum sheet as the counter electrode. The EIS spectra were analysed using the Echem Analyst™ software.

### 6.3.2.3 Attenuated total reflection FTIR spectroscopy

The in-situ ATR-FTIR was mounted on an attachment for ATR measurements within the sample compartment of a Bruker Vertex 70v FTIR spectrometer. Spectra were recorded at room temperature at a resolution of  $4\text{ cm}^{-1}$  by co-adding 128 scans. The Si-crystal served as reference. The agar film was applied to the Si-ATR crystal in the same way as for the iron samples. Spectra of the Agar film were recorded before and after exposure to m-SBF.

### 6.3.2.4 Surface analysis

The microstructure samples and agar film were characterized by FE-SEM, and the surface chemical composition was analysed by means of XPS. The experimental methods are described in detail in Chapter 5.

Raman spectra were recorded using an InVia Renishaw Raman microscope with a CCD detector. A YAG-Laser (532 nm), an 1800 l/mm grating was used to measure iron substrate and a NIR-Laser (785 nm), an 1200 l/mm grating was used to measure agar film. A 50X objective was used for all measurements.

The samples after removal of the agar film and corrosion product layer were characterized using DRIFT. The spectra were recorded between the wavenumbers 400 and  $4.000\text{ cm}^{-1}$  in 256 scans and at a spectral resolution of  $4\text{ cm}^{-1}$ . Bare iron was used as a reference.

## 6.3.3. Results and discussion

### 6.3.3.1 Electrochemical corrosion analysis

For the corrosion test, EIS data of iron samples were continuously measured with and without the applied agar hydrogel film for an immersion time of 24 h in m-SBF at OCP. Figure 6.33a) and b) show the impedance spectra obtained for samples with and without agar films at different times. The Bode plots show only one time constant for both samples. In the high frequency region (104 to 105 Hz), the impedance is almost independent of the frequency and can be used to describe the electrolyte resistance ( $R_{ely}$ ). In the low frequency

region, the two samples exhibited capacitive behaviour at the initial stage of immersion. With increasing immersion time, the low-frequency impedance values decreased in both cases due to the onset of corrosion. According to the measured values at 0.1 Hz, the corrosion rate was higher for the agar-coated surface.

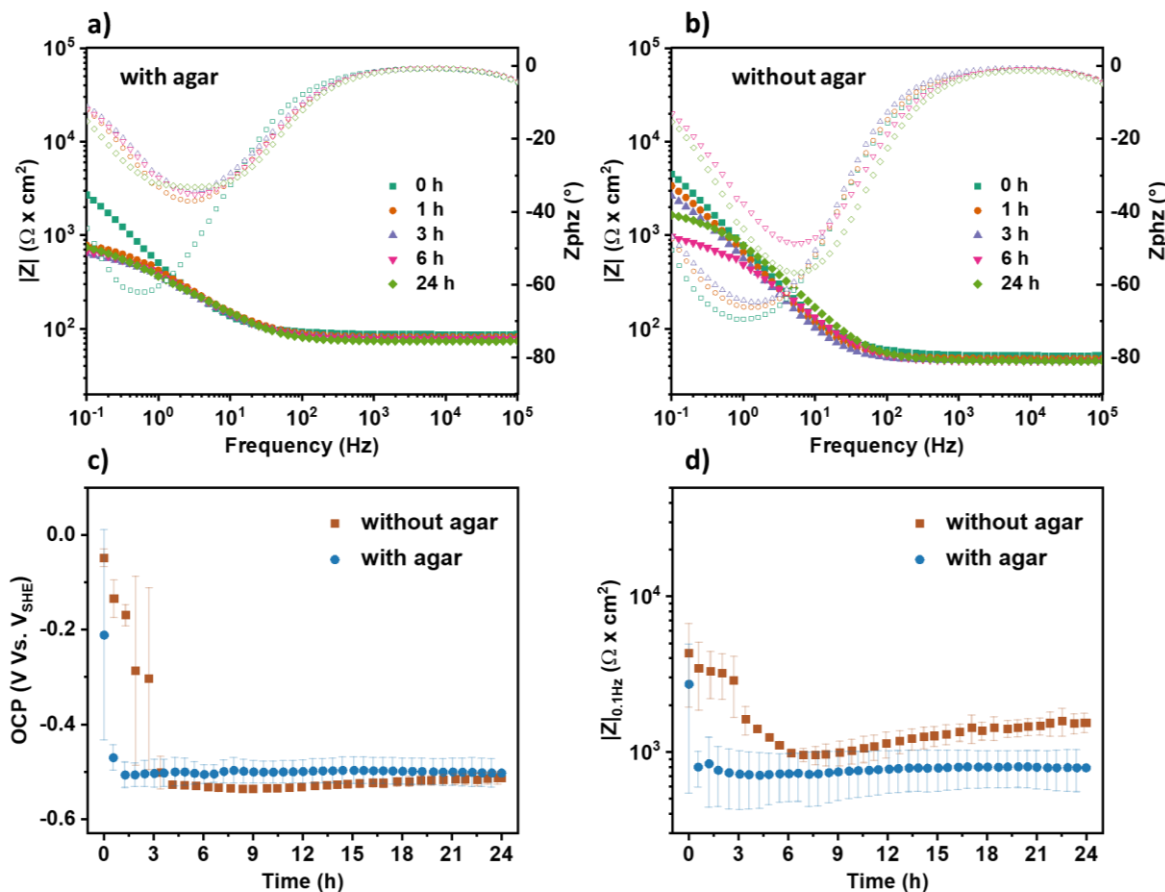


**Figure 6.33** Development of impedance spectra over time of immersion in m-SBF with (a) and without (b) an applied agar film; comparison of the time -dependent open circuit potential (OCP) (c) and impedance values at 0.1 Hz (d) of iron with and without an applied hydrogel film in m -SBF.

Figures 6.33c and 6.33d show the development of OCP values and impedance values at 0.1 Hz with incubation time, respectively. The transients of the free corrosion potential and the low frequency impedance values of the iron sample in m-SBF show both a certain incubation time of about three hours. Interestingly the incubation time with the applied agar film is slightly shorter than for the non-coated iron substrate, which indicates a fast electrolyte transport through the agar film. Both the measured free corrosion potentials and the impedance values at 0.1 Hz indicate a faster corrosion attack for the agar film -coated substrate during the first three hours of immersion. However, for extended times of immersion, the free corrosion potentials values and impedance values at 0.1 Hz are similar

for both samples (Figure 6.33), indicating that the applied agar film does not lead to any preferential inhibition of anodic or cathodic reactions.

The equivalent electrical circuit (EEC) in Figure 6.34 was used to analyse the EIS data. The non-ideal capacitive behaviour was described by the constant phase element (CPE) in the model EEC.  $R_s$  represents the electrolyte resistance.  $CPE_{dl}$  and  $R_{ct}$  are the capacitive and resistive elements of the electrolyte/metal interface, respectively.  $CPE_{film}$  and  $R_p$  are the capacitive and resistive elements of the surface film. The surface film is either the formed corrosion product layer on the base iron substrate or the combination of the agar film and the formed corrosion product layer in case of the agar coated substrate.

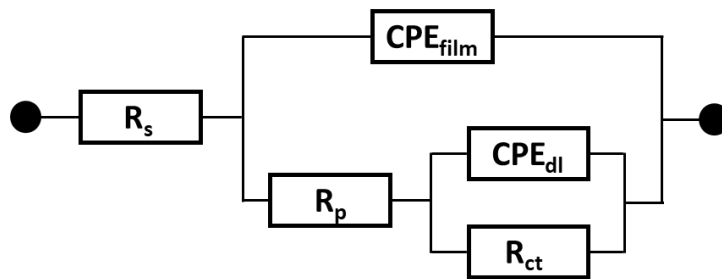


**Figure 6.34.** Equivalent circuit for the fitting of EIS data.

The simulated equivalent circuit parameters for iron with and without agar hydrogel film at different immersion times in m-SBF solution are presented in Table 6.10a, 6.10b. The presence of the hydrogel film leads to a higher electrolyte resistance. In agreement with Figure 6.33, the  $R_{ct}$  values indicate slightly higher corrosion current densities in comparison to the film without applied agar film.

**Table 6.10** Equivalent circuit parameters of iron **a**) without and **b**) with agar hydrogel film after different immersion times in *m*-SBF at 37 °C.**a) Without agar film**

Time (h)	R <sub>s</sub> (Ω cm <sup>2</sup> )	R <sub>ct</sub> (Ω cm <sup>2</sup> )	R <sub>p</sub> (Ω cm <sup>2</sup> )	CPE <sub>film</sub> (μSs <sup>n</sup> /cm <sup>2</sup> )	n <sub>1</sub>	CPE <sub>dl</sub> (μSs <sup>n</sup> /cm <sup>2</sup> )	n <sub>2</sub>	Goodness
<b>0</b>	51.1	6626.7	394.9	287.8	0.84	12.3	0.93	4.1 x 10 <sup>-4</sup>
<b>1</b>	48.4	6058.9	252.8	246.8	0.87	84.9	0.72	3.6 x 10 <sup>-4</sup>
<b>3</b>	45.5	5943.4	500.1	368.2	0.85	100.6	0.37	5.3 x 10 <sup>-4</sup>
<b>6</b>	45.1	799.8	257.8	238.3	0.85	401.7	0.54	4.1 x 10 <sup>-4</sup>
<b>12</b>	45.7	898.3	291.8	248.6	0.85	403.9	0.47	3.5 x 10 <sup>-4</sup>
<b>24</b>	45.1	1652.0	304.0	188.6	0.85	151.7	0.39	4.3 x 10 <sup>-4</sup>

**b) With the applied agar film**

Time (h)	R <sub>s</sub> (Ω cm <sup>2</sup> )	R <sub>ct</sub> (Ω cm <sup>2</sup> )	R <sub>p</sub> (Ω cm <sup>2</sup> )	CPE <sub>film</sub> (μSs <sup>n</sup> /cm <sup>2</sup> )	n <sub>1</sub>	CPE <sub>dl</sub> (μSs <sup>n</sup> /cm <sup>2</sup> )	n <sub>2</sub>	Goodness
<b>0</b>	86.4	2475.8	300.7	416.8	0.85	139.8	0.92	3.7 x 10 <sup>-4</sup>
<b>1</b>	81.5	630.0	164.2	261.9	0.83	432.1	0.67	2.9 x 10 <sup>-4</sup>
<b>3</b>	78.6	513.9	115.1	280.3	0.83	541.2	0.62	3.1 x 10 <sup>-4</sup>
<b>6</b>	77.6	556.2	136.0	252.4	0.84	601.7	0.61	2.9 x 10 <sup>-4</sup>
<b>12</b>	77.6	596.3	196.7	233.1	0.85	525.7	0.66	2.9 x 10 <sup>-4</sup>
<b>24</b>	73.7	608.9	208.7	247.6	0.83	874.0	0.71	3.0 x 10 <sup>-4</sup>

### 6.3.3.2 ATR-FTIR spectroscopy of electrolyte uptake in hydrogel films

For an improved understanding of the transport properties of the agar film, in-situ FTIR-ATR studies were performed. The agar film was applied to a Si-ATR crystal in the same way as for the iron samples. Figure 6.35 shows the absorption spectrum of the agar film.

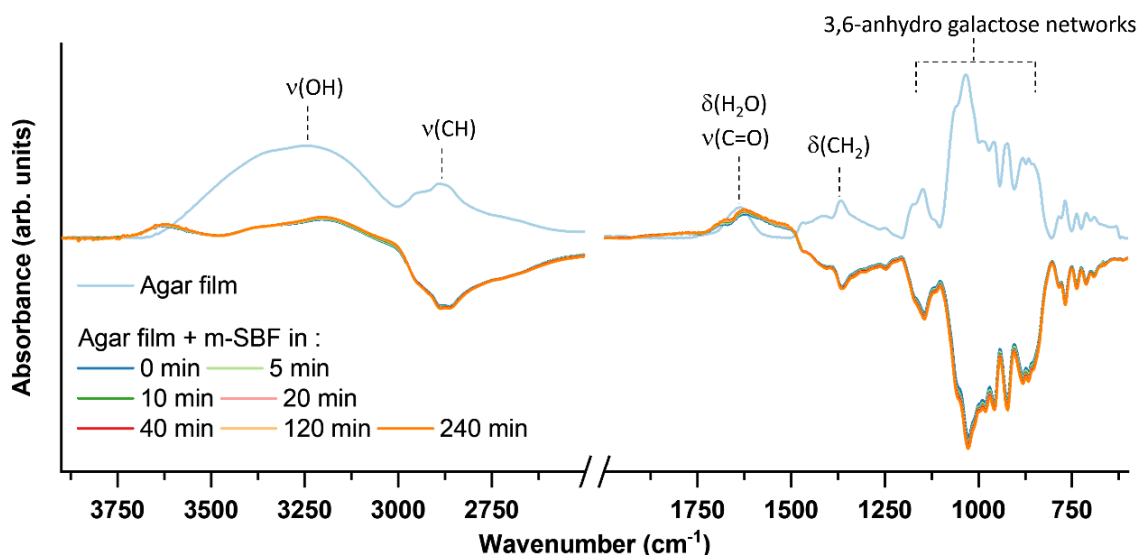


**Figure 6.35** *In-situ* ATR-FTIR spectra of the swelling process of the agar film in m-SBF at 25 °C. The spectrum of agar film is the differential spectrum with blank Si-ATR crystal. The difference spectra developed over time are referenced to the agar film spectrum.

The characteristic bands of agar are consistent with those reported in the literature. The adsorption band of agar at around 3230 cm<sup>-1</sup> and 2890 cm<sup>-1</sup> is attributed to the stretching vibration of -OH and -CH, respectively [262]. The band at about 1635 cm<sup>-1</sup> is assigned to the stretching mode of -C=O and also the absorption band of H<sub>2</sub>O [263]. The peaks between 880 and 1150 cm<sup>-1</sup> are typical vibrations of the 3,6-anhydro-galactose networks [262].

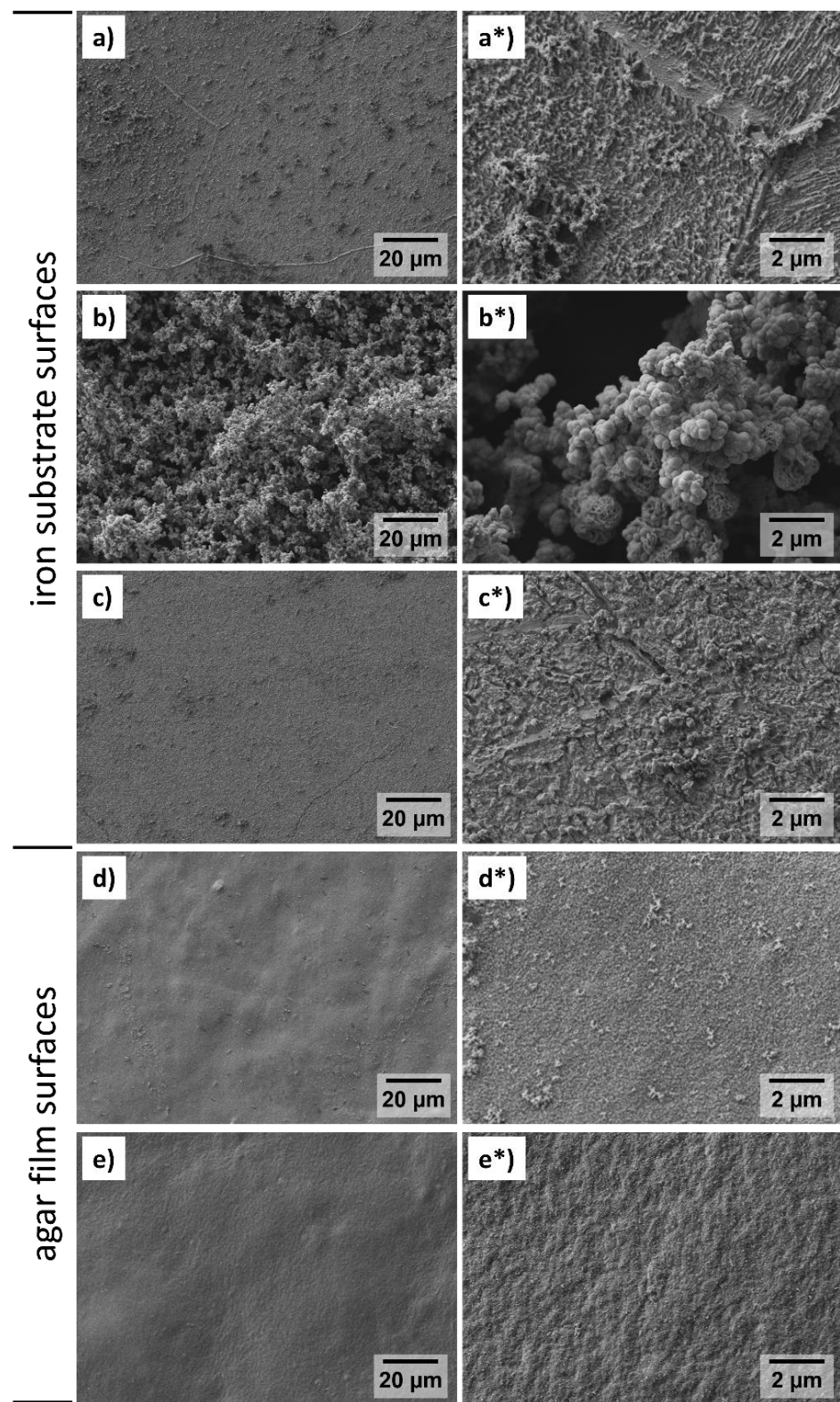
The difference spectra after the exposure of the agar film to m-SBF are given in Figure 6.35. Positive absorption bands were observed only in the -OH stretching and H<sub>2</sub>O absorption region. It is known that agar can reach 160% swelling at room temperature within 12 hours [264]. The difference spectra indicate that the m-SBF electrolyte rapidly penetrates the agar film and does not influence the incubation time. It is assumed that the applied agar film does not only act as a barrier but that the interfacial interaction with the oxide influences the stability of the passive film.

### 6.3.3.3 FE-SEM characterization of interface after exposure to m-SBF

After the immersion in m-SBF over 24 hours, both samples were analysed by means of microscopic and spectroscopic techniques. The agar film was peeled off the substrate prior to this characterization. Samples without agar films were just rinsed with pure water and blown dry with nitrogen to remove loosely bound corrosion products. For comparison, the removed agar film was analysed regarding its interface to the iron sample and the interface to the m-SBF.

The FE-SEM images of the corroded samples with and without agar film are shown in Figure 6.36. Obviously, the iron sample with applied agar film shows significantly fewer corrosion products in comparison to the iron surface which was in direct contact with m-SBF. However, as shown in Figure 6.36 corrosion products formed at the interface between the agar film and iron were partly transferred to the underside of the agar film.

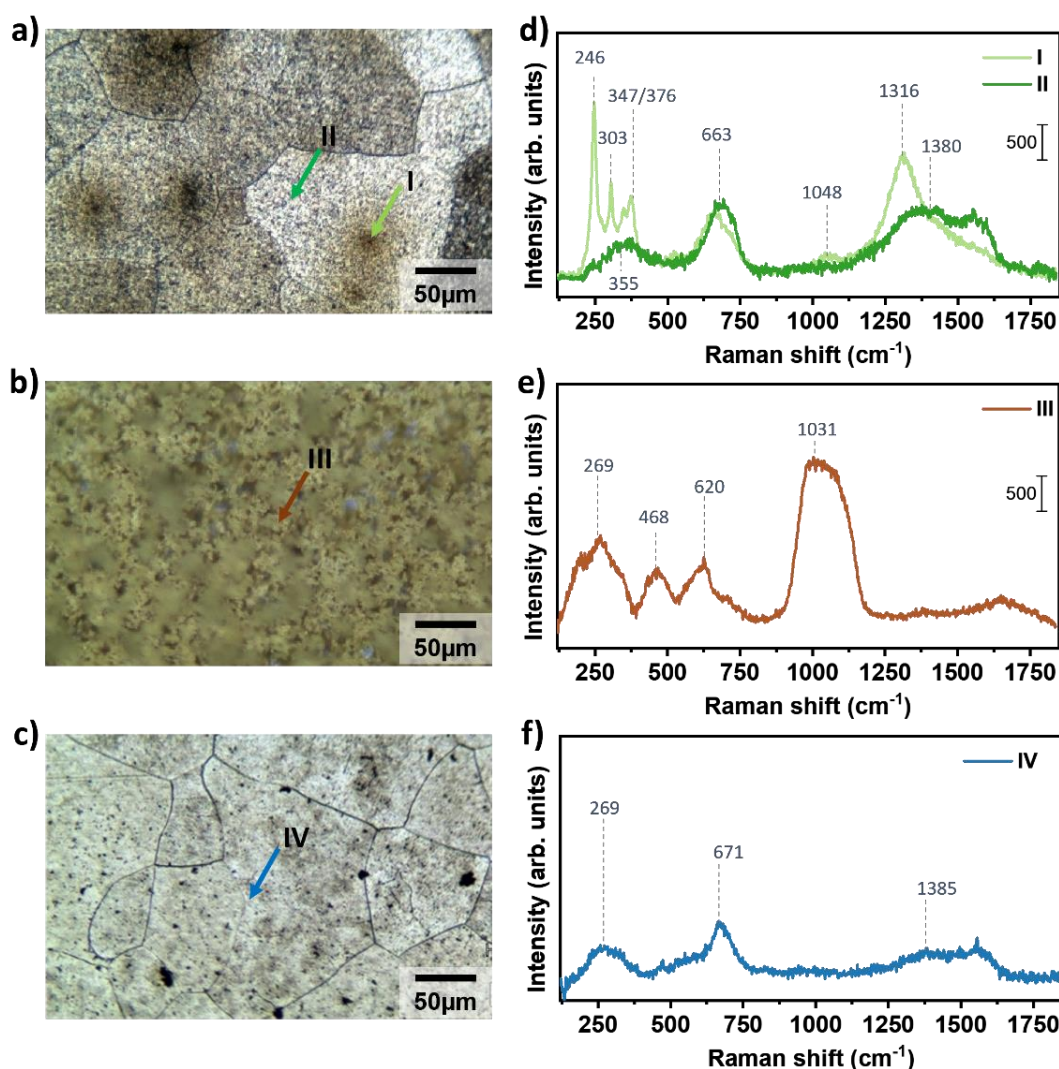
The thick layer of corrosion products on the surface of the sample directly exposed to the m-SBF was however only weakly binding to the iron surface and easily washed off. The resulting surface (see Figure 6.36c) rather resembles that already discussed in Figure 6.36a. This means that the corrosion product layer formation is not completely inhibited by the agar film but the transfer of released ions into the adhering agar film prevents the formation of thicker oxide scales at the iron interface. This assumption is supported by the FE-SEM image of the outer surface of the agar film (see Figure 6.36d) which indicates the formation of insoluble corrosion products.



**Figure 6.36** FE-SEM images of iron substrate and agar film surfaces: iron substrate after immersion in *m*-SBF for 24h with (a) and without (b) applied agar hydrogel film; FE-SEM image of the iron sample shown in (b) after mechanical removal of the corrosion product layer (c); FE-SEM images of the agar film after removal from the corroded iron sample (*m*-SBF/agar interface to the electrolyte (d), agar/Fe interface to iron (e) of the agar film. The corresponding high-resolution images are shown on the right (\*).

### 6.3.3.4 Raman spectroscopy and microscopic characterization

Microscopic images and Raman spectra on different sites of both samples are shown in Figure 6.37. The observed Raman bands and assignments are listed in Table 6.11. Raman measurements of the different areas proved the assumption that the agar film mainly influenced the distribution and amount of formed corrosion products. The chemical composition, however, remained rather unaffected. In both cases, the Raman peaks of the surface layer were assigned to a mixture of hematite, maghemite, and magnetite [247,265]. In addition, signals of phosphate at around  $1040\text{ cm}^{-1}$  were detected on the surface of samples with and without agar hydrogel [266]. The signal of phosphate was prominent for the samples without applied agar films.

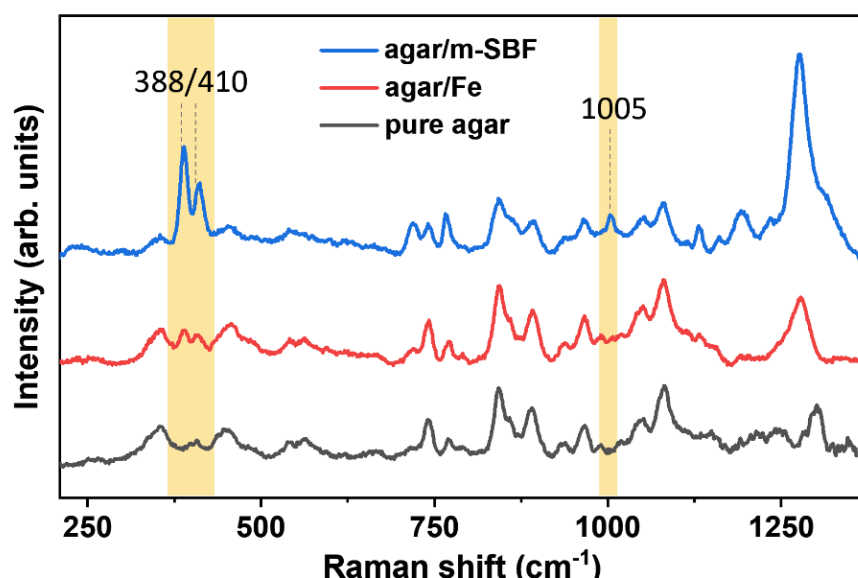


**Figure 6.37.** Microscopic image (left) and Raman spectra on labelled site (right) of iron substrate surfaces: after immersion in m-SBF for 24h with (a, d) and without (b, e) applied agar hydrogel film; iron substrate surface of the sample shown in b) after mechanical removal of the corrosion product layer (c, f).

**Table 6.11** Raman data of iron with and without agar after 24 hour exposure to m-SBF as measured on the iron substrate surface.

Raman shift (cm <sup>-1</sup> )				Assignment [247,265,266]	
with applied agar film		bare iron			
I	II	III	IV		
246	-	-	-	Hematite	
-	-	269	269	Magnetite	
303	-	-	-	Hematite	
347	355	-	-	Maghemite	
376	-	-	-	Maghemite	
	-	468	-	Hematite	
	-	620	-	Hematite	
663	663	-	671	Magnetite	
1048	-	1031	-	Phosphates/apatite	
1316	-	-	-	Hematite	
	1380	-	1385	Maghemite	

Raman spectroscopic analysis of the agar film as shown in Figure 6.38 support the interpretation of the FE-SEM results as peaks which can be assigned to iron oxides and more specifically to  $\alpha$ -FeOOH (388/410 cm<sup>-1</sup>) [247] and phosphates (about 1005 cm<sup>-1</sup>) [266] were mainly observed on the outer surface of the agar film.

**Figure 6.38** Raman spectroscopic data of the agar film interfaces after the corrosive exposure of the agar film coated iron in m-SBF in comparison to a freshly prepared agar film.

### 6.3.3.5 DRIFT-FTIR spectroscopy

The samples after removal of the agar film and corrosion product layer were characterized using DRIFT and the results are shown in Figure 6.39.

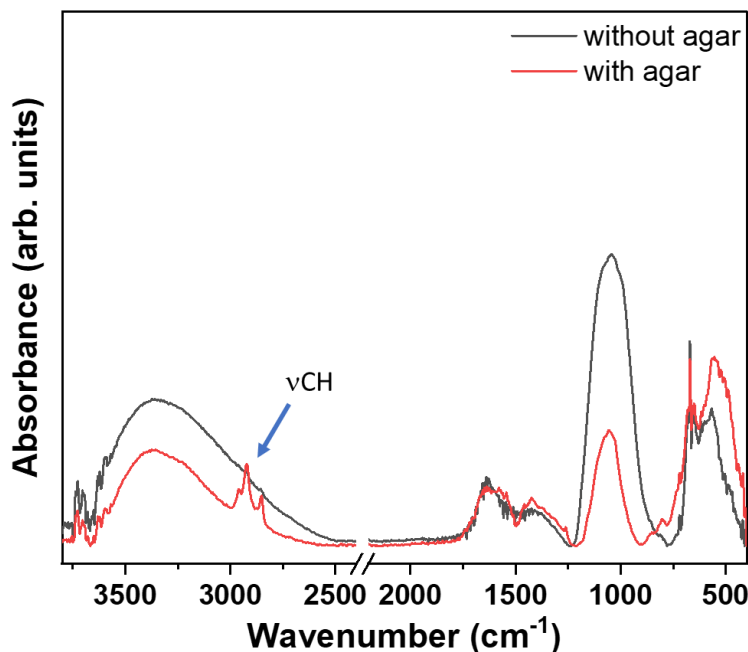


**Figure 6.39** DRIFT-FTIR spectra of samples with removed agar film and surface degradation layer. The polished pure iron is used as a reference.

The sample with the applied agar film shows peaks between 2800 and 2900  $\text{cm}^{-1}$  that are assigned to C-H stretching vibrations after the removal of the film (see Figure 6.39). This could be residual agar molecules. On the other hand, the samples without applied agar film did not show peaks in that region, but a strong signal around 1000  $\text{cm}^{-1}$  was observed, which is attributed to the presence of phosphates.

### 6.3.3.6 XPS characterization

XPS was performed for further characterization of the interface chemistry of the iron samples after exposure to m-SBF. Table 6.12 shows the calculated atomic concentration for the m-SBF/Fe and the m-SBF/hydrogel/Fe interface, i.e., the corroded surface with and without agar film, respectively. The just polished iron surface was used as a reference.

**Table 6.12.** Surface elemental composition (at. %) of the relevant interfaces determined by XPS after 24 hour immersion in m-SBF.

Interface	Atomic percentages (at-%)								
	O1s	C1s	Fe2p	N1s	Ca2p	P2p	Na1s	S2p	Si2p
Iron substrate surfaces	polished Fe	49.5	32.9	15.0	2.6	-	-	-	-
	Corrosion product layer m-SBF/Fe	55.2	19.4	3.6	1.1	6.3	13.9	0.5	-
	m-SBF/Fe after removal of corrosion product layer	48.2	35.1	14.7	0.7	-	-	-	1.3
	m-SBF/agar/Fe after removal of the agar film	48.4	42.0	8.8	0.8	-	-	-	-
Interfaces of the agar film	m-SBF/agar interface to the electrolyte	42.6	45.6	2.0	1.4	2.3	4.9	0.5	-
	agar/Fe interface to iron	32.7	62.2	0.5	1.4	0.7	1.3	0.4	-

The surface layer compositions indicate that residues of agar remained on the Fe-surface after the removal of the film. This conclusion is mainly based on the C1s contribution for the m-SBF/agar/Fe sample measured on the iron interface and the FTIR-data of the corresponding surfaces shown in Figure 6.39. The samples in direct contact with m-SBF formed a phosphate-rich layer of corrosion products on the surface (see Table 6.12). Interestingly, higher iron concentrations were detected on the outer surface of the agar film (m-SBF/agar) compared to the inner surface in contact with the iron (agar/Fe). In addition, the phosphate concentration at the agar interface was measured to be higher in the case of the m-SBF/agar interface. Both results are in excellent agreement with FE-SEM and Raman data shown in Figure 6.36d and Figure 6.37a. It can be assumed that iron ions can diffuse through the agar film, while the oxidic iron species or phosphates formed remain on the surface of the agar film.

#### 6.3.4. Conclusions

Surface corrosion studies indicate that the applied agar films prevent the formation of corrosion product layers at the electrolyte/iron interface. While the interfacial corrosion kinetics at extended times of immersion are not significantly affected by the agar film as measured by EIS. Combined Raman, XPS and FE-SEM data show that the applied agar film leads to the transport of released metal ions into the swollen hydrogel film. This process leads to the formation of phosphates and iron oxides within the hydrogel film and at the electrolyte/agar interface.

The comparison of the EIS studies and *in situ* FTIR measurements indeed showed that the kinetics of electrolyte transport in the agar film is very fast, which promotes the transfer of dissolved iron into the agar film. Overall, the studies in this section show that the application of agar as a hydrogel film on alloy surfaces for the study of corrosion in physiological electrolytes may affect the interfacial reaction and the formation of interfacial corrosion products. This influence is based on both the macromolecular adsorption and the transfer of dissolved metal ions into the hydrogel film.

## 6.4 Corrosion of pure iron in human serum

This section of the study focuses on investigating the corrosion behavior of pure iron in a human serum solution.

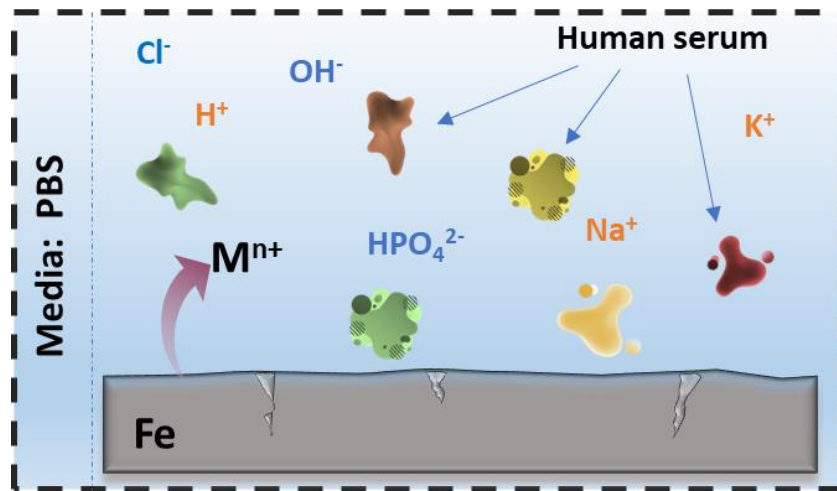


**Figure 6.40** The sketch overviews the main content of section 6.4. In this section, the corrosion behavior of iron in the presence of human serum in physiological solutions was investigated.

In the context of Fe-based materials, it has been demonstrated that alloying and additive manufacturing processes can modify the microstructure, resulting in an increased corrosion rate. However, the interpretation of these effects is often hindered by the intricate interfacial reactions occurring within the physiological environment [31,81].

The evaluation of promising Fe-based alloys is mostly carried out in pseudo-physiological solutions such as SBF, which is often the first step in in-vitro testing [267]. Nevertheless, the various media found in the human body are more complex and contain a variety of biomolecules, especially proteins. Adsorption of proteins is considered to be the first step that happens after the implant is implanted in the body, and it further affects the corrosion properties of metal materials [132]. Therefore, proteins are often added to the media used in the in-vitro testing of metallic implant materials. The most widely used model protein in this regard is serum albumin, as it is the most abundant protein class found in plasma [268]. However, using only serum albumin to assess the corrosion behavior of metals in the physiological environment is usually not sufficient, and several studies have reported differences in the influence of different protein species on the corrosion properties of metallic materials. Kocjan et al. reported the corrosion behavior of pure iron in Hank's solution containing either albumin,  $\gamma$ -globulin, fibrinogen or transferrin and observed different effects of particular proteins on iron dissolution [141]. Hedberg et al. investigated

the effect of different proteins and protein mixtures on metal release from stainless steel and found that the total amount of released metal is greater in protein mixtures than in the presence of a single protein species [142]. The reporting work in section 6.2 also shows that BSA and lysozyme have an opposite effect on the corrosion behavior of iron and iron alloys [31]. While comparing the effects of different protein species individually certainly helps to understand the possible interaction mechanisms between proteins and metal surfaces, in reality, the abundant proteins in body fluids interact competitively with material surfaces, resulting in rather complex phenomena. Therefore, in this work, the corrosion behavior of pure iron was assessed in contact with human serum as one of the most relevant bodily fluids in the context of bioresorbable implants.

### 6.4.1. Materials and chemicals

The high purity ARMCO® iron sheet (Purity P99.97%) used in the work of this section was produced by hot rolling. The samples were cut into plates of dimensions 20mm (length) x 20mm (width) x 5mm (thickness).

PBS was used in this study as a model electrolyte, and the preparation procedure can be found in Section 5.1.

For the preparation of multi-protein solutions, human serum from male AB clotted whole blood (HS, Sigma-Aldrich, H5667) was diluted in PBS to a volume ratio of 0.1%, 1% and 10%, respectively. All protein-containing solutions were freshly prepared.

### 6.4.2. Experimental approach

#### 6.4.2.1 Sample preparation

Mechanical polishing was carried out on the pure iron samples following the procedure detailed in Section 5.4. Prior to exposure to the electrolyte, the polished samples were etched in 5% Nital solution for 5s and then immediately rinsed with ethanol and dried with nitrogen. Fresh preparation of pure iron samples was conducted before each experiment.

#### 6.4.2.2 Electrochemical measurements

EIS was carried out in a three-electrode cell using a Reference 600 potentiostat. A platinum plate was used as a counter electrode and Ag/AgCl (sat. 3M KCl) was used as a reference electrode. EIS measurements were performed with an amplitude of 20 mV at OCP in the frequency range of 0.1–100000 Hz with 10 points per decade. The EIS spectra were recorded continuously at 37 °C for 24 hours.

#### 6.4.2.3 Surface characterization

Surface characterization after corrosion in HS solution was carried out by FE-SEM, EDX, Raman spectroscopy, XPS and FT-IRRAS. The experimental methods are described in detail in Chapter 5.

#### 6.4.3. Results and discussion

##### 6.4.3.1 Electrochemical measurement results

The effect of complex protein solutions with different HS concentrations on the corrosion behavior of Fe in PBS was investigated by electrochemical analyses. Prior to electrolyte exposure, all samples were etched in 5% Nital for 5 s. Figure 6.41 shows the development of the open circuit potential of Fe with time. The potential behavior of Fe in PBS appears to be independent of the HS concentration. The initial potential is more positive due to the presence of the existing natural oxide film on the surface. In all of the studied solutions, a steady-state value of around  $-0.7$  V<sub>Ag/AgCl</sub> was attained after 1 hour of incubation. The presence of HS proteins had no significant effect on the anodic and cathodic reactions in the interface.

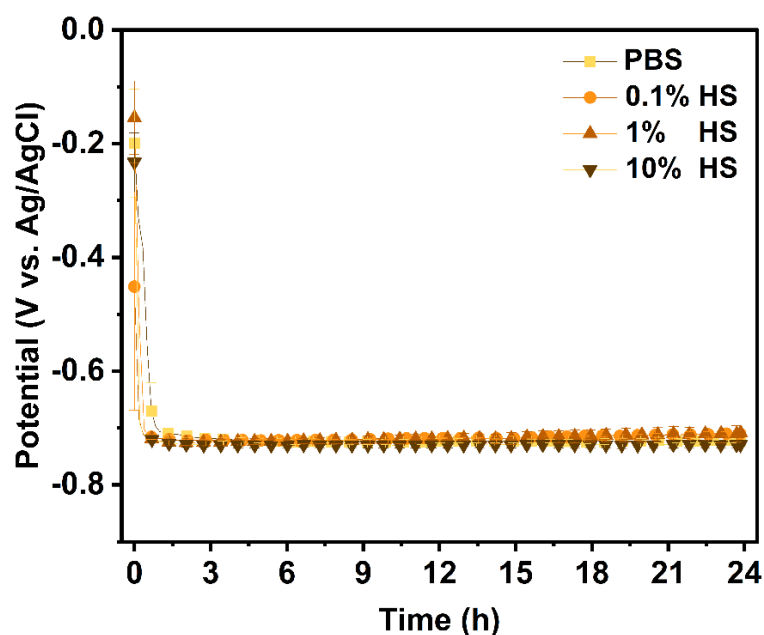


**Figure 6.41** Open circuit potential (OCP) of Fe in PBS, 0.1 % HS, 1% HS, and 10% HS at 37°C for 24 hours. Error bars indicate the standard deviations of three measurements.

The impedance spectroscopy results of Fe in PBS and in solutions with different HS concentrations are expressed in bode plots and shown in Figure 6.42a-d, respectively.

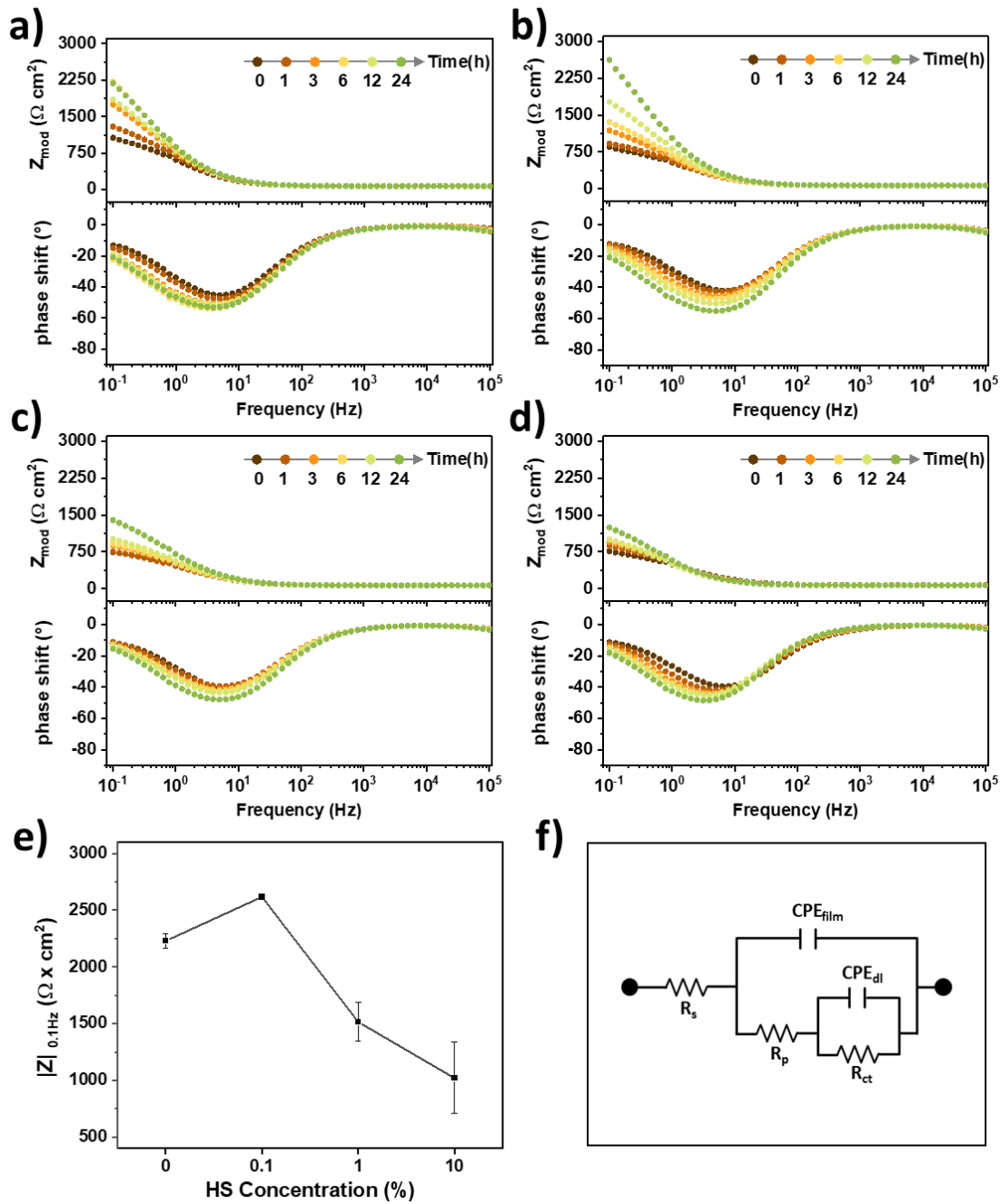


**Figure 6.42.** Bode plots of Fe incubated in **a)** PBS, **b)** 0.1 % HS, **c)** 1% HS, and **d)** 10% HS at 37°C for 24 hours. **e)** Impedance values at 0.1 Hz for Fe immersed in different HS concentrations after 24 hours. Error bars indicate the standard deviations of three measurements. **f)** Equivalent circuit for film formation.

Fe samples show only one time constant for all HS concentrations. The impedance values in the low frequency region allow for a rough assessment of the resistance behavior of the surface. Figure 6.42a-d shows that the low-frequency impedance value of the iron sample increases with time, which is an indication for the formation of a corrosion layer. The increase in maximum phase angle also indicates an overall decrease in corrosion rate with time. Figure 6.42e shows the low-frequency impedance modulus  $|Z|$  of the Fe samples at

0.1 Hz after 24 hours of exposure to the different solutions. The results show that the corrosion stability of Fe is highest at 0.1% HS. In addition, the impedance at low frequency after 24 hours of immersion is significantly lower at HS concentrations greater than 1%. This counterintuitive behavior may be caused by different compositions of the adsorbed multi-protein film modulating the inhibitive effect of the corrosion layer [269,270].

An equivalent circuit as shown in Figure 6.42f is created to further evaluate the corrosion mechanism, which includes the solution resistance ( $R_s$ ), the charge transfer resistance ( $R_{ct}$ ) and the resistance of the formed layer ( $R_f$ ). Constant phase element (CPE) is used to describe the nonideal behavior due to surface heterogeneity. The data was processed with Echem Analyst software (Gamey Instruments) and the results are listed in Table 6.13. The value of  $R_{ct}$  shows a consistent trend with the low frequency impedance data, i.e., it increases with immersion time. After 24 hours, 0.1%HS shows the highest  $R_{ct}$  ( $2035 \Omega \text{ cm}^{-2}$ ), while the lowest value is obtained for 10% HS ( $1391 \Omega \text{ cm}^{-2}$ ). Here it can be assumed that the interaction of the proteins with the surface of the Fe samples affects the charge transfer process. The species and relative amounts of adsorbed proteins may therefore lead to a differentiation of the surface layer. However, it should be mentioned that HS contains also a number of other molecular species, including various ions, carbohydrates, triglyceride, and cholesterol, which may also contribute to this effect. Rather than affecting the temporal inhibition process, the addition of HS to PBS appears to affect the passivation performance of forming adsorbate film and thus the rate of metal ion release from the surface into the electrolyte.

In summary, the similarities in the Bode plots and OCP values indicate a similar corrosion mechanism for all HS concentrations. The surface barrier accumulates over time but the protective properties of the passivated film are influenced by the HS concentration. This is most likely due to the differences in the composition of the formed corrosion layers.

**Table 6.13** The evolution of fitted result of electrochemical impedance spectra of Fe in different media.

Sample	Time (h)	$R_s$ ( $\Omega \text{ cm}^2$ )	$R_{ct}$ ( $\Omega \text{ cm}^2$ )	$R_p$ ( $\Omega \text{ cm}^2$ )	CPE <sub>film</sub> ( $\mu\text{Ss}^n/\text{cm}^2$ )	$n_1$	CPE <sub>dl</sub> ( $\mu\text{Ss}^n/\text{cm}^2$ )	$n_2$	Goodness
<b>PBS</b>	0.25	72	670	835	206	0.8	950	0.5	$1.4 \times 10^{-4}$
	0.5	72	693	842	206	0.8	976	0.5	$1.3 \times 10^{-4}$
	1	71	971	628	197	0.8	630	0.4	$1.3 \times 10^{-4}$
	3	70	1468	751	193	0.8	375	0.5	$1.8 \times 10^{-4}$
	6	70	2176	889	183	0.8	270	0.5	$2.1 \times 10^{-4}$
	12	70	1261	976	198	0.8	383	0.6	$2.6 \times 10^{-4}$
	24	70	1786	1002	175	0.8	288	0.6	$3.4 \times 10^{-4}$
<b>0.1% HS</b>	0.25	66	527	535	234	0.8	1377	0.4	$2.6 \times 10^{-4}$
	0.5	66	564	521	241	0.8	1033	0.4	$2.7 \times 10^{-4}$
	1	66	826	283	232	0.8	499	0.6	$2.6 \times 10^{-4}$
	3	67	848	539	220	0.8	512	0.3	$2.7 \times 10^{-4}$
	6	67	1191	501	204	0.8	383	0.3	$2.9 \times 10^{-4}$
	12	70	1327	782	176	0.8	332	0.2	$3.8 \times 10^{-4}$
	24	66	2035	1202	144	0.8	252	0.2	$4.9 \times 10^{-4}$
<b>1% HS</b>	0.25	66	341	395	296	0.8	1631	0.4	$1.5 \times 10^{-4}$
	0.5	66	205	488	303	0.8	1554	0.8	$1.9 \times 10^{-4}$
	1	66	430	378	288	0.8	958	0.5	$1.6 \times 10^{-4}$
	3	67	766	243	254	0.8	453	0.4	$1.5 \times 10^{-4}$
	6	67	891	212	248	0.8	435	0.4	$1.5 \times 10^{-4}$
	12	66	951	207	200	0.8	363	0.5	$1.7 \times 10^{-4}$
	24	66	1437	219	142	0.8	274	0.5	$2.1 \times 10^{-4}$
<b>10% HS</b>	0.25	70	541	516	262	0.8	1292	0.4	$1.2 \times 10^{-4}$
	0.5	70	530	571	269	0.8	1460	0.4	$1.0 \times 10^{-4}$
	1	69	613	412	270	0.8	852	0.4	$0.9 \times 10^{-4}$
	3	68	927	291	286	0.8	508	0.3	$1.1 \times 10^{-4}$
	6	69	1021	275	284	0.8	464	0.3	$1.4 \times 10^{-4}$
	12	69	1052	243	298	0.8	443	0.4	$1.5 \times 10^{-4}$
	24	68	1391	312	260	0.8	387	0.4	$1.6 \times 10^{-4}$

## 6.4.3.2 Surface Characterization by SEM

Figure 6.43 depicts the top-view and cross-sectional SEM images of Fe samples after 24h of immersion in PBS with different HS concentrations. SEM reveals differences in surface morphology, which agree with the electrochemical results.

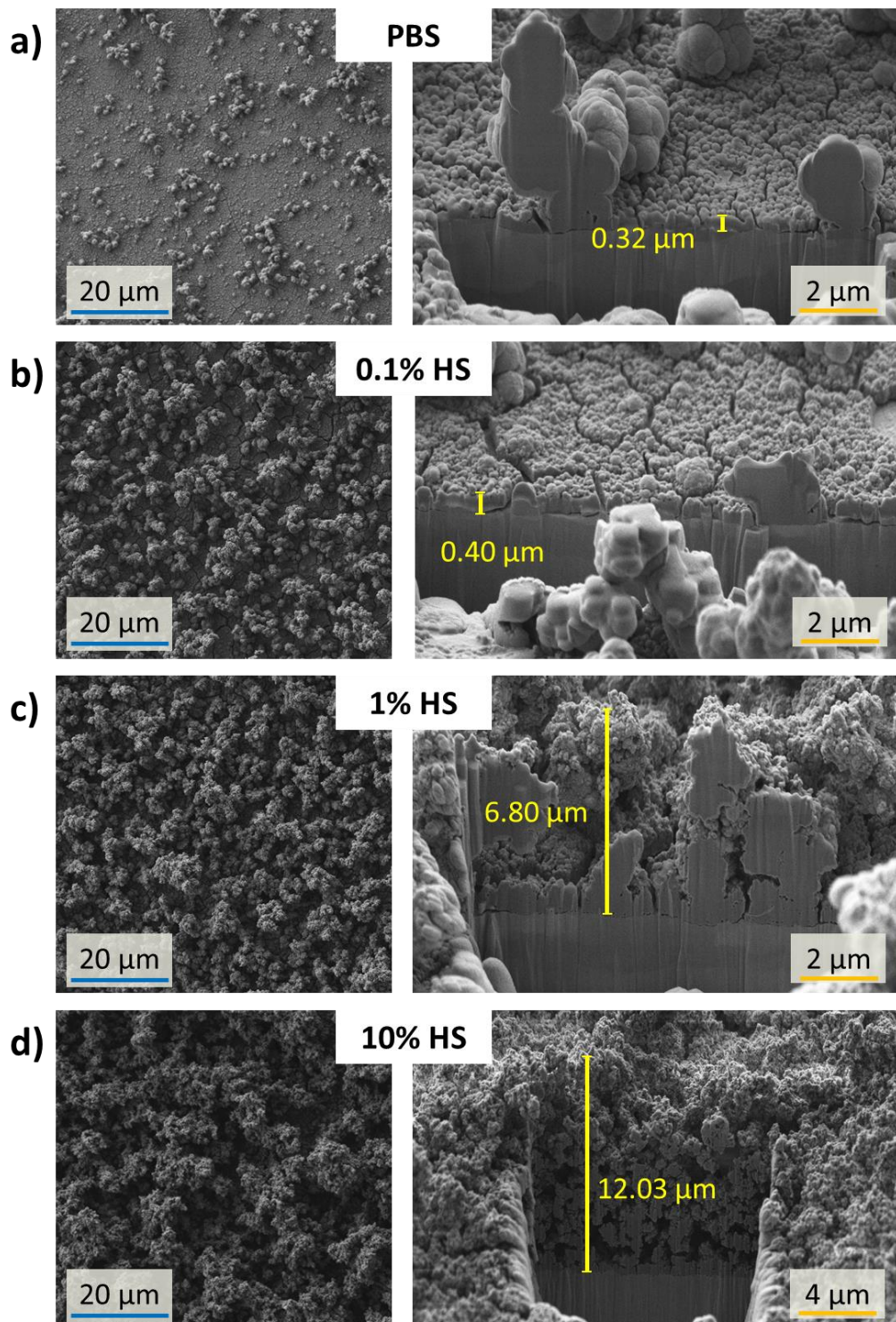


**Figure 6.43.** Top-view (left) and cross-sectional SEM images (right) of Fe after 24h immersion in **a)** PBS, **b)** 0.1% HS, **c)** 1% HS and **d)** 10% HS.

Particulate corrosion products with heterogeneous size and low surface coverage can be observed on the corroded Fe surface exposed to PBS (Figure 6.43a). In addition to this, a relatively dense surface layer with a thickness of about  $0.32\text{ }\mu\text{m}$  is observed below the larger particulates. This dense layer shows cracks due to surface dehydration. Such a dense layer can also be observed at 0.1% HS, on top of which significantly more particles are found. The thickness of the dense layer increases slightly to  $0.40\text{ }\mu\text{m}$ . The surface shows a flocculent morphology compared to PBS exposure, which is considered to be the formation layer with embedded protein molecules. The structure of the dense layer is hardly visible when the HS concentration is increased to 1%, and the same is true for 10% HS. Here, the surface is completely covered with a cauliflower-like product layer and the layer thickness increases strongly to more than  $10\text{ }\mu\text{m}$ . The SEM images in Figure 6.43 thus show that the layer thickness of the forming surface layer is continuously increasing with increasing HS concentration. This continuous buildup is probably due to the incorporation of proteins and protein-complexed metal ions into the film. Nevertheless, the profiles also show that the corrosion layers formed at the highest HS concentration is defective and porous. While this may to some point be related to the drying of the samples, the electrochemical measurements (see Figure 6.42 and Table 6.13) suggest that pores are also present *in situ*, so that ions can continue to be transported through the pores from the surface into the electrolyte. This explains why the corrosion in 10% HS is stronger than in PBS, even though the corroded layer is almost 40 times thicker. In contrast, the thin but dense layer formed in PBS seems to act as a more efficient corrosion barrier.

EDX data provide information on the chemical composition of the formed layers. Figure 6.44 shows the EDX maps of Fe samples exposed to different concentrations of HS and the atomic concentrations obtained from the EDX measurements are shown in Figure 6.45. The EDX mapping results for the surface show that the O and C content increase with increasing HS concentration, which indicates that the amount of protein incorporated in the formed surface layers is increased. The content of Fe, on the other hand, decreases with increasing HS concentration.

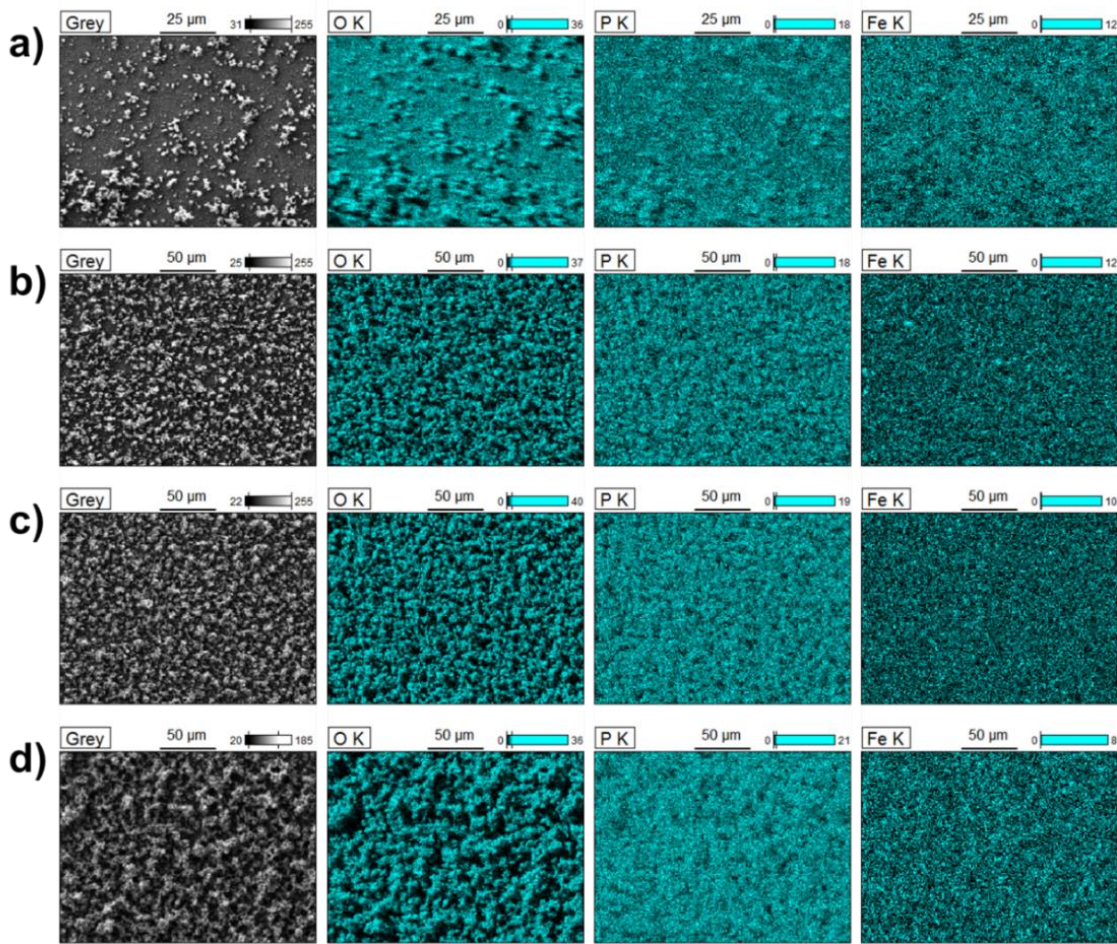


**Figure 6.44.** SEM images and EDX maps of Fe after 24h immersion in a) PBS, b) 0.1% HS, c) 1% HS and d) 10% HS.

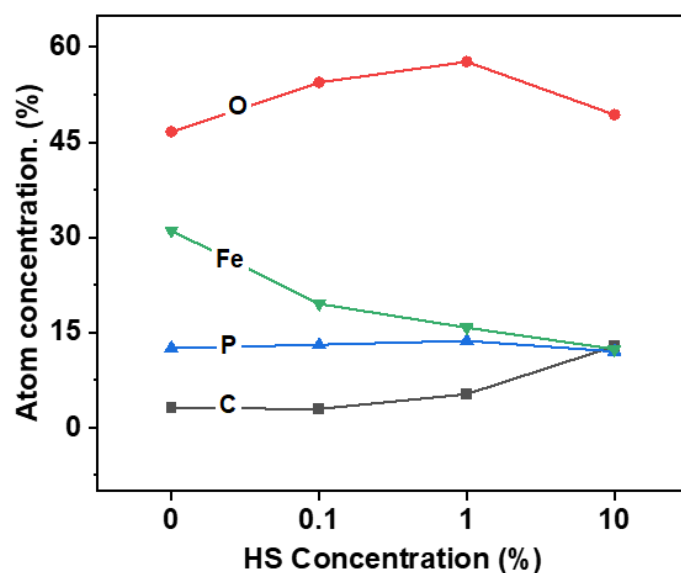


**Figure 6.45.** Atom concentration in % of Fe samples after immersion in PBS, 0.1% HS, 1% HS and 10% HS as measured by EDX mapping.

#### 6.4.3.3 Raman spectroscopy and FT-IRRAS

The Raman spectra of the sample surfaces are shown in Figure 6.46. The assignments of the peaks are listed in Table 6.14. The Raman spectra indicate that the surface layer contains  $\text{Fe}_2\text{O}_3$ ,  $\text{Fe}(\text{OH})_3$ ,  $\text{FeOOH}$  and  $\text{FePO}_4 \cdot 2\text{H}_2\text{O}$ . The presence of iron in the form of different oxides and hydroxides in the surface corrosion product layers formed is consistent with previous studies that investigated iron-based alloys in physiological solutions [108,110,271–273].

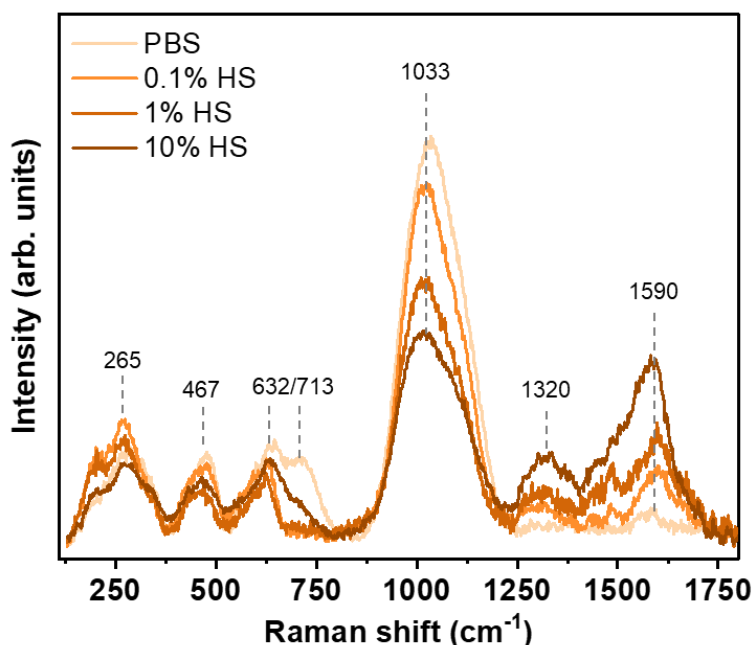


**Figure 6.46** Raman spectra of iron samples after immersion in PBS, 0.1% HS, 1% HS and 10% HS.

**Table 6.14** Raman data of the Fe samples after exposure to PBS, 0.1% HS, 1% HS and 10% HS.

Raman shift (cm <sup>-1</sup> )	Assignment [265,266,274]			
265	$\text{FePO}_4 \cdot 2\text{H}_2\text{O}$	$\text{Fe}_2\text{O}_3$	$\text{FeOOH}$	
467	$\text{FePO}_4 \cdot 2\text{H}_2\text{O}$			
632	$\text{FePO}_4 \cdot 2\text{H}_2\text{O}$	$\text{Fe}_2\text{O}_3$		$\text{Fe}_3\text{O}_4$
713		$\text{Fe}_2\text{O}_3$	$\text{FeOOH}$	$\text{Fe}(\text{OH})_3$
1033	$\text{FePO}_4 \cdot 2\text{H}_2\text{O}$			$\text{PO}_4^{2-}$
1320		$\text{Fe}_2\text{O}_3$		
1590		$\text{Fe}_2\text{O}_3$		

As shown in Figure 6.46, the shape of the Raman spectra is similar for all samples but the intensity of the peaks in specific regions different. The peak located at 1033 cm<sup>-1</sup> is attributed

mainly to phosphate and its intensity decreases with increasing HS concentration. The signal in the phosphate region is prominent and could have multiple origins [275]. Released Fe ions can form  $\text{FePO}_4 \cdot 2\text{H}_2\text{O}$ . In addition,  $\text{PO}_4^{2-}/\text{HPO}_4^-$  are readily adsorbed on the negatively charged iron oxide surface due to electrostatic interaction in the PBS environment [276]. The peaks located at  $1320\text{ cm}^{-1}$  and  $1590\text{ cm}^{-1}$  are assigned to  $\text{Fe}_2\text{O}_3$ . In contrast to the phosphate region, they increase with increasing protein concentration. In this region, contributions of various organic molecules in the serum may become important [277]. Peak intensity at  $1590\text{ cm}^{-1}$  was quantified relative to the peak intensity at  $1033\text{ cm}^{-1}$ , and the results were 8.2% (PBS), 21.6% (0.1% HS), 42.8% (1% HS) and 88.8% (10% HS), respectively. This indicates that although the overall composition of the surface layers is similar in the different environments, the addition of serum affects to some extent the formation and incorporation of iron oxides and insoluble salts.

Figure 6.47 shows the FT-IRRAS spectra of the Fe samples after 24 h exposure to PBS containing different concentrations of HS. The broad band in the range from  $900\text{ cm}^{-1}$  to  $1200\text{ cm}^{-1}$  is attributed to the contribution of  $\text{PO}_4^{3-}$  [266,278]. The broad band in this region indicates that it is mostly an amorphous structure. The phosphate band is centered around  $1010\text{ cm}^{-1}$  in the absence of plasma proteins. Upon the addition of serum, however, the peak shifts to larger wavenumbers. In the case of 10% HS it is located at around  $1100\text{ cm}^{-1}$  and exhibits a low-wavenumber shoulder.

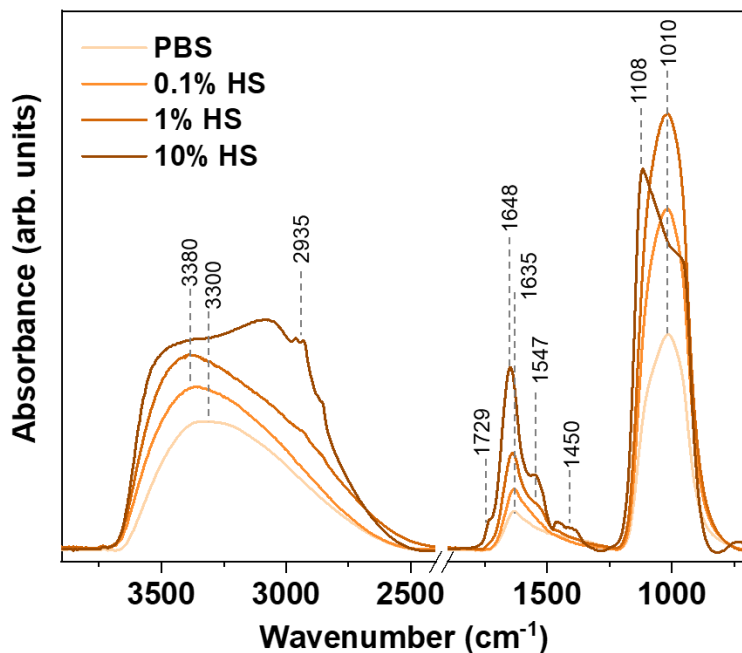


**Figure 6.47.** FT-IRRAS spectra of Fe samples after 24 h immersion in PBS, 0.1% HS, 1% HS and 10% HS.

A similar behavior has been observed for Mg alloys i.e. the phosphate band shifted with the addition of proteins [279]. The shift of the phosphate domain and the change of shape may imply the variability of the products containing phosphate groups in the layer. It was also observed that the O-H stretching band located at around  $3300\text{ cm}^{-1}$  was also slightly shifted with increasing HS concentration (see Figure 6.47).

Furthermore, Figure 6.47 shows that the spectra have typical amide bands associated with proteins located at  $1648\text{ cm}^{-1}$  for amide I and  $1547\text{ cm}^{-1}$  for amide II at HS concentrations of 1% and 10%. The characteristic amide II band was not observed in the case of 0.1% HS, probably because the amount of protein in the surface layer was too small. However, the surface exposed only to PBS also shows an absorption band at around  $1648\text{ cm}^{-1}$ , which can be attributed to residual water trapped in the surface layer. This was further verified by attenuated total reflectance Fourier transform infrared spectroscopy (ATR-FTIR) performed in PBS, which revealed notable amide I bands only for the samples exposed to 1% and 10% HS (see Figure 6.48).

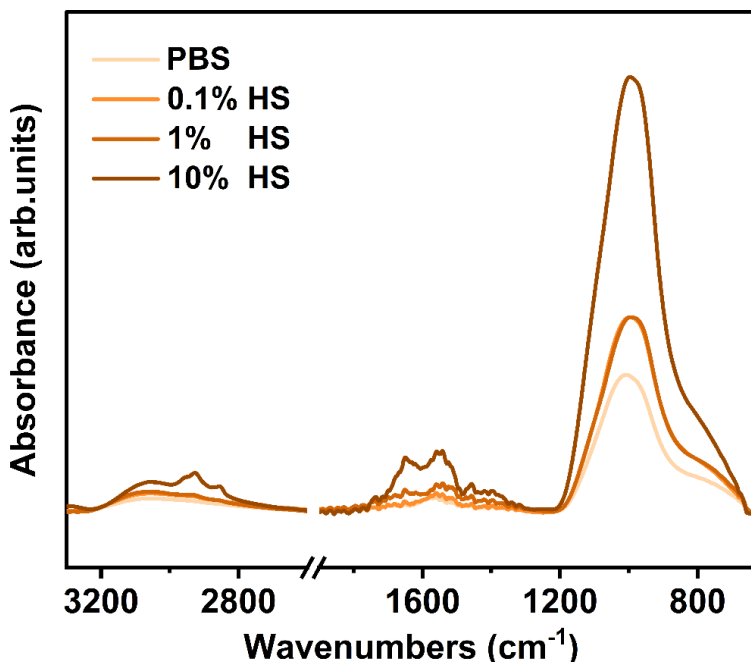


**Figure 6.48** ATR-FTIR spectra of iron after immersion in PBS, 0.1% HS, 1% HS and 10% HS.

Absorption bands located at  $2935\text{ cm}^{-1}$ ,  $1729\text{ cm}^{-1}$  and around  $1450\text{ cm}^{-1}$  (see Figure 6.48) appear only in 10% HS and thus may be contributions of organic molecules such as glucose and uric acid from the HS. The FT-IRRAS spectra therefore support the assumption that different HS concentrations likely result in different compositions of the formed surface layer.

#### 6.4.3.4 XPS analysis of iron surfaces after corrosion

XPS analysis was performed to characterize the composition of the formed surface layers on the Fe samples after immersion in PBS solutions containing different concentrations of HS. The main components of the formed surface layers are C, O, P, N, and Fe, as well as minor amounts of K and Na. The corresponding atomic concentrations are shown in Figure 6.49.

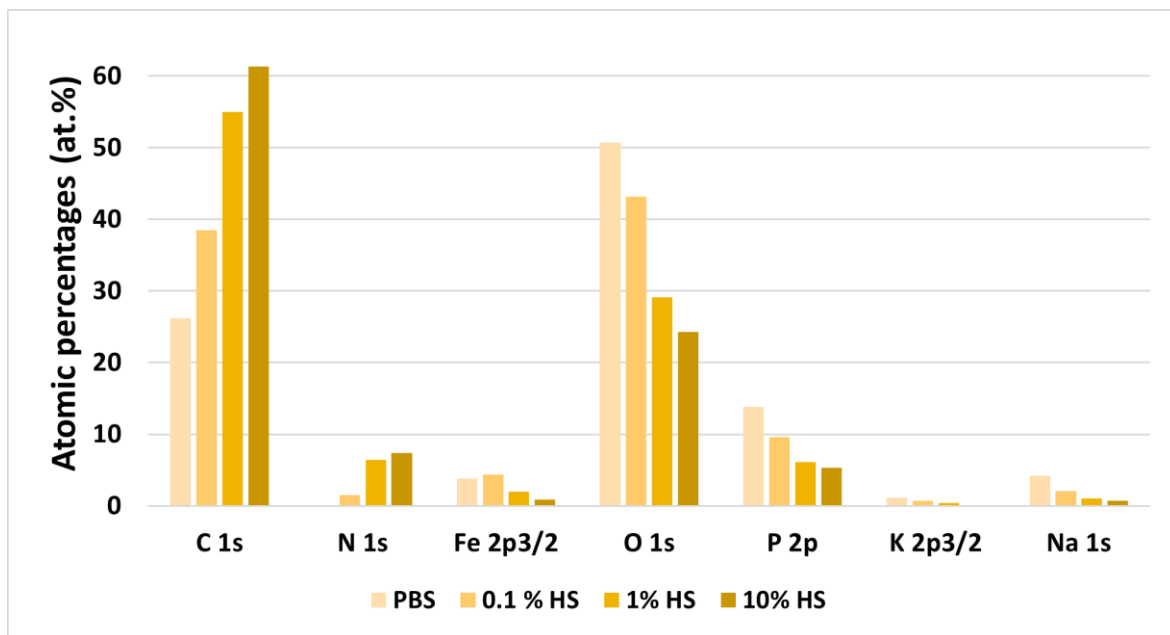


**Figure 6.49** Surface composition in at.-% measured by XPS of Fe samples after immersion in PBS and in HS at concentrations of 0.1%, 1% and 10% for 24 h.

Figure 6.49 indicates that the signals of C and N were positively correlated with HS concentrations, suggesting the presence of organic molecules like serum proteins in the surface layers. There was no N signal detected in PBS. The N content in 0.1% HS was about 1.5 at.%. When the concentration was increased to 1% the N content increased to 6.4 at.%. However, continuing to increase the HS concentration by a factor of ten, i.e., in 10% HS, the N content is approximately the same as that at 1% HS with no significant increase. The similar N contents at these high HS concentrations can be attributed to the high surface sensitivity of XPS, so that proteins buried deeper than a few nanometers in the micron-thick surface layers do not contribute to the spectra. Therefore, at plasma concentrations above 1% it is assumed that protein incorporation in surface-near region of the formed surface layer has reached a steady state. The signals of Fe, O and P decrease with increasing HS concentration, which indicates a reduction in the content of phosphate and Fe degradation products in the surface-near region of the top layer. This indicates that the increase in phosphate absorption with increasing HS concentration observed in the FT-IRRAS spectra

of Figure 6.47 is mostly related to the increasing thickness of the formed layer and not primarily to a change in the amount of incorporated phosphates.

To gain a better understanding of the surface layer characteristics formed on Fe samples after exposure in PBS solutions containing different concentrations of HS, high-resolution spectra of Fe2p, C1s, O1s and N1s were obtained, the spectra are shown in Figure 6.50.

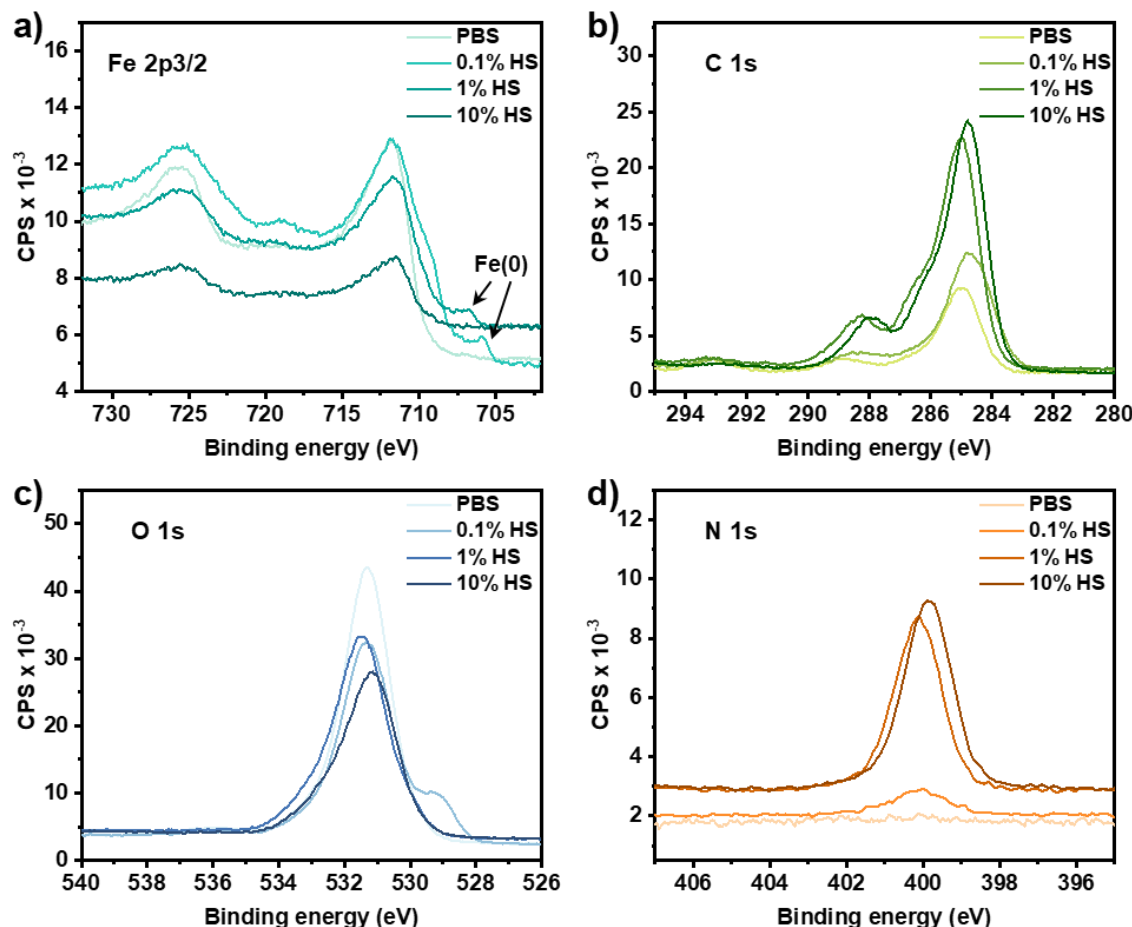


**Figure 6.50.** High resolution XPS spectra for Fe after 24h immersion in PBS and in HS at concentrations of 0.1%, 1% and 10%. **a)** Fe 2p3/2, **b)** C 1s, **c)** O 1s and **d)** N 1s.

As shown in Figure 6.50a, a characteristic asymmetric form and split spin orbit components are observed in the high-resolution spectra of Fe2p. Additionally, the contribution of the underlying metallic iron, Fe(0), is seen in the case of 0.1% and 1% HS, indicating the presence of defects in the formed surface layer.

#### 6.4.3.5 Discussion of the influence of HS on iron corrosion in PBS

In this study, electrochemical measurements were used to examine the corrosion behavior of pure iron in PBS that contained various concentrations of HS.

The addition of HS to PBS had no significant effect on the OCP values of Fe (Figure 6.41). Furthermore, the electrochemical impedance spectra of Fe in PBS containing different concentrations of HS have similar shapes (Figure 6.42). The electrochemical experiments thus showed that the addition of HS did not change the corrosion kinetics of Fe in PBS. This is further supported by the observation of similar iron degradation products in the surface layer in both the presence and absence of HS. As shown by Raman data as well as XPS, the surface layer consists mainly of iron phosphate, iron oxide, and iron hydroxide. This is consistent with the reported degradation behavior of iron-based alloys in physiological solutions [31,110,193,280]. The anodically dissolved  $\text{Fe}^{2+}$  can continue to be reduced to  $\text{Fe}^{3+}$  in the presence of oxygen. The iron ions react further with the OH produced by the cathode reaction and phosphate ions from the solution at the interface to form a variety of insoluble substances. The formation of  $\text{FeOOH}$  from hydroxide has also been reported under specific conditions [115].

Although the kinetics of iron corrosion are similar, the results of EIS clearly showed that the HS concentration had a significant effect on the corrosion behavior of Fe in PBS. The increase in low-frequency impedance with time in all cases indicates the formation of a corrosion layer. In the absence of protein, the formed surface layer is thin and compact as shown in Figure 6.43a, contributing to a high electron transfer resistance. Adsorbed proteins may be incorporated into the forming surface layer when a small amount of protein is present, but at this point metal oxides and phosphates still dominate in the corrosion layer. According to a study by Hedberg et al. [281], the concentration of BSA affects the metal release from 316L, but the effect is insignificant at low concentrations (less than 0.1g/L BSA). For the samples exposed to PBS with 0.1% HS, the dense surface layer and the large particles on top were characterized separately with EDX and Raman and the results are shown in Figure 6.51 and Table 6.15.

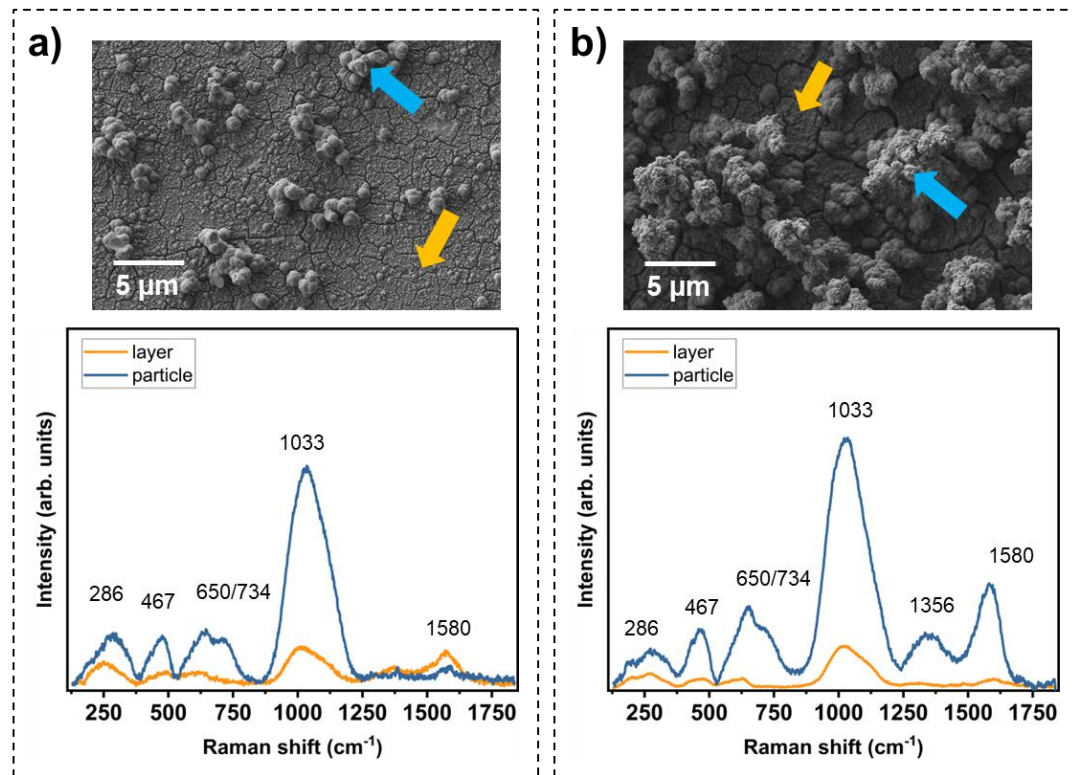


**Figure 6.51** SEM images and Raman spectra of different sites of Fe after 24h immersion in **a)** PBS and **b)** 0.1% HS. The blue arrow in the SEM images points to the surface particulate corrosion products; the yellow arrow points to the dense layer underneath.

**Table 6.15** Atomic percentages obtained by EDX (at. %).

		Elemental Composition (at. %)					
		C	O	Na	P	K	Fe
<b>PBS</b>	layer*	2.0	44.8	4.3	7.7	0.5	40.5
	particle**	2.2	60.6	4.3	14.4	1.4	16.7
<b>0.1% HS</b>	layer*	2.0	54.6	5.4	9.6	1.2	27.2
	particle**	2.9	59.0	4.8	15.1	2.1	15.2

The yellow arrow (\*) and blue arrow (\*\*) points to the area in the SEM images in Figure 6.51.

As shown in Figure 6.51, The distributed particles on top of the layer are rich in elemental phosphorus and thus probably consist mainly of phosphates. The dense layer underneath is thought to be a mixture of various iron oxides and iron hydroxides and has a higher iron content. The impedance values at 0.1 Hz after 24 h were the lowest in the case of high serum concentrations (10%HS), which suggests poor corrosion resistance (Figure 6.42e) of the much thicker surface layers obtained under those conditions (see Figure 6.42d).

High plasma protein concentrations thus cause thicker formation layers with worse protective properties. We speculate that this is related to the porous structure of the layers, which may be a result of protein-surface and protein-protein interactions. In multi-protein solutions, protein adsorption at the surface of the material is highly dynamic and competitive, a process also known as the Vroman effect [282]. Proteins with higher concentrations have a higher chance to reach the surface (e.g., albumins) and proteins with smaller sizes have faster diffusion rates, so they can rapidly occupy the surface, even though they might not have a high affinity for the surface. Proteins with greater affinity for the surface but lower concentrations (e.g., fibrinogen) may reach the surface and compete with previously adsorbed proteins for binding sites. This competition may result in conformational transitions in the different protein species and finally the desorption of already adsorbed proteins from the surface [121,282]. Typically, the winners of this competition are able to adsorb more strongly to the surface, for instance because they can more easily adjust their conformation and thereby maximize their contact area with the surface. Thus, the composition and molecular structure of the adsorbed layer is time-dependent [121]. This implies the existence of a dynamic protein layer on the material surface in a multi-protein solution. Generally, soft proteins such as albumin may become inactive after surface adsorption because they denature in the process, which reduces the number of exposed specific binding sites. This may reduce the protein's ability to bind or chelate metal ions, thus inhibiting degradation of the surface. As demonstrated in previous works, BSA has a tendency to inhibit iron corrosion at a later stage [31]. Hou et al. [279] showed that the content of Ca-P salts in the surface degradation layer of Mg increased when BSA, fibrinogen and fetal bovine serum (FBS) were added to DMEM, but Ca-P salts formation was inhibited in the protein mixtures solution. These differences indicate that it is necessary to consider protein variety when investigating the effect of proteins on metal degradation behavior.

Additionally, the Vroman effect may affect the extent of metal release. In a report by Hedberg et al [142], The authors investigated the impact of the Vroman effect on the extent of metal release and the corrosion resistance of medical-grade stainless steel in PBS. They exposed the 316L and 303 stainless steel samples to physiological concentration of BSA, fibrinogen and a mixture thereof. For type 316L, the overall metal release was enhanced in the presence of proteins compared to PBS, and the release of Fe, Cr and Ni was increased in the protein mixture. Protein-induced metal ion release produces metal-protein complexes, which may be present at the surface or in solution. The formation of complexes may reduce

the thickness of surface oxides, as at high concentration of HS, so that it is difficult to obtain a dense oxide layer.

The combined effect of protein adsorption, desorption, competition and repulsion processes at the interface under multi-protein conditions increases the interfacial activity and thus facilitates the release of metal ions. As indicated by the impedance and SEM results, the corrosion activity was higher even though the surface layer was thickened at increased HS concentrations. This may be triggered by a change in the variety of protein species interacting with the corroding surface and thus in different surface layer formation kinetics and compositions at different HS concentrations. In particular, proteins occupying active sites on the surface may slow down the formation of degradation products such as phosphate in a protein species-dependent way. In the case of low HS concentration, phosphate dominates and is more likely to adsorb quickly on the surface of the iron sample to form first a thin film and then insoluble corrosion products with the dissolved metal ions, forming a barrier on the surface.

#### 6.4.4. Conclusions

The results in this work show that Fe has similar corrosion kinetics in PBS with and without serum, but the concentration of serum has an effect on the corrosion behavior. Due to the Vroman effect, the different protein species found in HS compete for adsorption on the surface, resulting in the presence of a highly dynamic protein layer at the interface, which enhances the surface activity and subsequently affects surface electron transfer. The forming surface film inhibits the corrosion of iron mainly by reducing charge transfer. The presence of HS affected the stability and inhibition effect of the surface passivation film, with higher HS concentrations resulting in thicker surface layers but less inhibition of corrosion. For the application of Fe and its alloys as biodegradable implants, the results imply the feasibility of using human serum as *in vitro* corrosion test media, the use of a single protein may misestimate the true corrosion rate of iron-based alloys *in vivo*.

### 7 Overall conclusions and outlook

#### 7.1 Overall conclusions

The main focus of this thesis is to investigate the corrosion behavior of Fe-alloys in physiological electrolytes. It discusses the implications of the findings for the potential use of the Fe-alloy as a biodegradable implantable device. The composition and fabrication process of the alloy, as well as the microstructure of the alloy, the corrosive medium, and the type and concentration of proteins, all have varying degrees of impact on the corrosion behavior of Fe-based alloys.

Results of the study on the adsorption behavior of proteins on surfaces reveal the pH dependence of serum protein adsorption on gold and oxidized iron surfaces. AFM analysis showed that protein adsorption on the gold surface resulted in a smoother morphology, regardless of pH or serum concentration. Conversely, the iron surface did not exhibit significant morphology changes due to protein adsorption. PM-IRRAS revealed a pH dependence in the total amount of adsorbed proteins for both surfaces, with a more pronounced effect than serum concentration. Analysis of PM-IRRAS spectra indicated compositional differences in the adsorbed multiprotein films under different pH conditions. These effects were consistently observed on both surfaces, suggesting a primary influence of pH sensitivity in the adsorbing proteins. The adsorption of highly abundant proteins in serum at pH close to their isoelectric point is advantageous and can displace other proteins with lower surface affinity in multiprotein films.

The microstructure of Fe alloys manufactured by the conventional process is compared with that of additive manufacturing. SEM and EBSD provide information on the microstructure. The FeMn alloy fabricated by selective laser beam melting (FeMn-LBM) is characterized by a solidification structure resulting from the LBM process, connected to segregations of manganese. Both the larger grain size distribution and dendritic columnar structure with local enrichment of manganese are observed in the FeMn-LBM alloy compared to the conventional alloy.

The corrosion behavior of Fe alloys manufactured by the conventional process and additive manufacturing is compared. The corrosion behavior was analyzed by EIS, AFM, SEM, infrared, and Raman spectroscopy. The electrochemical impedance data clearly demonstrate that both FeMn alloys show higher corrosion rates than pure iron in all physiological

electrolyte tests, with FeMn-LBM being superior to conventional FeMn. The high corrosion rate is independent of the addition and type of protein and is determined by the properties of the alloy itself. The presented studies illustrate that the resulting corrosion rate of FeMn alloys strongly depends on their specific microstructure. Additive manufacturing allows the variation of the corrosion kinetics of FeMn-based alloys as a bioresorbable alloy based on their composition and microstructure variation.

The influence of proteins on the corrosion behavior of iron-based alloys is studied. First, two different proteins (BSA and LYZ) were added to m-SBF to evaluate the corrosion behavior of iron-based alloys in the presence of proteins and the effect of protein type on the corrosion behavior. The EIS results indicate that LYZ exhibits, on average, an inhibitive effect on corrosion, while BSA rather slightly promotes the corrosion process. It should be noted that the addition of BSA seems to attenuate the differences between the different alloys concerning their corrosion rates. The structure and morphology of the surface corrosion layer formed in the presence of different proteins differ. Studies using FTIR spectroscopy in reflection, Raman spectroscopy, AFM topographic images, and EDX show higher concentrations of phosphates in the formed surface layers in the presence of LYZ compared to surface layers formed in the presence of BSA. This formation of inorganic protective compounds likely contributes to the corrosion-inhibiting effect of LYZ in m-SBF electrolyte.

Next, Fe was exposed to different concentrations of human serum diluted in PBS to assess the effect of multi-component proteins on corrosion. Electrochemical data showed that adding HS did not change the corrosion kinetics of Fe in PBS, but the HS concentration affects the corrosion behavior. The multi-component proteins compete for adsorption on the surface, resulting in the presence of a highly dynamic protein layer at the interface, which enhances surface activity and subsequently affects surface electron transfer. The surface film formed inhibits iron corrosion mainly by reducing charge transfer. The presence of serum proteins affected the stability and inhibition of the surface passivation film, and the higher multiprotein concentration enhanced the competitive adsorption effect at the interface, which actually had less corrosion inhibition even though the surface layer was thickened.

The effect of hydrogel coating on corrosion of Fe is investigated. The previous discussion of the results has shown that corrosion kinetics of iron-based alloys are correlated with their surface film formation in physiological electrolytes. Surface corrosion studies indicate that the application of agar films prevent the formation of corrosion product layers at the

electrolyte/iron interface without affecting corrosion kinetics. Combined Raman, XPS and FE-SEM data show that the applied agar film leads to the transport of released metal ions into the swollen hydrogel film. This process leads to phosphates and iron oxides forming within the hydrogel film and at the electrolyte/agar interface.

Generally, it is evident that the corrosion and degradation of iron-based alloys in physiological electrolytes are influenced by various factors, including but not limited to the manufacturing process, alloy composition, microstructure, protein type and concentration, and the formation of the corrosion product layer. Therefore, a comprehensive consideration of these multiple factors is essential when conducting *in vitro* testing of potential biodegradable metallic implant materials.

### 7.2 Outlook

Over the past decade, researchers have been exploring the field of biodegradable materials, and it is expected that the medical applications of biodegradable metals will continue to receive attention in the foreseeable future. This work focuses on evaluating the corrosion and degradation of iron-based alloys in physiological electrolytes. The *in vitro* corrosion testing results will provide an impetus for developing ideal bioresorbable metallic materials.

The major challenge that needs to be addressed for the recognized Fe-based alloys to be used as biodegradable materials is their low corrosion rate. In this work, it can be confirmed that microstructural changes are beneficial in promoting corrosion by comparing the performance of additively manufactured and conventionally fabricated FeMn alloys in physiological electrolytes. SLM technology enables highly customizable and complex structural designs. By adjusting the laser scanning paths and parameters, precise control over the material's microstructure and surface characteristics can be achieved to meet the requirements of different applications. Therefore, advanced manufacturing techniques such as SLM offer more possibilities and new directions for the development of biodegradable materials, proving to be beneficial in the field of stent biomaterials.

Results of corrosion kinetics analysis and surface characterization indicate that the degradation rate is related to the surface film formed by corrosion, and the composition of the testing media largely influences the corrosion behavior of iron-based materials. The formation of degradation products often obscures the effects of corrosion rate changes caused by microstructure. In addition, the concentration and type of protein in the test

medium significantly affect the corrosion behavior. Among them, the addition of serum proteins to the electrolyte was used to explore the effect of multicomponent protein adsorption on corrosion behavior. The results demonstrated that the corrosion behavior of iron differs in a multicomponent protein environment compared to when only a single species protein is present. This attempt can be applied to in vitro testing of other biomaterials. So far, there is no clear standard for the selection of corrosion test media, and it is challenging to fully simulate the complexity of the in vivo environment in vitro. This is also a reason for the frequent discrepancies between in vitro and in vivo test results for the same material. Therefore, based on the findings in this work, the selection of corrosive media must be done carefully when investigating iron-based biodegradable materials. It is necessary to adjust physiological electrolytes and additional components appropriately to cater to specific application requirements and obtain a more comprehensive understanding of the corrosion behavior.

In summary, iron-based bioabsorbable materials have great attraction but also face many challenges. The influencing factors investigated in this work still have limitations. Further insights into the interaction mechanisms between iron-based materials and biological organisms are necessary, and new alloy designs as well as fabrication methods are sought to improve the material properties.

## References

- [1] Y. F. Zheng, X. N. Gu, and F. Witte, “Biodegradable metals,” *Materials Science and Engineering: R: Reports*, vol. 77, pp. 1–34, 2014.
- [2] R. Waksman, “Promise and challenges of bioabsorbable stents,” *Catheterization and cardiovascular interventions : official journal of the Society for Cardiac Angiography & Interventions*, vol. 70, no. 3, pp. 407–414, 2007.
- [3] M. M. El-Omar, G. Dangas, I. Iakovou et al., “Update on In-stent Restenosis,” *Current interventional cardiology reports*, vol. 3, no. 4, pp. 296–305, 2001.
- [4] R. Waksman, “Biodegradable stents: they do their job and disappear,” *The Journal of invasive cardiology*, vol. 18, no. 2, pp. 70–74, 2006.
- [5] R. D. Alexy and D. S. Levi, “Materials and manufacturing technologies available for production of a pediatric bioabsorbable stent,” *BioMed research international*, vol. 2013, p. 137985, 2013.
- [6] M. Moravej and D. Mantovani, “Biodegradable metals for cardiovascular stent application: interests and new opportunities,” *International journal of molecular sciences*, vol. 12, no. 7, pp. 4250–4270, 2011.
- [7] M. Peuster, P. Beerbaum, F.-W. Bach et al., “Are resorbable implants about to become a reality?,” *Cardiology in the young*, vol. 16, no. 2, pp. 107–116, 2006.
- [8] Y. Li, J. Yan, W. Zhou et al., “In vitro degradation and biocompatibility evaluation of typical biodegradable metals (Mg/Zn/Fe) for the application of tracheobronchial stenosis,” *Bioactive materials*, vol. 4, pp. 114–119, 2019.
- [9] F. Witte, “Biodegradable Metals,” in *Biomaterials Science*, pp. 271–287, Elsevier, 2020.
- [10] P. Zartner, M. Buettner, H. Singer et al., “First biodegradable metal stent in a child with congenital heart disease: evaluation of macro and histopathology,” *Catheterization and cardiovascular interventions : official journal of the Society for Cardiac Angiography & Interventions*, vol. 69, no. 3, pp. 443–446, 2007.
- [11] P. Zartner, R. Cesnjevar, H. Singer et al., “First successful implantation of a biodegradable metal stent into the left pulmonary artery of a preterm baby,” *Catheterization and cardiovascular interventions : official journal of the Society for Cardiac Angiography & Interventions*, vol. 66, no. 4, pp. 590–594, 2005.
- [12] D. Schranz, P. Zartner, I. Michel-Behnke et al., “Bioabsorbable metal stents for percutaneous treatment of critical recoarctation of the aorta in a newborn,” *Catheterization and cardiovascular interventions : official journal of the Society for Cardiac Angiography & Interventions*, vol. 67, no. 5, pp. 671–673, 2006.
- [13] C. J. McMahon, P. Oslizlok, and K. P. Walsh, “Early restenosis following biodegradable stent implantation in an aortopulmonary collateral of a patient with pulmonary atresia and hypoplastic pulmonary arteries,” *Catheterization and cardiovascular interventions : official journal of the Society for Cardiac Angiography & Interventions*, vol. 69, no. 5, pp. 735–738, 2007.
- [14] J. Bennett, Q. de Hemptinne, and K. McCutcheon, “Magmaris resorbable magnesium scaffold for the treatment of coronary heart disease: overview of its safety and efficacy,” *Expert review of medical devices*, vol. 16, no. 9, pp. 757–769, 2019.
- [15] X. Liu, J. Sun, Y. Yang et al., “Microstructure, mechanical properties, in vitro degradation behavior and hemocompatibility of novel Zn–Mg–Sr alloys as biodegradable metals,” *Materials Letters*, vol. 162, pp. 242–245, 2016.
- [16] P. K. Bowen, J. Drelich, and J. Goldman, “Zinc exhibits ideal physiological corrosion behavior for bioabsorbable stents,” *Advanced materials (Deerfield Beach, Fla.)*, vol. 25, no. 18, pp. 2577–2582, 2013.

[17] H.-S. Han, S. Loffredo, I. Jun et al., “Current status and outlook on the clinical translation of biodegradable metals,” *Materials Today*, vol. 23, pp. 57–71, 2019.

[18] B. Wegener, A. Sichler, S. Milz et al., “Development of a novel biodegradable porous iron-based implant for bone replacement,” *Scientific reports*, vol. 10, no. 1, p. 9141, 2020.

[19] G. Gąsior, J. Szczepański, and A. Radtke, “Biodegradable Iron-Based Materials-What Was Done and What More Can Be Done?,” *Materials (Basel, Switzerland)*, vol. 14, no. 12, 2021.

[20] J. Hufenbach, H. Wendrock, F. Kochta et al., “Novel biodegradable Fe-Mn-C-S alloy with superior mechanical and corrosion properties,” *Materials Letters*, vol. 186, pp. 330–333, 2017.

[21] A. Drynda, T. Hassel, F. W. Bach et al., “In vitro and in vivo corrosion properties of new iron-manganese alloys designed for cardiovascular applications,” *Journal of biomedical materials research. Part B, Applied biomaterials*, vol. 103, no. 3, pp. 649–660, 2015.

[22] M. Peuster, P. Wohlsein, M. Brügmann et al., “A novel approach to temporary stenting: degradable cardiovascular stents produced from corrodible metal-results 6-18 months after implantation into New Zealand white rabbits,” *Heart (British Cardiac Society)*, vol. 86, no. 5, pp. 563–569, 2001.

[23] M. Peuster, C. Hesse, T. Schloo et al., “Long-term biocompatibility of a corrodible peripheral iron stent in the porcine descending aorta,” *Biomaterials*, vol. 27, no. 28, pp. 4955–4962, 2006.

[24] H. Hermawan, D. Dubé, and D. Mantovani, “Development of Degradable Fe-35Mn Alloy for Biomedical Application,” *Advanced Materials Research*, 15-17, pp. 107–112, 2006.

[25] H. Hermawan, H. Alamdari, D. Mantovani et al., “Iron–manganese: new class of metallic degradable biomaterials prepared by powder metallurgy,” *Powder Metallurgy*, vol. 51, no. 1, pp. 38–45, 2008.

[26] H. Hermawan, A. Purnama, D. Dube et al., “Fe-Mn alloys for metallic biodegradable stents: degradation and cell viability studies,” *Acta biomaterialia*, vol. 6, no. 5, pp. 1852–1860, 2010.

[27] D.-T. Chou, D. Wells, D. Hong et al., “Novel processing of iron-manganese alloy-based biomaterials by inkjet 3-D printing,” *Acta biomaterialia*, vol. 9, no. 10, pp. 8593–8603, 2013.

[28] D. Carluccio, C. Xu, J. Venezuela et al., “Additively manufactured iron-manganese for biodegradable porous load-bearing bone scaffold applications,” *Acta biomaterialia*, vol. 103, pp. 346–360, 2020.

[29] Y. Nie, G. Chen, H. Peng et al., “In vitro and 48 weeks in vivo performances of 3D printed porous Fe-30Mn biodegradable scaffolds,” *Acta biomaterialia*, vol. 121, pp. 724–740, 2021.

[30] V. Wagener, A. Schilling, A. Mainka et al., “Cell Adhesion on Surface-Functionalized Magnesium,” *ACS applied materials & interfaces*, vol. 8, no. 19, pp. 11998–12006, 2016.

[31] J. Huang, A. Gonzalez Orive, J. T. Krüger et al., “Influence of proteins on the corrosion of a conventional and selective laser beam melted FeMn alloy in physiological electrolytes,” *Corrosion Science*, vol. 200, p. 110186, 2022.

[32] J. Huang, M. Voigt, S. Wackenrohr et al., “Influence of hydrogel coatings on corrosion and fatigue of iron in simulated body fluid,” *Materials and Corrosion*, vol. 73, no. 7, pp. 1034–1044, 2022.

[33] J. Huang, Y. Qiu, F. Lücke et al., “Multiprotein Adsorption from Human Serum at Gold and Oxidized Iron Surfaces Studied by Atomic Force Microscopy and Polarization-Modulation Infrared Reflection Absorption Spectroscopy,” *Molecules*, vol. 28, no. 16, p. 6060, 2023.

[34] L. Stanciu and S. Diaz-Amaya, “Biodegradable materials for medical applications,” in *Introductory Biomaterials*, pp. 307–346, Elsevier, 2022.

[35] K.J.L. BURG and D. E. ORR, “An overview of bioresorbable materials,” in *Degradation Rate of Bioreversible Materials*, pp. 3–18, Elsevier, 2008.

[36] H. G. Seiler and H. Sigel, *Handbook on toxicity of inorganic compounds*, Marcel Dekker, United States, 1988.

[37] F. Feyerabend, J. Fischer, J. Holtz et al., “Evaluation of short-term effects of rare earth and other

elements used in magnesium alloys on primary cells and cell lines,” *Acta biomaterialia*, vol. 6, no. 5, pp. 1834–1842, 2010.

[38] N. J. Hallab, C. Vermes, C. Messina et al., “Concentration- and composition-dependent effects of metal ions on human MG-63 osteoblasts,” *Journal of biomedical materials research*, vol. 60, no. 3, pp. 420–433, 2002.

[39] A. Yamamoto, R. Honma, and M. Sumita, “Cytotoxicity evaluation of 43 metal salts using murine fibroblasts and osteoblastic cells,” *Journal of biomedical materials research*, vol. 39, no. 2, pp. 331–340, 1998.

[40] Huse EC., “A new ligature? ,” 172-2.

[41] E. W. ANDREWS, “ABSORBABLE METAL CLIPS AS SUBSTITUTES FOR LIGATURES AND DEEP SUTURES IN WOUND CLOSURE,” *Journal of the American Medical Association*, LXIX, no. 4, p. 278, 1917.

[42] M. G. SEELIG, “A STUDY OF MAGNESIUM WIRE AS AN ABSORBABLE SUTURE AND LIGATURE MATERIAL,” *Archives of Surgery*, vol. 8, no. 2, p. 669, 1924.

[43] G. Katarivas Levy, J. Goldman, and E. Aghion, “The Prospects of Zinc as a Structural Material for Biodegradable Implants—A Review Paper,” *Metals*, vol. 7, no. 10, p. 402, 2017.

[44] C. T. Chasapis, A. C. Loutsidou, C. A. Spiliopoulou et al., “Zinc and human health: an update,” *Archives of toxicology*, vol. 86, no. 4, pp. 521–534, 2012.

[45] X. Liu, J. Sun, K. Qiu et al., “Effects of alloying elements (Ca and Sr) on microstructure, mechanical property and in vitro corrosion behavior of biodegradable Zn–1.5Mg alloy,” *Journal of Alloys and Compounds*, vol. 664, pp. 444–452, 2016.

[46] C.-C. Tai, Y.-M. Huang, C.-K. Liaw et al., “Biocompatibility and Biological Performance of Additive-Manufactured Bioabsorbable Iron-Based Porous Interference Screws in a Rabbit Model: A 1-Year Observational Study,” *International journal of molecular sciences*, vol. 23, no. 23, 2022.

[47] X. Wang, H.M. Lu, X.L. Li, L. Li, Y.F. Zheng, “Effect of cooling rate and composition on microstructures and properties of Zn-Mg alloys,” pp.s122-125.

[48] E. Mostaed, M. Sikora-Jasinska, A. Mostaed et al., “Novel Zn-based alloys for biodegradable stent applications: Design, development and in vitro degradation,” *Journal of the mechanical behavior of biomedical materials*, vol. 60, pp. 581–602, 2016.

[49] G. Papanikolaou and K. Pantopoulos, “Iron metabolism and toxicity,” *Toxicology and applied pharmacology*, vol. 202, no. 2, pp. 199–211, 2005.

[50] N. C. Andrews, “Disorders of iron metabolism,” *The New England journal of medicine*, vol. 341, no. 26, pp. 1986–1995, 1999.

[51] Y. Zhou, P. Wu, Y. Yang et al., “The microstructure, mechanical properties and degradation behavior of laser-melted Mg Sn alloys,” *Journal of Alloys and Compounds*, vol. 687, pp. 109–114, 2016.

[52] C. C. Ng, M. M. Savalani, M. L. Lau et al., “Microstructure and mechanical properties of selective laser melted magnesium,” *Applied Surface Science*, vol. 257, no. 17, pp. 7447–7454, 2011.

[53] P. Wen, M. Voshage, L. Jauer et al., “Laser additive manufacturing of Zn metal parts for biodegradable applications: Processing, formation quality and mechanical properties,” *Materials & Design*, vol. 155, pp. 36–45, 2018.

[54] B. Song, S. Dong, S. Deng et al., “Microstructure and tensile properties of iron parts fabricated by selective laser melting,” *Optics & Laser Technology*, vol. 56, pp. 451–460, 2014.

[55] B. Song, S. Dong, Q. Liu et al., “Vacuum heat treatment of iron parts produced by selective laser melting: Microstructure, residual stress and tensile behavior,” *Materials & Design (1980-2015)*, vol. 54, pp. 727–733, 2014.

[56] K. Kumar, H. Kalita, D. Zindani et al., “Mechanical Behaviour of Materials,” in *Materials and*

*Manufacturing Processes*, K. Kumar, H. Kalita, D. Zindani et al., Eds., pp. 21–34, Springer International Publishing, Cham, 2019.

[57] P. P. Mueller, T. May, A. Perz et al., “Control of smooth muscle cell proliferation by ferrous iron,” *Biomaterials*, vol. 27, no. 10, pp. 2193–2200, 2006.

[58] R. Waksman, R. Pakala, R. Baffour et al., “Short-term effects of biocorrodible iron stents in porcine coronary arteries,” *Journal of interventional cardiology*, vol. 21, no. 1, pp. 15–20, 2008.

[59] C. Wu, H. Qiu, X.-Y. Hu et al., “Short-term safety and efficacy of the biodegradable iron stent in mini-swine coronary arteries,” *Chinese medical journal*, vol. 126, no. 24, pp. 4752–4757, 2013.

[60] W. Lin, L. Qin, H. Qi et al., “Long-term in vivo corrosion behavior, biocompatibility and bioresorption mechanism of a bioresorbable nitrided iron scaffold,” *Acta biomaterialia*, vol. 54, pp. 454–468, 2017.

[61] J.-F. Zheng, Z.-W. Xi, Y. Li et al., “Long-term safety and absorption assessment of a novel bioresorbable nitrided iron scaffold in porcine coronary artery,” *Bioactive materials*, vol. 17, pp. 496–505, 2022.

[62] C.-C. Tai, H.-L. Lo, C.-K. Liaw et al., “Biocompatibility and Biological Performance Evaluation of Additive-Manufactured Bioabsorbable Iron-Based Porous Suture Anchor in a Rabbit Model,” *International journal of molecular sciences*, vol. 22, no. 14, 2021.

[63] E. Scarcello and D. Lison, “Are Fe-Based Stenting Materials Biocompatible? A Critical Review of In Vitro and In Vivo Studies,” *Journal of functional biomaterials*, vol. 11, no. 1, 2019.

[64] S. Zhu, N. Huang, L. Xu et al., “Biocompatibility of pure iron: In vitro assessment of degradation kinetics and cytotoxicity on endothelial cells,” *Materials Science and Engineering: C*, vol. 29, no. 5, pp. 1589–1592, 2009.

[65] M. Asgari, R. Hang, C. Wang et al., “Biodegradable Metallic Wires in Dental and Orthopedic Applications: A Review,” *Metals*, vol. 8, no. 4, p. 212, 2018.

[66] H. Hermawan, D. Dubé, and D. Mantovani, “Degradable metallic biomaterials: design and development of Fe-Mn alloys for stents,” *Journal of biomedical materials research. Part A*, vol. 93, no. 1, pp. 1–11, 2010.

[67] D. Hong, D.-T. Chou, O. I. Velikokhatnyi et al., “Binder-jetting 3D printing and alloy development of new biodegradable Fe-Mn-Ca/Mg alloys,” *Acta biomaterialia*, vol. 45, pp. 375–386, 2016.

[68] S. Mandal, R. Ummadi, M. Bose et al., “Fe–Mn–Cu alloy as biodegradable material with enhanced antimicrobial properties,” *Materials Letters*, vol. 237, pp. 323–327, 2019.

[69] M. S. Dargusch, J. Venezuela, A. Dehghan-Manshadi et al., “In Vivo Evaluation of Bioabsorbable Fe-35Mn-1Ag: First Reports on In Vivo Hydrogen Gas Evolution in Fe-Based Implants,” *Advanced healthcare materials*, vol. 10, no. 2, e2000667, 2021.

[70] T. Kraus, F. Moszner, S. Fischerauer et al., “Biodegradable Fe-based alloys for use in osteosynthesis: outcome of an in vivo study after 52 weeks,” *Acta biomaterialia*, vol. 10, no. 7, pp. 3346–3353, 2014.

[71] B. Liu and Y. F. Zheng, “Effects of alloying elements (Mn, Co, Al, W, Sn, B, C and S) on biodegradability and in vitro biocompatibility of pure iron,” *Acta biomaterialia*, vol. 7, no. 3, pp. 1407–1420, 2011.

[72] T. Huang, J. Cheng, D. Bian et al., “Fe-Au and Fe-Ag composites as candidates for biodegradable stent materials,” *Journal of biomedical materials research. Part B, Applied biomaterials*, vol. 104, no. 2, pp. 225–240, 2016.

[73] J. Čapek, Š. Msallamová, E. Jablonská et al., “A novel high-strength and highly corrosive biodegradable Fe-Pd alloy: Structural, mechanical and in vitro corrosion and cytotoxicity study,” *Materials science & engineering. C, Materials for biological applications*, vol. 79, pp. 550–562, 2017.

[74] J. Cheng, T. Huang, and Y. F. Zheng, "Microstructure, mechanical property, biodegradation behavior, and biocompatibility of biodegradable Fe-Fe<sub>2</sub>O<sub>3</sub> composites," *Journal of biomedical materials research. Part A*, vol. 102, no. 7, pp. 2277–2287, 2014.

[75] V. P. M. Rabeeh and T. Hanas, "Progress in manufacturing and processing of degradable Fe-based implants: a review," *Progress in biomaterials*, vol. 11, no. 2, pp. 163–191, 2022.

[76] M. Schinhammer, A. C. Hänzi, J. F. Löffler et al., "Design strategy for biodegradable Fe-based alloys for medical applications," *Acta biomaterialia*, vol. 6, no. 5, pp. 1705–1713, 2010.

[77] F. Moszner, A. S. Sologubenko, M. Schinhammer et al., "Precipitation hardening of biodegradable Fe–Mn–Pd alloys," *Acta Materialia*, vol. 59, no. 3, pp. 981–991, 2011.

[78] M. Schinhammer, P. Steiger, F. Moszner et al., "Degradation performance of biodegradable Fe–Mn–C(-Pd) alloys," *Materials science & engineering. C, Materials for biological applications*, vol. 33, no. 4, pp. 1882–1893, 2013.

[79] M. Moravej, F. Prima, M. Fiset et al., "Electroformed iron as new biomaterial for degradable stents: development process and structure-properties relationship," *Acta biomaterialia*, vol. 6, no. 5, pp. 1726–1735, 2010.

[80] M. Moravej, A. Purnama, M. Fiset et al., "Electroformed pure iron as a new biomaterial for degradable stents: in vitro degradation and preliminary cell viability studies," *Acta biomaterialia*, vol. 6, no. 5, pp. 1843–1851, 2010.

[81] M. Moravej, S. Amira, F. Prima et al., "Effect of electrodeposition current density on the microstructure and the degradation of electroformed iron for degradable stents," *Materials Science and Engineering: B*, vol. 176, no. 20, pp. 1812–1822, 2011.

[82] P. H. de Moraes, S. Olate, M. Cantín et al., "Anatomical Reproducibility through 3D Printing in Cranio-Maxillo-Facial Defects," *International Journal of Morphology*, vol. 33, no. 3, pp. 826–830, 2015.

[83] R. Bibb, D. Eggbeer, P. Evans et al., "Rapid manufacture of custom-fitting surgical guides," *Rapid Prototyping Journal*, vol. 15, no. 5, pp. 346–354, 2009.

[84] K. M. Abate, A. Nazir, and J.-Y. Jeng, "Design, optimization, and selective laser melting of vin tiles cellular structure-based hip implant," *The International Journal of Advanced Manufacturing Technology*, vol. 112, 7-8, pp. 2037–2050, 2021.

[85] N. Sharma, D. Ostas, H. Rotar et al., "Design and Additive Manufacturing of a Biomimetic Customized Cranial Implant Based on Voronoi Diagram," *Frontiers in physiology*, vol. 12, p. 647923, 2021.

[86] M. I. Mohammed, A. P. Fitzpatrick, and I. Gibson, "Customised design of a patient specific 3D printed whole mandible implant," *KnE Engineering*, vol. 2, no. 2, p. 104, 2017.

[87] A. Edelmann, M. Dubis, and R. Hellmann, "Selective Laser Melting of Patient Individualized Osteosynthesis Plates-Digital to Physical Process Chain," *Materials (Basel, Switzerland)*, vol. 13, no. 24, 2020.

[88] M. H. Ali, N. Sabyrov, and E. Shehab, "Powder bed fusion–laser melting (PBF–LM) process: latest review of materials, process parameter optimization, application, and up-to-date innovative technologies," *Progress in Additive Manufacturing*, vol. 7, no. 6, pp. 1395–1422, 2022.

[89] X. Wang, S. Xu, S. Zhou et al., "Topological design and additive manufacturing of porous metals for bone scaffolds and orthopaedic implants: A review," *Biomaterials*, vol. 83, pp. 127–141, 2016.

[90] C. Y. Yap, C. K. Chua, Z. L. Dong et al., "Review of selective laser melting: Materials and applications," *Applied Physics Reviews*, vol. 2, no. 4, 2015.

[91] B. Nagarajan, Z. Hu, X. Song et al., "Development of Micro Selective Laser Melting: The State of the Art and Future Perspectives," *Engineering*, vol. 5, no. 4, pp. 702–720, 2019.

[92] D. Carluccio, M. Bermingham, D. Kent et al., "Comparative Study of Pure Iron Manufactured

by Selective Laser Melting, Laser Metal Deposition, and Casting Processes," *Advanced Engineering Materials*, vol. 21, no. 7, p. 1900049, 2019.

[93] J. T. Krüger, K.-P. Hoyer, and M. Schaper, "Bioresorbable AgCe and AgCeLa alloys for adapted Fe-based implants," *Materials Letters*, vol. 306, p. 130890, 2022.

[94] J. T. Krüger, "Adjustment of AgCaLa Phases in a FeMn Matrix via LBM for Implants with Adapted Degradation," *Crystals*, vol. 12, no. 8, p. 1146, 2022.

[95] N. Eliaz, "Corrosion of Metallic Biomaterials: A Review," *Materials (Basel, Switzerland)*, vol. 12, no. 3, 2019.

[96] D.J. Blackwood, "Biomaterials: Past Successes and Future Problems," *Corrosion Reviews*, vol. 21, 2-3, pp. 97–124, 2003.

[97] N. Eliaz, *Degradation of Implant Materials*, Springer New York, New York, NY, 2012.

[98] M. Talha, Y. Ma, P. Kumar et al., "Role of protein adsorption in the bio corrosion of metallic implants - A review," *Colloids and surfaces. B, Biointerfaces*, vol. 176, pp. 494–506, 2019.

[99] M. Schnabelrauch, N. Grujovic, and K. L. Choy, eds., *Biomaterials in Clinical Practice: Advances in Clinical Research and Medical Devices*, Springer, Cham, 2018.

[100] A. S. L. Yu, G. M. Chertow, V. A. Luyckx, et al., eds., *Brenner & Rector's the kidney*, Elsevier, [Philadelphia, PA], 2020.

[101] H. Hermawan, *Biodegradable Metals: From Concept to Applications*, Springer Berlin / Heidelberg, Berlin, Heidelberg, 2012.

[102] T. Gold, R. Azhari, and N. Lotan, "Enzyme-Promoted Degradation of Polymeric Matrices for Controlled Drug Delivery: Analytical Model and Numerical Simulations," in *Degradation of Implant Materials*, N. Eliaz, Ed., pp. 173–194, Springer New York, New York, NY, 2012.

[103] Di Mei, S. V. Lamaka, X. Lu et al., "Selecting medium for corrosion testing of bioabsorbable magnesium and other metals – A critical review," *Corrosion Science*, vol. 171, p. 108722, 2020.

[104] T. Kokubo, K. Hata, T. Nakamura et al., "Apatite Formation on Ceramics, Metals and Polymers Induced by a CaO SiO<sub>2</sub> Based Glass in a Simulated Body Fluid," in *Bioceramics*, pp. 113–120, Elsevier, 1991.

[105] T. Kokubo, "Bioactive glass ceramics: properties and applications," *Biomaterials*, vol. 12, no. 2, pp. 155–163, 1991.

[106] A. Oyane, H.-M. Kim, T. Furuya et al., "Preparation and assessment of revised simulated body fluids," *Journal of biomedical materials research. Part A*, vol. 65, no. 2, pp. 188–195, 2003.

[107] A. Yavorskyy, A. Hernandez-Santana, G. McCarthy et al., "Detection of calcium phosphate crystals in the joint fluid of patients with osteoarthritis - analytical approaches and challenges," *The Analyst*, vol. 133, no. 3, pp. 302–318, 2008.

[108] H. Hermawan, A. Purnama, D. Dube et al., "Fe-Mn alloys for metallic biodegradable stents: degradation and cell viability studies," *Acta biomaterialia*, vol. 6, no. 5, pp. 1852–1860, 2010.

[109] Y. Chen, W. Zhang, M. F. Maitz et al., "Comparative corrosion behavior of Zn with Fe and Mg in the course of immersion degradation in phosphate buffered saline," *Corrosion Science*, vol. 111, pp. 541–555, 2016.

[110] H. Dong, F. Lin, A. R. Boccaccini et al., "Corrosion behavior of biodegradable metals in two different simulated physiological solutions: Comparison of Mg, Zn and Fe," *Corrosion Science*, vol. 182, p. 109278, 2021.

[111] X. Liu, W. Li, Y. Cheng et al., "The effect of simulated inflammatory conditions on the corrosion of Mg, Fe and CoCrMo," *Materials Letters*, vol. 308, p. 131197, 2022.

[112] A. H. M. Yusop, N. M. Daud, H. Nur et al., "Controlling the degradation kinetics of porous iron by poly(lactic-co-glycolic acid) infiltration for use as temporary medical implants," *Scientific reports*, vol. 5, p. 11194, 2015.

[113] J. Zhou, Y. Yang, M. Alonso Frank et al., "Accelerated Degradation Behavior and

Cytocompatibility of Pure Iron Treated with Sandblasting," *ACS applied materials & interfaces*, vol. 8, no. 40, pp. 26482–26492, 2016.

[114] A. A. Sakkaf, F. S. Januddi, A. H. M. Yusop et al., "Challenges in the use of Fe-based materials for bone scaffolds applications: Perspective from in vivo biocorrosion," *Materials Today Communications*, vol. 33, p. 104564, 2022.

[115] M. Kiyama and T. Takada, "Iron Compounds Formed by the Aerial Oxidation of Ferrous Salt Solutions," *Bulletin of the Chemical Society of Japan*, vol. 45, no. 6, pp. 1923–1924, 1972.

[116] R. Gorejová, L. Haverová, R. Oriňáková et al., "Recent advancements in Fe-based biodegradable materials for bone repair," *Journal of Materials Science*, vol. 54, no. 3, pp. 1913–1947, 2019.

[117] Y. Liu, Y. Zheng, X.-H. Chen et al., "Fundamental Theory of Biodegradable Metals—Definition, Criteria, and Design," *Advanced Functional Materials*, vol. 29, no. 18, p. 1805402, 2019.

[118] R. Tolouei, J. Harrison, C. Paternoster et al., "The use of multiple pseudo-physiological solutions to simulate the degradation behavior of pure iron as a metallic resorbable implant: a surface-characterization study," *Physical chemistry chemical physics : PCCP*, vol. 18, no. 29, pp. 19637–19646, 2016.

[119] M. Salama, M. F. Vaz, R. Colaço et al., "Biodegradable Iron and Porous Iron: Mechanical Properties, Degradation Behaviour, Manufacturing Routes and Biomedical Applications," *Journal of functional biomaterials*, vol. 13, no. 2, 2022.

[120] E. Mouzou, C. Paternoster, R. Tolouei et al., "CO<sub>2</sub>-rich atmosphere strongly affects the degradation of Fe-21Mn-1C for biodegradable metallic implants," *Materials Letters*, vol. 181, pp. 362–366, 2016.

[121] H. P. Felgueiras, J. C. Antunes, M.C.L. Martins et al., "Fundamentals of protein and cell interactions in biomaterials," in *Peptides and Proteins as Biomaterials for Tissue Regeneration and Repair*, pp. 1–27, Elsevier, 2018.

[122] J. E. Contreras-Naranjo and O. Aguilar, "Suppressing Non-Specific Binding of Proteins onto Electrode Surfaces in the Development of Electrochemical Immunosensors," *Biosensors*, vol. 9, no. 1, 2019.

[123] X. Chen, J. Chen, and N. Huang, "The structure, formation, and effect of plasma protein layer on the blood contact materials: A review," *Biosurface and Biotribology*, vol. 8, no. 1, pp. 1–14, 2022.

[124] K. Wang, C. Zhou, Y. Hong et al., "A review of protein adsorption on bioceramics," *Interface focus*, vol. 2, no. 3, pp. 259–277, 2012.

[125] D. A. Puleo, ed., *Biological Interactions on Materials Surfaces: Understanding and Controlling Protein, Cell, and Tissue Responses*, Springer US, New York, NY, 2009.

[126] J. D. Andrade and V. Hlady, "Plasma protein adsorption: the big twelve," *Annals of the New York Academy of Sciences*, vol. 516, pp. 158–172, 1987.

[127] S. L. Hirsh, D. R. McKenzie, N. J. Nosworthy et al., "The Vroman effect: competitive protein exchange with dynamic multilayer protein aggregates," *Colloids and surfaces. B, Biointerfaces*, vol. 103, pp. 395–404, 2013.

[128] L. Vroman and A. L. Adams, "Findings with the recording ellipsometer suggesting rapid exchange of specific plasma proteins at liquid/solid interfaces," *Surface Science*, vol. 16, pp. 438–446, 1969.

[129] M. Pourbaix, "Electrochemical corrosion of metallic biomaterials," *Biomaterials*, vol. 5, no. 3, pp. 122–134, 1984.

[130] F. Contu, B. Elsener, and H. Böhni, "Serum effect on the electrochemical behaviour of titanium, Ti6Al4V and Ti6Al7Nb alloys in sulphuric acid and sodium hydroxide," *Corrosion Science*, vol. 46, no. 9, pp. 2241–2254, 2004.

[131] N. T. Kirkland, N. Birbilis, J. Walker et al., “In-vitro dissolution of magnesium-calcium binary alloys: clarifying the unique role of calcium additions in bioresorbable magnesium implant alloys,” *Journal of biomedical materials research. Part B, Applied biomaterials*, vol. 95, no. 1, pp. 91–100, 2010.

[132] D. F. Williams, I. N. Askill, and R. Smith, “Protein absorption and desorption phenomena on clean metal surfaces,” *Journal of biomedical materials research*, vol. 19, no. 3, pp. 313–320, 1985.

[133] S. Höhn, S. Virtanen, and A. R. Boccaccini, “Protein adsorption on magnesium and its alloys: A review,” *Applied Surface Science*, vol. 464, pp. 212–219, 2019.

[134] O. Klok, A. Igual Munoz, and S. Mischler, “An Overview of Serum Albumin Interactions with Biomedical Alloys,” *Materials (Basel, Switzerland)*, vol. 13, no. 21, 2020.

[135] Y. Hedberg, X. Wang, J. Hedberg et al., “Surface-protein interactions on different stainless steel grades: effects of protein adsorption, surface changes and metal release,” *Journal of materials science. Materials in medicine*, vol. 24, no. 4, pp. 1015–1033, 2013.

[136] Y. S. Hedberg, M. S. Killian, E. Blomberg et al., “Interaction of bovine serum albumin and lysozyme with stainless steel studied by time-of-flight secondary ion mass spectrometry and X-ray photoelectron spectroscopy,” *Langmuir : the ACS journal of surfaces and colloids*, vol. 28, no. 47, pp. 16306–16317, 2012.

[137] W. Xu, F. Yu, L. Yang et al., “Accelerated corrosion of 316L stainless steel in simulated body fluids in the presence of H<sub>2</sub>O<sub>2</sub> and albumin,” *Materials science & engineering. C, Materials for biological applications*, vol. 92, pp. 11–19, 2018.

[138] S. Karimi, T. Nickchi, and A. Alfantazi, “Effects of bovine serum albumin on the corrosion behaviour of AISI 316L, Co–28Cr–6Mo, and Ti–6Al–4V alloys in phosphate buffered saline solutions,” *Corrosion Science*, vol. 53, no. 10, pp. 3262–3272, 2011.

[139] V. Wagener, A.-S. Faltz, M. S. Killian et al., “Protein interactions with corroding metal surfaces: comparison of Mg and Fe,” *Faraday discussions*, vol. 180, pp. 347–360, 2015.

[140] E. Mouzou, C. Paternoster, R. Tolouei et al., “In vitro degradation behavior of Fe-20 Mn-1.2C alloy in three different pseudo-physiological solutions,” *Materials science & engineering. C, Materials for biological applications*, vol. 61, pp. 564–573, 2016.

[141] A. Kocjan, I. Milosev, and B. Pihlar, “The influence of complexing agent and proteins on the corrosion of stainless steels and their metal components,” *Journal of materials science. Materials in medicine*, vol. 14, no. 1, pp. 69–77, 2003.

[142] Y. Hedberg, M.-E. Karlsson, Z. Wei et al., “Interaction of Albumin and Fibrinogen with Stainless Steel: Influence of Sequential Exposure and Protein Aggregation on Metal Release and Corrosion Resistance,” *CORROSION*, vol. 73, no. 12, pp. 1423–1436, 2017.

[143] M. Lundin, Y. Hedberg, T. Jiang et al., “Adsorption and protein-induced metal release from chromium metal and stainless steel,” *Journal of colloid and interface science*, vol. 366, no. 1, pp. 155–164, 2012.

[144] C. Fleck and D. Eifler, “Corrosion, fatigue and corrosion fatigue behaviour of metal implant materials, especially titanium alloys,” *International Journal of Fatigue*, vol. 32, no. 6, pp. 929–935, 2010.

[145] W. Choi, H.-C. Shin, J. M. Kim et al., “Modeling and Applications of Electrochemical Impedance Spectroscopy (EIS) for Lithium-ion Batteries,” *Journal of Electrochemical Science and Technology*, vol. 11, no. 1, pp. 1–13, 2020.

[146] V. Mirceski, S. Skrzypek, and L. Stojanov, “Square-wave voltammetry,” *ChemTexts*, vol. 4, no. 4, 2018.

[147] S. H. Lee, S.-m. Park, and L. P. Lee, “Optical Methods in Studies of Olfactory System,” in *Bioelectronic Nose*, T. H. Park, Ed., pp. 191–220, Springer Netherlands, Dordrecht, 2014.

[148] M. A. Trelles and R. G. Calderhead, “PHOTOTHERAPY UNVEILED: A REVIEW OF

THE PHOTOBIOLOGICAL BASICS BEHIND ATHERMAL PHOTOBIMODULATION WITH LASERS AND OTHER LIGHT SOURCES. PART 1: LIGHT - ITS PROPERTIES AND PARAMETERS," *LASER THERAPY*, vol. 14, no. 2, pp. 87–95, 2005.

[149] G. Grundmeier, A. von Keudell, and T. de los Arcos, "Fundamentals and Applications of Reflection FTIR Spectroscopy for the Analysis of Plasma Processes at Materials Interfaces," *Plasma Processes and Polymers*, vol. 12, no. 9, pp. 926–940, 2015.

[150] P. R. Griffiths and J. A. de Haseth, eds., *Fourier Transform Infrared Spectrometry*, John Wiley & Sons, Inc, Hoboken, NJ, USA, 2007.

[151] P. Hollins, "Infrared Reflection–Absorption Spectroscopy," in *Encyclopedia of Analytical Chemistry*, R. A. Meyers, Ed., John Wiley & Sons, Ltd, Chichester, UK, 2006.

[152] "Specular Reflection," in *Fourier Transform Infrared Spectrometry*, P. R. Griffiths and J. A. de Haseth, Eds., pp. 277–301, John Wiley & Sons, Inc, Hoboken, NJ, USA, 2007.

[153] A. H. Kycia, K. Koczkur, J. J. Leitch et al., "Application of PM-IRRAS to study thin films on industrial and environmental samples," *Analytical and bioanalytical chemistry*, vol. 405, no. 5, pp. 1537–1546, 2013.

[154] I. Brand, "Polarization Modulation Infrared Reflection Absorption Spectroscopy: From Theory to Experiment," in *Application of Polarization Modulation Infrared Reflection Absorption Spectroscopy in Electrochemistry*, I. Brand, Ed., pp. 7–45, Springer International Publishing, Cham, 2020.

[155] I. Brand, ed., *Application of Polarization Modulation Infrared Reflection Absorption Spectroscopy in Electrochemistry*, Springer International Publishing, Cham, 2020.

[156] M. B. Mitchell, "Fundamentals and Applications of Diffuse Reflectance Infrared Fourier Transform (DRIFT) Spectroscopy," in *Structure-Property Relations in Polymers*, M. W. Urban and C. D. Craver, Eds., vol. 236, pp. 351–375, American Chemical Society, Washington, DC, 1993.

[157] J. COATES, "A REVIEW OF SAMPLING METHODS FOR INFRARED SPECTROSCOPY," in *Applied Spectroscopy*, pp. 49–91, Elsevier, 1998.

[158] N. J. Harrick, "SURFACE CHEMISTRY FROM SPECTRAL ANALYSIS OF TOTALLY INTERNALLY REFLECTED RADIATION \*," *The Journal of Physical Chemistry*, vol. 64, no. 9, pp. 1110–1114, 1960.

[159] J. Fahrenfort, "Attenuated total reflection," *Spectrochimica Acta*, vol. 17, no. 7, pp. 698–709, 1961.

[160] H. Kaur, B. Rana, D. Tomar et al., "Fundamentals of ATR-FTIR Spectroscopy and Its Role for Probing In-Situ Molecular-Level Interactions," in *Modern Techniques of Spectroscopy*, D. K. Singh, M. Pradhan, and A. Materny, Eds., vol. 13, pp. 3–37, Springer Singapore, Singapore, 2021.

[161] C. V. RAMAN and K. S. KRISHNAN, "A New Type of Secondary Radiation," *Nature*, vol. 121, no. 3048, pp. 501–502, 1928.

[162] T. Dey, "Microplastic pollutant detection by Surface Enhanced Raman Spectroscopy (SERS): a mini-review," *Nanotechnology for Environmental Engineering*, vol. 8, no. 1, pp. 41–48, 2023.

[163] A. Hubin and H. Terryn, "Chapter 6 X-ray photoelectron and Auger electron spectroscopy," in *Non-Destructive Microanalysis of Cultural Heritage Materials*, vol. 42, pp. 277–312, Elsevier, 2004.

[164] J. Sharma and B. C. Beard, "Fundamentals of X-ray Photoelectron Spectroscopy(XPS) and Its Applications to Explosives and Propellants," in *Chemistry and Physics of Energetic Materials*, S. N. Bulusu, Ed., pp. 569–585, Springer Netherlands, Dordrecht, 1990.

[165] I. Plikusiene, V. Maciulis, A. Ramanavicius et al., "Spectroscopic Ellipsometry and Quartz Crystal Microbalance with Dissipation for the Assessment of Polymer Layers and for the Application in Biosensing," *Polymers*, vol. 14, no. 5, 2022.

[166] H. Fujiwara, *Spectroscopic ellipsometry: Principles and applications*, Wiley, Chichester, 2009.

[167] J. Liu, Di Zhang, D. Yu et al., “Machine learning powered ellipsometry,” *Light, science & applications*, vol. 10, no. 1, p. 55, 2021.

[168] G. Binnig, C. F. Quate, and C. Gerber, “Atomic force microscope,” *Physical review letters*, vol. 56, no. 9, pp. 930–933, 1986.

[169] R. Shahbazian-Yassar, “Atomic Force Microscopy (AFM),” in *Encyclopedia of Tribology*, Q. J. Wang and Y.-W. Chung, Eds., pp. 129–133, Springer, Boston, MA, 2013.

[170] *Instrumentelle Analytik: Grundlagen — Geräte — Anwendungen*, Springer, Berlin, Heidelberg, 1996.

[171] K. Akhtar, S. A. Khan, S. B. Khan et al., “Scanning Electron Microscopy: Principle and Applications in Nanomaterials Characterization,” in *Handbook of materials characterization*, S. K. Sharma and D. Singh Verma, Eds., pp. 113–145, Springer, Cham, 2018.

[172] Nanoimages, “SEM Technology Overview – Scanning Electron Microscopy,” 7/11/2023, <https://www.nanoimages.com/sem-technology-overview/>.

[173] Nano Science Instruments, “Scanning Electron Microscopy,” 7/11/2023, <https://www.nanoscience.com/techniques/scanning-electron-microscopy/>.

[174] W. Bian, M. Wang, and Z. Yang, “Scanning Electron Microscope Calibration with SE2 and Inlens Detectors,” in *2019 IEEE 19th International Conference on Nanotechnology (IEEE-NANO)*, pp. 76–79, IEEE, 22.07.2019 - 26.07.2019.

[175] C. Temiz, “Scanning Electron Microscopy,” in *Electron Microscopy*, M. Mhadhbi, Ed., IntechOpen, 2022.

[176] T. Niendorf, F. Brenne, P. Hoyer et al., “Processing of New Materials by Additive Manufacturing: Iron-Based Alloys Containing Silver for Biomedical Applications,” *Metallurgical and Materials Transactions A*, vol. 46, no. 7, pp. 2829–2833, 2015.

[177] T. Niendorf, F. Brenne, and M. Schaper, “Lattice Structures Manufactured by SLM: On the Effect of Geometrical Dimensions on Microstructure Evolution During Processing,” *Metallurgical and Materials Transactions B*, vol. 45, no. 4, pp. 1181–1185, 2014.

[178] D. Nečas and P. Klapetek, “Gwyddion: an open-source software for SPM data analysis,” *Open Physics*, vol. 10, no. 1, pp. 181–188, 2012.

[179] Y. Yang, M. Yu, F. Böke et al., “Effect of nanoscale surface topography on the adsorption of globular proteins,” *Applied Surface Science*, vol. 535, p. 147671, 2021.

[180] Y. Yang, S. Knust, S. Schwiderek et al., “Protein Adsorption at Nanorough Titanium Oxide Surfaces: The Importance of Surface Statistical Parameters beyond Surface Roughness,” *Nanomaterials (Basel, Switzerland)*, vol. 11, no. 2, 2021.

[181] A. G. Hemmersam, K. Rechendorff, M. Foss et al., “Fibronectin adsorption on gold, Ti-, and Ta-oxide investigated by QCM-D and RSA modelling,” *Journal of colloid and interface science*, vol. 320, no. 1, pp. 110–116, 2008.

[182] F. Höök, J. Vörös, M. Rodahl et al., “A comparative study of protein adsorption on titanium oxide surfaces using in situ ellipsometry, optical waveguide lightmode spectroscopy, and quartz crystal microbalance/dissipation,” *Colloids and Surfaces B: Biointerfaces*, vol. 24, no. 2, pp. 155–170, 2002.

[183] T. F. Keller, J. Schönfelder, J. Reichert et al., “How the surface nanostructure of polyethylene affects protein assembly and orientation,” *ACS nano*, vol. 5, no. 4, pp. 3120–3131, 2011.

[184] D. H. K. Nguyen, V. T. H. Pham, M. Al Kobaisi et al., “Adsorption of Human Plasma Albumin and Fibronectin onto Nanostructured Black Silicon Surfaces,” *Langmuir : the ACS journal of surfaces and colloids*, vol. 32, no. 41, pp. 10744–10751, 2016.

[185] M. J. Desroches, N. Chaudhary, and S. Omanovic, “PM-IRRAS investigation of the interaction of serum albumin and fibrinogen with a biomedical-grade stainless steel 316LVM

surface," *Biomacromolecules*, vol. 8, no. 9, pp. 2836–2844, 2007.

[186] M. Bergkvist, J. Carlsson, and S. Oscarsson, "Surface-dependent conformations of human plasma fibronectin adsorbed to silica, mica, and hydrophobic surfaces, studied with use of Atomic Force Microscopy," *Journal of biomedical materials research. Part A*, vol. 64, no. 2, pp. 349–356, 2003.

[187] I. Firkowska-Boden, C. Helbing, T. J. Dauben et al., "How Nanotopography-Induced Conformational Changes of Fibrinogen Affect Platelet Adhesion and Activation," *Langmuir : the ACS journal of surfaces and colloids*, vol. 36, no. 39, pp. 11573–11580, 2020.

[188] S. Pasche, J. Vörös, H. J. Griesser et al., "Effects of ionic strength and surface charge on protein adsorption at PEGylated surfaces," *The journal of physical chemistry. B*, vol. 109, no. 37, pp. 17545–17552, 2005.

[189] M. Wasilewska, Z. Adamczyk, A. Pomorska et al., "Human Serum Albumin Adsorption Kinetics on Silica: Influence of Protein Solution Stability," *Langmuir : the ACS journal of surfaces and colloids*, vol. 35, no. 7, pp. 2639–2648, 2019.

[190] L. Huang, D. Shao, Y. Wang et al., "Human body-fluid proteome: quantitative profiling and computational prediction," *Briefings in bioinformatics*, vol. 22, no. 1, pp. 315–333, 2021.

[191] K. C. Dee, D. A. Puleo, and R. Bizios, *An Introduction To Tissue-Biomaterial Interactions*, John Wiley & Sons, Inc, New York, USA, 2002.

[192] P. Li, E. Y. Jiang, and H. L. Bai, "Fabrication of ultrathin epitaxial  $\gamma$ -Fe<sub>2</sub>O<sub>3</sub> films by reactive sputtering," *Journal of Physics D: Applied Physics*, vol. 44, no. 7, p. 75003, 2011.

[193] S. Wackenrohr, C. J. J. Torrent, S. Herbst et al., "Corrosion fatigue behavior of electron beam melted iron in simulated body fluid," *npj Materials Degradation*, vol. 6, no. 1, 2022.

[194] X. Gao, N. Yokota, H. Oda et al., "One Step Preparation of Fe–FeO–Graphene Nanocomposite through Pulsed Wire Discharge," *Crystals*, vol. 8, no. 2, p. 104, 2018.

[195] M. Li, J. Shen, C. Cheng et al., "Mulberry-like heterostructure (Fe-O-Ti): a novel sensing material for ethanol gas sensors," *RSC Advances*, vol. 9, no. 16, pp. 9022–9029, 2019.

[196] K. C. Dee, D. A. Puleo, and R. Bizios, eds., *An introduction to tissue-biomaterial interactions*, Wiley-Liss, Hoboken, N.J, Ü2002.

[197] Y. Shen, J. M. Jacobs, D. G. Camp et al., "Ultra-high-efficiency strong cation exchange LC/RPLC/MS/MS for high dynamic range characterization of the human plasma proteome," *Analytical chemistry*, vol. 76, no. 4, pp. 1134–1144, 2004.

[198] I. M. Vlasova and A. M. Saletsky, "Study of the denaturation of human serum albumin by sodium dodecyl sulfate using the intrinsic fluorescence of albumin," *Journal of Applied Spectroscopy*, vol. 76, no. 4, pp. 536–541, 2009.

[199] D. Yang, R. Kroe-Barrett, S. Singh et al., "IgG Charge: Practical and Biological Implications," *Antibodies (Basel, Switzerland)*, vol. 8, no. 1, 2019.

[200] "Protein Calculator v3.4," <http://protcalc.sourceforge.net/>.

[201] A. G. Hemmersam, M. Foss, J. Chevallier et al., "Adsorption of fibrinogen on tantalum oxide, titanium oxide and gold studied by the QCM-D technique," *Colloids and Surfaces B: Biointerfaces*, vol. 43, 3-4, pp. 208–215, 2005.

[202] A. Dolatshahi-Pirouz, N. Kolman, A. Arpanaei et al., "The adsorption characteristics of osteopontin on hydroxyapatite and gold," *Materials Science and Engineering: C*, vol. 31, no. 3, pp. 514–522, 2011.

[203] Y. Yang, S. Schwiderek, G. Grundmeier et al., "Strain-Dependent Adsorption of *Pseudomonas aeruginosa*-Derived Adhesin-Like Peptides at Abiotic Surfaces," *Micro*, vol. 1, no. 1, pp. 129–139, 2021.

[204] C. D. Tidwell, D. G. Castner, S. L. Golledge et al., "Static time-of-flight secondary ion mass spectrometry and x-ray photoelectron spectroscopy characterization of adsorbed albumin and fibronectin films," *Surface and Interface Analysis*, vol. 31, no. 8, pp. 724–733, 2001.

[205] K. P. Ishida and P. R. Griffiths, "Comparison of the Amide I/II Intensity Ratio of Solution and Solid-State Proteins Sampled by Transmission, Attenuated Total Reflectance, and Diffuse Reflectance Spectrometry," *Applied Spectroscopy*, vol. 47, no. 5, pp. 584–589, 1993.

[206] A. Barth, "The infrared absorption of amino acid side chains," *Progress in Biophysics and Molecular Biology*, vol. 74, 3-5, pp. 141–173, 2000.

[207] D. A. Belinskaia, P. A. Voronina, A. A. Batalova et al., "Serum Albumin," *Encyclopedia*, vol. 1, no. 1, pp. 65–75, 2021.

[208] A. L. Shaw, D. W. Mathews, J. E. Hinkle et al., "Absorption and safety of serum-derived bovine immunoglobulin/protein isolate in healthy adults," *Clinical and experimental gastroenterology*, vol. 9, pp. 365–375, 2016.

[209] T. Peters, "Serum Albumin," in *Advances in Protein Chemistry Volume 37*, vol. 37, pp. 161–245, Elsevier, 1985.

[210] M. Talha, Y. Ma, Y. Lin et al., "Corrosion behaviour of austenitic stainless steels in phosphate buffer saline solution: synergistic effects of protein concentration, time and nitrogen," *New Journal of Chemistry*, vol. 43, no. 4, pp. 1943–1955, 2019.

[211] M. A. Khan, R. L. Williams, and D. F. Williams, "The corrosion behaviour of Ti–6Al–4V, Ti–6Al–7Nb and Ti–13Nb–13Zr in protein solutions," *Biomaterials*, vol. 20, no. 7, pp. 631–637, 1999.

[212] Z. Wang, Y. Yan, and L. Qiao, "Protein adsorption on implant metals with various deformed surfaces," *Colloids and surfaces. B, Biointerfaces*, vol. 156, pp. 62–70, 2017.

[213] R. Oriňáková, R. Gorejová, Z. O. Králová et al., "Influence of albumin interaction on corrosion resistance of sintered iron biomaterials with polyethyleneimine coating," *Applied Surface Science*, vol. 509, p. 145379, 2020.

[214] S. A. Ragland and A. K. Criss, "From bacterial killing to immune modulation: Recent insights into the functions of lysozyme," *PLoS pathogens*, vol. 13, no. 9, e1006512, 2017.

[215] T. Imoto, L. N. Johnson, A. C.T. North et al., "Vertebrate lysozyme in Enzymes Vol. 7,".

[216] "Allied Metals-AlliedPureIron," <https://alliedmet.com/alliedpureiron/>.

[217] T. Niendorf, C. Lotze, D. Canadinc et al., "The role of monotonic pre-deformation on the fatigue performance of a high-manganese austenitic TWIP steel," *Materials Science and Engineering: A*, vol. 499, 1-2, pp. 518–524, 2009.

[218] J. Hankiewicz and E. Swierczek, "Lysozyme in human body fluids," *Clinica Chimica Acta*, vol. 57, no. 3, pp. 205–209, 1974.

[219] Z. Wei, J. Edin, A. E. Karlsson et al., "Can gamma irradiation during radiotherapy influence the metal release process for biomedical CoCrMo and 316L alloys?," *Journal of biomedical materials research. Part B, Applied biomaterials*, vol. 106, no. 7, pp. 2673–2680, 2018.

[220] Y. Yan, H. Yang, Y. Su et al., "Albumin adsorption on CoCrMo alloy surfaces," *Scientific reports*, vol. 5, p. 18403, 2015.

[221] S. E. Harandi, P. C. Banerjee, C. D. Easton et al., "Influence of bovine serum albumin in Hanks' solution on the corrosion and stress corrosion cracking of a magnesium alloy," *Materials science & engineering. C, Materials for biological applications*, vol. 80, pp. 335–345, 2017.

[222] M.J.K. Lodhi, K. M. Deen, Z. U. Rahman et al., "Electrochemical characterization and thermodynamic tendency of  $\beta$ -Lactoglobulin adsorption on 3D printed stainless steel," *Journal of Industrial and Engineering Chemistry*, vol. 65, pp. 180–187, 2018.

[223] T. Niendorf, F. Rubitschek, H. J. Maier et al., "On the Fatigue Crack Growth in High-Manganese Austenitic TWIP Steel - Influence of the Microstructure," in *Fatigue of Materials*, T. S. Srivatsan and M. A. Imam, Eds., pp. 55–66, John Wiley & Sons, Inc, Hoboken, NJ, USA, 2010.

[224] C. J. Rüsing, T. Niendorf, J. Lackmann et al., "Microstructure – deformation relationships in fine grained high manganese TWIP steel – the role of local texture," *International Journal of*

*Materials Research*, vol. 103, no. 1, pp. 12–16, 2012.

[225] Y. Zhong, L. Liu, S. Wikman et al., “Intragranular cellular segregation network structure strengthening 316L stainless steel prepared by selective laser melting,” *Journal of Nuclear Materials*, vol. 470, pp. 170–178, 2016.

[226] D. Carluccio, A. G. Demir, L. Caprio et al., “The influence of laser processing parameters on the densification and surface morphology of pure Fe and Fe-35Mn scaffolds produced by selective laser melting,” *Journal of Manufacturing Processes*, vol. 40, pp. 113–121, 2019.

[227] M. Nematollahi, M. Heidarian, M. Peikari et al., “Comparison between the effect of nanoglass flake and montmorillonite organoclay on corrosion performance of epoxy coating,” *Corrosion Science*, vol. 52, no. 5, pp. 1809–1817, 2010.

[228] A. Gebert, F. Kochta, A. Voß et al., “Corrosion studies on Fe-30Mn-1C alloy in chloride-containing solutions with view to biomedical application,” *Materials and Corrosion*, vol. 69, no. 2, pp. 167–177, 2018.

[229] C. Valero Vidal and A. Igual Muñoz, “Electrochemical characterisation of biomedical alloys for surgical implants in simulated body fluids,” *Corrosion Science*, vol. 50, no. 7, pp. 1954–1961, 2008.

[230] C. Tonna, C. Wang, Di Mei et al., “Biodegradation behaviour of Fe-based alloys in Hanks' Balanced Salt Solutions: Part I. material characterisation and corrosion testing,” *Bioactive materials*, vol. 7, pp. 426–440, 2022.

[231] Di Mei, C. Wang, S. V. Lamaka et al., “Clarifying the influence of albumin on the initial stages of magnesium corrosion in Hank's balanced salt solution,” *Journal of Magnesium and Alloys*, vol. 9, no. 3, pp. 805–817, 2021.

[232] F. Wang, X. de Ji, and X. L. Liu, “Synergistic Effect of Lysozyme and Vitamin B1 on the Corrosion Inhibition of Carbon Steel in Sulphuric Acid,” *Advanced Materials Research*, 463–464, pp. 895–899, 2012.

[233] L. He, Y. Cui, and C. Zhang, “The corrosion resistance, cytotoxicity, and antibacterial properties of lysozyme coatings on orthodontic composite arch wires,” *RSC Advances*, vol. 10, no. 31, pp. 18131–18137, 2020.

[234] S. R. Sousa and M. A. Barbosa, “Electrochemistry of AISI 316L stainless steel in calcium phosphate and protein solutions,” *Journal of Materials Science: Materials in Medicine*, vol. 2, no. 1, pp. 19–26, 1991.

[235] Y. Hedberg, M.-E. Karlsson, Z. Wei et al., “Interaction of Albumin and Fibrinogen with Stainless Steel: Influence of Sequential Exposure and Protein Aggregation on Metal Release and Corrosion Resistance,” *CORROSION*, vol. 73, no. 12, pp. 1423–1436, 2017.

[236] C. Wang, C. Tonna, Di Mei et al., “Biodegradation behaviour of Fe-based alloys in Hanks' Balanced Salt Solutions: Part II. The evolution of local pH and dissolved oxygen concentration at metal interface,” *Bioactive materials*, vol. 7, pp. 412–425, 2022.

[237] R. D. K. Misra and C. Nune, “Biological response to self-assembly of preadsorbed proteins at biointerfaces: significance, cellular activity and perspective,” *Materials Technology*, vol. 29, sup1, B41-B48, 2014.

[238] E. Rahimi, R. Offoia, S. Hosseinpour et al., “Effect of hydrogen peroxide on bovine serum albumin adsorption on Ti6Al4V alloy: A scanning Kelvin probe force microscopy study,” *Applied Surface Science*, vol. 563, p. 150364, 2021.

[239] M. Rabe, D. Verdes, and S. Seeger, “Understanding cooperative protein adsorption events at the microscopic scale: a comparison between experimental data and Monte Carlo simulations,” *The journal of physical chemistry. B*, vol. 114, no. 17, pp. 5862–5869, 2010.

[240] M. Rabe, D. Verdes, J. Zimmermann et al., “Surface organization and cooperativity during nonspecific protein adsorption events,” *The journal of physical chemistry. B*, vol. 112, no. 44, pp. 13971–13980, 2008.

[241] L. Müller and F. A. Müller, "Preparation of SBF with different HCO<sub>3</sub><sup>-</sup> content and its influence on the composition of biomimetic apatites," *Acta biomaterialia*, vol. 2, no. 2, pp. 181–189, 2006.

[242] V. Wagener and S. Virtanen, "Protective layer formation on magnesium in cell culture medium," *Materials science & engineering. C, Materials for biological applications*, vol. 63, pp. 341–351, 2016.

[243] V. Wagener, A. R. Boccaccini, and S. Virtanen, "Protein-adsorption and Ca-phosphate formation on chitosan-bioactive glass composite coatings," *Applied Surface Science*, vol. 416, pp. 454–460, 2017.

[244] M. Schinhammer, I. Gerber, A. C. Hänzi et al., "On the cytocompatibility of biodegradable Fe-based alloys," *Materials science & engineering. C, Materials for biological applications*, vol. 33, no. 2, pp. 782–789, 2013.

[245] H. Yang, S. Yang, J. Kong et al., "Obtaining information about protein secondary structures in aqueous solution using Fourier transform IR spectroscopy," *Nature protocols*, vol. 10, no. 3, pp. 382–396, 2015.

[246] K. V. Abrosimova, O. V. Shulenina, and S. V. Paston, "FTIR study of secondary structure of bovine serum albumin and ovalbumin," *Journal of Physics: Conference Series*, vol. 769, p. 12016, 2016.

[247] A. P. Kozlova, S. Sugiyama, A. I. Kozlov et al., "Iron-Oxide Supported Gold Catalysts Derived from Gold-Phosphine Complex Au(PPh<sub>3</sub>)(NO<sub>3</sub>): State and Structure of the Support," *Journal of Catalysis*, vol. 176, no. 2, pp. 426–438, 1998.

[248] W. Chen, Z. Fan, L. Gu et al., "Enhanced capacitance of manganese oxide via confinement inside carbon nanotubes," *Chemical communications (Cambridge, England)*, vol. 46, no. 22, pp. 3905–3907, 2010.

[249] G. Ren, Y. Yan, M. Sun et al., "Considerable Bacterial Community Structure Coupling with Extracellular Electron Transfer at Karst Area Stone in Yunnan, China," *Geomicrobiology Journal*, vol. 35, no. 5, pp. 424–431, 2018.

[250] S. Bernardini, F. Bellatreccia, G. Della Ventura et al., "A Reliable Method for Determining the Oxidation State of Manganese at the Microscale in Mn Oxides via Raman Spectroscopy," *Geostandards and Geoanalytical Research*, vol. 45, no. 1, pp. 223–244, 2021.

[251] C. A. Melendres, N. Camillone, and T. Tipton, "Laser raman spectroelectrochemical studies of anodic corrosion and film formation on iron in phosphate solutions," *Electrochimica Acta*, vol. 34, no. 2, pp. 281–286, 1989.

[252] Y. Chen, S. Zhang, J. Li et al., "Dynamic degradation behavior of MgZn alloy in circulating m-SBF," *Materials Letters*, vol. 64, no. 18, pp. 1996–1999, 2010.

[253] F. Barrère, P. Layrolle, C. A. van Blitterswijk et al., "Fast Formation of Biomimetic Ca-P Coatings on Ti6Al4V," *MRS Proceedings*, vol. 599, 1999.

[254] S. Keim, J. G. Brunner, B. Fabry et al., "Control of magnesium corrosion and biocompatibility with biomimetic coatings," *Journal of biomedical materials research. Part B, Applied biomaterials*, vol. 96, no. 1, pp. 84–90, 2011.

[255] J. G. Acheson, S. McKillop, P. Lemoine et al., "Control of magnesium alloy corrosion by bioactive calcium phosphate coating: Implications for resorbable orthopaedic implants," *Materialia*, vol. 6, p. 100291, 2019.

[256] S. Jiang, S. Cai, Y. Lin et al., "Effect of alkali/acid pretreatment on the topography and corrosion resistance of as-deposited CaP coating on magnesium alloys," *Journal of Alloys and Compounds*, vol. 793, pp. 202–211, 2019.

[257] W.-J. Lin, D.-Y. Zhang, G. Zhang et al., "Design and characterization of a novel biocorrodible iron-based drug-eluting coronary scaffold," *Materials & Design*, vol. 91, pp. 72–79, 2016.

[258] T. M. Di Palma, F. Migliardini, D. Caputo et al., “Xanthan and  $\kappa$ -carrageenan based alkaline hydrogels as electrolytes for Al/air batteries,” *Carbohydrate polymers*, vol. 157, pp. 122–127, 2017.

[259] F. Di Turo, P. Matricardi, C. Di Meo et al., “PVA hydrogel as polymer electrolyte for electrochemical impedance analysis on archaeological metals,” *Journal of Cultural Heritage*, vol. 37, pp. 113–120, 2019.

[260] W. G. Moon, G.-P. Kim, M. Lee et al., “A biodegradable gel electrolyte for use in high-performance flexible supercapacitors,” *ACS applied materials & interfaces*, vol. 7, no. 6, pp. 3503–3511, 2015.

[261] B. Ramírez Barat and E. Cano, “Agar versus Agarose Gelled Electrolyte for In Situ Corrosion Studies on Metallic Cultural Heritage,” *ChemElectroChem*, vol. 6, no. 9, pp. 2553–2559, 2019.

[262] E. A. El-hefian, M. M. Nasef, and A. H. Yahaya, “Preparation and Characterization of Chitosan/Agar Blended Films: Part 1. Chemical Structure and Morphology,” *E-Journal of Chemistry*, vol. 9, no. 3, pp. 1431–1439, 2012.

[263] T. Lpez, M. Picquart, G. Aguirre et al., “Thermal Characterization of Agar Encapsulated in TiO<sub>2</sub> Sol?Gel,” *International Journal of Thermophysics*, vol. 25, no. 5, pp. 1483–1493, 2004.

[264] M. Mahmoud Nasef, E. A. El-hefian, S. Saalah et al., “Preparation and Properties of Non-Crosslinked and Ionically Crosslinked Chitosan/Agar Blended Hydrogel Films,” *E-Journal of Chemistry*, vol. 8, s1, S409-S419, 2011.

[265] D. L. A. de Faria, S. Venâncio Silva, and M. T. de Oliveira, “Raman microspectroscopy of some iron oxides and oxyhydroxides,” *Journal of Raman Spectroscopy*, vol. 28, no. 11, pp. 873–878, 1997.

[266] K. Zaghib and C. M. Julien, “Structure and electrochemistry of FePO<sub>4</sub>·2H<sub>2</sub>O hydrate,” *Journal of Power Sources*, vol. 142, 1-2, pp. 279–284, 2005.

[267] J. He, F.-L. He, D.-W. Li et al., “Advances in Fe-based biodegradable metallic materials,” *RSC Advances*, vol. 6, no. 114, pp. 112819–112838, 2016.

[268] O. Klok, A. Igual Munoz, and S. Mischler, “An Overview of Serum Albumin Interactions with Biomedical Alloys,” *Materials (Basel, Switzerland)*, vol. 13, no. 21, 2020.

[269] R. J. Green, M. C. Davies, C. J. Roberts et al., “Competitive protein adsorption as observed by surface plasmon resonance,” *Biomaterials*, vol. 20, no. 4, pp. 385–391, 1999.

[270] A. Higuchi, K. Sugiyama, B. O. Yoon et al., “Serum protein adsorption and platelet adhesion on pluronic-adsorbed polysulfone membranes,” *Biomaterials*, vol. 24, no. 19, pp. 3235–3245, 2003.

[271] S. Gambaro, C. Paternoster, B. Occhionero et al., “Mechanical and degradation behavior of three Fe-Mn-C alloys for potential biomedical applications,” *Materials Today Communications*, vol. 27, p. 102250, 2021.

[272] S. Loffredo, S. Gambaro, L. Marin de Andrade et al., “Six-Month Long In Vitro Degradation Tests of Biodegradable Twinning-Induced Plasticity Steels Alloyed with Ag for Stent Applications,” *ACS biomaterials science & engineering*, vol. 7, no. 8, pp. 3669–3682, 2021.

[273] R. Oriňáková, R. Gorejová, Z. O. Králová et al., “Influence of albumin interaction on corrosion resistance of sintered iron biomaterials with polyethyleneimine coating,” *Applied Surface Science*, vol. 509, p. 145379, 2020.

[274] S. Sobanska, D. Deneele, J. Barbillat et al., “Natural weathering of slags from primary Pb–Zn smelting as evidenced by Raman microspectroscopy,” *Applied Geochemistry*, vol. 64, pp. 107–117, 2016.

[275] L. Parca, P. F. Gherardini, M. Helmer-Citterich et al., “Phosphate binding sites identification in protein structures,” *Nucleic acids research*, vol. 39, no. 4, pp. 1231–1242, 2011.

[276] E. Rahimi, R. Offoiach, K. Baert et al., “Role of phosphate, calcium species and hydrogen

peroxide on albumin protein adsorption on surface oxide of Ti6Al4V alloy,” *Materialia*, vol. 15, p. 100988, 2021.

[277] S. Huang, P. Wang, Y. Tian et al., “Blood species identification based on deep learning analysis of Raman spectra,” *Biomedical optics express*, vol. 10, no. 12, pp. 6129–6144, 2019.

[278] W. Querido, L. G. Abraçado, A. L. Rossi et al., “Ultrastructural and mineral phase characterization of the bone-like matrix assembled in F-OST osteoblast cultures,” *Calcified tissue international*, vol. 89, no. 5, pp. 358–371, 2011.

[279] R.-Q. Hou, N. Scharnagl, R. Willumeit-Römer et al., “Different effects of single protein vs. protein mixtures on magnesium degradation under cell culture conditions,” *Acta biomaterialia*, vol. 98, pp. 256–268, 2019.

[280] Z. Mardina, J. Venezuela, M. S. Dargusch et al., “The influence of the protein bovine serum albumin (BSA) on the corrosion of Mg, Zn, and Fe in Zahrina’s simulated interstitial fluid,” *Corrosion Science*, vol. 199, p. 110160, 2022.

[281] Y. Hedberg, X. Wang, J. Hedberg et al., “Surface-protein interactions on different stainless steel grades: effects of protein adsorption, surface changes and metal release,” *Journal of materials science. Materials in medicine*, vol. 24, no. 4, pp. 1015–1033, 2013.

[282] K. C. Dee, *An Introduction to Tissue-Biomaterial Interactions*, John Wiley & Sons Inc, Hoboken, 2003.

**List of abbreviations and symbols****ABBREVIATIONS**

Mg	Magnesium
Zn	Zinc
Fe	Iron
Mn	Manganese
FeMn	Iron–manganese alloy
Ca	Calcium
C	Carbon
Sr	Strontium
Li	Lithium
Cu	Copper
Ag	Silber
Au	Glod
Pd	Palladium
Co	Cobalt
Al	Aluminium
W	Tungsten
Sn	Zinn
B	Boron
S	Sulfur
V	Vanadium
Na	Sodium
K	Potassium
Cl	Chloride
$\text{HCO}_3^-$	Bicarbonate

---

## LIST OF ABBREVIATIONS AND SYMBOLS

---

Ge	Germanium
Si	Silicon
MRI	Magnetic resonance imaging
SBF	Simulated body fluid
m-SBF	Modified simulated body fluid
SMC	Smooth muscle cell
ISs	Based porous interference Screws
PM	Powder metallurgy
TWIP	Twinning-induced plasticity
SPS	Spark plasma sintering
AM	Additive manufacturing
SAD	Computer-aided design
PBF	Powder bed fusion
SLM	Selective laser melting
EBM	Electron beam melting
ECF	Extracellular fluids
ICF	Intracellular fluid.
NaCl	Sodium chloride
KCl	Potassium chloride
Na <sub>2</sub> HPO <sub>4</sub>	Disodium phosphate
KH <sub>2</sub> PO <sub>4</sub>	Monopotassium phosphate
HEPES	2-(4-(2-hydroxyethyl)-1-piperazinyl)ethanesulfonic acid
TRIS	Tris(hydroxymethyl)aminomethane.
PBS	Phosphate buffered saline
DMEM	Eagle's minimal essential medium
ROS	Reactive oxygen species

## LIST OF ABBREVIATIONS AND SYMBOLS

---

RMS	Root-mean-square
$\text{H}_2\text{O}_2$	Hydrogen peroxide
$\text{O}_2^-$	Superoxide
$\alpha\text{-FeOOH}$	Goethite
$\text{Fe}_3\text{O}_4$	Magnetite
IgG	Immunoglobulin G
IgA	Immunoglobulin A
LDL	Low-density lipoprotein
HDL	High-density lipoprotein
BSA	Bovine serum albumin
HSA	Human serum albumin
LYZ	Lysozyme
FBS	Fetal bovine serum
DC	Direct current
AC	Alternate current
CPE	Additional constant phase elements
IHP	Inner Helmholtz Plane
OHP	Outer Helmholtz Plane
EIS	Electrochemical impedance spectroscopy
CV	Cyclic voltammetry
AFM	Atomic force microscope
IR	Infrared spectrum
FTIR	Fourier-transformed infrared spectroscopy
FT-IRRAS	Fourier-transformed infrared reflection absorption spectroscopy
PM-IRRAS	Polarization modulation infrared reflection absorption spectroscopy
ATR-FTIR	Attenuated total reflection FTIR spectroscopy

---

## LIST OF ABBREVIATIONS AND SYMBOLS

---

IRE	Internal reflection elements
S/N	Signal-noise ratio
XPS	X-ray Photoelectron Spectroscopy
SEM	Scanning Electron Microscopy
LaB <sub>6</sub>	lanthanum hexaboride
FE-SEM	Field Emission Scanning Electron Microscopy
FEG	Field emission gun
ETD	Everhart-Thornley detector
EDX	Energy-dispersive X-ray spectroscopy
EtOH	Ethanol
OES	Optical emission spectroscopy
SiC	Silicon carbide
OCP	Open-circuit potential
FIB	Focused ion beam
LMIS	Liquid metal ion source
MCT	Mercury cadmium telluride
DTGS	Deuterated triglycine sulfate
IEP	Isoelectric point
EEC	Electrical equivalent circuit
EBSD	Electron backscattered diffraction

**SYMBOLS**

$Z$	Impedance
$R$	Resistor
$V$	Voltage
$I$	Current
$I_{corr}$	Corrosion current density
$V_{corr}$	Corrosion potential
$v_{corr}$	Corrosion rate in terms of penetration rate
$E$	Potential
$E_t$	Potential at time
$E_0$	Amplitude of the signal
$\omega$	Angular frequency
$f$	Frequency
$\varphi$	Phase angle shift
$t$	Time
$j$	Imaginary unit
$e$	Natural logarithm
$Z_{Re}$	Real component of impedance
$Z_{Im}$	Imaginary component of impedance
$R$	Resistor
$C$	Capacitor
$L$	Inductor
$Q_{CPE}$	Constant phase element
$R_{ct}$	Resistance of the charge transfer
$C_{dl}$	Capacitance of the double layer
$R_s$	Solution resistance
$\lambda$	Wavelength
$v$	Wave speed
$\Delta E$	Energy differences
$c$	Speed of light
$h$	Planck's constant
$n$	Refractive index
$\theta$	Angle of incidence
$\theta_c$	Critical angle

## LIST OF ABBREVIATIONS AND SYMBOLS

---

$d_p$	Penetration depth
$N$	Total number of internal reflections
$l$	Length
$d$	Thickness
$E_{kin}$	Kinetic energy
$E_b$	Binding energy
$\Phi$	Work function
$\Psi$	Amplitude ratio
$\Delta$	Phase difference
$k$	Extinction coefficient

## List of publications and conferences

### PUBLICATIONS

**J. Huang**, A. Suma, M. Cui, G. Grundmeier, V. Carnevale, Y. Zhang, C. Kielar, A. Keller; *Arranging Small Molecules with Sub-Nanometer Precision on DNA Origami Substrates for the Single-Molecule Investigation of Protein-Ligand Interactions*, Small Structures (2020), 1, 2000038.

**J. Huang**, A. Gonzalez Orive, J.T. Krüger, K.-P. Hoyer, A. Keller, G. Grundmeier; *Influence of proteins on the corrosion of a conventional and selective laser beam melted FeMn alloy in physiological electrolytes*, Corrosion Science (2022), 200, 110186.

**J. Huang**, M. Voigt, S. Wackenrohr, C. Ebbert, A. Keller, H.J. Maier, G. Grundmeier; *Influence of hydrogel coatings on corrosion and fatigue of iron in simulated body fluid*, Materials and Corrosion (2022), 73, 1034.

Christof J. J. Torrent, Philipp Krooß, **Jingyuan Huang**, Markus Voigt, Christoph Ebbert, Steffen Knust, Guido Grundmeier, Thomas Niendorf; *Oxide Modified Iron in Electron Beam Powder Bed Fusion—From Processability to Corrosion Properties*, Alloys 2022, 1(1), 31-53.

Jan Tobias Krüger, Kay-Peter Hoyer, **Jingyuan Huang**, Viviane Filor, Rafael Hernan Mateus-Vargas, Hilke Oltmanns, Jessica Meißner, Guido Grundmeier, Mirko Schaper; *Enhancing the degradation behavior of FeMn by degradable phases of an Ag alloy for adapted resorbable implants*, Journal of Functional Biomaterials (2022).

Y. Yang, **J. Huang**, D. Dornbusch, G. Grundmeier, K. Fahmy, A. Keller, D. Cheung; *Effect of surface hydrophobicity on the adsorption of a pilus-derived adhesin-like peptide*, Langmuir 2022, 38, 30, 9257–9265.

**J. Huang**, Y. Qiu, F. Lücke, J. Su, G. Grundmeier, A. Keller; *A. Multiprotein Adsorption from Human Serum at Gold and Oxidized Iron Surfaces Studied by Atomic Force Microscopy and Polarization-Modulation Infrared Reflection Absorption Spectroscopy*, Molecules 2023, 28, 6060.

CONFERENCES

EUROCORR 2022 - Corrosion in a Changing World: Energy, Mobility, Digitalization- **J. Huang** “*Influence of Hydrogel Coatings on Corrosion and Fatigue of Iron in Simulated Body Fluid*”-Poster presentation, Berlin, Germany

## **Funding and Contributions**

### **FUNDING**

This thesis research is part of two research projects funded by the German Research Foundation (DFG) under grant number 414365989 and 413259151, respectively.

### **CONTRIBUTIONS**

Chapter 6, section 6.1 - “Multiprotein adsorption on oxidized metal surfaces”:

Yunshu Qiu and Felix Lücke contributed to the preparation of gold and oxidized iron thin films as well as to the AFM measurements.

Chapter 6, section 6.2 - “Influence of proteins on the corrosion of a conventional and selective laser beam melted FeMn alloy”:

The FeMn-LBM samples were produced and provided by Jan Tobias Krüger, University of Paderborn, Direct Manufacturing Research Center. SEM and EBSD characterization of FeMn-LBM before corrosion tests was also done by Jan Tobias Krüger.

Chapter 6, section 6.3 - “Influence of Hydrogel Coatings on Corrosion of Iron in m-SBF”:

The electropolishing of the pure iron samples was done by Steffen Wackenrohr, Leibniz Universität Hannover, Institut für Werkstoffkunde (Materials Science).

XPS characterization was done by Markus Voigt, Paderborn University, Technical and Macromolecular Chemistry

Chapter 6, section 6.4 - “Corrosion of pure iron in human serum”:

XPS characterization of thin iron films was done by Jiangling Su, Paderborn University, Technical and Macromolecular Chemistry.

## Permissions

Part of the information (text, figures, and tables) presented in section 6.1 was reprinted from the journal *Molecules* (2023), 28(16), 6060, Multiprotein Adsorption from Human Serum at Gold and Oxidized Iron Surfaces Studied by Atomic Force Microscopy and Polarization-Modulation Infrared Reflection Absorption Spectroscopy, J. Huang, Y. Qiu, F. Lücke, J. Su, G. Grundmeier, and Adrian Keller. Inclusion of the manuscript in a thesis/dissertation is permitted by the Journal *Molecules* (<https://creativecommons.org/licenses/by/4.0/>).

Part of the information (text, figures, and tables) presented in section 6.2 was reprinted from the journal *Corrosion Science* (2022), 200, 110186, Influence of proteins on the corrosion of a conventional and selective laser beam melted FeMn alloy in physiological electrolytes, J. Huang, A. Gonzalez Orive, J.T. Krüger, K.-P. Hoyer, A. Keller, G. Grundmeier. Inclusion of the manuscript in a thesis/dissertation is permitted by the Journal of *Corrosion Science* (<https://www.elsevier.com/about/our-business/policies/copyright#Author-rights>).

Part of the information (text, figures, and tables) presented in section 6.3 was reprinted from the journal *Materials and Corrosion* (2022), 73, 1034, Influence of hydrogel coatings on corrosion and fatigue of iron in simulated body fluid, J. Huang, M. Voigt, S. Wackenrohr, C. Ebbert, A. Keller, H.J. Maier, G. Grundmeier. Inclusion of the manuscript in a thesis/dissertation is permitted by the Journal of *Materials and Corrosion* (<https://authorservices.wiley.com/author-resources/Journal-Authors/licensing/index.html>).

## Acknowledgement

Over the course of my researching and writing this thesis, I would like to express my thanks to all those who have helped me.

First of all, I would like to express my deepest gratitude to my academic supervisor Professor Dr. Guido Grundmeier, for his invaluable guidance throughout this research project. His patience, encouragement, support and understanding were instrumental in bringing this work to completion. This thesis would not have been possible without his keen insight and continuous motivation.

I am thankful to thank my research co-supervisor, Dr. Adrian Keller, for his guidance and numerous insightful discussions throughout my thesis and publications. His assistance has been present throughout my entire academic journey at Paderborn University, significantly impacting my learning experience.

I wish to extend my appreciation to the following organizations and people for providing support: Thanks to Nadine Buitkamp from the Department Coating Materials & Polymers for helping microstructure observations by SEM, FIB and EDX; Thanks to Christoph Ebbert for his invaluable contributions to the experimental design and technical support throughout the entire research process; I also wish to thank Markus Voigt and Jiangling Su for the experimental support at the XPS and the help with the data analysis. I am grateful for my SHK, Felix Lücke, in my work. They have consistently shown diligence, responsibility, and a willingness to share good ideas and new perspectives.

Further, I would like to express my gratitude to my colleagues for their help in both life and learning.

I thank Prof. Dr.-Ing. Thomas Niendorf, Dr. Jürgen Schmidtke and Prof. Dr. Martin Brehm for participating in the examination board of this work.

Additionally, I would like to thank my friends and family who have always been there for me, whether by my side, in my hometown, or in other countries. Although our daily lives may differ, you have always reminded me that I am not alone.

Lastly, I extend my appreciation to the funding agency that supported this research project.